Epitaxial Oxide Thin Films

Yuhan Zhu

St Anne's College

University of Oxford

A thesis submitted for the degree of

Doctor of Philosophy

Trinity Term 2022

Abstract

Growing transition metal oxides in the form of an ultrathin film can create new stoichiometries and structures that do not exist naturally, which may open new perspectives on the studies of oxide properties. This thesis focuses on the structural characterization of Nb, Ti, and V oxide thin films on the Au(111) substrates using scanning tunneling microscopy (STM).

The work starts with ring patterns created by *M*-Au substitutions (*M* = Nb, Ti, V, Mn). According to the rings' radii and centers, we can conduct a three-dimensional (3D) mapping of the substitutional sites. The ring's morphology is related to the curvature anisotropy of the Au isoenergy surface in ***k***-space.

Nb oxide has been studied most intensively in this project. Four structures of oxide monolayers have been identified which are (i) NbO_x cluster, (ii) NbO_y triangle, (iii) pinwheel, and (iv) the (2 × 2) Nb_2O_3 honeycomb (HC) structure. The pinwheel and honeycomb structures can form free films on the surface or embedded monolayers on the second layer. Nb-induced rings act as a precursor structure for an embedded monolayer.

Fourfold coordinated Nb atoms in Nb_2O_3 HC appear much brighter in STM images. The actual oxidation state of a fourfold coordinated Nb atom is between +4 and +5 due to the electron transfer to Au. According to the contrast difference and coordination number, mapping the Nb oxidation states with atomic resolution at room temperature can be realized. Besides, fourfold coordinated Nb atoms are involved in point defects, edges, and domain boundaries. Discussions on HC edges and defects are organized in two chapters. Comparative analysis between Nb_2O_3 and Ti_2O_3 constitutes pivotal sections.

Triangles and pinwheels are common structures in 2D materials. Nb and Ti oxides can form independently-standing triangles, and Nb/Ti/V oxides can generate both free and embedded pinwheel monolayers. A triangle building block model is proposed to elucidate the pinwheel comprising various sizes of triangle elements. Besides, Nb/Ti oxide triangles/pinwheels can be incorporated into HC monolayers by forming unique boundaries.

Preface

The work presented in this thesis was carried out by the author, under the supervision of Professor M. R. Castell, at the Department of Materials, University of Oxford from October 2018 to May 2022. The information derived from the literature has been duly acknowledged in the text and a list of references provided. No part of this thesis was previously presented for another degree or diploma at this or any other institution. All the data is my own work except for the theoretical results as follows.

- DFT-simulated STM images and the theoretical analysis of *M*-induced (*M* = Nb, Ti, V, Mn) ring pattern in Chapter 4 with Appendix II and Section 5.3 (Nb-induced rings); DFT-simulated STM images of fourfold coordinated Nb atoms in Chapter 6. They were carried out by Xinze Yang, a 2nd-year DPhil student of our research group.

- DFT-simulated STM images of Nb oxide tripod clusters in Section 5.4. It was carried out by Jacek Goniakowski and Claudine Noguera from CNRS-Sorbonne Université.

Parts of this work that have been published in peer-reviewed journals and presented at scientific conferences are as follows.

- Mapping the 3D Distribution and Vacancy-mediated Diffusion of Impurity Atoms below the Au(111) Surface
  Yuhan Zhu, Xinze Yang, Christopher E. Patrick and Martin R. Castell
  Submitted to *Physical Review B*, after peer-review, in correction.

- Determining the oxidation state of Nb ions in Nb_2O_3 honeycomb monolayer at atomic resolution
  Yuhan Zhu, Xinze Yang, and Martin R. Castell
  In preparation.

- The edge structure of Nb_2O_3 honeycomb monolayers on Au(111)
  Yuhan Zhu and Martin R. Castell
  Interdisciplinary Surface Science Conference (ISSC-23), 2021.
  Won the Poster Prize

Acknowledgment

This project would not have been possible without the support of many people. First of all, I would like to say a special thank you to my supervisor, Prof. Martin R. Castell. His support, guidance, and overall insights in this field have made this an inspiring experience for me. I would also like to thank the following people: Chris Spencer from JEOL, for instrument maintenance; Fubiao Gu, for teaching me how to use the instrument and helping me get through the first couple of months after my arrival; Xinze Yang, for doing the DFT calculations in the GR paper and fourfold Nb paper; Jacek Goniakowski and Claudine Noguera from CNRS-Sorbonne Université, for theoretical works in the edge, domain boundary, and cluster papers; and my colleagues Peiyu, Tairu, and Sisheng, who helped me a lot over the past three years.

I would like to express my sincere gratitude to China Scholarship Council (CSC) for awarding me a High-level Post-graduate (DPhil) Scholarship with tuition fees covered from 2018 to 2021. This is the second time that I have benefited from the CSC programs. The first time was when I was a master student in Germany in 2016. I would like to thank the Institute of Physics, UK, for awarding me the Physics Benevolent Fund. I am also thankful to the Department of Materials and St Anne's College, for providing me with the financial means to complete this project in 2022.

Finally, I would like to thank my parents for being my biggest supporter. I am truly blessed to have such wonderful parents. I cannot forget to thank my friends for their understanding, kindness, and positive influence.

List of Abbreviation

STM	Scanning tunneling microscope/microscopy
TEM	Transmission electron microscope/microscopy
STEM	Scanning transmission electron microscope/microscopy
APT	Atom probe tomography
LEED	Low-energy electron diffraction
RHEED	Reflection high-energy electron diffraction
HREELS	High-resolution electron energy loss spectroscopy
EDS	Energy-dispersive X-ray spectroscopy
AES	Auger electron spectroscopy
EELS	Electron energy loss spectroscopy
UHV	Ultra-high vacuum
RT	Room temperature
1D/2D/3D	One-/two-/three-dimensional
SMSI	Strong metal support interaction
ML	Monolayer
STO	Strontium titanate $SrTiO_3$
TMD	Transition metal dichalcogenides
h-BN	Hexagonal boron nitride
HC	Honeycomb
fcc	Face-centered cubic
hcp	Hexagonal close-packed
ZZ (Z)	Zigzag
AC (A)	Armchair
DV	Divacancy
TV	Tetravacancy
SW defect	Stone Wales defect
GB	Grain boundary
DB	Domain boundary
kMC	kinetic Monte Carlo
DFT	Density functional theory
DOS	Density of state
LDOS	Local density of state
DDOS	Directional density of state
SNR	Signal-to-noise ratio
MFA	Multiple-frame averaging
FFT	Fast Fourier transform
ROI	Region of interest
V_s	Sample bias
I_t	Tunneling current

Contents

Chapter 1 Introduction

1.1 Research background

Oxides play a significant role in materials science and have a wide range of applications in various fields such as optoelectronics, magneto-electronics, catalysis, and sensing [1–5]. Over the past decade, oxide thin films have attracted great research interest because they exhibit unique characteristics and potential applications compared with traditional bulk oxides [6]. Surface characterization techniques such as electron-based microscopy and spectroscopy can provide experimental details on atom configurations and electronic structures of the films. Computational approaches such as density functional theory (DFT) [7–9] and molecular dynamics (MD) simulation [10,11] offer supplementary information and can predict specific properties. By combining appropriate characterization methods and theoretical calculations, we can correlate the 2D structures to the properties and potential applications at the atomic level.

Nb, Ti, and V are three transition metal elements that sit closely in the periodic table and are capable of multiple oxidation states. Their oxide phases have many applications, for example, Nb_2O_5 is well known as a catalyst promoter [12]; TiO_2 show peculiar properties in photocatalytic reactions [13]; V_2O_5 is used for fabricating photochromic composite films [14]. Research concerning Nb/Ti/V oxide thin films has been carried out on metal substrates. Many new structures have been experimentally identified and theoretically simulated. But compared with graphene, 2D metal oxide thin films have received less attention in recent years.

Therefore, we are excited to further explore Nb, Ti, and V oxide thin films on the Au(111) substrates. This project focuses on the structural characterization of epitaxial oxide thin films using scanning tunneling microscopy (STM). Theoretical support comes from our collaborators, and hence the calculation details are not shown in this thesis. Nb has been most intensively

studied in this project. Ti oxides are often used to compare with Nb oxides because there are a number of commonalities between the two systems. Besides, the research work also involves V, Mn, and their oxide phases. Some V/Mn results are presented within the main text, and the other part that has not yet been well studied is put into the future work.

1.2 Outline of the thesis

The present study aims to provide structural information on Au-supported Nb/Ti/V oxide thin films. The comparative analysis between different oxides reveals the intrinsic properties of materials. This thesis is structured as follows:

Chapter 2 reviews three transition metal Nb/Ti/V oxides on noble metal substrates including Au, Pt, Pd, and Rh. Honeycomb and pinwheel are two typical structures that can be seen in many two-dimensional (2D) materials. The epitaxial oxide thin films in this study can form these two structures under certain conditions and exhibit distinctive characteristics. Apart from oxide thin films, reviews of honeycomb and pinwheel structures are extended to other 2D materials such as graphene, silicene, and transition-metal dichalcogenide.

Chapter 3 introduces experimental techniques and image processing methods. The working principle of the STM and the related quantum physics are emphasized. Besides, STM tip making, materials selection, and general preparation procedures are briefly illustrated. Image processing is critical for interpreting the STM images. We used SmartAlign to do image averaging in order to improve the signal-to-noise ratio. The operating principle is described in the subsection, and the mathematical support can be found in Appendix I.

Chapter 4 demonstrates how to achieve a 3D mapping of the impurity distribution below the Au(111) surface based on ring patterns. The ring patterns are created by Nb, Ti, V, and Mn atoms that substituted Au atoms before being oxidized. The STM results are of excellent quality,

some of which can resolve Au atoms. We can precisely determine the radius and center of a ring and thus deduce the buried site of the impurity atom. The ring patterns are not perfectly circular as they possess three brighter corners. This can be explained by the curvature anisotropy of the Au isoenergy surface in ***k***-space. Compared with previous reports, our work is more systematic and demanding as four metals are studied under room temperature. A paper based on this chapter has been reviewed and is currently in the correction process.

Nb oxides have been systematically studied in this project, so the following chapters center around their structural properties. First of all, Chapter 5 gives a general description of Nb oxides on Au(111) that we have observed within the range of experimental conditions. Basically, Nb oxide nanostructures on Au(111) include clusters, triangles, the pinwheel, and the most thermodynamically stable honeycomb structures. A variety of Nb oxide clusters is presented in a section, and parts of the work have been integrated into a research paper that is in preparation. Nb oxide triangle and pinwheel structures have not yet been reported, a section gives a brief introduction and our nomenclature for the triangles. The Nb_2O_3 honeycomb structure has been identified and reported by our research group before, whereas many detailed features are worth further study. The key features are indicated at the end of Chapter 5, and each will be separately expanded in the following chapters.

Chapter 6 is mainly concerned with the fourfold coordinated Nb atoms. We often observed protrusions with fourfold coordination and elevated brightness in the (2×2) Nb_2O_3 honeycomb monolayers, especially at the defective sites. We attributed them to Nb cations with a higher oxidation state and carried out the DFT simulation to confirm. In other words, simply by the coordination number and contrast in the STM images, we are able to map the oxidation state of Nb cations in the HC monolayers at the atomic level. Besides, we also demonstrate that these fourfold coordinated Nb play an important role in defects and domain boundaries. The sections in this chapter will be integrated into a research paper soon.

Chapter 7 and Chapter 8 focus on the features of honeycomb monolayers, including edge structures, defects, and domain boundaries. Chapter 7 presents a number of reconstructed edges with certain periodicities of the Nb_2O_3 HC monolayers. Possible structural models are given correspondingly based on the STM images. Ti_2O_3 HC exhibits distinct edge reconstruction with a higher density of edge atoms. Discussions of point defects and line defects, namely the domain boundaries, are written in Chapter 8. Two tetravacancies in Nb_2O_3 HC are newly found and have not yet been reported in other 2D materials. We summarize the structural solutions to four different types of boundaries and show some rare results of triple junctions in the Nb_2O_3 HC monolayers. The comparative analysis between two oxides with the same structure indicates the effect of cation type. Combined with the theoretical calculations, which are currently with our collaborators from Paris, these excellent results will be written in two papers.

Chapter 9 displays the experimental results of the triangle and pinwheel structures of Nb, Ti, and V oxides. Without the support from theoretical simulations, the interpretation of the STM images and the proposed structural models are tentative. We collected a full set of Nb/Ti single triangles with sizes *n* ranging from one to ten. Therefore, we are able to propose a triangle building block model to elucidate the structure of the pinwheel networks that comprise triangle elements with various sizes. V oxide pinwheel is distinct and more complex than Nb/Ti. Neither the triangle building block model nor the Moiré pattern model can well reproduce the atom configurations revealed in the STM images. Except for the Ti oxide pinwheel structure, the results present in this chapter have not yet been found in the previous reports. But careful interpretation and theoretical support are required before writing up papers.

Chapter 10 summarizes the research work in this thesis and highlights the conclusions from each chapter. In future work, we point out the major limitations in the present work and show some preliminary results of V oxides and Mn oxides on Au(111). These promising results require further investigations and analysis in both experimental and theoretical aspects.

Chapter 2 Literature review

Oxides play a significant role in materials science because they have a wide application in many fields such as inorganic pigments [15], optoelectronics [1], digital storage media [2], electrochemical energy storage [16], heterogeneous catalysis [3,4], gas sensing [5] to name a few. Oxide thin films have attracted significant research interest over many years because they exhibit distinctive features and application potential compared with traditional bulk oxides [6]. An ultrathin oxide film consists of only a few monolayers (MLs) with a typical thickness of 1 ~ 2 nm [17]. The term "monolayer" refers to a single, close-packed layer of atoms or molecules [18] and is commonly used to describe the coverage of 2D materials. In the oxide/metal substrate systems, it is well accepted to define ML with respect to the substrate [19]. Due to the ultrathin nature, new stoichiometries, structures, and peculiar properties can be induced, which are rarely seen in the natural bulk oxides.

This chapter provides a brief review of three oxide thin films: Nb, Ti, and V oxides, as they are the three materials that have been studied in this DPhil project. Oxide thin films are able to exhibit a variety of structures, among which the honeycomb and the pinwheel structures are commonly observed with distinct features. Therefore, these two structures will be discussed and summarized in Section 2.2 and Section 2.3.

2.1 Oxide thin films

2.1.1 Nb oxides

Nb is an intriguing transition metal element and has a wide application in the forms of alloy and oxides. Niobium alloys are commonly found in structural steels [20], superalloys [21], and superconducting magnets [22]. Whereas Nb oxides exhibit peculiar properties in the catalytic

process [23]. As a catalyst promoter or catalyst support, niobium oxide (e.g., Nb_2O_5) can remarkably enhance the catalytic activity and prolong the catalyst life [12]. Due to the electron configuration of Nb atom ([Kr] $4d^45s^1$), niobium oxides are reducible with a wide range of stoichiometries and oxidation states (up to +5) [24]. The molecular structures of surface niobium oxides have been investigated on Al_2O_3, TiO_2, ZrO_2, MgO, and SiO_2 supports with Raman spectroscopy [25]. Studies of niobium oxides have also been carried out on noble metal substrates such as Pt [26], Cu [24], Au [27], and Cu_3Au [28].

Xie *et al*. studied niobium thin films on the Pt(111) substrates using electron spectroscopic techniques. They found that the Pt-supported Nb oxide thin films could form an epitaxial monolayer composed of NbO, NbO_2, and Nb_2O_5. The Nb_2O_5 thin films on Pt(111) have a similar electronic structure but different surface periodicity compared with the bulk counterpart. The low electron energy diffraction (LEED) pattern showed that Nb_2O_5 formed a (1 × 1) hexagonal lattice with respect to the Pt(111) when the thickness reached two monolayers [26]. Nakayama and co-workers investigated Nb_xO_y clusters on the Cu(111) substrates [24]. They used a dc magnetron sputtering to fabricate the Nb_xO_y clusters, thus producing various sizes and stoichiometries such as Nb_3O_7, Nb_5O_{10}, and the reduced counterparts Nb_3O_5, Nb_4O_7. It was shown that the oxide clusters had an average radius of 3 Å at a coverage of 0.13-0.3 ML on Cu(111). Therefore, they were insufficient to form thin films without any post-treatment [24]. Unfortunately, there had been no microscopic studies of niobium oxide thin films on Pt or Cu.

Wang *et al*. studied the niobium oxide submonolayers on the Au(111) substrates using STM. It has been demonstrated that a rumpled (2 × 2) Nb_2O_3 honeycomb structure can be formed on Au(111), as shown in Figure 2-1. Nb atoms sit at the threefold hollow sites of the Au(111) surface, and O atoms locate on the top of Au atoms. The O layer is above the Nb layer by 0.93 Å to release the compressive stress due to the lattice mismatch. Besides, DFT calculation shows

that the film has a large electron transfer from Nb to Au (1.28*e* per Nb_2O_3), which means the oxidation state of the Nb atoms in an Au-supported Nb_2O_3 thin film is higher than +3.

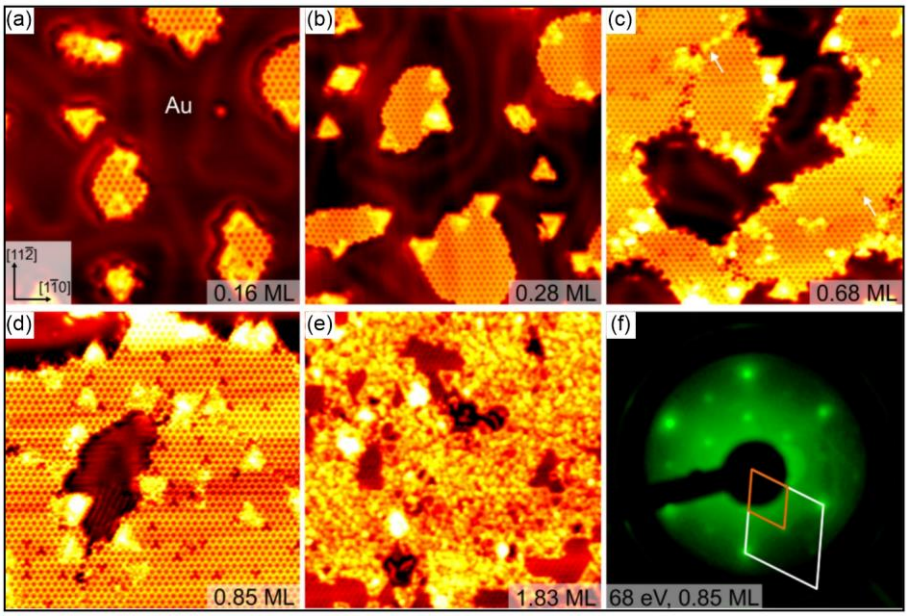

Figure 2-1 STM images of the (2 × 2) Nb_2O_3 honeycomb structure on the Au(111) substrates. (a) – (e) show the thin film by increasing the coverage. (f) LEED pattern of the (2 × 2) Nb_2O_3 honeycomb structure on the Au(111). Image width: (a) 21 nm; (b) 27 nm; (c) 24.7 nm; (d) 24 nm; (e) 30 nm. STM images were taken at V_s = 0.4 – 1 V, I_t = 0.16 – 0.26 nA [27].

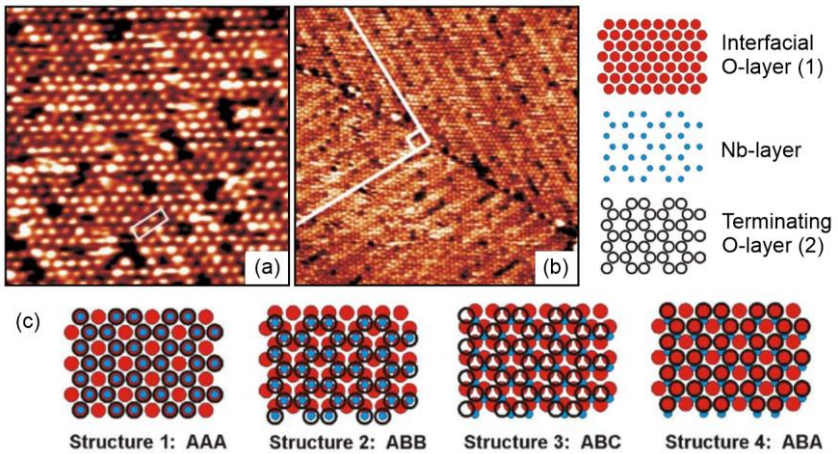

Figure 2-2 STM images of Nb_2O_5 thin films on the $Cu_3Au(100)$. (a) Hexagonal structure with a few vacancies (15 nm × 15 nm). (b) Two domains rotated by 90°. (40 nm × 40 nm) Imaging condition: V_s = 1.4 V, I_t = 1.0 nA (c) Four proposed structural models for the stacking sequence of Nb_2O_5 with O-Nb-O triple layers [28].

Apart from pure noble metal substrates, an alloy of noble metals can also be used as a substrate for epitaxial growth of Nb oxide thin film. Starr *et al*. reported that Nb_2O_5 film exhibited a

hexagonal symmetry on the $Cu_3Au(100)$ substrate when it covered the entire surface, as shown in Figure 2-2. Four structural models were proposed for the Nb_2O_5 film with different registries in the stacking sequences. However, unlike the Nb atoms forming the honeycomb lattice in Figure 2-1(a) – (d), the protrusions in the STM images in Figure 2-2(b) were not attributed to Nb atoms but the bridge sites between two "open" Nb atoms with unoccupied d-states.

2.1.2 Ti oxides

Nanostructured Titania (TiO_2) has attracted much research interest due to its peculiar properties in photocatalytic reactions [13], solar cells [29], and hydrogen sensors [30]. In particular, the catalytic effect of Pt on CO hydrogenation can be significantly enhanced when it is dispersed on TiO_2 supports due to the strong metal support interaction (SMSI) [31]. The well-known SMSI has been intensively studied through inverse models, namely oxides supported on metal substrates [32]. Such systems can provide more ordered structures and make the application of surface characterization techniques more convenient and efficient. For instance, titanium oxide thin films grown on noble metal substrates have been one of the best-characterized model systems in surface science [33]. This section will give a short review of the Ti oxide thin films on Pt [33–39], Pd [40], Ag [41], and Au [42,43] substrates.

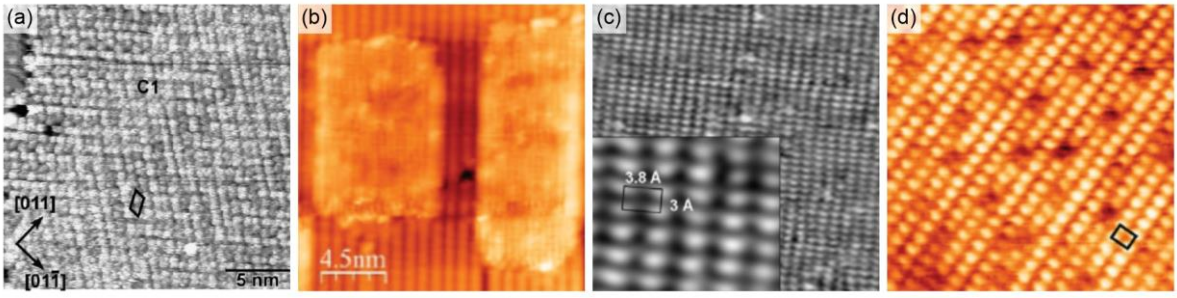

Figure 2-3 STM images of (a) $\left(4 \times 3\sqrt{5}\right)R60°$ TiO_2 thin film on Pt(100) (21.5 nm × 21.5 nm, V_s = 0.18 V, I_t = 0.36 nA) [35]. The parallelogram superimposed on the image indicates the unit cell. (b) 1 ML-equivalent TiO_2 ultrathin film on (1 × 2)-Pt(110) (20.1 nm × 20.1 nm, V_s = 1.9 V, I_t = 2.3 nA) [38]. (c) The *rect*-TiO_2 phase on Pt(111) (11.1 nm × 11.1 nm, V_s = 0.8 V, I_t = 0.9 nA). The inset shows the structure at atomic resolution [36]. (d) TiO_2 monolayer on Ag(100) (6.3 nm × 6.3 nm, V_s = 0.12 V, I_t = 0.2 nA) [41].

Ti oxide thin films exhibit a variety of structures depending on the metal substrates, film thickness, and growth condition. Matsumoto *et al*. investigated Ti oxides on Pt(100) using two synthesis methods [35]. They obtained a flat Ti_2O_3 layer with a (3 × 5) periodicity by oxidizing a Pt_3Ti alloy in ozone, and a TiO_2 layer with $\left(4 \times 3\sqrt{5}\right)R60°$ periodicity using reactive deposition in oxygen [Figure 2-3(a)]. Figure 2-3(b) shows a STM image of 1 ML-equivalent TiO_2 on the (1 × 2)-Pt(110) reconstructed surface. The morphology of the epitaxial films gives rise to a (14 × 4) coincidence superstructure [34,38]. Besides, TiO_2 thin film with a rectangular phase (*rect*-TiO_2) can also be obtained on Pt(111) by a large deposition amount (> 0.8 ML) in high-pressure oxygen (> 10^{-4} Pa). As shown in Figure 2-3(c), the size of the unit cell is 3.8 Å × 3 Å, but the axes of the rectangular structure are not aligned with the principal directions of Pt(111) with a tilting angle of 8.3° [33,36]. Andrea and co-workers studied Ti oxides on Ag(100) and provided the STM image in Figure 2-3(d). Combining with the DFT calculations, they reported that the Ag-supported TiO_2 with a lepidocrocite-like structure was more stable than other structures derived from crystallographic planes of bulk TiO_2 phases [41].

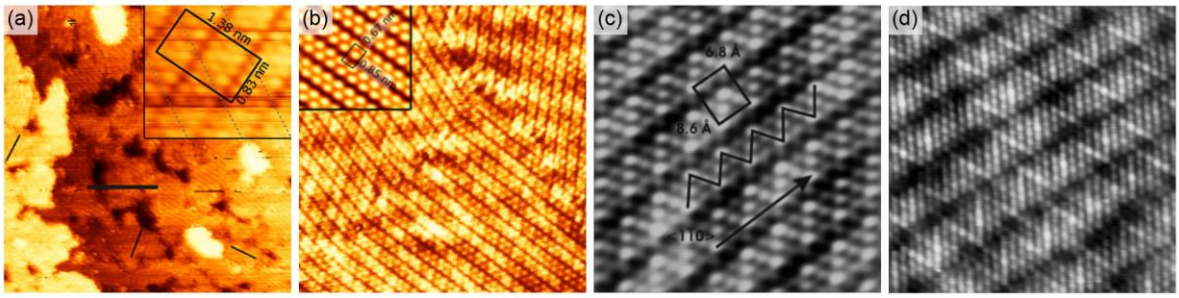

Figure 2-4 STM images of (a) TiO_x, x ~ 0.75 on Pd(100) (40.6 nm × 40.6 nm). The inset shows the (3 × 5) unit cell [40]. (b) TiO_x, x < 2 on Pd(111) (21.7 nm × 21.7 nm) [40]. (c) *z*-TiO_x phase on Pt(111) (6 nm × 6 nm, V_s = 0.1 V, I_t = 1.5 nA); (d) *z*'-TiO_x phase on Pt(111) (9 nm × 9 nm, V_s = 0.8 V, I_t = 1.5 nA [33].

In contrast to the simple parallelogram or rectangular unit, the partially oxidized TiO_x (x ~ 0.75) on Pd(100) exhibits a (3 × 5) periodicity with a zigzag pattern [40]. The inset in Figure 2-4(a) indicates the unit cell where a trench can be seen every three rows. Protrusions in the rows were attributed to Ti atoms with a close-packed arrangement. Interestingly, the structure of the

partially oxidized TiO_x (x < 2) layers on Pd(111) resembles that on Pd(100), but it only consists of two Ti rows in the zigzag pattern [Figure 2-4(b)]. The zigzag motifs of partially oxidized TiO_x thin film have also been observed on Pt(111). Sedona *et al*. reported two dense phases of TiO_x at a coverage of 0.8 ML on Pt(111) and denoted them as *z*-TiO_x and *z*'-TiO_x [Figure 2-4(c), (d)]. *z*'-TiO_x can be transformed from the *z*-TiO_x phase in a reduced environment [33].

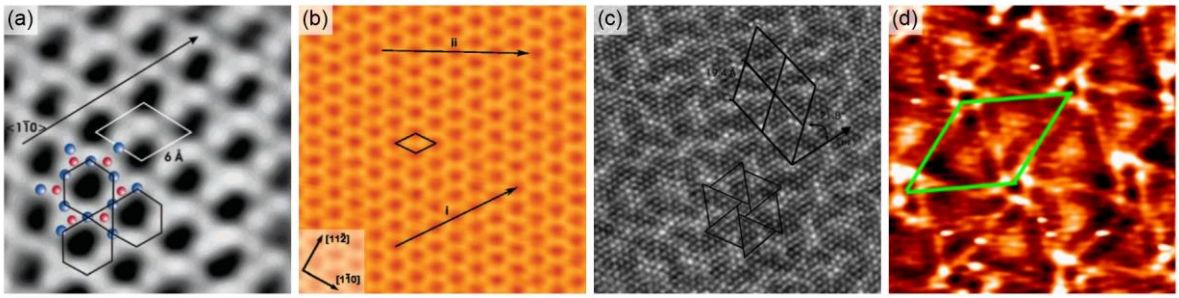

Figure 2-5 STM images of (a) *k*-TiO_x phase on Pt(111) (3 nm × 3 nm, V_s = -0.4 V, I_t = 1.06 nA) [33]. (b) (2 × 2) Ti_2O_3 honeycomb structure on Au(111) (7.8 nm × 7.8 nm, V_s = 0.98 V, I_t = 0.2 nA) [42]. (c) *w*'-TiO_x phase on Pt(111) (12.6 nm × 12.6 nm, V_s = 0.2 V, I_t = 1.0 nA) [33]. (d) Ti oxide pinwheel structure on Au(111) (8.9 nm × 8.9 nm, V_s = 0.1 V, I_t = 1.5 nA) [43].

TiO_x on Pt(111) at low coverages (i.e., 0.4 ML) gives rise to a Kagomé-like phase (*k*-TiO_x). The STM image in Figure 2-5(a) was obtained at a negative sample bias and the protrusions are therefore attributed to oxygen atoms [33]. Combining the STM results with the LEED pattern, it is straightforward to construct the structural model, as indicated by blue (Ti) and red (O) balls on the image, and determine the stoichiometry of Ti_2O_3. The hexagonal superstructure of Ti_2O_3 has been found on Au(111) as well. Wu *et al*. reported the (2 × 2) Ti_2O_3 on Au(111) using the term honeycomb structure, as the STM image in Figure 2-5(b) was obtained at a positive bias showing the Ti configuration [42]. The periodicities of Ti_2O_3 monolayers epitaxially grown on Au(111) and Pt(111) are approximate (~ 6 Å) due to the close lattice constants of the substrate surface unit cells ($a_{Au} = 2.87$ Å, $a_{Pt} = 2.77$ Å). Moreover, Ti oxide thin films with "wagon wheel" or "pinwheel" structures have been found on Pt(111) as well as Au(111) [Figure 2-5(c), (d)] [33,42,43]. The pinwheel structure is common in 2D thin films. A detailed discussion can be seen in Section 2.3.

2.1.3 V oxides

It is well-known that vanadium has several stable oxidation states (+2, +3, +4, and +5), each of which corresponds to a specific color in solution (purple, green, blue, and yellow) [44]. The conversion between vanadium compounds with different oxidation states and stoichiometries is relatively easy to realize through redox reactions. For example, V_2O_5 photochromism can be generated by photo-reduction of V^{5+} with a visible laser light, which results in the yellow V_2O_5 turning into blue-black [45]. Besides, vanadium oxides exhibit peculiar electronic, magnetic, and catalytic properties due to multiple oxidation states and easy transition. VO_2 and V_2O_3 are potential materials for developing high-speed electronics. V_3O_5 calls attention due to the anti-ferromagnetic-paramagnetic transition at 75 K upon heating. Monoclinic VO_2 and the layered V_2O_5, V_3O_7, V_4O_9, and V_6O_{13} can be used to fabricate cathodes of lithium-ion batteries [46].

In the 2D regime, vanadium oxide thin films have been grown on a wide range of substrates, including oxide supports (e.g., Al_2O_3, TiO_2, SiO_2, etc.) [47] and noble metals. Netzer's group has intensively studied vanadium oxides on Pd and Rh substrates. Various structures have been characterized by STM images and LEED patterns, with oxidation states and stoichiometries determined by high-resolution electron energy loss spectroscopy (HREELS) and DFT structural models. A brief review of VO_x thin films on Au [48–53], Cu_3Au [54], Pd [32,55,64,56–63], and Rh [60,62,65–71] regarding the structural properties will be presented as follows.

VO_x on Au(111) and Cu_3Au(100)

Lewis *et al*. were the first to study vanadium oxide on Au(111) using LEED and Auger electron spectroscopy (AES). As the results showed a $\left(\sqrt{3} \times \sqrt{3}\right)R30°$ pattern and +3 oxidation state for all coverages on the substrate, they concluded that both monolayer and multilayers of V oxide were attributed to the (0001) face of V_2O_3 corundum structure [48]. Guimond and co-workers used a dedicated high-pressure cell to carry "in-situ" oxidation in 50 mbar O_2 on

Au(111), which directly oxidized vanadium to high oxidation states. They found that the oxide thin films altered the stripe structures with the coverage, as shown in Figure 2-6 [50,51].

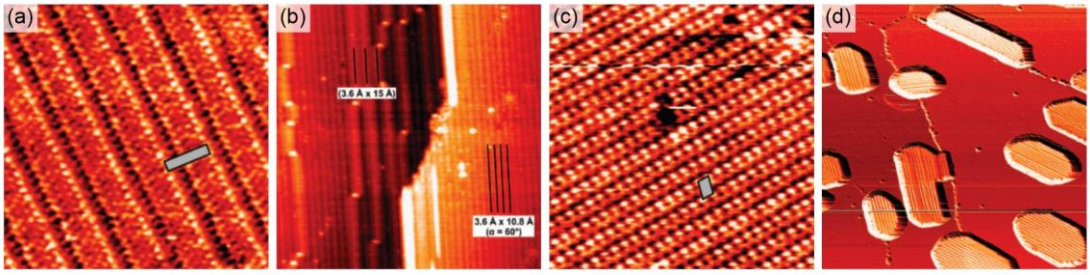

Figure 2-6 STM images of V oxide (V_2O_y, y ≈ 5) thin films on Au(111) with different coverage. (a) 0.26 ML (8 nm × 8 nm, V_s = 2.5 V, I_t = 0.2 nA). (b) 0.52 ML, two stripe structures coexisted in the layer (35 nm × 35 nm, V_s = 2.0 V, I_t = 0.2 nA). (c) 1.04 ML (8 nm × 8 nm, V_s = 2.0 V, I_t = 0.2 nA). (d) 1.56 ML, V_6O_{13}(001)-like film (90 nm × 90 nm, V_s = 3.0 V, I_t = 0.2 nA) [51].

Romanyshyn *et al*. [49] provided the STM images of the V_2O_3(0001) with $\left(\sqrt{3} \times \sqrt{3}\right)R30°$ superstructure on Au(111) and assumed the surface was vanadyl terminated [Figure 2-7 (a), (b)]. The hexagonal V_2O_3(0001) monolayer has also been observed on Cu_3Au(100). The STM result and the schematic of the structure model are displayed in Figure 2-7(c) and (d). It is found that the oxygen, which is marked in the large grey dot in the model, occupies the pseudo bridge location and can stabilize the unstable polar surface of V_2O_3(0001) [54].

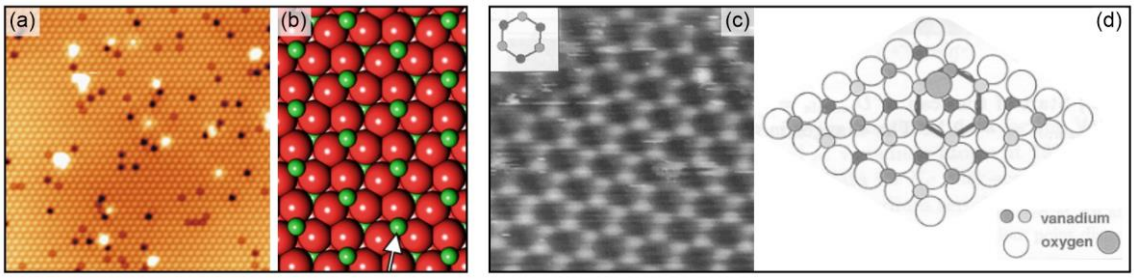

Figure 2-7 (a) STM image (18 nm × 18 nm, V_s = -1.5 V, I_t = 0.2 nA) and (b) the structural model of the vanadyl-terminated V_2O_3(0001) on Au(111) (green balls: V; red balls: 1st-layer surface O) [49]. (c) STM image (3 nm × 3 nm) and (d) schematic of V_2O_3(0001) on Cu_3Au(100) [54].

VO_x on Pd(111)

Vanadium oxide thin films on Pd(111) have been thoroughly studied by Surnev *et al*. from Netzer's group in terms of the growth behaviors and the atomic structures with increasing the

coverage [32,55,56,58]. In the initial stage, V oxide formed a porous network that preferentially grew from the substrate steps [Figure 2-8(a)]. Later, an intermediate phase with quasi-ordered and non-periodic ring arrangements [Figure 2-8(b)] was observed prior to a well-ordered (4 × 4) monolayer [Figure 2-8(c) and Figure 2-9(a)]. By exposing to H_2 at room temperature, the reactive (4 × 4) phase can be transformed into a porous structure with an internal (2 × 2) periodicity. Further annealing of the (2 × 2) phase leads to a (2 × 2) s-V_2O_3 honeycomb structure. Figure 2-8(d) shows a large (2 × 2) s-V_2O_3 honeycomb monolayer with domain boundaries indicated by white arrows, and the atomically-resolved STM image can be seen in Figure 2-9(b).

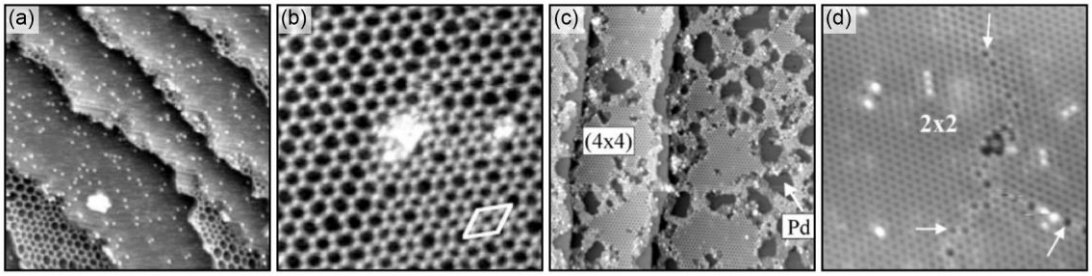

Figure 2-8 STM images of V oxides on Pd(111). (a) 0.1 ML, a porous V oxide network (45 nm × 45 nm, V_s = -1.03 V, I_t = 0.46 nA) [61]. (b) 0.2 ML, coexistence of quasi-ordered and non-periodic phases (21 nm × 21 nm, V_s = -1.05 V, I_t = 0.46 nA) [61]. (c) 0.3 ML, (4 × 4) phase (85 nm × 85 nm, V_s = 1.5 V, I_t = 0.03 nA) [55]. (d) 0.25 ML (2 × 2) s-V_2O_3 honeycomb structure with domain boundaries indicated by white arrows (15 nm × 15 nm, V_s = 0.1 V, I_t = 1.0 nA) [58].

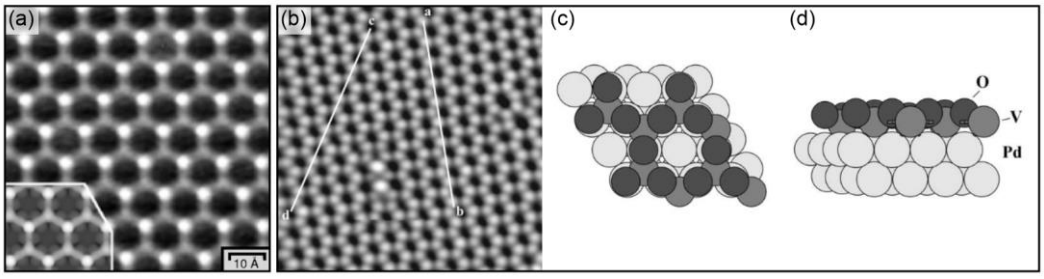

Figure 2-9 Atomically-resolved STM images of (a) (4 × 4) phase (7.6 nm × 7.6 nm, V_s = -1.0 V, I_t = 0.46 nA); inset: simulated STM image [61]. (b) (2 × 2) phase (6.5 nm × 6.5 nm, V_s = 0.05 V, I_t = 1.0 nA) [58]. (c) Top and (d) side view of the (2 × 2) s-V_2O_3 honeycomb structural model [55].

The structural model of the (2 × 2) s-V_2O_3 honeycomb on Pd(111) [Figure 2-9(c), (d)] is consistent with the (2 × 2) Nb_2O_3 on Au(111), (2 × 2) Ti_2O_3 on Pt(111) and Au(111). Besides, V oxides can also form a wagon wheel structure on Pd(111) that coexisted with the V_2O_3

honeycomb [Figure 2-10(a), (b)], and a zigzag stripe pattern that was transformed from the V_2O_3 honeycomb structure by annealing at 300°C [Figure 2-10(c), (d)].

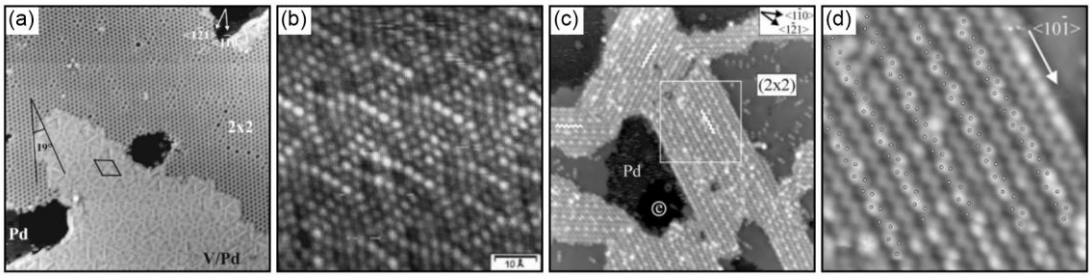

Figure 2-10 STM images of V oxide thin films on Pd(111). (a) Coexistence of the (2 × 2) s-V_2O_3 honeycomb structure and wagon wheel structure (29 nm × 29 nm, V_s = 2.0 V, I_t = 0.6 nA) [58]. (b) Atomically-resolved wagon wheel structure with a VO stoichiometry (6.5 nm × 6.5 nm, V_s = 0.1 V, I_t = 1.0 nA) [57]. (c) 0.5 ML, (2 × 2) s-V_2O_3 and a zigzag stripe structure (40 nm × 40 nm, V_s = 2.0 V, I_t = 0.1 nA). (d) Close-up of the zigzag stripe structure in the white box in (c) (10.5 nm × 10.5 nm, V_s = 1.5 V, I_t = 0.1 nA) [55].

When the film coverage is above 1 ML, several phases can coexist on the Pd(111) substrate. Figure 2-11(a) shows a rectangular V oxide phase that possesses a VO_2 stoichiometry. A new zigzag structure that differs from the zigzag stripe pattern can be seen in Figure 2-11(b). Two V oxide thin films with hexagonal periodicities (1 × 1) and (2 × 2) were observed and attributed to VO_2 and V_6O_{11} [Figure 2-11(c)]. A bulk-type V_2O_3(0001) termination [Figure 2-11(d)], which has the same structure as that on Au(111) [Figure 2-7(a)], was obtained at high coverages.

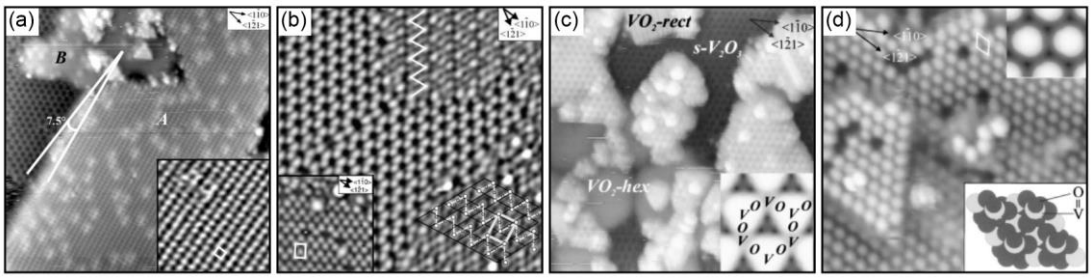

Figure 2-11 STM images of V oxide thin films on Pd(111) above 1 ML. (a) Rectangular V oxide phase (VO_2-rect) (20 nm × 20 nm, V_s = 0.25 V, I_t = 0.5 nA); inset: atomically-resolved VO_2-rect with the unit cell indicated (4.4 nm × 4.4 nm, V_s = 0.5 V, I_t = 0.5 nA) [55]. (b) coexistence of s-V_2O_3 honeycomb and a new zigzag structure (8.8 nm × 8.8 nm, V_s = 0.1 V, I_t = 1.0 nA); inset: atomically-resolved zigzag structure with unit cell indicated (7 nm × 7 nm, V_s = 1.75 V). (c) 1.3 ML, coexistence of the VO_2-rect, (2 × 2) s-V_2O_3 honeycomb, and VO_2-hex phases (20 nm × 20 nm, V_s = 0.7 V, I_t = 1.0 nA); inset: simulated STM image of a V_6O_{11} layer. (d) 3ML, bulk-type V_2O_3(0001) (9.7 nm × 9.7 nm, V_s = -0.3 V, I_t = 0.1 nA); inset: structural model of V_2O_3 with the O-V-O_3 termination [56].

VO_x on Rh(111)

Schoiswohl *et al*. from Netzer's group studied V oxide thin films on Rh(111) using the same strategies as Surnev did. Overall, there are a lot of similarities between V oxides on Rh(111) and on Pd(111). A variety of structures have been characterized by altering the vanadium coverage and preparation conditions. The bulk-type V_2O_3(0001) termination with hexagonal periodicity can always be observed in the high-coverage regime. Nevertheless, in the low-coverage regime, some unique structures were found on Rh(111) and not observed on Pd(111), indicating that the substrate metal can strongly affect the thin film structure.

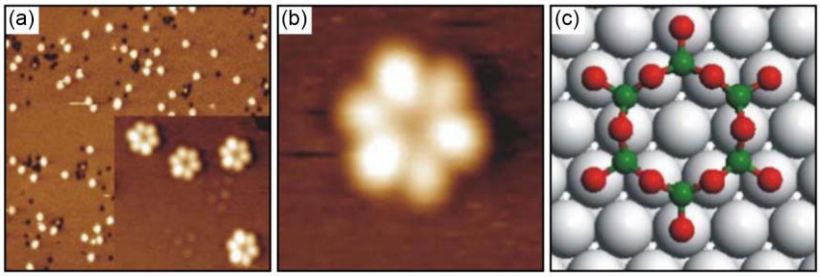

Figure 2-12 (a) STM images of 0.01 ML V oxide on Rh(111) showing star-like clusters (40 nm × 40 nm, V_s = 2.0 V, I_t = 0.2 nA); inset: close-up of the clusters (6.3 nm × 6.3 nm, V_s = 0.5 V, I_t = 0.1 nA). (b) High-resolution STM image of the star-like cluster (6.3 nm × 6.3 nm, V_s = 0.5 V, I_t = 0.1 nA). (c) DFT derived model of the planar V_6O_{12} cluster on Rh(111) (green balls: V; red balls: O; gray balls: Rh) [60].

In contrast to the porous V oxide network on Pd(111), V oxides emerged as star-like clusters on Rh(111) at the very beginning (Figure 2-12). DFT calculations suggested a structural model that resembles the hexagon unit in the (2 × 2) s-V_2O_3 honeycomb lattice with the stoichiometry of V_6O_{12} [60]. With increasing the coverage, two ordered phases were identified from the STM images (Figure 2-13), which were denoted as $\left(\sqrt{7} \times \sqrt{7}\right)R19.1°$ and $\left(\sqrt{13} \times \sqrt{13}\right)R13.8°$ with vanadium oxidation state approximated to +5. The STM image of $\left(\sqrt{7} \times \sqrt{7}\right)R19.1°$ in Figure 2-13(c) is visually similar to Figure 2-5(a) which shows *k*-TiO_x on Pt(111). However, it should be noted that Figure 2-5(a) was obtained at a negative sample bias so the protrusions were attributed to O atoms. While Figure 2-13(c) shows the empty-state STM image so the

protrusions were due to V atoms. The HREELS results and DFT calculations revealed a stoichiometry of V_3O_9 with V oxidation state approximated to +5. A pyramidal $O_4V{=}O$ unit can be seen as a building block for the $\left(\sqrt{7}\times\sqrt{7}\right)R19.1°$ monolayer [Figure 2-14(a) – (c)].

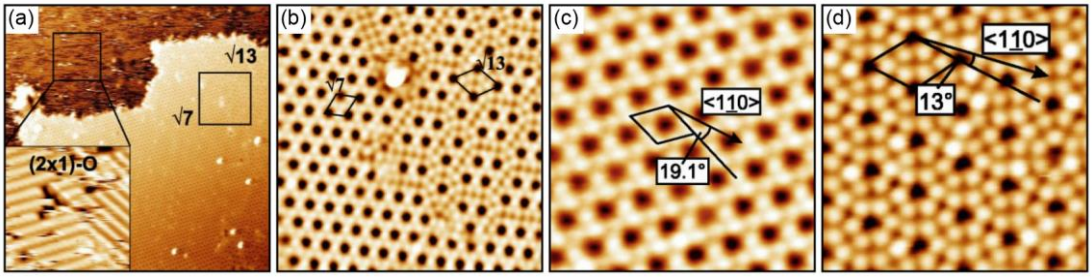

Figure 2-13 STM images of V oxide thin films on Rh(111) showing two ordered structures. (a) Coexistence of $\left(\sqrt{7}\times\sqrt{7}\right)R19.1°$ and $\left(\sqrt{13}\times\sqrt{13}\right)R13.8°$ with the (2 × 1)-O-covered Rh substrate (50 nm × 50 nm, V_s = 1.5 V, I_t = 0.2 nA; inset: 5 nm × 5 nm, V_s = 0.4 V, I_t = 0.1 nA). (b) Close-up of the coexistence region (10 nm × 10 nm, V_s = 0.69 V, I_t = 0.1 nA). (c) Atomically-resolved $\left(\sqrt{7}\times\sqrt{7}\right)R19.1°$ structure (5 nm × 5 nm, V_s = 0.75 V, I_t = 0.2 nA). (d) Atomically-resolved $\left(\sqrt{13}\times\sqrt{13}\right)R13.8°$ structure (5 nm × 5 nm, V_s = -1.0 V, I_t = 0.4 nA) [70].

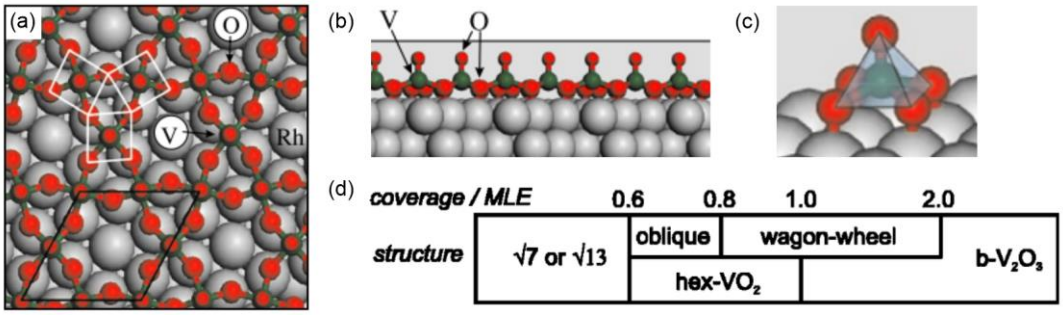

Figure 2-14 (a) Top and (b) side view of the structural model of the $\left(\sqrt{7}\times\sqrt{7}\right)R19.1°$ phase with the stoichiometry of V_3O_9. (c) A detailed view of the pyramidal $O_4V{=}O$ unit [67]. (d) Growth sequence of the V oxide thin films on Rh(111) [70].

Figure 2-14(d) is a diagram demonstrating the growth sequence of V oxide thin films on Rh(111) with increasing coverage. An "oblique" structure and Moiré patterns were found at 0.7 ML [Figure 2-15(a)]. The wagon wheel structure and the hex-VO_2 with a (2 × 2) periodicity were observed on both Pd(111) [Figure 2-10(a), Figure 2-11(c)] and Rh(111) [Figure 2-15 (b), (c)]. Again, the bulk-type $V_2O_3(0001)$ termination was detected by STM when the oxide thin film was of multiple layers [Figure 2-15(d)].

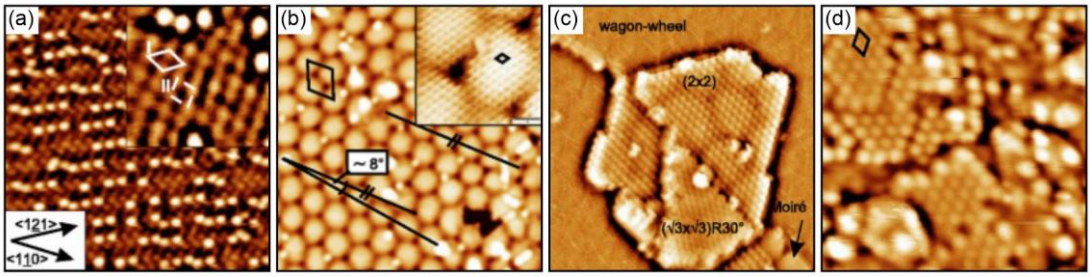

Figure 2-15 STM images of V oxide thin films on Rh(111) showing various structures by increasing the film coverage. (a) 0.7 ML, the "oblique" structure (14 nm × 14 nm, V_s = 2.0 V, I_t = 0.1 nA); inset: two possible unit cells (5 nm × 5 nm, V_s = 1.5 V, I_t = 0.1 nA). (b) 0.7 ML, the parallelogram indicated the unit cell of the Moiré superstructure (28 nm × 28 nm, V_s = 1.75 V, I_t = 0.05 nA); inset: atomically-resolved STM image showing the unit cell of the hex-VO_2 (5 nm × 5 nm, V_s = 0.025 V, I_t = 1.5 nA). (c) 1.0 ML, coexistence of the wagon wheel, (2 × 2), $\left(\sqrt{3} \times \sqrt{3}\right)R30°$, and the Moiré pattern (19 nm × 19 nm, V_s = 1.8 V, I_t = 0.1 nA). (d) 10 ML, hexagonal bulk V_2O_3(0001) surface (8.8 nm × 8.8 nm, V_s = 1.25 V, I_t = 0.25 nA) [70].

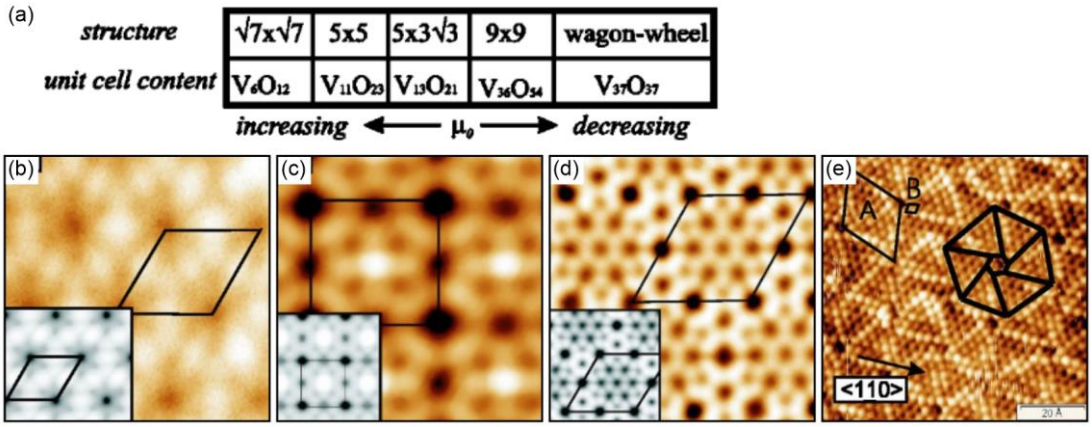

Figure 2-16 (a) Vanadium oxide monolayer structures on Rh(111) and corresponding unit cell stoichiometries under different oxygen chemical potentials μ_O. STM images of (b) (5 × 5) phase (3.6 nm × 3.6 nm, V_s = 2.0 V, I_t = 0.02 nA). (c) $\left(5 \times 3\sqrt{3}\right)$ phase (3.0 nm × 3.0 nm, V_s = 2.0 V, I_t = 0.1 nA). (d) (9 × 9) phase (5.7 nm × 5.7 nm, V_s = 2.0 V, I_t = 0.1 nA). The insets are DFT simulated STM images. (e) Wagon wheel phase (7.5 nm × 7.5 nm, V_s = 2.0 V, I_t = 0.1 nA) [69].

Schoiswohl and Surnev *et al*. also investigated the V oxide monolayers as a function of oxygen chemical potentials μ_O and demonstrated a simplified "phase diagram" [Figure 2-16(a)]. Note that there is an error in the unit cell content: the $\left(\sqrt{7} \times \sqrt{7}\right)R19.1°$ phase should correspond to a V_3O_9 stoichiometry, while V_6O_{12} is the stoichiometry of the star-like cluster. With decreasing μ_O, which was realized by annealing in an ultra-high vacuum (UHV) environment or exposure to H_2, the (5 × 5) phase with a $V_{11}O_{23}$ unit cell, the $\left(5 \times 3\sqrt{3}\right)$ phase with a $V_{13}O_{21}$ unit cell, and the (9 × 9) phase with a $V_{11}O_{23}$ unit cell have been identified in sequence [Figure 2-16(b)

– (d)]. Finally, at a relatively low oxygen chemical potential, the wagon wheel structure with the V/O ratio of 1:1 was observed. This wagon wheel structure on Rh(111) is similar to that on Pd(111) [Figure 2-10(b)] and will be further discussed in Section 2.3.

2.2 2D materials with a honeycomb structure

2D materials with a honeycomb structure have attracted considerable research interest due to their unique electronic, optical, electrochemical and mechanical properties [72]. 2004 marked the year of the 2D honeycomb materials when Novoselov and Geim successfully extracted graphene from bulk graphite [73]. Since then, graphene and graphene-like materials such as silicene, germanene, hexagonal boron nitride (h-BN), transition metal oxides, and transition metal dichalcogenides (TMDs) have been intensively studied. Unlike graphene with a perfectly flat structure due to the sp^2-hybridization, many graphene-like materials adopt a buckled honeycomb structure and therefore exhibit versatile electronic and magnetic properties [74,75].

It is unavoidable to generate defects in the honeycomb monolayer during the material synthesis process. Many theoretical and experimental studies have been performed on point defects, grain boundaries, and edge structures which can strongly affect the material properties. On the other hand, the properties of the 2D materials can be manipulated by defect engineering or edge functionalization, showing great potential for nanoelectronics [76,77]. A set of models for defect structures in graphene have been proposed and used as references for other 2D materials with a honeycomb lattice. This section will discuss point defects first, then move on to line defects including the grain/domain boundaries and edge structures. The elucidation of relevant features will be helpful for discussions of Nb_2O_3 and Ti_2O_3 honeycomb structures in Chapter 7 and Chapter 8.

2.2.1 Point defects

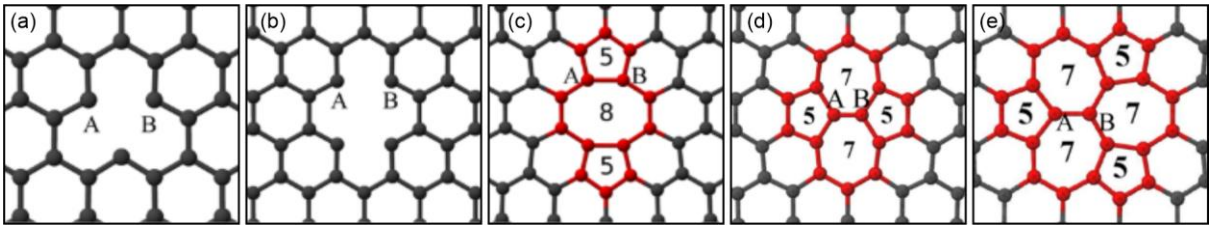

Figure 2-17 Structural models for (a) a single vacancy; (b) unreconstructed double vacancy; (c) divacancy defect 5-8-5; (d) Stone-Wales (SW) defect; (e) Divacancy defect 555-777 [78].

A point defect in a honeycomb monolayer does not literately mean a single point but a small defective area without a specific extended direction. Such area is originated from vacancies and can be either unreconstructed or reconstructed. The simplest point defect is a single vacancy, forming by losing one atom in the lattice, as shown in Figure 2-17(a). Divacancy (DV) means two lattice atoms are missing with double holes created [Figure 2-17(b)]. It has been proved that a divacancy intends to reconstruct and form non-hexagonal rings, such as 5-8-5 and 555-777 [Figure 2-17(c), (e)], so-called divacancy defects [79]. In contrast, no atom is lost in the Stone-Wales (SW) defect in Figure 2-17(d), but a pair of adjacent atoms rotates by 90° and re-connects to the surrounding lattice atoms, thus creating two pentagons and two heptagons [80]. Theoretical calculations have predicted that the formation energy of a SW defect is ~ 5 eV, which means that it is hard to form at room temperature without any treatment [81].

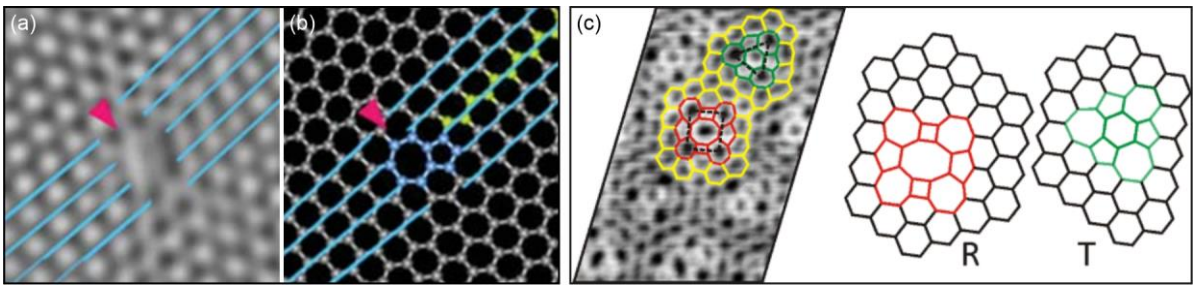

Figure 2-18 (a) TEM image and (b) structural model of a defect domain in graphene [79]. (c) TEM image and structural models of defect domains of a silica honeycomb monolayer [82].

Although many theoretical works have been conducted on the defect structures [83–85], experimental works such as imaging the defects at the atomic scale are still challenging.

Hashimoto *et al*. were the first to report direct evidence for defect formation in graphene by high-resolution transmission electron microscopy (TEM) [Figure 2-18(a)]. They attributed the formation to a knock-on atom displacement induced by the high-energy electron beam [79]. Meyer *et al*. pointed out that the acceleration voltage in TEM was crucial for the stability of defects. They used aberration-correction TEM under 80 kV and obtained atomically-resolved TEM images of the SW and DV defects (Figure 2-19) [86].

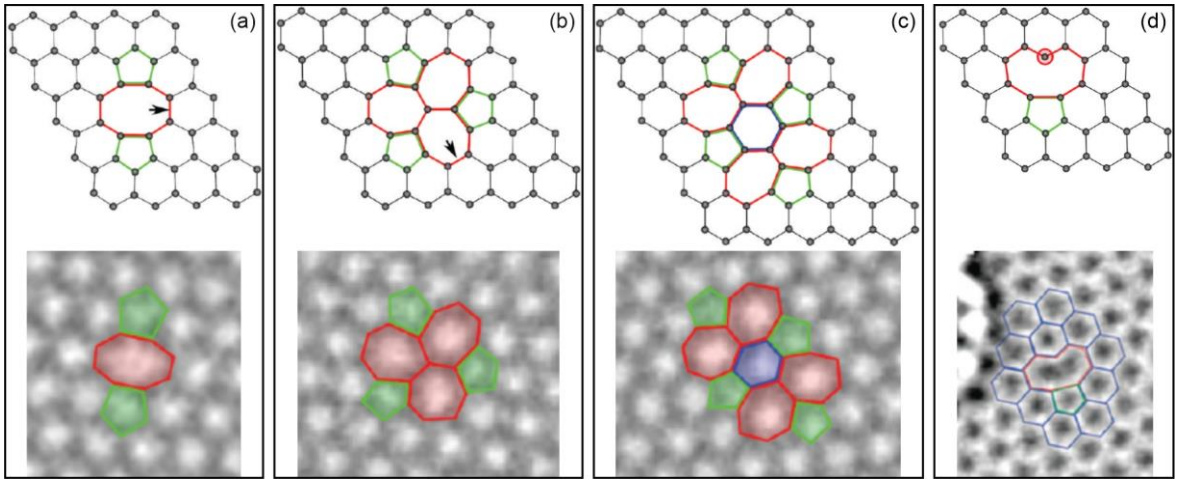

Figure 2-19 Structural models and TEM images of (a) DV 5-8-5; (b) DV 555-777; (c) DV 5555-6-7777 [87]; (d) a half-reconstructed divacancy defect [86].

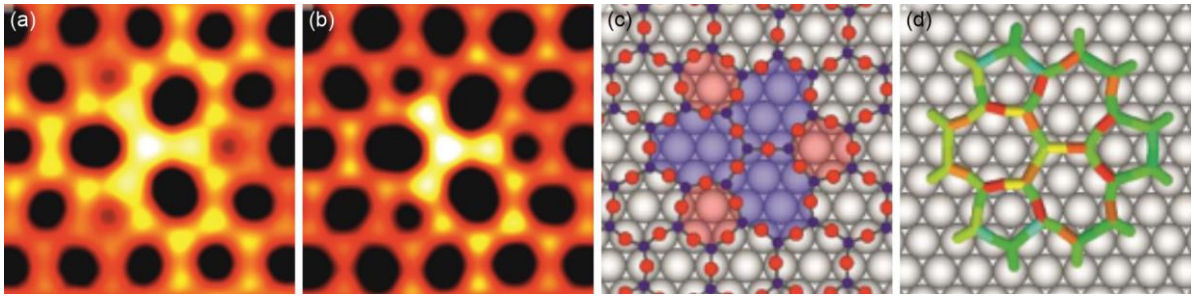

Figure 2-20 DV 555-777 in Ti_2O_3 HC monolayer. (a) Experimental STM image (V_s = 1.0 V, I_t = 0.2 nA). (b) Simulated STM image. (c) The corresponding model showing the atomic arrangement of Ti (dark blue) and O (red) atoms. (d) Schematic drawing showing the calculated bond lengths (red and yellow: length increased; blue: length decreased) [88].

Experimental works on point defects of the graphene-like materials can also be seen in h-BN [89], silica on Ru(0001) [Figure 2-18(c)] [82], and Ti_2O_3 honeycomb on Au(111) (Figure 2-20) [88]. Since these materials contain two elements in the thin films, the defect structures

and atom arrangement can be much more complicated than in the basal honeycomb plane. It is generally accepted that the defective sites are more chemically reactive than the pristine lattice [90]. However, Xin *et al*. claimed that the central C-C bond of the SW defect in a carbon nanotube was chemically less reactive [91]. Besides, the point defects can affect the mechanical properties of the thin films. It has been reported that the Young's modulus and the failure strength are decreased due to point defects [78].

2.2.2 Line defects

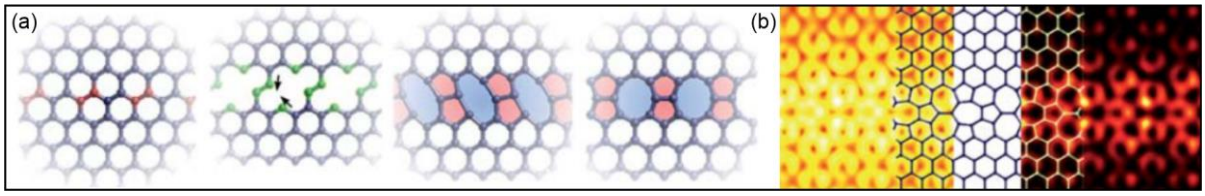

Figure 2-21 (a) Structural models for extended line defect derived from arrays of the divacancy defect 5-8-5. (b) Simulated STM image of extended 5-8-5 line defect [90].

A boundary in a honeycomb lattice is constructed by an agglomeration of multiple-membered rings that extend along a linear path, as shown in Figure 2-21. It can be further categorized into grain boundary (GB) and domain boundary (DB) according to the crystallographic orientation of two lattices separated by the boundary gap. The grain boundary can be found at the interfaces between two lattices with different crystallographic orientations [92]. GB is generally used in graphene studies and is formed by two graphene sheets with a small tilting angle. Domain boundary can be seen as a unique type of GB where the tilting angle is zero. DB is usually applied to 2D materials supported on a substrate which may strongly affect the film growth and confine the crystallographic orientation of domains. In addition, it is common to see the term phase boundary in 3D bulk materials which describes the interface between two domains with different crystal structures. The phase boundary is not reviewed in this section, but similar concepts will appear in the discussion of the junctions between Nb/Ti oxide pinwheel and honeycomb monolayers which are named H-T boundary and H-P boundary, respectively.

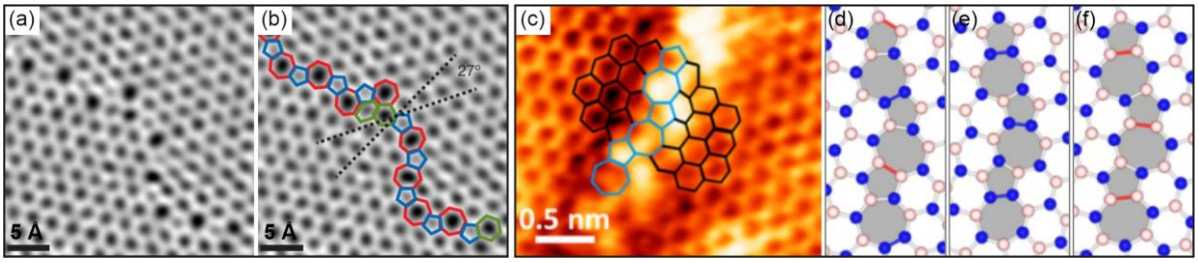

Figure 2-22 (a) STEM image of graphene sheet with a grain boundary. (b) A superimposed boundary model on the STEM image [93]. (c) STM image of h-BN on the Cu(111) substrate showing a 57-grain boundary with the model superimposed on the image. (d) Three possible models for the 57-boundary of a h-BN honeycomb monolayer [94].

GBs or DBs in honeycomb monolayers can be either periodic or non-periodic. Periodic boundaries are formed by an array of multiple-membered rings with repetitive units such as 57 (pentagon-heptagon), 48 (square-octagon), and 585 (pentagon-octagon-pentagon). Non-periodic boundaries do not show a periodicity along the extending direction. Figure 2-22(a), (b) show a scanning transmission electron microscopy (STEM) image of a graphene sheet with a 57-grain boundary. Figure 2-22(c) is a STM image of a 57-boundary in a h-BN monolayer on Cu(111) with three possible structural models in Figure 2-22(d). Yazyev *et al*. introduced a general approach to denote the boundary in graphene by arbitrary Burgers vectors, which can sort out various ring combinations and describe the misorientation angles [85].

It is predicted that the aperiodicity of the boundaries could severely weaken the mechanical strength of graphene [93,95,96]. Regarding the electronic properties, researchers have different views on the boundary effect. Huang *et al*. proved that GBs could hardly influence graphene's electrical properties using electrostatic force microscopy (AC-EFM) [93]. Lahiri *et al*. found that the GB with a well-defined atomic structure in graphene was like a quasi-one-dimensional (1D) metallic wire, showing great potential for graphene-based electronics [97]. In contrast, Kim *et al*. reported that the electronic mobility was reduced in low-quality graphene [98].

The substrate plays a critical role in film growth and boundary formation. Figure 2-23(a) – (c) show the boundaries of graphene grown on the SiO_2 [99], SiC $(000\bar{1})$ [100], and the

Ni(111) [97] substrates, respectively. The boundary may evolve into a ridge structure, as shown in Figure 2-23(d), which can be detrimental to the mechanical strength [97,99,101].

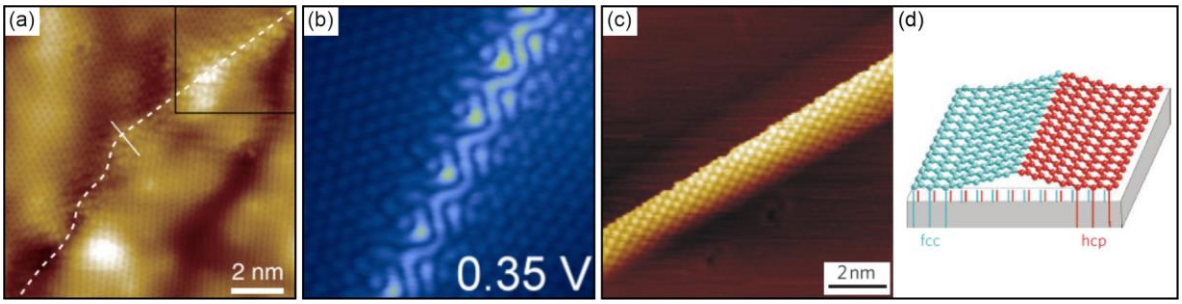

Figure 2-23 STM image showing a grain boundary in graphene on (a) SiO_2 substrate [99]; (b) $SiC(000\bar{1})$ substrate [100]; (c) Ni(111) substrate. (d) Schematic drawing of the ridge structure due to the domain boundary in the graphene grown on Ni(111) [97].

Similar to point defects, there are also many experimental studies and theoretical predictions on the line defects of graphene-like materials such as h-BN [94,102,103], silica [82,104–106], silicene [107], metal disulfides MS_2 [108], and metal oxides [58]. Figure 2-24(a) shows the STM images of the 48-DB in silica on Mo(112). Figure 2-24(b) demonstrates the structural model of pristine silica. Figure 2-24(c) shows DBs in silicene with a unique pattern. The bright protrusions where the boundaries locate could be depressions when using a different sample bias [107]. Interestingly, it was predicted that the misalignment of two domains of metal disulfides MS_2 gave rise to three-dimensional atom stacking, as shown in Figure 2-24(d) [108].

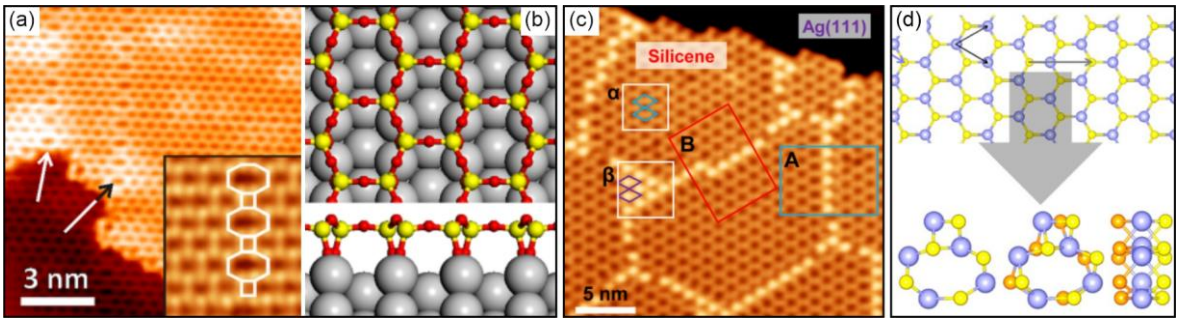

Figure 2-24 (a) STM image showing a 48 domain boundary of silica on the Mo(112) substrate. Inset: a close-up of the 48 domain boundary. (b) Structural model of a monolayer silica film on Mo(112) [82,104–106]; (c) STM image showing domain boundaries of silicene on Ag(111) (V_s = 1.75 V, I_t = 1.0 nA) [107]. (d) Possible structural models for grain boundaries of metal disulfides MS_2 (M = Mo or W). The 48-grain boundary can be extended in the third direction, forming concave dreidel-shaped polyhedra [108].

2.2.3 Edge structure and edge reconstruction

If a pristine honeycomb lattice is cut along the direction that only breaks bonds between two atoms, the edge can be either zigzag (ZZ)- or armchair (AC)-terminated, as shown in Figure 2-25. A periodic edge with an array of single atoms extending from a ZZ edge is called Klein edge [109,110]. A chiral edge refers to a mixed edge with an intermediate orientation [111].

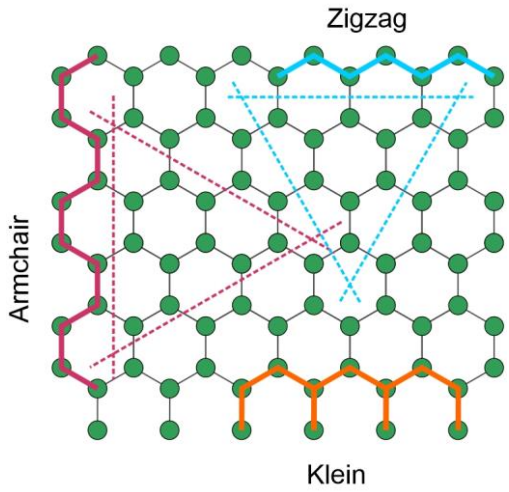

Figure 2-25 Schematic diagram of ZZ, AC, and Klein edge by cutting along specific directions

The edge structure of graphene has been theoretically and experimentally studied [75,112]. It is predicted that for a freestanding graphene sheet, the pristine zigzag edge possesses electronic edge states due to the unpaired electrons (dangling bonds), while the armchair edge has no edge state as the atoms can form stable C ≡ C triple bonds [113]. Therefore, the pristine zigzag edge is metastable and can undergo edge reconstruction or self-passivation even at room temperature. In other words, edge atoms no longer retain the hexagonal arrangement but form polygon pairs (e.g., 5-7 pairs), by which the system energy and edge stress can be effectively minimized and released [114,115]. Edge reconstructions in graphene have been observed and modeled, some examples are displayed in Figure 2-26. DFT calculations reveal that the ZZ-57 edge has the lowest energy in graphene; AC-677 is slightly higher than pristine AC but still lower than ZZ; in contrast, the AC-56 edge possesses the highest energy [114].

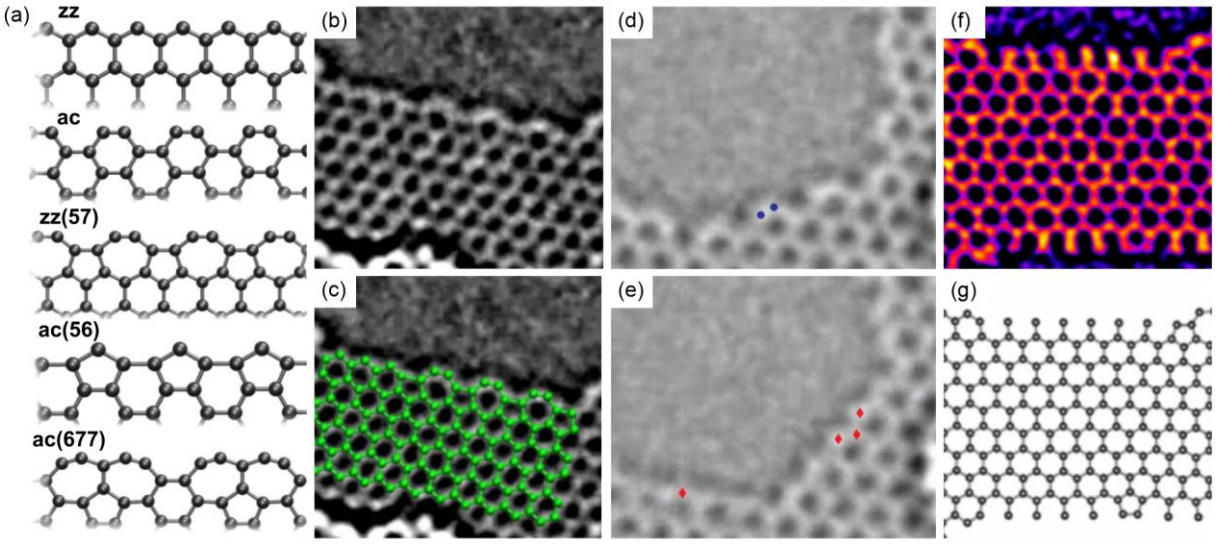

Figure 2-26 (a) Models for different types of reconstructed edge in graphene [114]. (b) TEM image of a graphene sheet with ZZ and ZZ-57 reconstructed edge, with lattice model superimposed in (c) [116]. (d), (e) TEM image showing the transition from an AC edge to a ZZ edge in a graphene sheet by atom diffusion due to electron beam ejection [117]. (f) TEM image showing a graphene nanoribbon with Klein edge. The lattice model is shown in (g) [110].

Many factors can affect the edge reconstruction such as substrate and impurity atoms. Gao *et al*. found that the reconstructed edge with 5-7 pairs in graphene supported on transition metals is not energetically favorable due to the surface passivation effect [118]. Girit *et al*. reported that the zigzag type could become the most prominent edge in graphene under the electron beam ejection in the TEM [Figure 2-26(d), (e)] [117]. Besides, theoretical calculations have confirmed that the hydrogen-terminated zigzag edge can be remarkably stable [119].

The edges of graphene-like materials are also inclined to reconstruct in order to lower the system energy. Figure 2-27 provides schematics of three edge structures in a silicene monolayer. Ding *et al*. theoretically demonstrated that the 5-7 reconstructed edges of silicene were favored in H-poor conditions, whereas di-hydrogenated Klein edges were more stable in H-rich surroundings [120]. Some unique features in reconstructed edges can be found in films with multiple elements. For example, Figure 2-28 shows four possible atom configurations of the AC-677 edge in a h-BN monolayer [121]. Edge reconstruction has also been investigated on other 2D materials such as germanene [122], phosphorene [123], and MoS_2 [124,125].

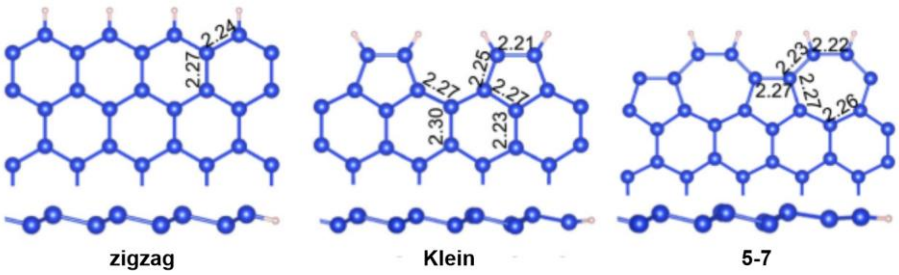

Figure 2-27 Three types of silicene edge reconstruction with bonding length denoted on the model. The drawing at the bottom is a side view showing the silicene buckled structure [120].

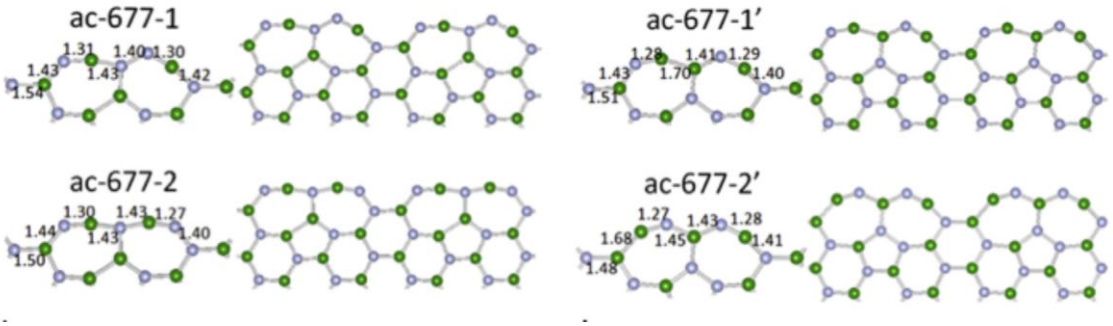

Figure 2-28 The reconstructed edge ac-677 can have four possible structural models according to the atom configuration of B and N in the terminal pentagons and heptagons [121].

The edge structures of metal oxide honeycomb monolayers have attracted much research interest. However, the edge reconstruction could be very complicated if oxygen atoms are taken into account. Some calculations have been done in Zn oxide [126] and Cu oxide [127]. Many experimental works focused on the broad structures or internal defects of oxide thin films, but few papers revealed detailed information on edge structures or reconstruction. Therefore, our studies of Ti_2O_3 and Nb_2O_3 honeycomb edge structures are of significance in this field.

2.3 2D materials with a pinwheel structure

The pinwheel structure, also referred to as the “wagon wheel” structure, comprises hexagonal units in which six triangle elements are enclosed by “spokes”. The description of the wagon wheel structure was found for the first time by Zhang *et al*. in the studies of Cr/Pt surface alloy [128,129]. It is a common structure that has been observed in many 2D materials including oxide thin films and transition metal dichalcogenides. Three models are generally used to

demonstrate the pinwheel formation depending on the film-substrate interaction. Zhang's proposal for the Cr/Pt surface alloy can be taken as an example for the first model. The second model attributes the pinwheel structure to a Moiré pattern formed by two commensurate hexagonal lattices with a slight rotation. The alloy model and the Moiré model have been well classified by Sedona *et al.* [39] and will be discussed in the following subsections. The third model is proposed for the van der Waals materials with a weak interlayer interaction, such as $MoTe_2$ and $MoSe_2$ submonolayer films on MoS_2 single crystal substrates. The mirror-twin domain boundaries can be regarded as the "spokes" of the pinwheel network [130]. It should be noted that models proposed for the pinwheel structure are tentative models that may not reproduce or explain all information in the STM images.

Different papers may use either "pinwheel" or "wagon wheel" in descriptions, so these two terms are used interchangeably in this section. We will keep to "pinwheel" in Chapter 8 when discussing relevant structures formed by Nb, Ti, and V oxides on Au(111). In addition, a brief review concerning triangular nanostructures is included in this section. The triangle elements can somehow be regarded as "building blocks" for the pinwheel structure. This idea is critical for our analysis of the pinwheel structures created by Nb or Ti oxides on Au(111), and will be the basis for proposing the fourth model – the triangle building block model.

2.3.1 Alloy model

In the alloy model, the contrast between the hub, the spokes and the triangle elements is attributed to a local variation of chemical composition [39,128,129]. Noting that we emphasize the contrast here because the spokes can be either brighter or darker than the triangle elements. Figure 2-29(a) – (d) are STM images of a reconstructed Pt(111) surface with 1.5 – 3 ML Cr after annealing to 800 K. The triangles are bright and the spokes are dark in frame (a), (c), while

an opposite situation can be seen in frame (b), (d). As they were obtained at different imaging conditions, it indicates that the pinwheel pattern is sensitive to the sample bias.

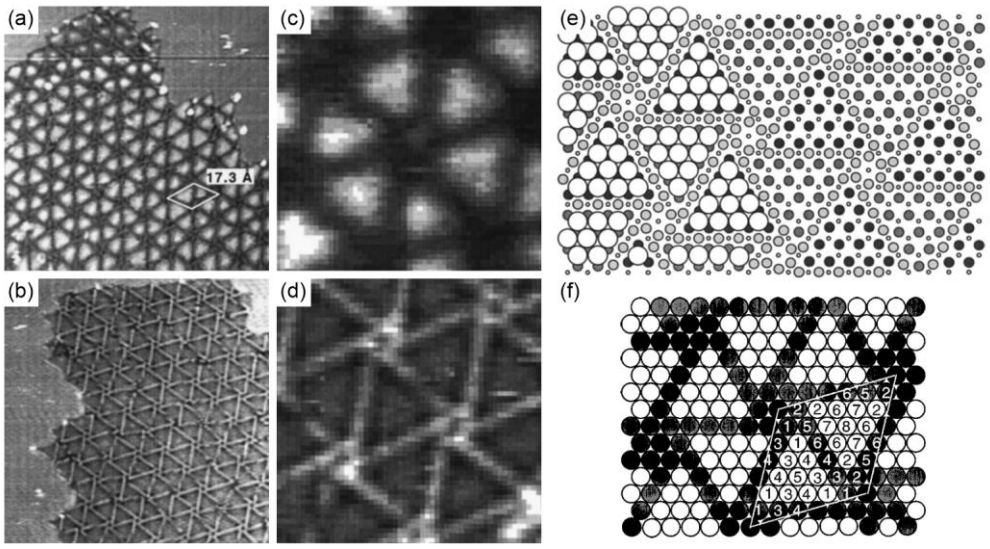

Figure 2-29 STM images of Cr-induced Pt(111) reconstruction. (a) 18 nm × 18 nm, V_s = 2.0 V, I_t = 0.6 nA; (b) 18 nm × 18 nm, V_s = -2.0 V, I_t = 0.6 nA; (c), (d) close-ups of the STM images in (a), (b) (4 nm × 4 nm). (e) Model for Cr atoms on a reconstructed Pt(111) surface. The grey and black circles represent the fcc and hcp domains of the reconstructed Pt layer, respectively. The small dots represent Pt atoms. The large circles on the left side represent Cr atoms. (f) Simplified structural model of the wagon wheel pattern on a reconstructed Pt(111) surface. The parallelogram marks the unit cell of the pinwheel structure; the numbers indicate the atom positions in different environments; four corners of the unit cell are void sites. [128,129].

Cr atoms induced the Pt(111) surface to reconstruct, which gives rise to the face-centered cubic (fcc) and hexagonal close-packed (hcp) domains separated by boundary lines, as shown in the simplified model in Figure 2-29(f). The left side of Figure 2-29(e) shows the schematic in which ten Cr atoms formed triangular clusters in the fcc and hcp domains while Pt atoms comprised the boundary lines acting as the spokes of the wagon wheel network. The phenomenon of the contrast reversal between (a), (c) and (b), (d) indicates a strong bias dependence and can be attributed to the electronic structure of Cr atoms. Due to the high unoccupied density of states, Cr atoms appeared as protrusions in empty-state STM images (positive V_s), while as depressions in filled-state STM images (negative V_s). In addition, it is worth noting that the sublattice formed by Cr atoms follows a strict registry to the Pt(111) with no rotation angle.

2.3.2 Moiré pattern model

The Moiré pattern model is widely applied to the pinwheel structure created by a transition metal oxide thin film on a noble metal substrate. Generally, the oxide thin film and the substrate surface have hexagonal lattices with a small lattice mismatch and a slight rotation angle. As a result, a modulation of the occupancy sites of the film atoms can be found periodically on the surface, which is associated with the contrast difference in the empty-state STM images. For example, the atoms that occupy on-top sites or bridge sites of the substrate are usually brighter. In comparison, the atoms at the hollow sites or the substrate "void" sites with no external metal atom occupied are darker or appear as depressions. This straightforward interpretation can work for the surface dominated by topographic features. However, it may fail to explain some fine details related to the electronic structures. Theoretical calculations can compensate in a way, but it is still challenging in practice because the unit cell of the Moiré superstructure is relatively large.

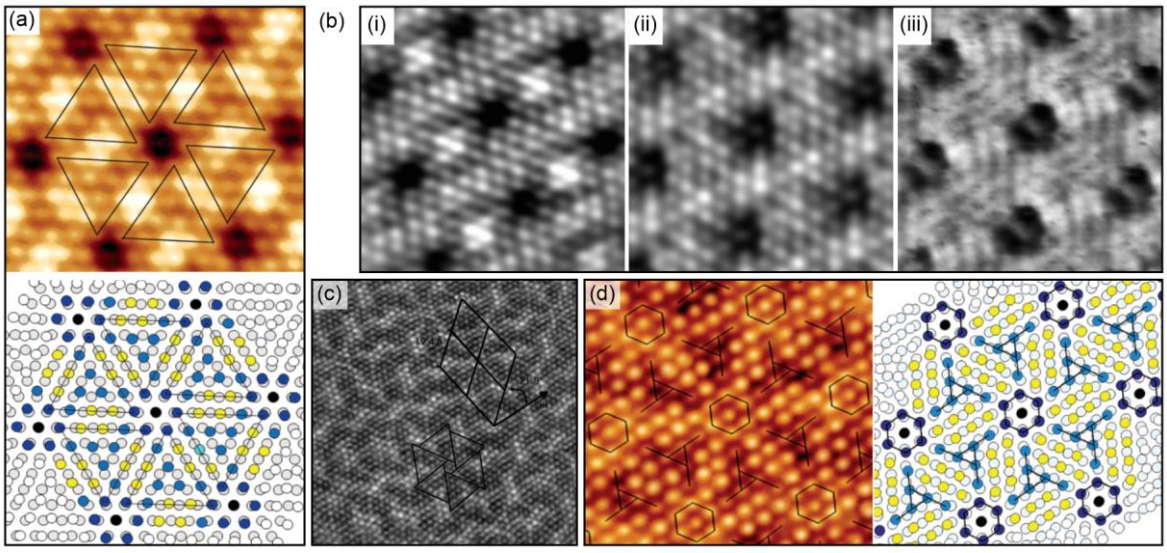

Figure 2-30 (a), (d) STM images and schematic drawings showing the Moiré-like coincidence between Ti oxide wagon wheel structures and Pt(111) lattice. Different sites are indicated by different colors, yellow: quasi-bridge; light blue: quasi-hollow; dark blue: quasi-top; black: on-top or Ti vacancy (void site). (a) *w*-TiO_x phase [33]. (b) STM images (4.8 nm × 4.8 nm) of *w*-TiO_x phase showing bias dependence: (i) V_s = 1.3 V, I_t = 1.9 nA; (ii) V_s = 0.9 V, I_t = 1.6 nA; (iii) V_s = -1.0 V, I_t = 1.6 nA [39]. (c) *w'*-TiO_x phase, identical to Figure 2-5(c) (12.6 nm × 12.6 nm, V_s = 0.2 V, I_t = 1.0 nA) [33]. (d) *w'*-TiO_x phase [39].

Figure 2-30(a) and (d) show the STM images and corresponding structural models of two wagon wheel structures of Ti oxide thin films on Pt(111), termed as *w*-TiO_x and *w'*-TiO_x. *w'*-TiO_x is a reduced phase that can be transformed from *w*-TiO_x by UHV annealing [39]. The model in Figure 2-30(d) can reproduce the topographic contrast in the STM image of the *w'*-TiO_x phase, as we can see that the on-top (black circles), the quasi-on-top sites (dark blue), and the bridge sites (yellow) are much brighter than the quasi-hollow sites (light blue). However, the model in Figure 2-30(a) does not work very well for the STM image of the *w*-TiO_x pinwheel pattern. For example, the six atoms surrounding the hub center at the quasi-top sites should be brighter, but the actual signal intensity was close to the quasi-hollow sites. This discrepancy should be related to the electronic structure of the oxide thin film. In addition, the wagon wheel structure of the *w*-TiO_x phase exhibited a strong bias dependence [Figure 2-30(b)], which also indicates that the electronic effects play a critical role in the contrast difference.

Figure 2-31(d) has been presented in Section 2.1.2 when discussing Ti oxide on Au(111). The TiO pinwheel structure was revealed and modeled by Wu *et al*. for the first time [Figure 2-31(a) – (c)]. The oxide monolayer produced a $\left(\sqrt{67} \times \sqrt{67}\right)R12.2°$ reconstruction with a stacking sequence O-Ti-Au due to the charge transfer from Ti atoms to the Au substrate [42]. However, the model that Tumino *et al*. proposed is not in agreement with Wu's model [43]. The STM images that Tumino *et al*. obtained displayed well-developed pinwheel motifs [Figure 2-31(a), (b)]. They proposed a $\left(4\sqrt{7} \times 4\sqrt{7}\right)R19.1°$ reconstruction and re-built the structural model [Figure 2-31(f)]. The periodicity of Ti atoms and tilting angle (3.43 Å, 2.11°) is larger than that in Wu's model (3.27 Å, 1.68°). There are two possible explanations for the disagreement: one is correct, or both are correct. Compared with Wu's model, Tumino's model is more convincing due to better resolution in the STM images and good reproduction of the contrast difference. But it is also possible that both of them are correct if Ti oxide thin films possess multiple pinwheel structures on Au(111), similar to the *w*-TiO_x and *w'*-TiO_x phases on Pt(111).

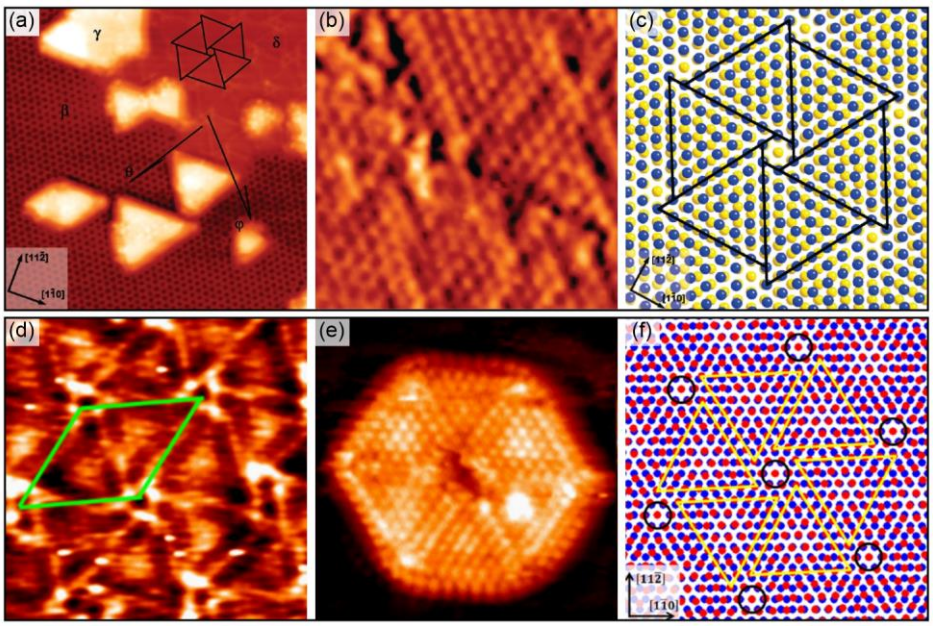

Figure 2-31 (a) STM image showing the coexistence of the (2 × 2) Ti_2O_3 honeycomb structure (β) and the TiO pinwheel structure (δ) on Au(111) (24 nm × 24 nm, V_s = 0.98 V, I_t = 0.2 nA). (b) Atomically-resolved STM image of the TiO pinwheel structure (5 nm × 5 nm, V_s = -0.12 V, I_t = 0.5 nA). (c) Model for the pinwheel structure. Blue balls: Ti atoms with a periodicity of 3.27 Å; yellow balls: Au atoms with a periodicity of 2.89 Å; rotation angle: 1.68° [42]. (d) STM image of the Ti oxide pinwheel structure on Au(111) with the coverage of 1.5 ML (8.5 nm × 8.5 nm, V_s = 0.1 V, I_t = 1.5 nA). (e) A Ti oxide pinwheel island (8.5 nm × 8.5 nm, V_s = 0.1 V, I_t = 2.5 nA). (f) Model for the pinwheel structure. Magenta balls: Ti atoms with a periodicity of 3.43 Å; blue balls: Au atoms with a periodicity of 2.89 Å; rotation angle: 2.11° [43].

The titania/Pt system is a well-known example of the strong metal support interaction effect [31]. Such phenomena have also been observed in Pd/TiO_2 [131], $Pd/SrTiO_3$ (STO) [132,133], and Rh/TiO_2 [134,135] systems. Due to the SMSI effect, the substrate Ti atoms can diffuse onto the as-deposited metal layer, forming a TiO_x thin film that encapsulates the metal islands, as shown in the models in Figure 2-32(a), (b) and Figure 2-33(a). The atomically-resolved STM image in Figure 2-32(c) displays the TiO_x pinwheel structure on a nanocrystalline Au/Pd alloy as a result of the SMSI effect [131]. Figure 2-32(d) shows a STM image of a TiO_x-encapsulated Pd nanocrystal on the STO(100) substrate with a wagon wheel termination. A hexagonal superstructure could coexist with the wagon wheel structure on the same Pd nanocrystal, as indicated by B and A respectively in Figure 2-32(e) [132]. However, there is a disagreement on the atom stacking sequence of the oxide layer and the underlying

metal compared with Wu's model [42] mentioned above. Here the author believed that the Moiré pattern was due to the superimposition of the O lattice and the Ti lattice with a stacking sequence of Ti-O-Pd (-STO). A further study by Gao *et al*. shows that the structure of the TiO_x-encapsulated layer depends on the size of the underlying Pd crystal [133]. When the width of the Pd crystal is larger than 100 nm, the encapsulation layer only exhibits the hexagonal Moiré pattern which is sensitive to the sample bias, as shown in Figure 2-32(f) – (i).

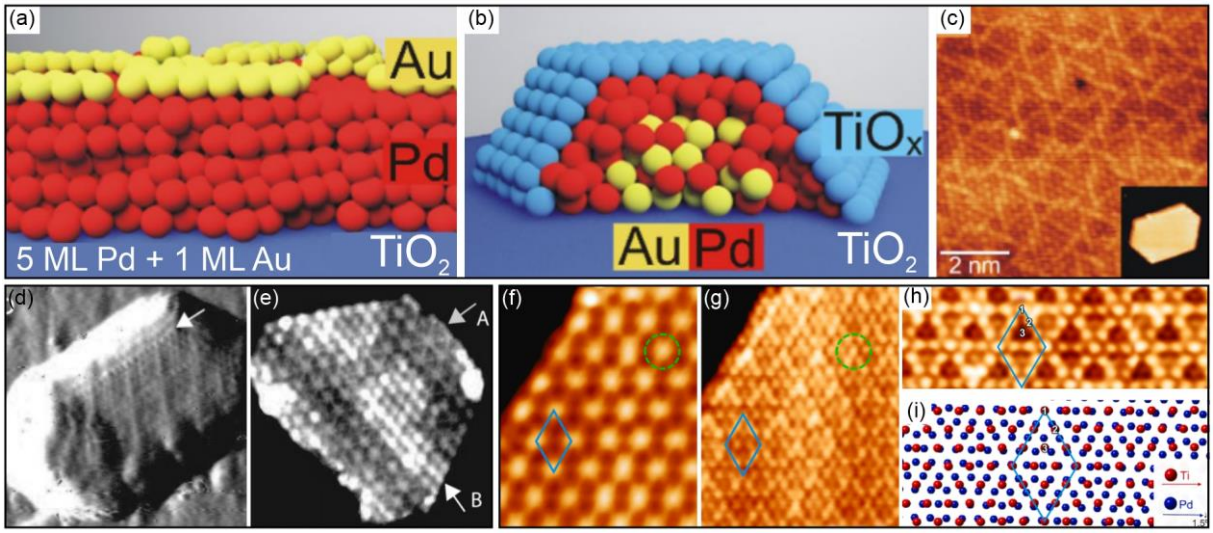

Figure 2-32 (a) Schematic ball models of TiO_2(110) with 5 ML Pd and1 ML Au at 300 K. (b) after annealing at 973 K for 20 min, TiO_x encapsulated the Au/Pd alloy due to the SMSI effect. (c) STM image showing the TiO_x-encapsulated surface (8 nm × 8 nm, V_s = 1.3 V, I_t = 0.1 nA) [131]. (d) An Pd nanocrystal island encapsulated by TiO_x wagon wheel structure on the STO(100) substrate (10 nm × 10 nm, V_s = 0.8 V, I_t = 0.3 nA). (e) Encapsulated Pd nanocrystal on STO(100) with a mixed Ti oxide structure. A: wagon wheel structure; B: hexagonal superstructure (19 nm × 19 nm, V_s = 0.8 V, I_t = 0.3 nA) [132]. (f), (g) Ti oxide hexagonal Moiré superstructure of the same area (6.3 nm × 7.9 nm, f: V_s = 0.45 V, I_t = 0.52 nA; g: V_s = 0.66 V, I_t = 0.58 nA). (h) Magnified STM image and (i) structural model of the hexagonal superstructure (8.5 nm × 3.8 nm, f: V_s = 0.48 V, I_t = 0.58 nA). Red balls: Ti atoms with a periodicity of 3.686 Å; bue balls: Pd atoms with a periodicity of 2.751 Å; rotation angle: 1.5° [133].

Another example can be seen on Rh(111) using TiO_2 as the substrate [134,135]. The STM images of the $TiO_{\sim 1.2}$-encapsulated ultrathin oxide (w-TiO-UTO) layer and the contrast scheme are presented in Figure 2-33. The surface comprises triangles with two sizes, indicated by T5 and T6. It is worth noting that the w-TiO-UTO layer is aligned with the Rh(111) lattice without rotation. The contrast variation, which enables us to see the spokes and triangle elements, is due

to the coordination difference of Ti atoms. In the relaxed structural model [Figure 2-33(f)], the Ti atoms at the triangle borders are fourfold coordinated (Ti_4) bonding to four oxygen atoms, while those inside the triangles are threefold coordinated (Ti_3) and less bright than the Ti_4 atoms.

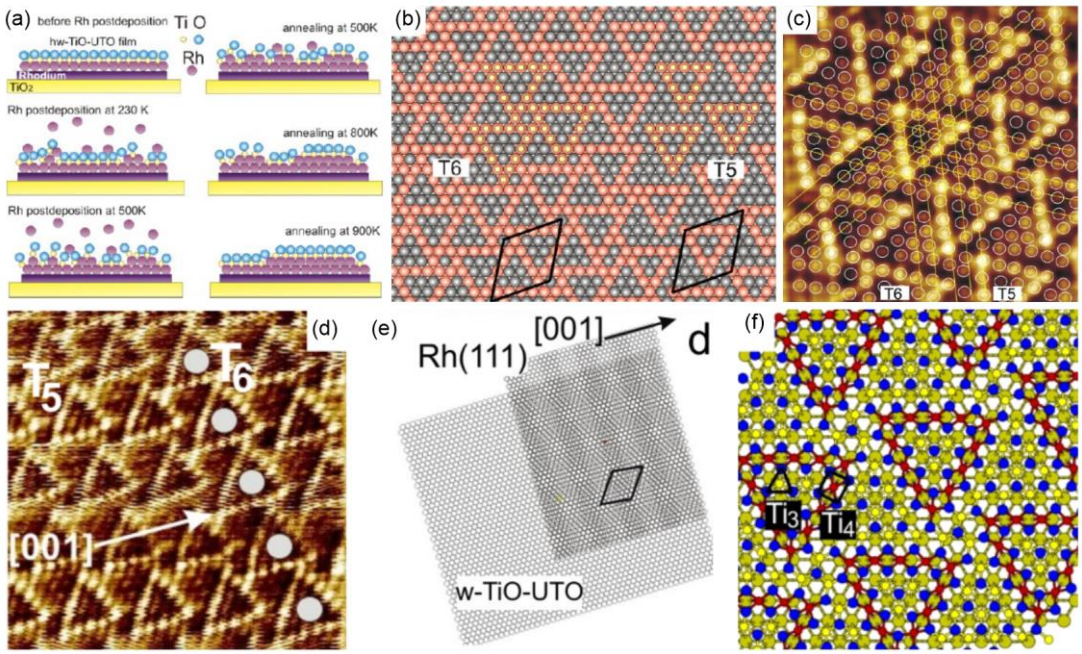

Figure 2-33 (a) Schematic showing the re-arrangement of Rh atoms deposited on the w-TiO-UTO layer on the TiO_2(110) substrate at different temperatures. (b) Contrast scheme of $TiO_{\sim 1.2}$-encapsulated layer on Rh (111). (c) STM image of the w-TiO-UTO layer showing triangle patterns with different sizes (T5, T6). (b) STM image of the w-TiO-UTO layer with the crystallographic direction and triangle size indicated (8 nm × 8 nm). (e) Moiré pattern formed by overlapping w-TiO-UTO and Rh(111) without rotation. (f) Relaxed atomic positions of the w-TiO-UTO layer. Balls in chartreuse: Rh; yellow: Ti_3; red: Ti_4; blue: O [134,135].

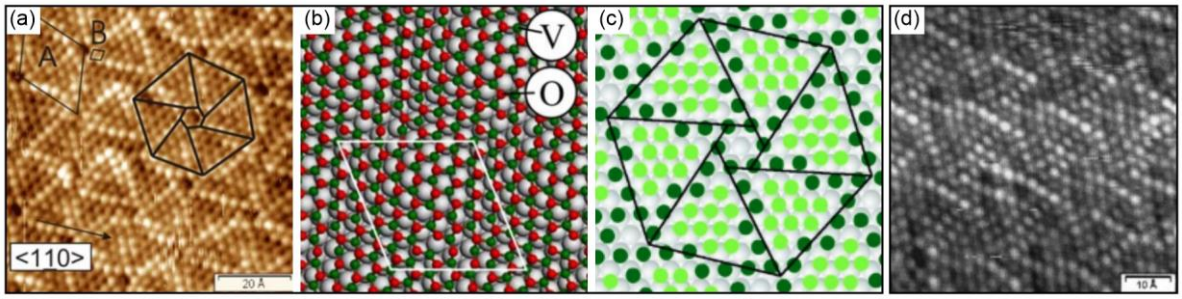

Figure 2-34 (a) Atomically-resolved STM image of V oxide wagon wheel structure on Rh(111), identical to Figure 2-16(e) (8 nm × 8 nm, V_s = 2.0 V, I_t = 0.1 nA) [66]. (b) DFT calculated model and (c) Billard ball model of the V oxide wagon wheel structure on Rh(111) [69]. (d) Atomically-resolved STM image of V oxide wagon wheel structure on Pd(111), identical to Figure 2-10(b) (6.5 nm × 6.5 nm, V_s = 0.1 V, I_t = 1.0 nA).

The wagon wheel structures of V oxide thin films have been mentioned in Section 2.1.3. Structural models on Rh(111) are displayed in Figure 2-34(b), (c). The film was supposed to be an oxygen-terminated VO(111) bilayer with periodicities of $\left(\sqrt{63} \times \sqrt{63}\right)R19.1°$ and $(7 \times 7)R21°$ [66]. The atom configuration of the VO wagon wheel on Pd (111) [Figure 2-34(a)] resembles that on Rh(111). In addition, a distinct difference can be seen at the pinwheel spokes between TiO and VO. In Figure 2-31(c) or (f), an array of Ti atoms forms the spoke, while in Figure 2-34(c), the spoke comprises two arrays of V atoms with a position shift in the middle.

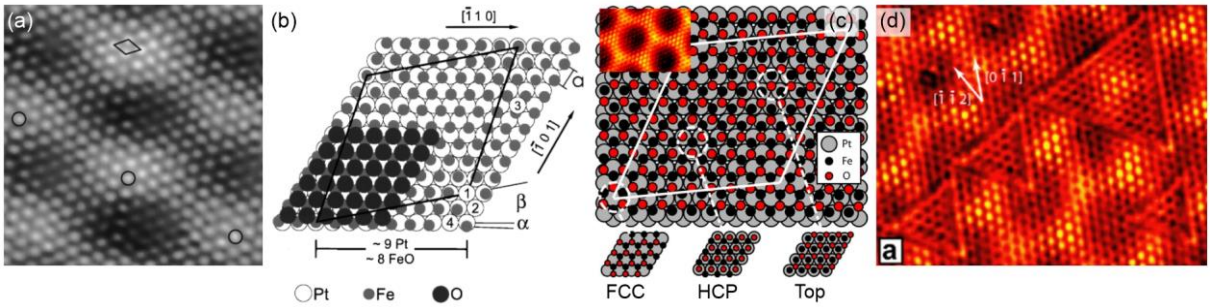

Figure 2-35 (a) STM image of the Moiré pattern generated by a FeO submonolayer on Pt(111) (5.5 nm × 5.5 nm, V_s = 0.9 V, I_t = 0.3 nA). The parallelogram indicates the FeO(111) unit cell with a periodicity of 3.1 Å. The periodicity of the Moiré superstructure is 25 Å, namely the distance between two circles. (b) Model of the FeO(111) on Pt(111) with a rotation angle of 1.3°. The atom position with the number 1 indicates the coincidence site [136]. (c) Ball model of the Moiré pattern formed by FeO(111) on Pt(111). Three domains are indicated by circles and enlarged at the bottom. (d) STM image of a partially-reduced FeO film on Pt(111) showing three small triangles and a large triangle (9.2 nm × 7.2 nm, V_s = 0.01 V, I_t = 2.5 nA) [137].

Epitaxial growth of well-ordered FeO(111) thin film has been observed on Pt(111) with a lattice mismatch of ~ 10% [136]. The oxygen-terminated FeO(111) hexagonal lattice is slightly rotated against the Pt(111) substrate by 1.3°, forming a Moiré pattern as shown in Figure 2-35(a) along with the structural model in Figure 2-35(b). The Moiré model can well reproduce the contrast difference due to the modulation of Fe atom positions [Figure 2-35(c)], but it is more like a hexagonal superstructure than a pinwheel network. Furthermore, the Moiré superstructure could be altered if the oxide thin film was partially reduced. Triangle elements with different sizes are outlined on the STM image in Figure 2-35(d) [137].

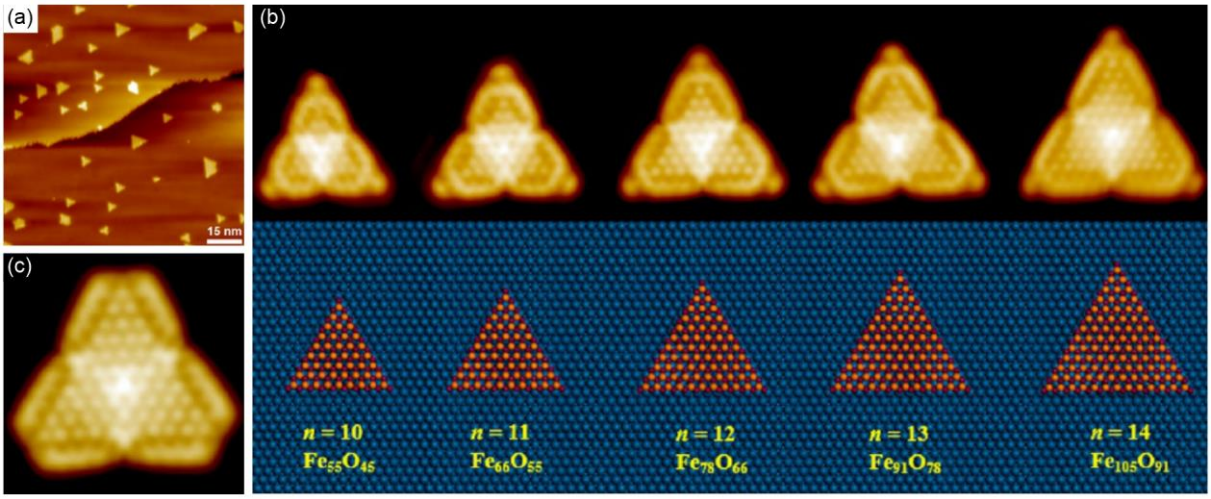

Figure 2-36 (a) Large-scale STM image of FeO triangular nanostructures on Pt(111) (40 nm × 40 nm). (b) STM images of FeO nanostructures with different sizes ranging from n = 10 to n = 14 (V_s = 0.007 V, I_t = 5.1 – 6.4 nA). The tiny red balls in the structural models represent Fe atoms, and the orange balls represent O atoms. (c) STM image of a FeO nanostructure with truncated shape. If assuming a perfect triangle structure then n = 14 (4.2 nm × 4.2 nm, V_s = 0.007 V, I_t = 4.9 nA) [138].

FeO can be fabricated on Pt(111) in the form of triangular nanostructures that can stand on the substrate independently rather than growing into a large continuous thin film [Figure 2-36(a)]. A series of FeO triangles with different sizes is demonstrated in Figure 2-36(b). The side lengths (> 3 nm from n = 10, n is the number of Fe atoms at one side) have a discrete distribution because the growth of the triangular nanostructures was confined due to a strong interfacial interaction. The triangular nanostructures may have some defects, for example, Figure 2-36(c) shows a truncated FeO triangle with three corners removed. We can also see several imperfect FeO triangles with either one or two corners damaged in Figure 2-36(a) [138].

2.3.3 Domain boundary model

The third model to explain the contrast variation in a pinwheel pattern works for the van der Waals materials such as $MoTe_2$ or $MoSe_2$ film on MoS_2 substrate [130], as shown in Figure 2-37(a) – (c). The spokes have a sandwich structure with a bright-dark-bright sequence. It is called a mirror-twin domain boundary (MTB) with a distinctive atom configuration. The central

dark line is due to the deficiency of Mo atoms, which leads to the fourfold coordination of Te or Se atoms [Figure 2-37 (c), (d)]. On the contrary, two arrays of Te or Se atoms next to the dark gap remain the initial bonding with three Mo atoms but appear much brighter in the STM images. However, the other threefold coordinated Te or Se atoms inside the triangle elements are less bright or even appear as depressions. The formation of the pinwheel structure is not relevant to the MoS_2 substrate, which is in sharp contrast to the former two models.

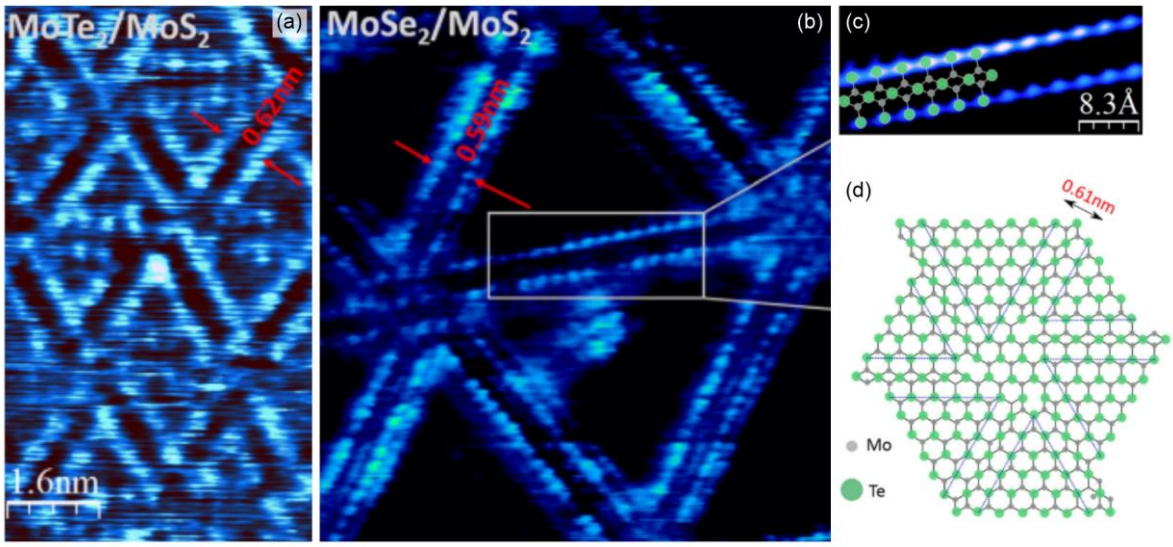

Figure 2-37 STM image of wagon wheel structure of (a) $MoTe_2/MoS_2$ (5.3 nm × 9.2 nm, V_s = 0.8 V, I_t = 0.3 nA). (b) $MoSe_2/MoS_2$ (8.8 nm × 9.2 nm, V_s = 0.8 V, I_t = 0.3 nA). (c) Enlarged STM image of the boxed area in (b). (d) Model of the wagon wheel structure with intersecting MTBs. Gap distance is calculated by $MoTe_2$ lattice parameter 0.3522 nm [130].

2.3.4 Triangular nanostructures

The pinwheel structure is highly relevant to the triangular elements which can be regarded as building blocks. As shown in Figure 2-33(c) and Figure 2-35(d), the pinwheel pattern can be composed of triangle elements with different sizes. In addition to FeO triangles, some nanostructures with triangular shapes have been identified at the atomic level. For example, single-layer MoS_2 can exhibit triangular morphologies on sapphire [139], Si or Si/SiO_2 [140], $SrTiO_3$ [141], and Au substrates [142]. The STM image and corresponding structural model of a MoS_2 nanoparticle on Au(111) are displayed in Figure 2-38(a) and (b). The edges of

nanostructures usually arouse attention as they are critical for some properties, particularly the catalytic properties. Figure 2-38(c) shows a hypothetical bulk-truncated MoS_2 nanoparticle with the exposed $(10\bar{1}0)$ Mo-edge and $(\bar{1}010)$ S-edge. The edge terminations can possess various S and H coverages [142]. Figure 2-38(d) displays structural models of MoS_2 triangular clusters obtained by DFT calculations. The triangle expands with more atoms involved in the cluster, and the edge structures could be diverse [143]. Without the confinement by the substrate, the 2D nanostructure can maintain the triangular shape during expansion. A similar growth mode has also been found in cerium oxide on the Ru(0001) substrate [144]. Figure 2-38(e) is a STM image showing the Moiré pattern with a (5 × 5) periodicity with respect to CeO_2 (111). The growth of CeO_2 triangles on a flat Ru surface can be described by a carpet growth model, as depicted in Figure 2-38(f).

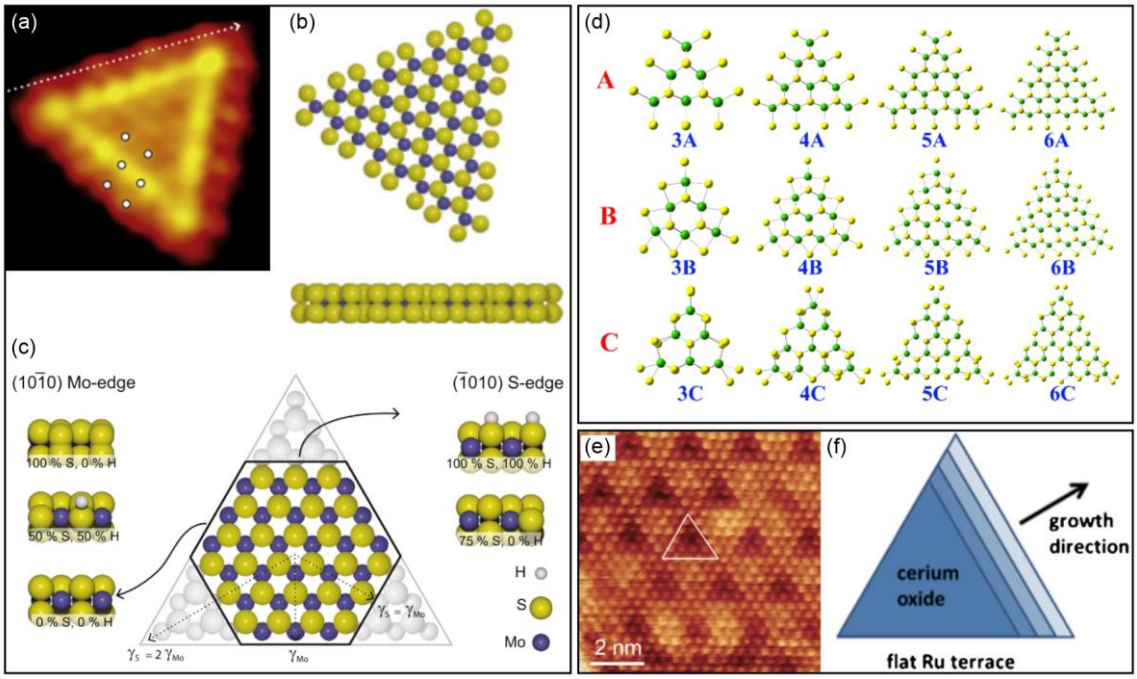

Figure 2-38 (a) STM image of a triangular MoS_2 nanoparticle synthesized by H_2S. (b) Ball models (top and side view) showing the MoS_2 triangular structure with Mo-terminated edges. (c)Wulff construction for a hypothetical bulk-truncated MoS_2 nanoparticle showing the exposed $(10\bar{1}0)$ Mo-edge and $(\bar{1}010)$ S-edge. The edge terminations can possess various S and H coverages [142]. (d) Structural models of MoS_2 triangular clusters with different sizes and edges. Green and yellow balls represent Mn and S, respectively [143]. (e) Moiré pattern formed by CeO_2(111) on Ru(0001) (9 nm × 9 nm). (f) Schematic of the carpet growth model of CeO_2 on Ru(0001) with a flat terrace [144].

2.4 Summary

This chapter gives an overview of several topics that are highly relevant to this DPhil project, including oxide thin films, 2D materials with a honeycomb structure, and 2D materials with a pinwheel structure. Oxide thin films have been widely studied experimentally regarding their structures and stoichiometries using microscopies and spectroscopies as well as the mechanical, electrical, and chemical properties. Theoretical works are usually involved in predicting properties that are difficult to be directly measured, solving the structural models, and supporting relevant hypotheses. In this chapter, Nb oxides on Pt/Au/Cu_3Au substrates, Ti oxides on Pt/Pd/Au substrates, and V oxides on Au/Pd/Rh substrates have been discussed and the corresponding structural models have been presented. However, investigations of these three oxide monolayers on Au(111) substrates were not as sufficient as on other substrates. The structures and stoichiometries of the Au-supported oxides have not yet been studied systematically with altering the oxygen chemical potential. Therefore, these remaining challenging questions are about to be explored in this thesis work.

Oxide thin films with the same transition metal elements can exhibit multiple structures and stoichiometries on the same substrate by varying the preparation conditions. They can also display similar structures with distinct characteristics on different substrates. Moreover, two different oxide thin films, such as Ti_2O_3 and Nb_2O_3, can have the same (2 × 2) epitaxial relationship with respect to the Au(111) surface. However, the honeycomb features like the domain boundary or edge reconstruction are non-identical. In this thesis, a systematic study of Nb oxides structures on Au(111) is presented, involving the clusters, triangles, pinwheels, and honeycomb monolayers. Comparative analysis between Nb oxides and Ti oxides regarding the honeycomb, triangle, and pinwheel structures is shown. In addition, V oxides on Au(111) are discussed in contrast to Nb/Ti oxides in the last two chapters.

Chapter 3 Experimental methods

This chapter demonstrates the instruments, materials, basic preparation procedures, and characterization methods in the study. Specific synthesis routes, conditions, and characterization parameters will be described in detail in relevant sections.

3.1 JEOL 4500XT vacuum system

3.1.1 Instrumentation

The experimental setup in this project is based on JEOL JSTM4500XT vacuum system [145] with several attachments, as shown in Figure 3-1(a) and (b). The instrument consists of three chambers: the treatment chamber, the image chamber, and the exchange chamber. The treatment chamber and the image chamber are connected by valve V1. Sample transfer between these two chambers is achieved by a horizontal transfer arm controlled by Magnetic Load 1 (MGL1). The exchange chamber provides the exchange channel between the ambient and the instrument. It is connected to the treatment chamber by valve V2, through which the exchange rod can put in or take out samples and STM tips by MGL2. Up to three samples and tips can park on a rotatable plate adjusted by MGL3 in the treatment chamber. The key component of the image chamber is the STM part. It consists of a specimen stage, a piezo scanner to precisely control the movement of the tip, and a manual retract lever which directly connects with the tip holder and can be plugged or unplugged manually. Several apparatuses are attached to the instrument. An ion Source ISIS3000 is mounted on the treatment chamber for sample cleaning (see Section 3.4), and an e-beam evaporator is mounted on the image chamber for metal deposition (see Section 3.5). The instrument is equipped with Ar and O_2 gas lines for sputtering and oxidizing.

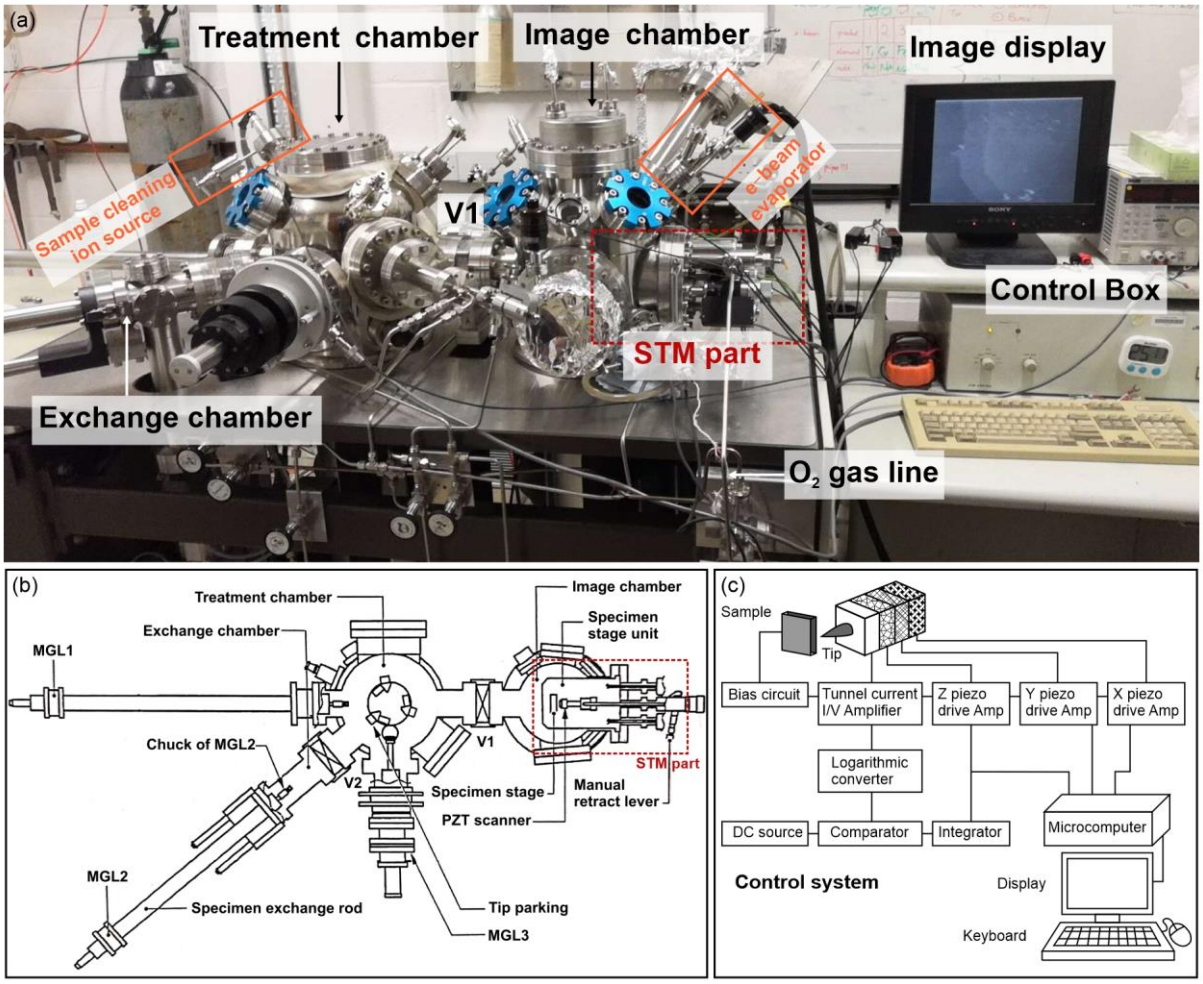

Figure 3-1 (a) JEOL JSTM 4500XT. (b) Schematic of the instrument (top view). (c) The control system of the instrument. The sample is designed to be biased with the tip grounded. The tip movement is precisely controlled by three piezo units along x-, y-, and z-directions [145].

The vacuum environment is achieved by vacuum pumps and monitored by various gauges. The evacuation of the exchange chamber is achieved by a turbomolecular pump connected with an oil rotary pump in series. The pressure of the exchange chamber is measured by a Penning gauge and a Pirani gauge. To avoid vibration, the treatment chamber and the image chamber are equipped with two individual ion pumps with two independent ion gauges measuring the pressures. Besides, two titanium sublimation pumps are equipped in both chambers but are not activated in daily evacuation. They are used after instrument baking or operating for a long time. The baking operation is an effective way to purify the vacuum system, particularly after exposing the chambers to the atmosphere. The heating temperature can reach 150 °C during baking, which can effectively remove the water molecules and some hydroxide groups.

3.1.2 Control system of the STM part

The control system of JEOL JSTM 4500XT is illustrated in Figure 3-1(c). The sample is designed to be biased and driven by coarse motors that enable the movement on a relatively large scale (millimeter range). The tip is grounded and attached to three piezo units that can precisely control the tip movement in x-, y-, and z- directions within a fine range of 0.2 μm × 0.2 μm × 0.5 μm. Tunneling current I_t can be generated between the sample and the tip when they are brought to 1 nanometre or even less. The tunneling current gives rise to the primary signal that will pass through the amplifier and converter and be compared with a reference value. The difference is integrated and amplified to drive the z-piezo. The feedback loop is not shown in the diagram. Whether the feedback is activated or not depends on the mode set for imaging. In a constant height mode, the feedback is switched off, and the tip is kept at a constant height during the scanning process. In a constant current mode, if the detected tunneling current is larger than the reference value, the negative feedback will impose a voltage to the z-piezo to withdraw the tip; if it is smaller than the reference, the z-piezo will drive the tip to approach the sample surface. The signal is collected over the xy plane by tip scanning the sample surface, which results in a STM image in grayscale on the display screen. The STM images reflect the topographical information of the sample surface with protrusions representing high z values and depressions representing low z values. However, the interpretation of a STM image at the atomic scale should not simply consider the topography as the electronic structure of the surface and the tip termination may play a dominant role (see Section 3.2.2). JEOL JSTM 4500XT usually detects the tunneling current around 0.05 ~ 2 nA, although the designed parameter has a broader range.

A vibration isolation system is essential for obtaining STM images with high quality. The instrument is equipped with an air suspension and 3-stage stacks to realize the passive vibration isolation.

3.2 STM working principle

3.2.1 Acquisition of the STM images

General description

Scanning tunneling microscopy is a surface characterization technique based on the tunneling effect between the sample and the tip [146–151], as shown in Figure 3-2(a), (b). When the gap between two electrodes is in the order of several angstroms, their electron wavefunctions overlap, thus creating a finite tunneling conductance. If a bias is applied to either the tip or the sample, a current can be generated between the two electrodes.

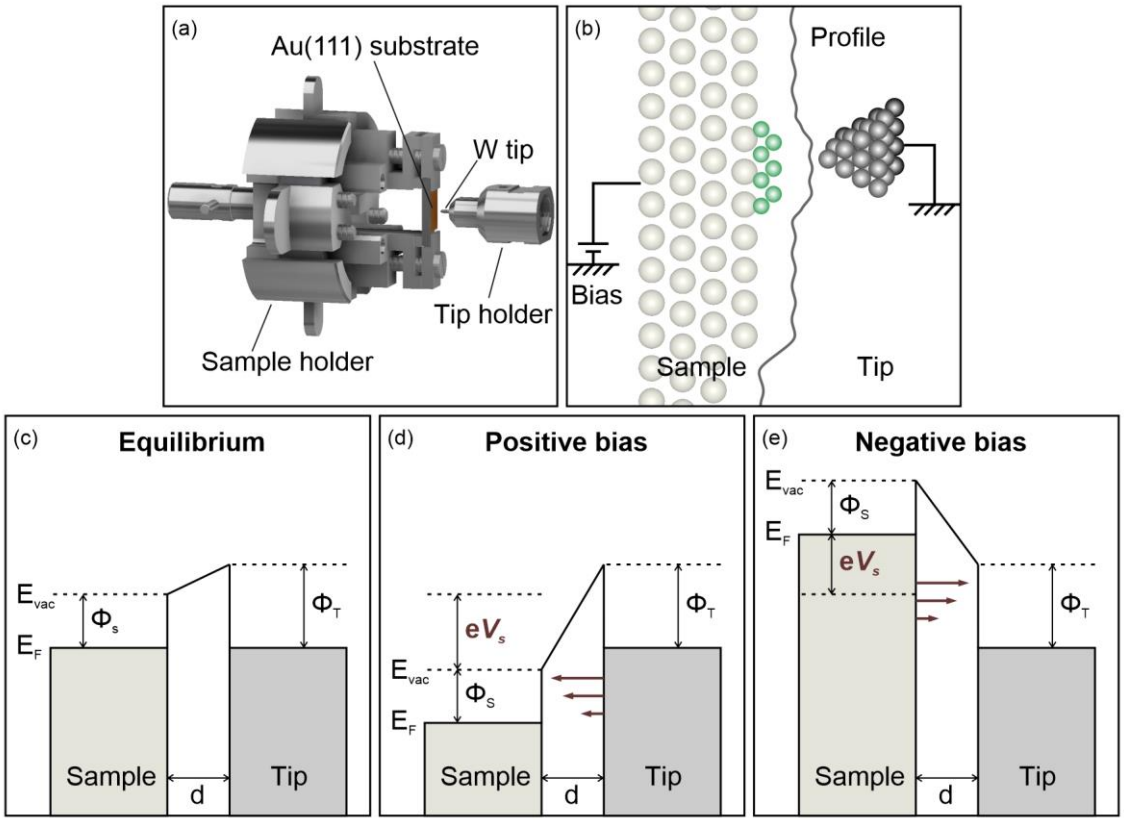

Figure 3-2 (a) Relative position of the sample and the tip in the image chamber in JEOL JSTM 4500XT. (b) Schematic drawing of the sample and the tip at the atomic level. The sample is biased, and the tip is grounded. (c) Energy diagram of the sample and the tip at equilibrium without applying a bias. (d) The sample is positively biased, so its Fermi level is shifted downward. Electrons can tunnel from the filled states of the tip to the empty states of the sample. (e) The sample is negatively biased with the Fermi level lifted. Electrons tunnel from the filled states of the sample to the empty states of the tip.

The workfunctions of the sample and the tip are denoted as Φ_s and Φ_t respectively. The workfunction represents the minimum energy that is required to isolate an electron at the Fermi level from the bulk to the vacuum. We can see that an energy barrier with a trapezoidal shape is formed when Φ_s does not equal to Φ_t in Figure 3-2(c). This is a general approximation when solving the barrier height in theoretical models. A rectangle barrier with $\Phi_s = \Phi_t$ is also commonly used in simplified models. The average value of the work function is around 5 eV. When the sample bias V_s is positive, as shown in Figure 3-2(d), the Fermi energy of the sample is shifted downward. Electrons from the filled states of the tip can tunnel to the empty states of the sample; When V_s is negative, as shown in Figure 3-2(e), electrons can tunnel from the filled states of the sample to the empty states of the tip.

STM imaging

The instrumentation and the control system have been presented in Section 3.1. Two operation modes can be selected: the constant current mode or the constant height mode. The constant current mode is more commonly used than the constant height mode for most STMs. All STM images presented in this thesis were obtained at constant current mode in JEOL JSTM 4500XT with the tunneling current I_t = 0.05 ~ 2 nA at room temperature (RT). The maximum scanning area is 200 nm × 200 nm constrained by the x- and y-piezo. Images are recorded in grayscale with a pixel size of 512 × 512. Apart from the tip's quality, the scanning speed is also a key factor for obtaining a STM image with high quality. A few trials are required to find the balance between the scan time and the thermal drift. Although imaging with a low scan speed generally means higher stability, other undesired factors such as the thermal drift of the sample stage, hysteresis of the piezo scanner, and the external vibration can contribute to the image distortion simultaneously. By comparison, the constant height mode is more challenging to implement in a practical experiment. It is usually applied to conduct a fast scan of the sample surface that is atomically flat at a low temperature.

Voltage-dependent imaging is a method to see different types of atoms in the experiment. They could be different chemical elements or one element with varying oxidation states. Applying a positive bias to the sample allows its empty states to be observed, while a negative sample bias is for imaging the filled states. A typical example is using positive and negative sample biases to discriminate Ga and As atoms. The covalent bond of GaAs has an ionic property due to the charge transfer from Ga to As. Therefore, filled states are accumulated around As atoms, while empty states are located around Ga atoms. When scanning the GaAs surface with a positive sample bias, the empty states of GaAs contribute to the tunneling signal, namely Ga atoms appear as protrusions in the STM images. While As atoms can be seen as protrusions under a negative sample bias. In this research work, voltage-dependent imaging was occasionally used. We have obtained good results from the studies of the (2 × 2) Nb_2O_3 honeycomb structure, in which Nb atoms were usually observed at a positive bias (V_s = 0.5 ~ 2 V) and O atoms were visible at a negative bias (V_s = -1.5 ~ -0.5 V). However, switching the sign of sample bias during imaging may change the tip's electronic structure due to complex surface-tip interaction. As a result, the atomic resolution is hardly retained and thus the interpretation of the images would be more complicated.

3.2.2 Interpretation of the STM images

As a surface characterization technique, STM can provide topographical information on the sample surface. The bright spots or regions with high z values are protrusions, while the dark part with small z values are depressions. In other words, the grayscale corresponds to the height difference. This simple interpretation of the STM image can be applied to a surface with large height variance, such as an area with several steps on a large scale. However, it is not suitable to interpret images with atomic resolution or any features at the atomic scale, and it cannot explain different contours obtained from voltage-dependent imaging either. Another interesting phenomenon that can be frequently observed is the inverted atomic corrugation, which means

atoms situated at higher sites appear as depressions while atoms at lower sites appear as protrusions in the STM images. Therefore, the interpretation of the STM images at the atomic scale should be related to the electronic structures of the sample surface and the tip termination rather than a straightforward explanation from the surface topography.

In this section, an electron tunneling through the 1D rectangle barrier will be discussed first. Based on this simplest model, the vertical and spatial resolution of the STM can be estimated. Secondly, the Bardeen Model is applied to calculate the tunneling current between two electrodes in more general cases. Two approximations of the Bardeen Model: Energy-dependent Approximation and Tersoff-Hamann Approximation are reviewed. By the end, it is shown that the tunneling current relates to the sample bias (V_s), the gap distance (d), and the density of states (DOS) of the sample (ρ_{sample}) and tip (ρ_{tip}). In other words, an atomically-resolved STM image is able to reflect the electronic structure of the sample and the tip.

An electron in a 1D rectangle barrier

In quantum mechanics, an electron described by the wavefunction $\Psi(z)$ with energy E can penetrate a region with a potential barrier $U(z) > E$, which is called tunneling.

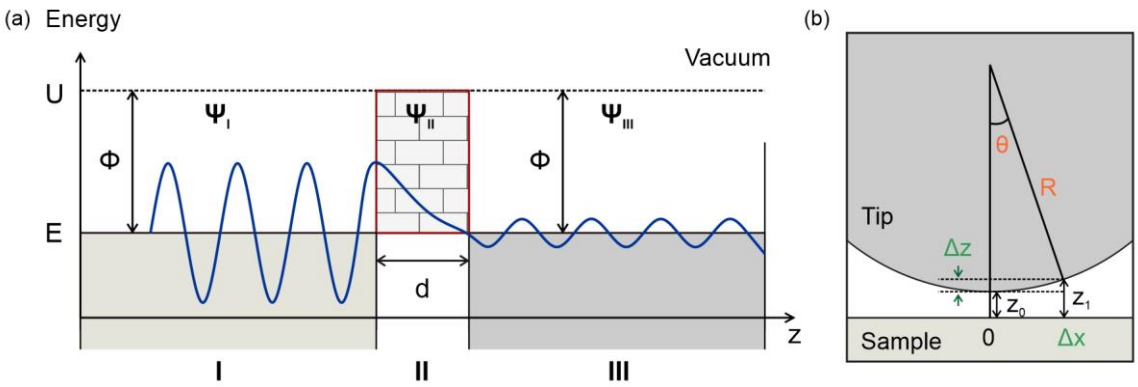

Figure 3-3 (a) An electron in a 1D rectangle barrier. The electron is incident from Region I with an oscillating wavefunction, then penetrates Region II with a decaying wavefunction, and finally enters Region III with an oscillating wavefunction. (b) Schematic drawing showing the height difference Δz due to a lateral shift by Δx.

The wavefunction in Region I, II, and III shown in Figure 3-3(a) satisfies the 1D Schrödinger equation:

$$-\frac{\hbar^2}{2m}\frac{d^2}{dz^2}\Psi(z) + U(z)\Psi(z) = E\Psi(z), \tag{3-1}$$

in which ħ is the Plank Constant, m is the electron mass. The wavefunction solutions in the three regions can be written as:

$$\Psi(z) = \begin{cases} Ae^{ikz} + Be^{-ikz}, & \text{Region I} \\ Ce^{-\kappa z} + De^{\kappa z}, & \text{Region II} \\ Fe^{ikz}, & \text{Region III} \end{cases} \tag{3-2}$$

The electron at Region I and III has oscillating waves with imaginary wave vector k:

$$k = \sqrt{\frac{2m}{\hbar^2}(E - U)}. \tag{3-3}$$

The wavefunction in Region II does not have an oscillating solution but decays exponentially with the decay constant κ defined by $\kappa = ik$. So the real variable κ can be expressed as:

$$\kappa = \sqrt{\frac{2m}{\hbar^2}(U - E)}. \tag{3-4}$$

A is the amplitude of the incident electron wave in Region I and is set to be unity. Coefficients B, C, D, F are complex numbers that can be calculated from the boundary continuity conditions. We cared about the transmission factor T defined in Formula (3-5), which means the probability of finding the tunneling electron on the right side of the potential barrier in Region II.

$$T = \frac{\Psi(d)^2}{\Psi(0)^2} = |F|^2 e^{-2\kappa d} = \frac{16E(U - E)}{U^2}\exp\left[-2d\sqrt{\frac{2m}{\hbar^2}(U - E)}\right]. \tag{3-5}$$

We take the vacuum level as the zero-energy reference point for a metal-vacuum-metal system. Assuming the electron is at the energy state around the Fermi level, the energy difference ($U - E$) is equal to the metal workfunction Φ. To simplify the derivation, we assume two metals have an identical workfunction, as shown in Figure 3-3(a). Then the transmission factor T has a simple relationship with the gap distance d:

$$T \propto e^{-2\kappa d}, \tag{3-6}$$

where κ satisfies:

$$\kappa = \sqrt{\frac{2m\Phi}{\hbar^2}}. \tag{3-7}$$

As mentioned above, the average value of the workfunction is $\Phi \approx 5$ eV, so $\kappa \approx 1.14\ \text{Å}^{-1}$. From Formula (3-6) we can see that the transmission factor T decays $1/e^{-2.28} \approx 9.78$ times when the gap distance d increases by 1 Å, approximately an order of magnitude per angstrom. Though here we only consider one electron in the 1D rectangle barrier, the decay concept also applies to an electron flux, namely the tunneling current in the STM. It can explain why the STM tip is sensitive to any height change on the surface as well as the origin of the atomic resolution in the vertical direction.

The lateral resolution of the STM can also reach the atomic level, which allows the atomic corrugation of the sample surface to be recorded. As shown in Figure 3-3(b), we assume that the tip is terminated with one atom or several atoms forming a cluster with a radius R, which is much larger than the height difference Δz due to the lateral shift by Δx.

$$\Delta z = R - R\sqrt{1 - \sin^2\theta} \approx \frac{\Delta x^2}{2R}. \tag{3-8}$$

Substituting Formula (3-8) into Formula (3-5) we can get

$$\Psi(Z_1)^2 = T \cdot \Psi(Z_0)^2,$$

$$I(Z_1)^2 \propto \exp\left(-\kappa \frac{\Delta x^2}{R}\right). \quad (3\text{-}9)$$

Assuming $R = 1$ nm, a lateral shift by $\Delta x = 3$ Å gives rise to a decay of 3 times ($1/e^{-1.03} \approx 2.79$). This roughly explains how the STM achieves the atomic resolution in the lateral plane. In an actual STM experiment, the spatial resolution can even reach 2 Å. It is worth noting that we deduce the vertical and lateral resolution of the STM from a fundamental perspective of the wavefunction, which means this is the limit of the STM resolution.

The Bardeen Model and approximations

The simplified model presented above shows the exponential decay with increasing the gap distance, but it does not reflect any material property or the relation with the applied sample bias. To interpret an experimental STM image, we need to consider the tunneling current, namely the flux of electrons [152].

The transmission factor T can also be defined as the ratio of the tunneling current collected at the tip end (z = d) to the incoming current at the surface (z = 0):

$$T = \frac{I(d)}{I(0)} \propto e^{-2\kappa d}. \quad (3\text{-}10)$$

In the simplified 1D case, only one electron with its wavefunction solutions that satisfy 1D Schrödinger equations is considered. However, as electrons are fermions, each electron contributed to the electric flux has its 3D complete wavefunction with corresponding energy eigenvalue. Here, an electron engaged in the elastic tunneling process can be treated as being scattered from an initial state (i) to a final state (f) with energy conserved. To calculate the tunneling current, we need to know the number of electrons per time, which is defined as the

transition rate between two metal electrodes. Fermi's golden rule, which is also known as the first-order time-independent perturbation theory, describes the transition rate *w* from the tip to the sample as:

$$w_{\mathrm{tip,i}\rightarrow\mathrm{sample,f}} = \frac{2\pi}{\hbar}|\mathrm{M_{fi}}|^2\delta\left(\mathrm{E_{sample,f}} - \mathrm{E_{tip,i}}\right), \tag{3-11}$$

in which the $\mathrm{M_{fi}}$ is the matrix element of the perturbation potential between the initial state and the final state. The calculation detail of the matrix element is not presented here, but its connection with the transmission factor T will be shown later. The Dirac delta function ensures energy conservation as the energy of the final state $\mathrm{E_{sample,f}}$ must be equal to the energy of the initial state $\mathrm{E_{tip,i}}$.

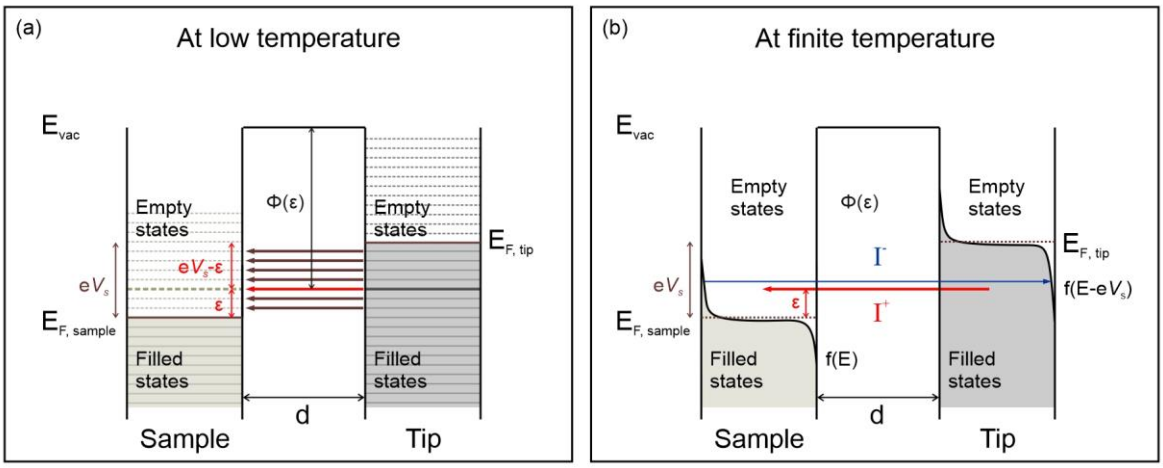

Figure 3-4 (a) Schematic diagram of the energy states of the sample and the tip at low temperature. Assuming their workfunctions are equal, a rectangular potential barrier is formed by applying a positive sample bias in the gap. Colored regions with solid lines represent the filled states, white regions with dash lines represent the empty states. The sample is positively biased by V_s, so electrons with energy states within the energy window eV_s can tunnel from the tip to the sample. No thermal excitation is considered at the low temperature, so the Fermi functions of both the sample and the tip are step functions. An electron from the tip with initial energy state ε is scattered to the sample with final energy state ε due to the energy conservation. (b) Schematic diagram at finite temperature. Due to the thermal excitation, the Fermi functions are no longer step functions but follow the Fermi-Dirac distributions. Within the energy window eV_s, electrons can tunnel from the filled states of the tip to the empty states of the sample, which is denoted as I^+. The red arrow indicates the electron moving direction, but I^+ is in the opposite direction. A small number of electrons that are thermally excited can tunnel from the sample to the tip (the blue arrow), which is denoted as I^-.

Figure 3-4(a) shows that when the sample is positively biased by V_s, tunneling occurs within the energy window eV_s. An electron with an initial energy state ε elastically tunnels from the tip to the sample with a final energy state ε. Consequently, the tunneling current can be obtained by first computing the sum of tunneling electrons of any energy state within the energy window and then multiplying the charge. Besides, considering the spin degeneracy, the tunneling current can finally be expressed as the Bardeen equation:

$$I = \frac{4\pi e}{\hbar}\sum_{i,f}|M_{fi}|^2\delta\left(E_{sample,f} - E_{tip,i}\right). \tag{3-12}$$

Formula (3-11) and (3-12) are results after applying the Bardeen model, in which the coupling between the sample and the tip is assumed to be very weak. In other words, the tip potential is set to be zero in the sample region and vice versa. The Bardeen model was created to solve superconductor issues before the invention of the STM. Formula (3-12) is a very general result, in order to further connect it with the material properties, the sample bias, and the sample-tip gap distance, we need to evaluate the matrix element M_{fi} through a few approximations.

The energy-dependent approximation of the Bardeen equation

In the energy-dependent approximation, the sum of the sample and the tip states is replaced by the density of states of the sample and the tip. It can be proved that:

$$|M_{fi}|^2\delta\left(E_{sample,f} - E_{tip,i}\right) = \int_{-\infty}^{\infty}|M(\varepsilon)|^2\,\delta(\varepsilon - E_i)\delta(\varepsilon - E_f)d\varepsilon. \tag{3-13}$$

Therefore, Formula (3-11) can be written as:

$$w_{tip,i\rightarrow sample,f} = \frac{2\pi}{\hbar}\int_{E_{F,sample}}^{E_{F,tip}}|M(\varepsilon)|^2\sum_i\delta(\varepsilon - E_i)\sum_f\delta(\varepsilon - E_f)\,d\varepsilon. \tag{3-14}$$

The density of states $\rho(E)$ is defined as $\rho(E) = dN(E, E + \Delta E)/dE$, which calculates the number of states N within the energy range $(E, E + \Delta E)$. It can also be written as:

$$\rho(\varepsilon) = \sum_{n} \delta(\varepsilon - E_n), \tag{3-15}$$

for a system with discrete energy states n. Substituting into Formula (3-14) results in:

$$w_{tip,i\rightarrow sample,f} = \frac{2\pi}{\hbar} \int_{E_{F,sample}}^{E_{F,tip}} |M(\varepsilon)|^2 \rho_{tip}(\varepsilon)\rho_{sample}(\varepsilon)d\varepsilon. \tag{3-16}$$

Within the energy window eV_s, the tunneling current can be calculated by:

$$I = \frac{4\pi e}{\hbar} \int_{0}^{eV_s} |M(\varepsilon)|^2 \rho_{tip}(\varepsilon - eV_s)\rho_{sample}(\varepsilon)d\varepsilon. \tag{3-17}$$

By far, the tunneling current has been related to the density of states of the sample and the tip. The matrix element $M(\varepsilon)$ will be discussed according to the potential barrier and the distribution of energy states as follows.

(i) 1D rectangular barrier

The simplest model for the potential barrier is the 1D rectangle barrier which assumes the sample and the tip have the same workfunction Φ. The transmission factor T is then a function of the workfunction Φ and tip-sample gap d. Applying the result in Formula (3-6) we can get:

$$T = T(\Phi, d) \propto \exp\left(-2d\sqrt{\frac{2m\Phi}{\hbar^2}}\right). \tag{3-18}$$

Related Formula (3-17) to Formula (3-10), in the case of the 1D rectangle barrier, the square of the matrix element $|M(\varepsilon)|^2$ can be approximated by the transmission factor $T(\Phi, d)$.

(ii) A general barrier as a function of energy and sample bias

A more general case for the potential barrier is that the barrier no longer remains a rectangle shape but depends on the workfunctions of the sample and the tip as well as the applied sample bias V_s. For example, a trapezoidal barrier shown in Figure 3-2(c) – (e) is usually modeled by the Wentzel-Kramers-Brillouin (WKB) approximation. The concept of effective barrier is introduced here, which considers the average workfunction of the sample and tip, and the median value of the energy window. Therefore, for a tunneling electron with energy state ε, the corresponding effective workfunction can be written as:

$$\Phi_{\mathrm{eff}} = \frac{\Phi_{\mathrm{tip}} + \Phi_{\mathrm{sample}}}{2} + \frac{\mathrm{e}V_s}{2} - \varepsilon. \tag{3-19}$$

Similarly, we can approximate the matrix element $|\mathrm{M}(\varepsilon)|^2$ by the transmission factor T,

$$\mathrm{T} = \mathrm{T}(\varepsilon, V_s, \mathrm{d}) \propto \exp\left(-2\mathrm{d}\sqrt{\frac{2\mathrm{m}\Phi_{\mathrm{eff}}}{\hbar^2}}\right). \tag{3-20}$$

If $\mathrm{e}V_s \ll \Phi$, the average of the energy states of all tunneling electrons $\bar{\varepsilon}$ is equal to the median value of the energy window. Then Φ_{eff} can be calculated by the average value of the tip and sample workfunctions in the case of a trapezoidal barrier. Hence the transmission factor T only depends on the gap distance d. The tunneling current can be calculated by

$$\mathrm{I} = \frac{4\pi\mathrm{e}}{\hbar}\mathrm{T}(\mathrm{d})\int_0^{\mathrm{e}V_s} \rho_{\mathrm{tip}}(\varepsilon - \mathrm{e}V_s)\rho_{\mathrm{sample}}(\varepsilon)\mathrm{d}\varepsilon\,. \tag{3-21}$$

(iii) Distribution of energy states at finite temperature

At the low temperature, the distribution of energy states follows a step function as shown in Figure 3-4(a). However, at a finite temperature T_p, electrons can be thermally excited, so the energy states possess a Fermi-Dirac distribution which is defined as:

$$f(\varepsilon - E_F) = \frac{1}{1 + \exp\left(\frac{\varepsilon - E_F}{k_B T_p}\right)}. \quad (3\text{-}22)$$

When the sample is positively biased, electrons cannot only tunnel from the filled states of the tip to the empty states of the sample, but a small amount of thermally-excited electrons can tunnel from the sample to the tip, as shown in Figure 3-4(b). Electrons that tunnel from the tip to the sample generate a tunneling current I^+, while electrons that tunnel from the sample to the tip give rise to an opposite current defined as I^-. As a result, the total tunneling current I_{total} related to the occupation numbers can be expressed as:

$$I_{total} = I^+ - I^- \propto f\left(\varepsilon - E_{F,tip}\right) - f\left(\varepsilon - E_{F,sample}\right). \quad (3\text{-}23)$$

By setting $E_{F,sample} = 0$ and $E_{F,tip} = eV_s$, the total current can be written as:

$$I_{total} = I^+ - I^- \propto f(\varepsilon - eV_s) - f(\varepsilon). \quad (3\text{-}24)$$

And the tunneling current defined by Formula (3-17) can be written as:

$$I = \frac{4\pi e}{\hbar} \int_0^{eV_s} |M(\varepsilon)|^2 \left[f(\varepsilon - eV_s) - f(\varepsilon)\right] \rho_{tip}(\varepsilon - eV_s)\rho_{sample}(\varepsilon)d\varepsilon. \quad (3\text{-}25)$$

The Tersoff-Hamann Approximation of the Bardeen Model

After the invention of the STM, Tersoff and Hamann suggested a method by making some assumptions about the tip to simplify the Bardeen Model. It avoids complex calculations of the tunneling matrix element and thus has been widely applied to interpret the STM images and generate simulated STM images. The basic assumptions in the Tersoff-Hamann approximation can be summarized as follows [153,154]. (i) The matrix element is no longer a function of energy. It is assumed that $eV_s \ll \Phi$, therefore electron states E_n at the Fermi level are mainly considered. (ii) The wavefunction of the outermost tip atom is assumed to be a simple s-wave

function. (iii) The wavefunction of the surface is assumed to be a plane wave described by Fourier expansion, in which the structural information is implied in the Fourier components.

As a result, the tunneling current defined in Formula (3-12) can be simplified as:

$$I \propto \sum_{n} |\Psi_n(r_t)|^2 \delta(E_n - E_F), \tag{3-26}$$

where $\Psi(r_t)$ is the surface wavefunction of an electron at position r_t with respect to the effective tip center, namely the center of the spherical s-wave. The density of states is given in Formula (3-15). By multiplying the square of the wavefunction $|\Psi_n(r_t)|^2$, it is modified to be a spatial distribution that is called the local density of states (LDOS) denoted as $\rho_{sample}(E_F, r_t)$. Finally, the tunneling current can be directly related to the sample's LDOS.

$$I \propto \rho_{sample}(E_F, r_t). \tag{3-27}$$

The Tersoff-Hamann approximation is popular in STM image interpretation and simulation. However, it sometimes fails due to the simple s-wave assumption for the tip wavefunction. The extended Tersoff-Hamann approximation considers other orbital types for the tip wavefunction, for example, the d_{z^2}-wave, which can better reproduce the experimental results.

3.3 Tungsten tip making

The STM is based on the tunneling current between the conducting sample surface and the scanning tip. The tunneling signal is a convolution of the local density of states and topography of the sample surface as well as the tip front. Therefore, the tip's size, shape, and cleanliness are critical for reaching a satisfying resolution. An STM tip is usually made of tungsten or platinum/platinum-iridium (Pt/Pt-Ir) alloy and produced by various methods such as electrochemical etching or mechanical cutting [155–161].

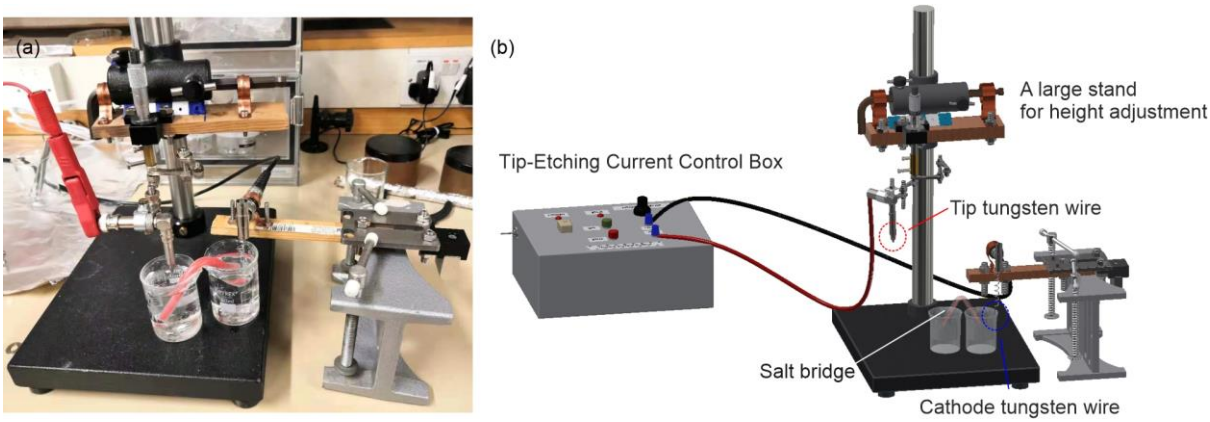

Figure 3-5 (a) Photo of the new tip etcher. The anode and the cathode are separated by two beakers but connected by a salt bridge (the red arc); (b) Schematic diagram showing the key components of the new tip etcher.

In this study, tungsten wire (99.95%, Goodfellow) with a diameter of 0.3 mm was used for making tips by electrochemical etching in NaOH solution. I was involved in the improvement of a tip etcher device. As shown in Figure 3-5, the new etcher separates the anode and the cathode with two beakers, which significantly improves the stability of the etching process and shrinks the etching time. The tungsten wire was cut in 15 mm and inserted into a tip holder. It acts as the anode in the electrochemical reaction, which can be written as:

$$\mathrm{W(s) + 2OH^- + 2H_2O \xrightarrow{electrolysis} WO_4^{2-} + 3H_2(g)}, \qquad (3\text{-}28)$$

The electrochemical etching occurs at the interface of NaOH solution and the air, as shown in Figure 3-6(a). The tungsten wire at the interface is gradually etched until the end finally falls off, giving rise to a sharp and convergent tip above the liquid. The etching process was recorded by a digital camera, as shown in Figure 3-6(b) – (e).

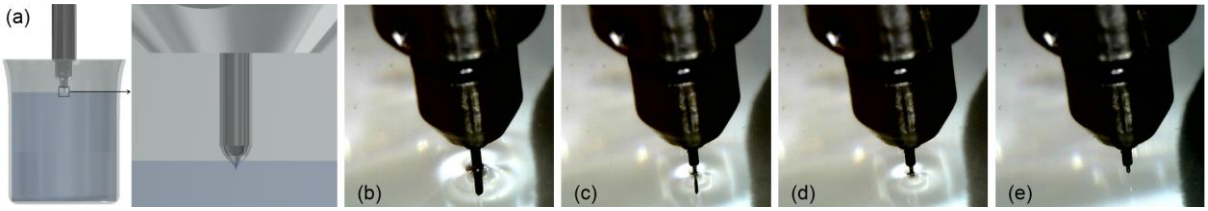

Figure 3-6 (a) Schematic diagram of the W wire at the interface between NaOH solution and the air. (b) – (e) A series of photos recording the etching process of the W wire at the interface between the air and the liquid; a sharp tip was finally formed above the liquid in (e).

The concentration of the NaOH solution affects the tip shape and the etching time. Test results are shown in Figure 3-7 and Figure 3-8. A low concentration (~ 1 mol/L) gives rise to a very long etching duration and an extremely long tip, while a high concentration (> 4 mol/L) leads to a quick reaction but the tip's quality is unstable. Therefore, in this study, an appropriate concentration of NaOH solution is 2 ~ 3 mol/L, and the etching time generally takes 10 mins.

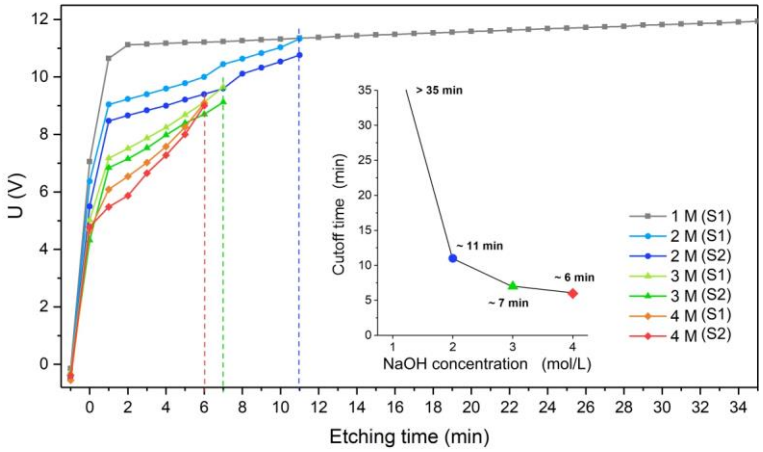

Figure 3-7 The relationship between the etching time and the tip potential. The dash lines indicate the cut-off time when the end of the W wire falls off. The inset shows the cut-off time versus the NaOH concentration.

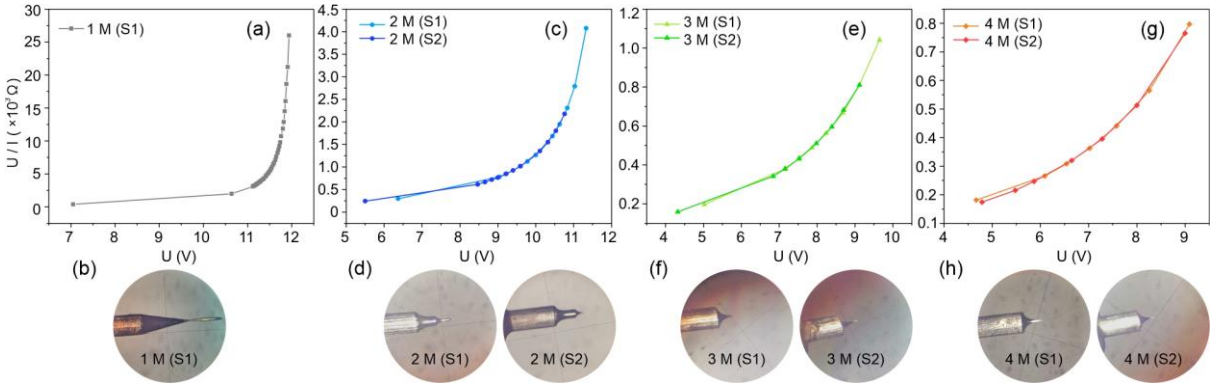

Figure 3-8 The R-U relationship of the anode etching in NaOH solution with different concentrations and corresponding tip products. (a), (b) 1 mol/L; (c), (d) 2 mol/L (S1 and S2 refer to two recorded samples); (e), (f) 3 mol/L; (g), (h) 4 mol/L.

3.4 Sample cleaning ion source

The surface of Au substrates in UHV can be cleaned by ion bombardment and reconstructed by annealing. Therefore, a substrate can be repeatedly used 5 ~ 8 times depending on the remaining

thickness. A PSP Vacuum Technology Ion Source ISIS3000 [162] is mounted on the treatment chamber of the JEOL JSTM 4500XT system, as shown in Figure 3-1.

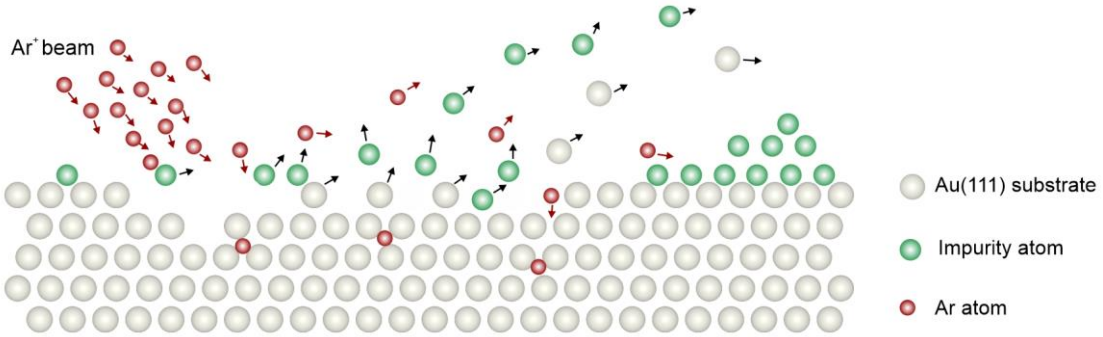

Figure 3-9 Schematic diagram of the sample cleaning process by sputtering. Arrows indicate the moving directions of the particles.

Argon sputtering gun allows Ar^+ ions with variable beam energy to clean the sample surface with minimum damage [163,164]. Figure 3-9 is a schematic diagram of the sputtering process, in which the Au substrate is subjected to an irradiation by energetic Ar^+ ions. Impurity atoms and some Au atoms are removed by colliding with the incoming Ar^+ ions. Empirical parameters for sample cleaning were used and proved to be efficient and reliable. For a general Au substrate grown by a submonolayer thin film, the beam energy for an effective cleaning is 700 ~ 1000 eV. The substrate was mounted on the specimen plate and rotated to a horizontal position with the maximum area facing the incident Ar^+ ion beam. The cleaning process usually took 8 ~ 15 mins to ensure that the impurity atoms could be thoroughly removed. Insufficient sputtering time results in a remnant of metal oxides, which will negatively affect the subsequent sample preparation and characterization. For a complete cleaning, samples with more metal deposition require a longer sputtering time. The thickness of the remaining Au substrate is roughly judged by the color and should be often monitored. The Au(111) substrate needs to be replaced once the golden color is invisible, otherwise the tip is insensitive to detecting the tunneling current when approaching the sample surface. Besides, in Figure 3-9 we can see that the incident Ar^+ ions also remove surface Au atoms and are buried in the bulk. Therefore, annealing at a high

temperature (600 ~ 700 ℃) for 1 ~ 1.5 h is an essential step to remove the buried Ar atoms and reconstruct the Au(111) surface. Au(111) surface reconstruction is demonstrated in Section 3.6.2. Apart from surface cleaning, low beam energy (50 ~ 100 eV) with a short sputtering time (10 ~ 60 s) was used to artificially create point defects in the (2 × 2) Nb_2O_3 honeycomb structure, which will be discussed in Section 4.6.3 and Section 8.3.

3.5 E-beam deposition

A mini e-beam evaporator (Oxford Applied Research EGN4) [165] is used for the metal deposition on a fixed substrate. The evaporator is mounted on the image chamber of the JEOL JSTM 4500XT and designed for operation at chamber pressure lower than 5×10^{-5} Pa.

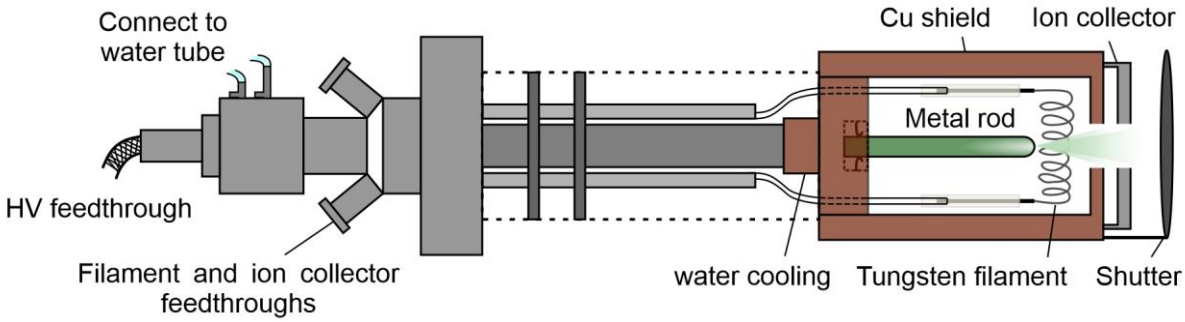

Figure 3-10 Schematic of e-beam evaporator.

Figure 3-10 shows the schematic of the EGN4 e-beam evaporator. It provides four independent pockets for metal rods and separates them by a Cu shield that connects to the water cooling at one end. The metal rods are applied to a high voltage (i.e., 2 kV). Each pocket is fitted with a tungsten filament at earth potential. The emitted electrons from the filament can be accelerated in the electric field and bombard the target metal rod, inducing a large amount of heat to evaporate the metal. During this electron-beam-induced thermal evaporation, some metal atoms are ionized. The ion collector intercepts a small fraction of the positive ions and transfers the ion current to a readable flux value on the ion meter, by which we can monitor the evaporation amount of the studied metal.

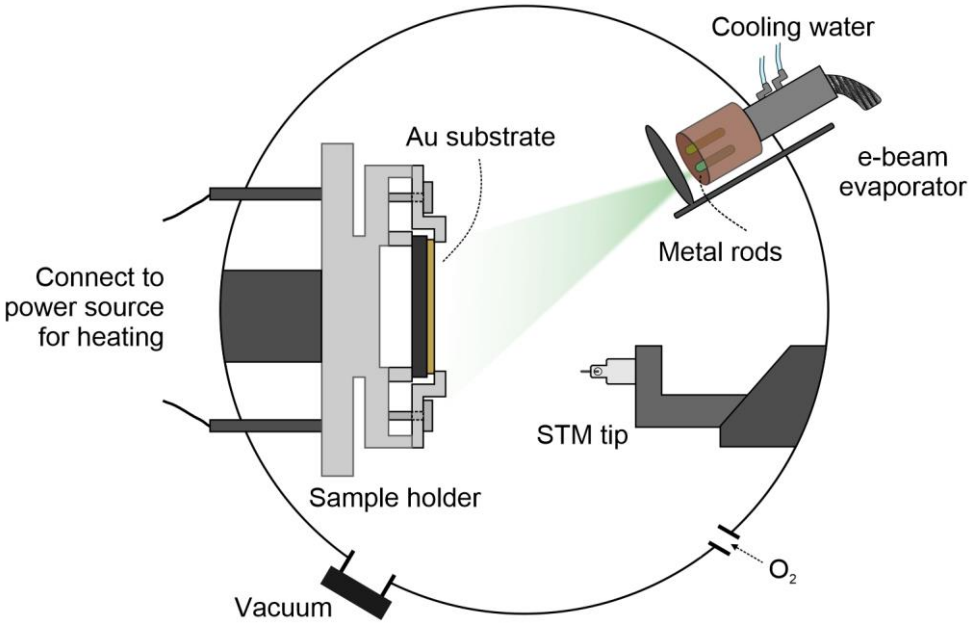

Figure 3-11 Schematic of metal deposition on Au substrate showing the relative positions of the components in the image chamber; they do not represent the actual sizes.

Figure 3-11 shows the schematic of the metal deposition. The green part represents the metal atoms emitted from the e-beam evaporator. The gaseous metal atoms will disperse in the whole chamber during evaporation, and just a tiny part of them will impinge on the Au substrate. The deposition amount on the Au(111) substrate is manually controlled by opening and closing the shutter. Later it is evaluated from the STM images rather than the ion flux displayed on the ion meter. The image chamber is equipped with an oxygen gas line, which allows either reactive deposition in a low-pressure oxygen atmosphere or post-oxidation after the deposition.

3.6 Au substrate preparation

3.6.1 Substrate selection criterion

Oxide thin films MO_x can be directly grown on the single crystalline M substrate, such as SiO_2 on Si(100) [166], NiO on Ni(100) [167]. However, oxides grown by this method usually have a relatively large lattice mismatch with the substrate, leading to some problems that arise from the poor quality. By comparison, it can be better to grow oxide thin films on noble metal surfaces thanks to a smaller lattice mismatch, flexible preparation procedures, and the chemical

inertness of the substrates. Besides, the high electrical conductivity of noble metal substrates may also help avoid charging problems when applying electron-based characterization techniques if the oxide on the surface cannot provide sufficient conductance [17].

Au(111) is used as the substrate for growing metal oxide thin films in this study. Apart from the general advantages of noble metal substrates, Au possesses the unique advantage of being the only face-centered cubic metal with a surface reconstruction [168]. The Au(111)-$(22 \times \sqrt{3})$ surface reconstruction is demonstrated in detail in the following section. The reconstruction gives rise to some interesting phenomena. For example, an impurity-induced (e.g., Nb-induced) ring pattern has a 60° rotation if it is situated at the hcp region on the surface with respect to the others at the fcc region (see Figure 4-5).

3.6.2 Au(111) surface reconstruction

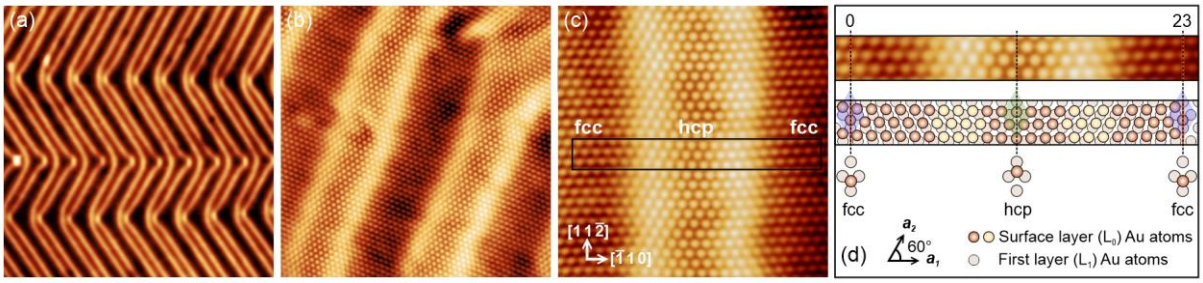

Figure 3-12 STM images of the Au(111)-$(22 \times \sqrt{3})$ reconstructed surface: (a) 60 nm × 60nm, V_s = 2.0 V, I_t = 0.16 nA; (b) 12.8 nm × 12.8 nm, V_s = 0.2 V, I_t = 0.15 nA; (c) 6.4 nm × 6.4 nm, V_s = 0.2 V, I_t = 0.15 nA. The fcc region and hcp region are indicated on the image. (d) Close-up of the region in the black frame in (c) and the corresponding atom configuration.

Surface reconstruction gives rise to a surface structure that differs from the bulk structure in a crystalline material. The reconstruction of the Au(111) surface was well-studied by diffraction techniques in the early stage including LEED [169] and reflection high-energy electron diffraction (RHEED) [170]. A nearly 5% contraction along $[1\bar{1}0]$ has been found out. Wöll *et al*. [168] were the first to show the STM images of the surface reconstruction with atomic resolution in the real space. Takeuchi *et al*. [171] then applied first-principles calculations to

study the reconstruction. They found that the resulting fcc and hcp sites have degenerate energy due to the surface contraction. They also proved that the surface band structure is rather insensitive to two different sites after the surface reconstruction.

Figure 3-12 displays the STM images of the herringbone structure due to surface reconstruction on a large scale and at atomic resolution. Specifically, 23 Au atoms of the surface layer are compressed into a region that originally accommodates 22 atoms along the $[1\bar{1}0]$ direction, as shown in the close-up and corresponding model in Figure 3-12(d). The reconstruction gives rise to two atomic configurations at the surface: the fcc region and the hcp region, which are separated by two "soliton" walls. The fcc regions keep the stacking sequence along [111] direction as ABCABC (from the surface to the bulk), while the hcp regions alter the surface stacking type with stacking sequence as CBCABC.

3.6.3 Clean Au(111) surface preparation

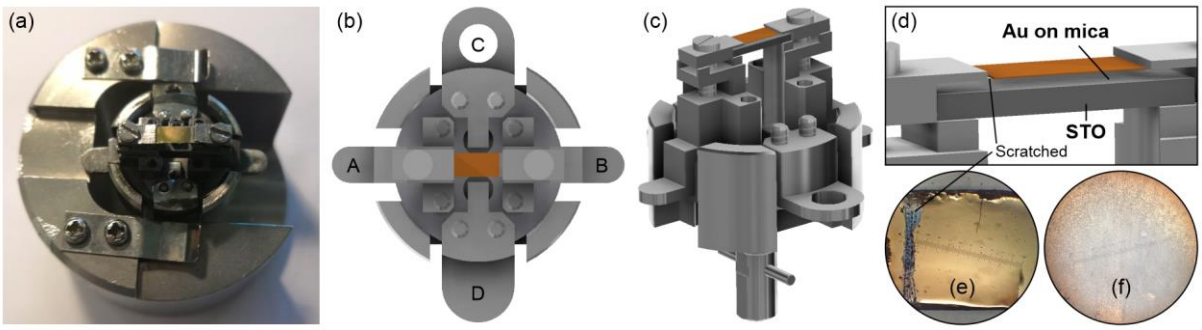

Figure 3-13 (a) Photo of the sample holder with Au substrate clipped on the top. (b) Schematic drawing of the sample from the top-view showing the four corners for fixing the position. (c) Schematic drawing from the side-view. (d) Close-up of the Au substrate with one end scratched. The STO substrate is put under the Au-mica substrate. (e) An optical microscope image of the Au surface and the scratch. (f) The Au surface after annealing at 950 ℃.

Commercial mica-supported Au(111) substrates with a gold thickness of around 300 nm were bought from Unisoku, Japan. A 2 mm × 7 mm substrate is cut to fit the sample holder, as shown in Figure 3-13(a) – (c). The four corners of the sample holder (A, B, C, and D) are designed for position fixing. The hole at corner C can be referred to when rotating the sample. The Au

substrate is always scratched at the end, which is on the right side with respect to corner C. The continuity of the Au film has to be broken as annealing is achieved by heating the STO under the Au-mica substrate, as shown in Figure 3-13(d) and (e). The other end of the Au film should contact closely with the holder's clip, through which an electrical potential, namely the sample bias, is applied to the Au substrate during imaging.

The substrate can be repeatedly used for a few experiments after cleaning by sputtering and annealing at 600 ℃ for 1.5 h. The annealing procedure is essential for surface reconstruction and the removal of embedded Argon atoms after the sputtering process, as stated in Section 3.4. Substrates should be replaced to avoid cross-contamination when investigating different metal elements. The cleanness of the substrate surface was confirmed by STM before doing the metal deposition. The substrate temperature is one of the critical parameters for sample preparation. Though both mica and Au can sustain a high temperature up to 1000 ℃, annealing at around 950 ℃ causes the Au substrate to melt in certain regions due to the uneven heating of the STO. The melted region of the Au substrate re-crystallizes during cooling to room temperature, resulting in a rough surface shown in Figure 3-13(f). Therefore, annealing was usually carried out under 900 ℃ in this study.

3.7 Sample preparation

3.7.1 Materials selection

The present work focuses on the transition metal oxide on the Au(111) substrates. Four transition metals have been studied: Nb (99.8%, Goodfellow), Ti (99.8%, ADVENT), V (99.8%, Goodfellow), and Mn (99.5%, Goodfellow). All of them are commercial products in the form of metal rods with a diameter of 2.0 mm in order to fit the pockets of the e-beam evaporator. Most transition metals have multiple oxidation states due to the valence electrons. For example, vanadium has oxidation states in its bulk oxides of +2, +3, +4 and +5, corresponding to VO,

V_2O_3, VO_2, and V_2O_5. Besides, new stoichiometries such as V_8O_{15}, V_7O_{13}, and V_6O_{11} can be generated from oxides in the form of thin films [172], which significantly enlarge the oxide family and raise new research interests regarding the structures and properties.

The four transition metal elements in this study are close to each other in the periodic table. Hence they may share some common characteristics but also have their distinctive features. Comparative studies of the similarities and the differences give us a better understanding of material properties and potential applications. In addition, considering the conditions that can be achieved in the practical experiments, the four metals with moderate vapour pressures can be evaporated by an e-beam evaporator without much difficulty in contrast to W or Ta that has a very low vapour pressure. Oxidizing is achieved by annealing the sample in an oxygen atmosphere in the range of 10^{-7} ~ 10^{-5} Pa, while reduction is realized by annealing in UHV. Therefore, another requirement for selecting the transition metals is that the studied metal can be oxidized and meanwhile, the substrate is still stable under such experimental conditions.

3.7.2 General sample preparation procedures

The deposition amount of the studied metal is critical to the oxide structure and thus needs to be carefully calibrated at the beginning. The e-beam ion collector can monitor the evaporation amount, but the actual deposition on the substrate should be confirmed by the STM images. When using a new metal rod that lacks information about its behavior in the e-beam evaporator, a few test samples need to be made for calibration.

The oxidation process can be either post-oxidation which means oxidizing the metal after the deposition, or reactive deposition which means depositing metal in an oxygen environment. Annealing is achieved by indirect heating the STO placed under the Au-mica, as shown in Figure 3-13(d). An external power controller is employed to control the temperature and the heating speed by adjusting the applied current and voltage. A typical preparation route can be

seen in Figure 3-14, in which the preparation of the Nb_2O_3 honeycomb structure adopted the post-oxidation method. The preparation conditions of Nb oxide thin films will be introduced in Chapter 5; Ti or V oxide will be presented in relevant sections in the following chapters.

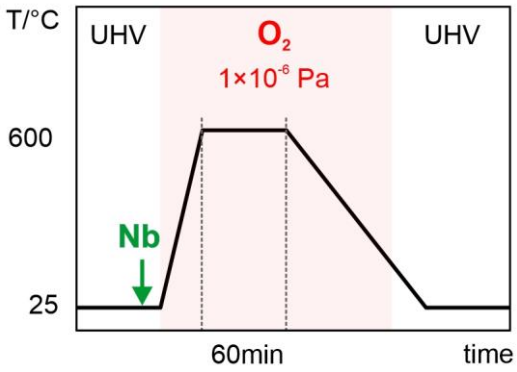

Figure 3-14 An example of the preparation route. This example shows that Nb is deposited on Au(111) at room temperature. After finishing the deposition, oxygen is introduced into the chamber with a pressure of 1×10^{-6} Pa. At the same time, the substrate is heated up to 600 ℃. Annealing at 600 ℃ lasts for 1 hour. Finally, the system is cooled down to room temperature, and the oxygen valve is closed. The chamber goes back to an UHV environment.

3.8 Image processing

3.8.1 Processing procedures

Most of the STM images in this thesis are results of image processing that can be divided into three stages. In the first stage, a software package called SmartAlign is used to do multiple-frame averaging (MFA) on the original STM images acquired from serial scanning. The averaged STM image will get a significant improvement in terms of the signal-to-noise ratio (SNR) and the resolution. In the second stage, the averaged STM image is further processed in Gwyddion and Image J, by which we can align rows, level a local region of interest, remove scars, adjust the brightness and contrast, and perform some basic operations like rotation and coloring. It is worth noting that these operations should not distort the objective information or produce artefacts in the images. The last stage is not always necessary unless a precise length measurement is required. An image calibration should be done before adding a scale bar or measuring the size of a subject. The STM images, which can reflect the Au(111) substrate with

atomic resolution, are undoubtedly perfect for calibration as we already know the atom arrangement and the theoretical periodicity. However, most images taken at room temperature are not able to resolve Au atoms but can atomically resolve oxide thin films that are epitaxially grown on the surface. An oxide thin film with a known structure, for example, the (2×2) Nb_2O_3 honeycomb structure, can act as an excellent crystallographic and size marker, which can help to calibrate the whole image size or mark a specific length in the STM image. In addition, 2D Fast Fourier Transform (FFT) high-pass image filtering is used occasionally to get a filtered image. An example can be seen in Figure 4-1(g), (h), in which the FFT filtering was performed to remove the bright herringbone background to better view the ring patterns' positions.

3.8.2 Image averaging by SmartAlign

SmartAlign is a software package developed by Lewys Jones and operated as a plug-in (HREM Research Inc) for Digital Micrograph [173,174]. It is used for performing image alignment and scan-distortion compensation on serial-scanning images with the same imaging conditions. For a single data point or a 1D spectrum, one of the most common ways to improve the data accuracy and reliability is to repeat the measurement and calculate the mean value. Similarly, for a 2D data set like digital images, data averaging is also an effective way to improve the SNR. Repeating experiments on an imaging system with shot noise can improve of the SNR by a square root of the repeating number n ($SNR \propto \sqrt{n}$), see Appendix I for detail.

However, we cannot directly perform pixel averaging on 2D images. On the one hand, acquiring a frame series usually takes some time depending on the scan speed, during which thermal drift may occur between the sample and the tip. On the other hand, external effects like the non-linearity of piezo scanners and electrical interference may give rise to scan distortion and noise on the STM images. The distortion may vary from each frame, so it makes no sense to calculate a pixel's mean value without aligning the registry of the image series at the beginning.

SmartAlign can be used to correct the low- and intermediate-frequency distortion, namely the drift and scan distortion. High-frequency noise can be partially removed in Gwyddion.

A typical workflow of multiple-frame averaging by SmartAlign is as follows. Firstly, the serial-scanning images with the same imaging conditions undergo a data resampling to increase the sampling by a factor of 2 ~ 4 to improve the digital resolution. Secondly, the rigid registration is performed on the pre-processed image series to remove the translation offset due to thermal drift between image frames. A 3 × 3 median filter or a 5 × 5 Wiener filter is implemented at the beginning to improve the reliability of the registry. The rigid registration is then executed based on the correction function which is applied to assess the translation distance between two frames in the image series. SmartAlign provides three correlation functions to be selected: the cyclical cross-correlation, the mutual-correlation function (MCF), and the phase-correlation function (PCF). Thirdly, the non-rigid registration can further improve the image series by removing the linear affine and non-linear scan distortion. The linear affine due to image shear, scale, or small-angle rotation is corrected using affine transformation. In contrast, the non-linear scan distortion is solved by iterative cycles and assessed by the convergence value. We should be cautious when performing rigid or non-rigid registration on image series with dynamic changes.

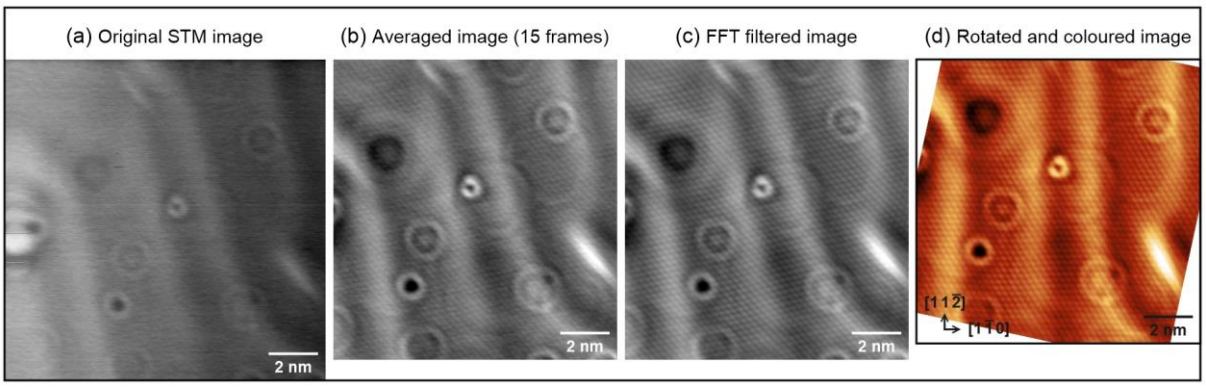

Figure 3-15 Image processing procedures. (a) An original STM image taken at room temperature (V_s = 0.2 V, I_t = 0.15 nA). (b) After doing MFA on 15 image frames with the same imaging condition by SmartAlign. (c) After using FFT filtering to better visualize the substrate Au atoms. (d) A colored image after calibration showing a set of ring patterns caused by V impurities below the Au(111) surface with atomic resolution.

To sum up, doing multiple-frame averaging on the serial-scanning images by SmartAlign is a robust method that can significantly improve the SNR and resolution of the STM images. Figure 3-15 shows an example of the Au(111) surface with a set of ring patterns created by V impurities buried below the surface. Figure 3-15(a) is an original STM image, from which the Au atoms are barely seen. After doing MFA on 15 image frames by SmartAlign, the SNR has a nearly fourfold ($\sqrt{15} \approx 3.87$) improvement so that the Au atoms are well resolved in Figure 3-15(b). The averaged STM result was further filtered [Figure 3-15(c)], processed, calibrated, changed the lookup table by other image processing applications including Gwydionn and Image J. As a result, the image in Figure 3-15(d) shows a set of ring patterns with three maximum intensities along $[01\bar{1}]$, $[\bar{1}01]$, and $[1\bar{1}0]$ directions with a high SNR and satisfactory resolution.

Chapter 4 Mapping the distribution of impurity atoms below the Au(111) surface

4.1 Introduction

Mapping the distribution of point defects such as impurities, dopants, and vacancies is key for a detailed understanding of the properties of all functional materials. This is particularly the case for nanomaterials where atomic-scale changes in point defect distributions can give rise to significant changes in their properties [76,175–177]. The distribution in the near-surface region is also critical for materials systems which are dominated by their surface properties such as catalysts and semiconductors. Compared with impurity atoms located on the surface of a material, which can act as strong scattering centers [178–182], it is difficult to map the atomic distribution of single impurity atoms or defects inside a material. Established techniques include atom probe tomography (APT) [183,184] and aberration-corrected scanning transmission electron microscopy with depth sectioning [185–188], which are capable of detecting single buried impurity atoms and enable 3D reconstruction of the atomic structure. However, these techniques require advanced sample preparation and/or are destructive and are therefore not suitable for the observation of dynamic phenomena over a range of temperatures.

Scanning tunneling microscopy is a highly surface sensitive technique that probes only the surface atomic layer of atoms, however information from buried impurities in the near-surface region of a metal can be obtained because the defects give rise to surface electronic state perturbations [189,190]. Significant STM work has also been carried out on detecting dopants in semiconductor substrates [191–196] where the observation of surface hillocks and depressions with voltage-dependent intensity is attributed to buried dopants within the top few atomic layers. STM has also been applied to the study of subsurface Kondo impurities and it was shown that the depth of an impurity can be derived from the period of the oscillation [197–

200]. Pioneering STM work of investigating the mobility of surface-embedded impurities includes Co/Cu on Ru(1000) [201]; Mn [202], Pd [203], In [204,205], Co [190,206–208] on Cu(100); and Pd on Cu(111) [209]. Adatom-mediated diffusion [201] and vacancy-mediated diffusion [190,202–209] are two general mechanisms that have been used to interpret the motion of the impurities. The latter has also been studied through theoretical methods based on molecular dynamics [210], kinetic Monte Carlo (kMC) [211–213], and density functional theory [214]. These studies concerned embedded impurities that were not buried below the surface but rather incorporated in the substrate surface, where tip-induced diffusion can be influential [207,208].

In this chapter, we show STM images of ring patterns observed on Au(111). The rings are created by substitutional impurities of Ti, Nb, V, and Mn within the top 10 atomic layers (~ 2.4 nm depth). We can determine the 3D location of each impurity atom using the center and radii of the rings. In addition, the ring patterns are not perfectly circular as they possess three brighter corners along $[\bar{1}10]$, $[0\bar{1}1]$, $[10\bar{1}]$. DFT calculations show that the anisotropy of the curvature of an isoenergy surface in ***k***-space of Au is responsible for the enhanced directional density of states (DDOS) along the <110> directions.

4.2 Experimental methods and theoretical calculations

Pure metals including Nb (99.8%, Goodfellow), Ti (99.8%, ADVENT), V (99.8%, Goodfellow), and Mn (99.5%, Goodfellow) were deposited on Au(111) substrates (Unisoku Co., Ltd) by e-beam evaporation (Oxford Applied Research EGN4). The Au substrates were replaced for each metal deposition experiment to avoid cross-contamination. Our ultra-high vacuum STM (JSTM4500XT) was manufactured by JEOL and operates at a base pressure of 10^{-8} Pa. STM imaging was achieved by applying a sample bias in constant current tunneling mode using etched tungsten tips at room temperature. The STM images in this paper are results obtained

after multi-frame averaging of a few to several tens of original STM images using SmartAlign, which significantly improves the image signal-to-noise ratio [173,215].

Theoretical works were done by Xinze Yang, and the calculation methods can be seen in Appendix II. DFT-simulated STM images were obtained by placing single impurity atoms (Nb, Ti, V, and Mn) in the 2nd, 3rd, 4th, and 5th layers (labeled as L_2, L_3, L_4, and L_5) below the surface (labeled as L_1), integrating the local density-of-states from the Fermi energy ϵ_F to $\epsilon_F + eV_s$.

4.3 Impurity atoms buried below the Au(111) surface

Figure 4-1 shows STM images of the Au(111) surface before and after impurity metal deposition. Figure 4-1(a) is an STM image of a pristine Au(111)-$\left(22 \times \sqrt{3}\right)$ reconstructed surface with the herringbone structure [168]. After evaporating very low concentrations of impurity metals (Ti, Nb, V, Mn) and annealing, a set of ring patterns with radii ranging from 1.5 Å to 20 Å can be observed. These rings are not perfectly circular but are triangular with three rounded corners. The rings are due to buried impurities located in substitutional sites, and deeper impurities give rise to larger rings but with reduced contrast [189,190]. DFT calculations indicate that a buried impurity of Ti, Nb, V, or Mn in Au is in a lower thermodynamic state by 0.5 to 1 eV compared with an impurity in the top Au(111) atomic layer, explaining why we only observe buried impurities. Figure 4-1(b) is an STM image obtained after depositing a trace amount of Ti at room temperature. Aggregation of several rings can be seen at the elbows of the herringbone structure. A large ring pattern with a radius of about 1 nm at the bottom left of the image is indicated by a yellow arrow indicating a deeper substitutional Ti impurity. Figure 4-1(c) shows the surface ring patterns generated by depositing more Ti and annealing at 500°C in UHV. The image is of sufficiently high resolution to be able to identify the surface Au atoms, which helps to precisely determine the orientation of the rings and their radii. A particular tip condition appears to be required to resolve this type of structure, and we did not observe the

ring patterns during routine imaging. Presumably, on occasion our W tip was unintentionally functionalised, which resulted in enhanced resolution in a similar way to the CO front atom identification (COFI) method used in non-contact atomic force microscopy [216–219].

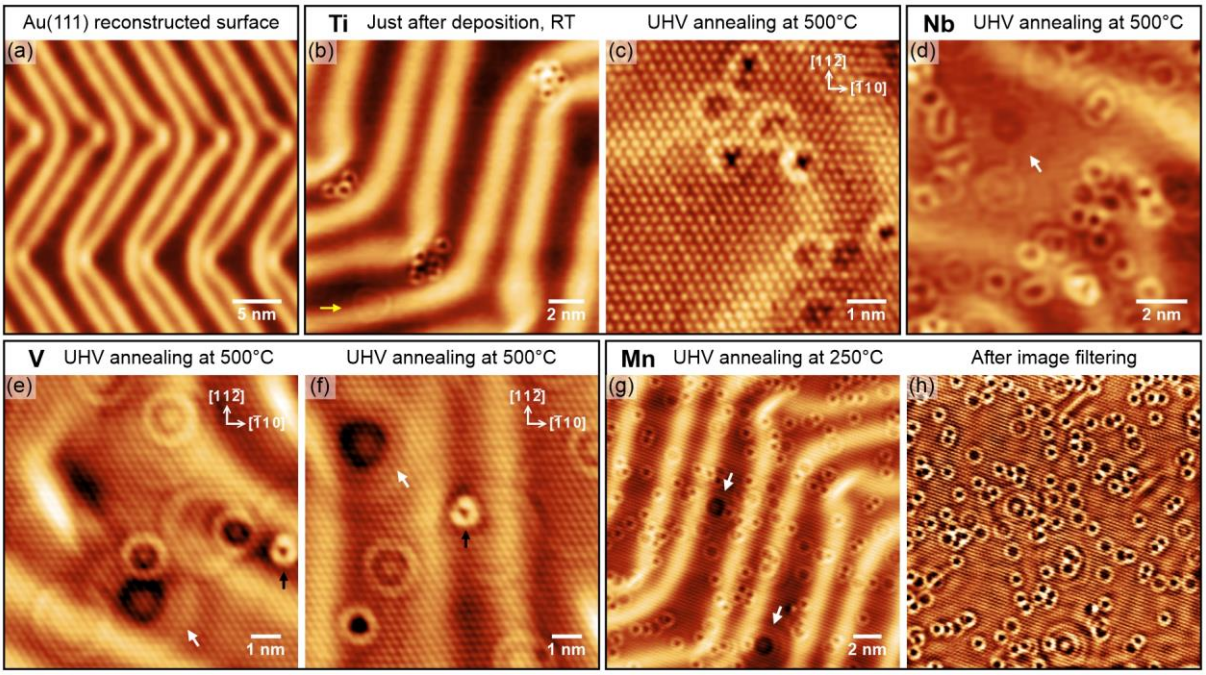

Figure 4-1 STM images of the Au(111) surface (a) in pristine condition (V_s = 2 V, I_t = 0.16 nA). (b) After depositing Ti at RT (V_s = 0.8 V, I_t = 0.6 nA) showing small rings clustered at the elbow sites and a larger ring indicated with a yellow arrow. (c) The surface after annealing at 500 °C in UHV showing the Au atoms and Ti-induced rings with atomic resolution (V_s = 0.4 V, I_t = 0.8 nA). (d) After depositing Nb and annealing (V_s = 0.8 V, I_t = 0.5 nA). (e, f) After depositing V and annealing at 500 °C (V_s = 0.2 V, I_t = 0.15 nA). (g) After depositing Mn and annealing at 250 °C (V_s = 0.6 V, I_t = 0.6 nA), and the same image with high-pass image filtering (h) to remove the herringbones. The white arrows indicate multiple ring structures, and the black arrows in (e, f) point at rings located within the hcp-stacked termination of the reconstructed Au(111) surface.

Ring patterns can also be obtained from samples with Nb [Figure 4-1(d)], V [Figure 4-1(e), (f)], or Mn [Figure 4-1(g), (h)] impurities, where concentric rings patterns are indicated with white arrows and rings located between the soliton walls of the herringbone structure are indicated with black arrows. The concentric rings are in appearance similar to standing wave patterns caused by Friedel oscillations, which are usually observed at cryogenic temperatures [178–181,220–222]. We therefore conclude that concentric rings are due to two or more impurities located above one another at different depths. The dominant herringbone structure can obscure

the observation of the rings [Figure 4-1(g)]. This can be remedied by using a high-pass image filter to remove the herringbone background, as shown in Figure 4-1(h), which enables straightforward measurement of the ring sites.

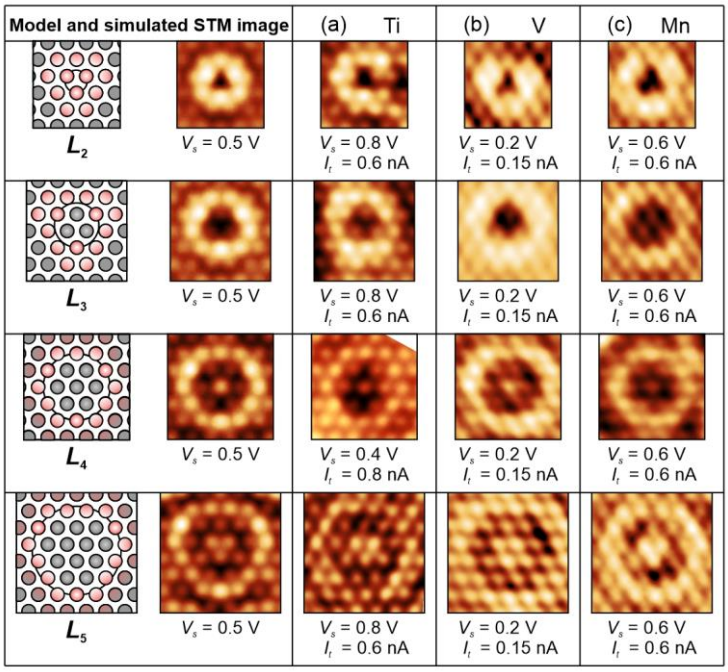

Figure 4-2 The left columns show models and DFT-simulated STM images of the ring structures for a V impurity buried to successively greater depths from layers L_2 to L_5. Columns (a) – (c) are of corresponding experimental STM images of single Ti, V, or Mn impurities with increasing ring radii.

Figure 4-2 compares DFT-simulated STM images of the ring patterns generated by a V substitution at L_2, L_3, L_4, and L_5 with experimental results from buried Ti, V, and Mn impurities. In the simulation process, we found that there was a negligible difference of the visual appearance of the ring structures for the four elements we studied (Ti, Nb, V, and Mn) for sample biases between V_s = 0.2 – 0.8 V. The simulated images of vanadium at V_s = 0.5 V are used to represent the simulation results for all the impurity elements in the second column. The good qualitative agreement between simulation and experiment confirms our observation that the ring sizes and shapes do not differ substantially between the impurity elements, and that the size expands with increasing buried depth.

The first column in Figure 4-2 shows the schematic models for the ring patterns. The inside circles in the models always pass through three atoms at the corners, corresponding to the three brightest atoms in the simulated and experimental STM images. DFT calculations show that this phenomenon can be correlated to the curvature anisotropy of the Au isoenergy surface in ***k***-space. The <110> directions possess a higher directional density of states due to a small Gaussian curvature of the isoenergy surface, which gives rise to triangular ring patterns with three bright rounded corners. Detailed analysis can be seen in Appendix II.

The models also reflect that there are three types of symmetry center. Due to the nature of atomic stacking of an fcc crystal along the <111> directions, the symmetry centers of the rings created by buried impurity atoms in layers L_2, L_3, and L_4 are at B, C, and A sites, respectively, as shown in Figure 4-3(d). For example, this means that impurity atoms located in L_3, L_6, and L_9, are all located on C sites and hence have the center of their rings on a hollow site with respect to the L_1 surface atoms.

The discrete distribution of measured ring radii for V and Mn is shown in Figure 4-3(a). The anneal temperature of the V sample (500 °C) was higher than that of the Mn sample (250 °C), allowing us to collect a more extensive range of radius data due to deeper impurity diffusion. A plot of the average radius versus the buried depth is depicted in Figure 4-3(b). The regression line reveals that the angle between it and the y-axis is around 35°, approximately equal to the angle between the [110] and [111] directions. After replacing the regression line and the y-axis by extended [110] and [111] vectors, we can see that the theoretical radii can be obtained from the intercept lengths between two vectors when cutting layer by layer. The symmetric centers of the ring patterns alter in accordance with the stacking sequence of the Au fcc structure (ABCABC…) as marked on the 3D model in Figure 4-3(c).

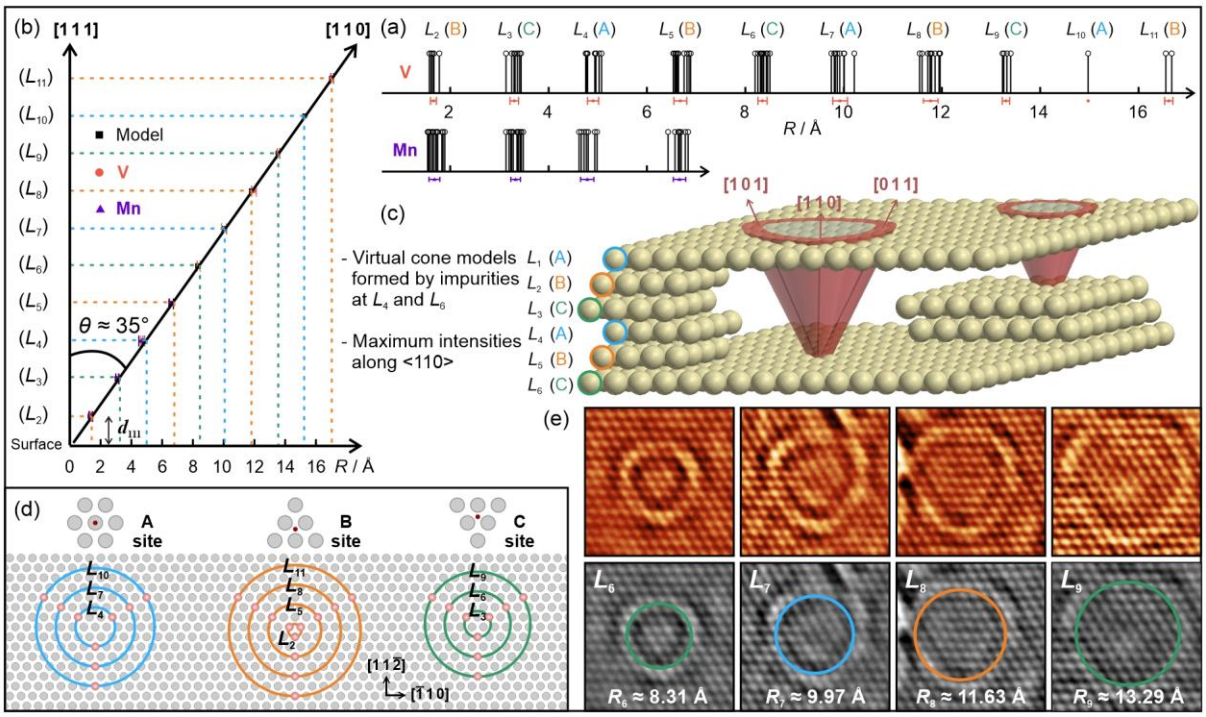

Figure 4-3 (a) Discrete radii distribution with average values and error bars shown under the axis from V (83 ring samples) and Mn (54 ring samples) impurities. (b) Plot of average ring radius versus buried depth with a regression line. The vertical axis is replaced by extended vectors along [111]. The angle of the [110] vector coincides with the regression line. (c) A 3D model of the Au(111) substrate showing the fcc stacking sequence. Two scattering cones caused by buried impurities in L_4 and L_6 are depicted in red. Au atoms are partially omitted for clarity. (d) The inside circles can be classified into three groups according to the symmetry centers referred to as A, B, and C sites. (e) STM images of ring patterns created by V-Au substitution at $L_5 - L_8$ (V_s = 0.2 V, I_t = 0.15 nA).

A buried impurity atom gives rise to a ring pattern on the surface layer, and the size of the ring depends on the distance between the buried site and the surface plane. This behavior can be represented by a virtual cone with three arrises along the [011], [101], and [110] directions. We have drawn two impurity scattering cones from layers L_4 and L_6 in Figure 4-3(c). The STM tip always scans the surface, so our observation plane is fixed, and hence the radius of each ring (R) is a discrete value determined by

$$R_n = (n-1)\, d_{111}/\sqrt{2}\,. \tag{4-1}$$

where n is the layer number (n = 2, 3, 4…) and $d_{111} \approx 2.35$ Å is the Au(111) interplanar spacing. The rings with calculated radii are classified into three groups according to their symmetry

centers, as depicted in Figure 4-3(d). A ring created by a buried impurity atom in layers L_{3m+1} possesses an A site symmetric center which is located directly above a surface atom; a ring pattern created by an impurity atom at L_{3m-1} has its symmetric center at a B site; a ring pattern created by an impurity atom at L_{3m} has its symmetric center at a C site, (m = 1, 2, 3…). Figure 4-3(e) shows STM images of the ring patterns caused by impurity atoms in layers $L_6 - L_9$ with the colored circles showing the calculated rings.

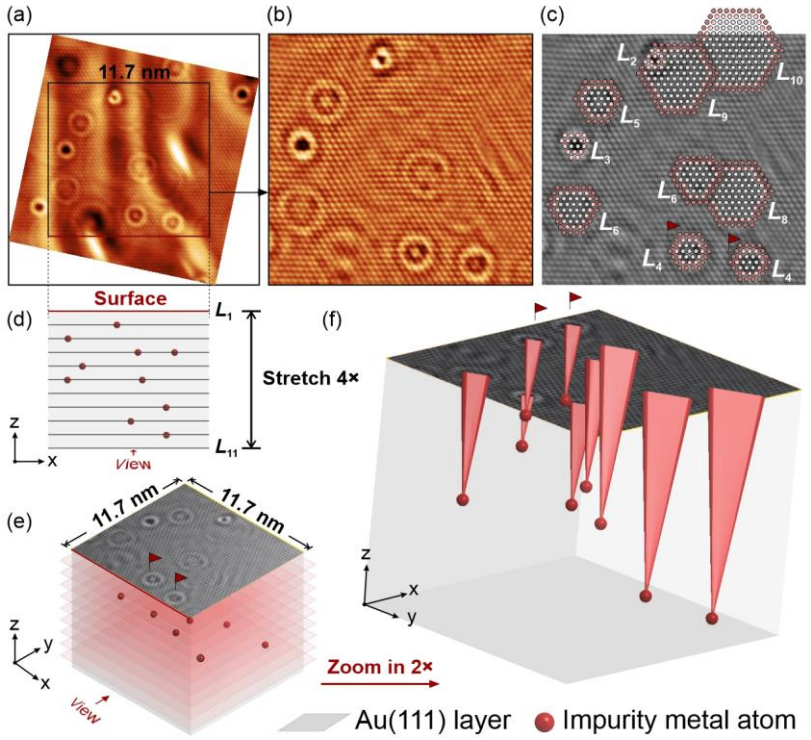

Figure 4-4 Mapping the atomic distribution of buried impurities. (a) STM image of a V impurity sample (V_s = 0.2 V, I_t = 0.15 nA). (b) Filtered image with herringbone structure removed (image size 11.7 nm × 11.7 nm.) (c) The same image as (b) in grey with ring masks. (d) Side view of the 3D model of impurity distribution showing atoms at different layers. The actual depth of 10 Au(111) layers is 2.35 nm, but the model is stretched in the depth direction by a factor of four. (e) A 3D model of the impurity distribution. (f) The 3D model with scattering cones from buried impurity atoms to surface ring patterns. Red flags in (c), (e), and (f) mark the same rings to aid positioning.

We are able to determine the exact location of a buried impurity atom according to Formula (4-1) and the symmetric center of the ring patterns. To demonstrate this capability we selected the STM image obtained from a V sample in Figure 4-4(a) to show the process of mapping the atomic distribution of buried impurities from the surface ring patterns. The herringbone

structure is removed by a high-pass image filter in Figure 4-4(b). After careful image calibration, ring masks are placed on the image in Figure 4-4(c) to assess the ring sizes. Figure 4-4(d) is a side view that shows the buried layers of substitutional V atoms with a relative depth stretching factor of four. Figure 4-4(e) and (f) are 3D models showing the distribution of V impurities in the near-surface region of the Au(111) substrate, in which the red flags are placed next to two rings for positioning. The virtual cone models in Figure 4-4(f) indicate that an impurity buried in a deeper layer results in a larger ring pattern on the surface.

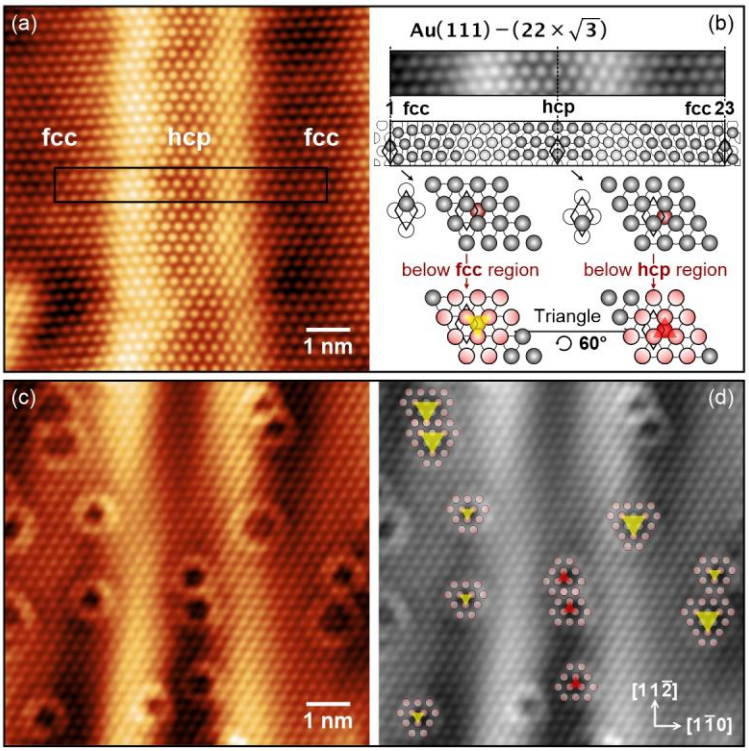

Figure 4-5 (a) STM image of a pristine Au(111)-$\left(22 \times \sqrt{3}\right)$ reconstructed surface with fcc and hcp regions (V_s = 0.7 V, I_t = 1.3 nA). (b) Upper part: close-up of the region in the black frame in (a) and its schematic model. Grey solid circles represent the surface atoms; hollow circles represent atoms of L_2. Lower part: the schematic models show the 60° ring rotation between an impurity atom below the fcc region and the hcp region. Dark red circles represent substitutional impurity atoms at L_2. (c) STM image from a Mn impurity sample showing rings within the "soliton" walls and beyond the walls (V_s = 0.6 V, I_t = 0.6 nA). (d) The same image as (c) in grey with ring masks. The triangles connect the three maximum intensities with specific directions. The triangles of rings in the fcc region are yellow, while triangles within the hcp region have a 60° rotation and are drawn in red.

The gold substrate is advantageous for studying the impurity ring patterns because the $(22 \times \sqrt{3})$ reconstruction gives rise to hcp and fcc domains separated by "soliton" walls [Figure 4-5(a), (b)] [168]. An interesting phenomenon of the ring patterns can be found in Figure 4-5(c) when comparing the rings located in the fcc region with those in the hcp region. By putting ring masks on Figure 4-5(d) and using an equilateral triangle to connect the three maximum intensities, it can be seen that the rings in the hcp region are rotated by 60° with respect to those in the fcc regions. This rotation can be explained by the stacking fault due to the surface reconstruction, as shown in the lower part of Figure 4-5(b). The same phenomena can also be seen in Figure 4-1(e) and (f) indicated by the black arrows.

4.4 Conclusion

In summary, we investigated a set of ring patterns on the Au(111) surface by STM at room temperature which are caused by buried substitutional impurity atoms. We demonstrated a method to precisely determine the impurity sites and construct a 3D map based on the ring radii and centers. DFT calculations have shown that the <110> directions possess much higher directional density of states due to small Gaussian curvature of the isoenergy surface, which gives rise to triangular ring patterns with three bright rounded corners.

Chapter 5 Nb oxides on the Au(111) substrate

5.1 Introduction

Niobium oxides are well-known for their catalytic properties, for example, Nb_2O_5 is a promising promoter for V_2O_5/TiO_2 catalysts in selective catalytic reduction [223]. A Nb atom has five valence electrons, and it is capable of oxidation states up to +5. Nb oxides clusters and thin films have been studied on various substrates including Pt [26], Cu [24,224], Cu_3Au [28], and Au [27]. It has been found that Nb_2O_3, which is hardly seen under natural conditions, can be grown in 10^{-6} Pa oxygen on the Au(111) substrates with a (2 × 2) epitaxy relationship [27]. A recent study on the Nb oxide clusters on Au(111) shows that they can exhibit a variety of structures with stoichiometries NbO_x, x >1.5. This work is in collaboration with our colleagues from Paris and has not yet been published.

Nb oxides have been studied most intensively and systematically in this DPhil project compared with Ti, V, and Mn. Nb oxides were prepared under the conditions that oxygen pressure was preferably less than 10^{-4} Pa, and annealing temperature $T < 900$ ℃. Higher oxygen pressure is not friendly to the UHV system and the e-beam evaporator, and a higher temperature is not suitable for the Au-mica substrates we used, as discussed in Section 3.6.3. A general description of experimental results under different conditions will be presented in this chapter. It starts with the ring patterns caused by Nb-Au substitutions and ends with the (2 × 2) Nb_2O_3 honeycomb monolayers, which is the most stable structure within the range of oxygen chemical potential in our experiments. This chapter aims to set up a systematic understanding of the behavior of Nb and Nb oxides on the Au(111) substrate. Different structures or characteristics will be discussed separately and compared with Ti or V oxides in the following chapters.

5.2 Nb and Nb oxides on Au(111)

5.2.1 General description of all observed structures

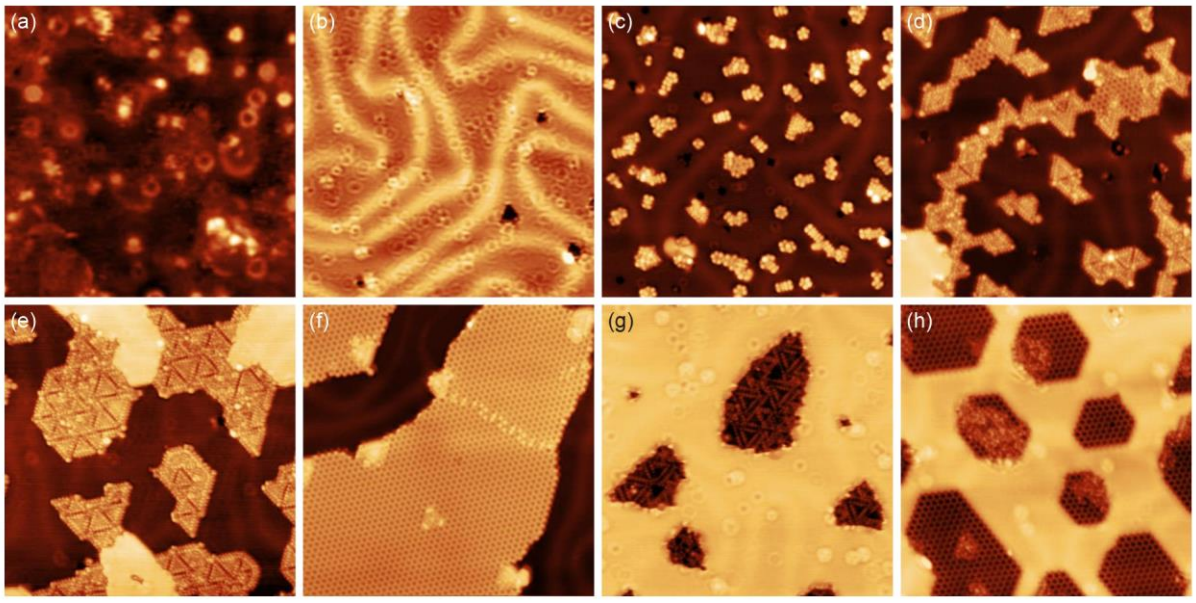

Figure 5-1 STM images of Nb and Nb oxides on the Au(111) surfaces (25 nm × 25 nm). (a) Nb-induced rings formed just after deposition at room temperature (V_s = 1.5 V, I_t = 0.2 nA). (b) Abundant Nb-induced rings distributed homogeneously on the surface after annealing at 700 ℃ in UHV (V_s = 0.7 V, I_t = 0.6 nA). (c) NbO_x clusters formed in 1 × 10^{-7} Pa O_2 at 400℃ (V_s = 1.0 V, I_t = 0.35 nA). (d) Triangles and triangle continuous film formed in 1 × 10^{-7} Pa O_2 at 500℃ (V_s = 1.0 V, I_t = 0.3 nA). (e) Pinwheel structure formed in 1 × 10^{-7} Pa O_2 at 700℃ (V_s = 0.7 V, I_t = 0.35 nA). (f) (2 × 2) Nb_2O_3 honeycomb structure formed in 1 × 10^{-6} Pa O_2 at 500℃ (V_s = 1.0 V, I_t = 0.5 nA). (g) Embedded pinwheel structure with lots of Nb-induced rings. The sample was oxidized in 5 × 10^{-8} Pa O_2 at 700℃ (V_s = 0.8 V, I_t = 0.3 nA). (h) Embedded Nb_2O_3 honeycomb islands (V_s = 1.0 V, I_t = 0.3 nA).

Nb was deposited on the Au(111) substrates by e-beam evaporator with an evaporation pressure around 3 × 10^{-6} Pa. Figure 5-1(a) shows an STM image obtained just after the deposition at room temperature, in which the evaporated Nb atoms are strewed over the Au surface and generates a few ring patterns. The DFT calculations have confirmed that these ring patterns are caused by buried Nb atoms, which can form Nb-Au substitutions below the surface. Annealing the sample at 700℃ in UHV results in a surface with abundant rings that are distributed homogeneously, and the Au(111) herringbone structures are distorted due to the Nb-Au substitutions, as shown in Figure 5-1(b). It is worth noting that annealing at a higher temperature also leads to diffusion and substitution at deeper layers so that large-sized rings can be seen in

the image. Besides, there are several dark "pits", which may be resulted from removing a collection of surface Au atoms.

NbO_x clusters start to form by introducing a small amount of oxygen into the chamber and annealing the substrate at a relatively low temperature (i.e., 400 ℃). We found that the clusters are sensitive to the pressure and annealing time. Usually, we oxidized the sample in 1×10^{-7} Pa O_2 for 1 – 2 h or used a higher oxygen pressure (1×10^{-6} Pa) with a shorter time (~ 15 min). The NbO_x clusters exhibit various structures, including rings, rectangles, bipods, and tripods, as shown in Figure 5-1(c). In contrast, when oxidizing the sample at a relatively high temperature (500 – 800 ℃) after finishing the deposition, Nb atoms no longer form clusters but grow into triangles or triangle continuous thin films [Figure 5-1(d)]. A further enhancement of the annealing temperature results in the (1 × 1) pinwheel structure, which can be regarded as an aggregation of triangles with different sizes [Figure 5-1(e)]. In other words, Nb oxides prefer to adopt a condensed growth in the form of triangle structures on the Au(111) surface at a low oxygen chemical potential. Finally, the (2 × 2) Nb_2O_3 honeycomb structure [Figure 5-1(f)] has been proved to be the most stable structure on Au(111) within the range of the experimental conditions. It was usually synthesized by annealing in 1×10^{-6} Pa O_2 at 500℃ for 30 min after depositing Nb on Au(111). Higher temperatures (up to 900℃) and $p(O_2)$ (e.g., 5×10^{-5} Pa) will not significantly change the epitaxial structure, although some features in the honeycomb monolayers may alter.

In addition, we observed that the pinwheel and honeycomb monolayers could grow on the second Au(111) layers, forming embedded structures that are confined to the surface. Figure 5-1(g) and (h) display embedded pinwheel and HC islands, which possess essentially the same structures as the free counterparts on the surface. It is worth noting that the embedded monolayers are accompanied by many ring patterns in the STM images, which indicates that the Nb-Au substitutions are critical to the embedded structures.

5.2.2 Structure transitions to honeycomb monolayers

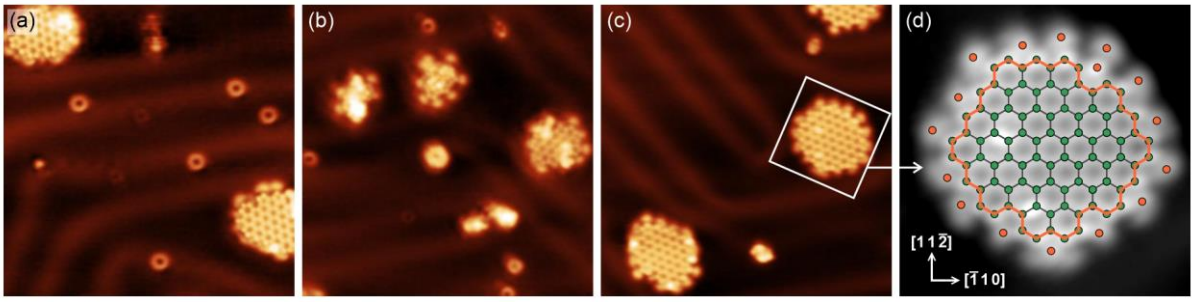

Figure 5-2 STM images of Nb-induced rings and small Nb_2O_3 islands on the Au(111) substrates (4 nm × 18 nm). (a) Two HCs with a few rings (V_s = 1.0 V, I_t = 0.3 nA); (b) after oxidizing and annealing for 30 min, the number of rings was significantly reduced (V_s = 1.0 V, I_t = 0.8 nA); (c) repeated the step, rings were barely seen (V_s = 1.0 V, I_t = 0.5 nA). (d) Close-up of the Nb_2O_3 island in the white box in (c). The edge of the honeycomb island denoted in the orange line is completely reconstructed. Nb atoms in the HC lattice are represented by green circles. Nb atoms involved in the edge reconstruction are marked by orange circles around the island.

Figure 5-2 (a) – (c) are STM images showing the transformation from Nb-induced rings to the Nb_2O_3 honeycomb structure by successive oxidizing in 10^{-7} O_2 at 350 °C. The Nb-induced rings were turned into the HC rather than forming clusters or triangles in this process, which suggests that the growth kinetics could play a non-negligible role in the structures of clusters and triangles. Besides, the resulting small HC islands possess unique edge structures, a close-up can be seen in Figure 5-2(d). The edge is completely reconstructed as a few protrusions can be found in the dent sites of the zigzag or armchair units. Notably, they look faint compared with the Nb atoms in the HC lattice. One of the possible explanations is that these faint protrusions are Nb atoms that substituted the surface Au atoms and connected to the HC monolayer, so they may have a lower location than the lattice Nb atoms (see Chapter 7).

The transition from NbO_x clusters to Nb_2O_3 HC monolayers is displayed in Figure 5-3. Similarly, this process also excluded the formation of triangle continuous thin films although there were some individual single triangles. Small clusters with various structures gradually grew together and arranged in ordered monolayers with a (2 × 2) epitaxial relationship with Au(111). Therefore, it can be seen as a ripening process driven by thermodynamics.

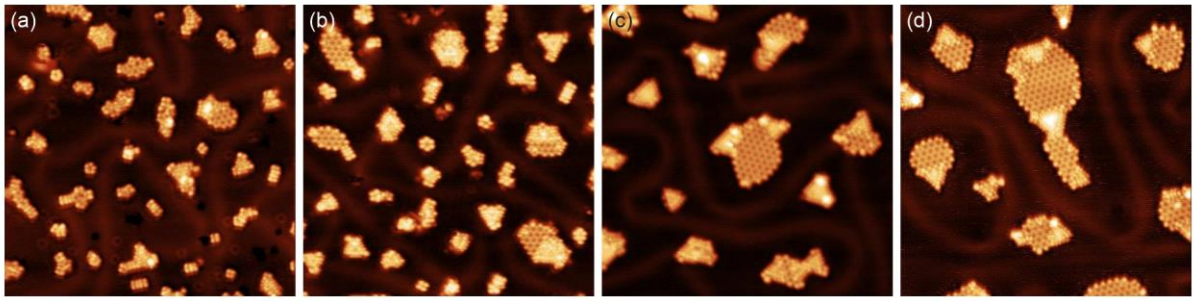

Figure 5-3 (a) STM image of NbO_x clusters prepared in 1×10^{-7} O_2 at 400 ℃ for one hour on Au(111) (V_s = 0.85 V, I_t = 1.0 nA). (b) – (d) STM images showing the transition from NbO_x clusters to honeycomb monolayers by successive oxidizing in 10^{-7} O_2 at (b) 500 ℃ for one hour (V_s = 0.8 V, I_t = 1.0 nA); (c) plus 600 ℃ for one hour (V_s = 1.0 V, I_t = 0.35 nA); (d) plus 700 ℃ for one hour (V_s = 0.8 V, I_t = 0.5 nA). Image size: 30 nm × 30 nm.

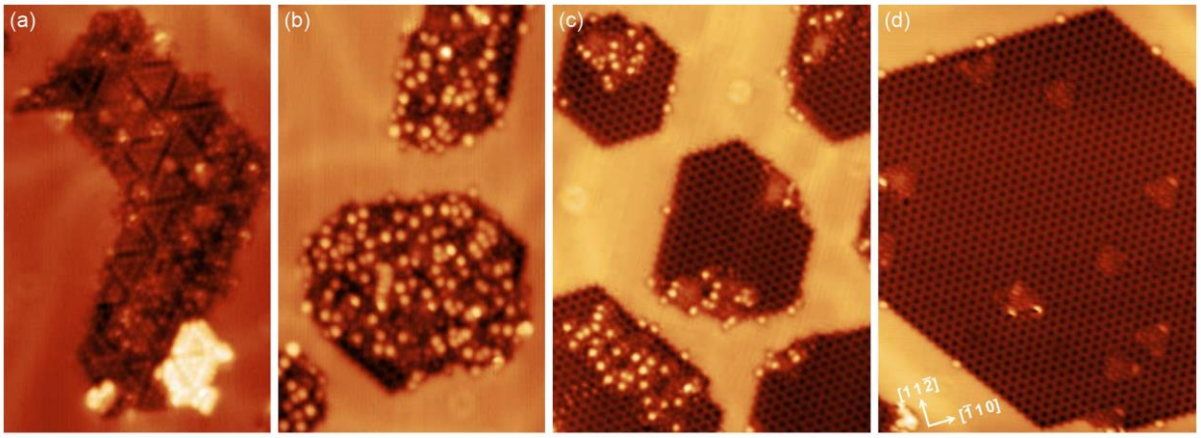

Figure 5-4 (a) STM image of an embedded pinwheel island prepared in 5×10^{-8} Pa O_2 at 700℃ for one hour. The bright region attached at the edge of the island is Nb oxide triangles grown on the surface layer (12.5 nm × 20 nm, V_s = 1.3 V, I_t = 0.5 nA). (b) – (d) STM images showing the transition from the pinwheel structure to the HC structure by successive oxidizing in 1×10^{-7} O_2 at (b) 500 ℃ for one hour (12.5 nm × 20 nm, V_s = 1.0 V, I_t = 0.2 nA); (c) plus 600 ℃ for one hour (17.5 nm × 23.5 nm, V_s = 0.8 V, I_t = 0.5 nA); (d) plus 700 ℃ for one hour (17.5 nm × 23.5 nm, V_s = 0.8 V, I_t = 0.5 nA).

The structure transition process shown in Figure 5-4 started from an embedded pinwheel structure and ended with an embedded HC structure. The pinwheel structure is supposed to have a (1 × 1) relationship with Au(111) and therefore, an area can accommodate more Nb atoms in the form of the pinwheel structure compared with the (2 × 2) honeycomb structure. In other words, the transition from the (1 × 1) pinwheel to the (2 × 2) honeycomb requires rearrangement of the excessive Nb atoms. That is why we can see lots of bright protrusions on the top of the embedded islands in Figure 5-4(b), and still some sharp spots in Figure 5-4(c).

These bright protrusions can be regarded as adatoms at the second or third layer above the embedded monolayer. It is difficult to judge their oxidation states or bonding characteristics, and the analysis of growth kinetics is beyond the scope of the present work. The transition between Figure 5-4(c) and (d) reflects that the number of the adatoms was further reduced, and the embedded HC islands were turned into a larger HC monolayer due to ripening.

5.3 Nb-induced ring patterns on the surface

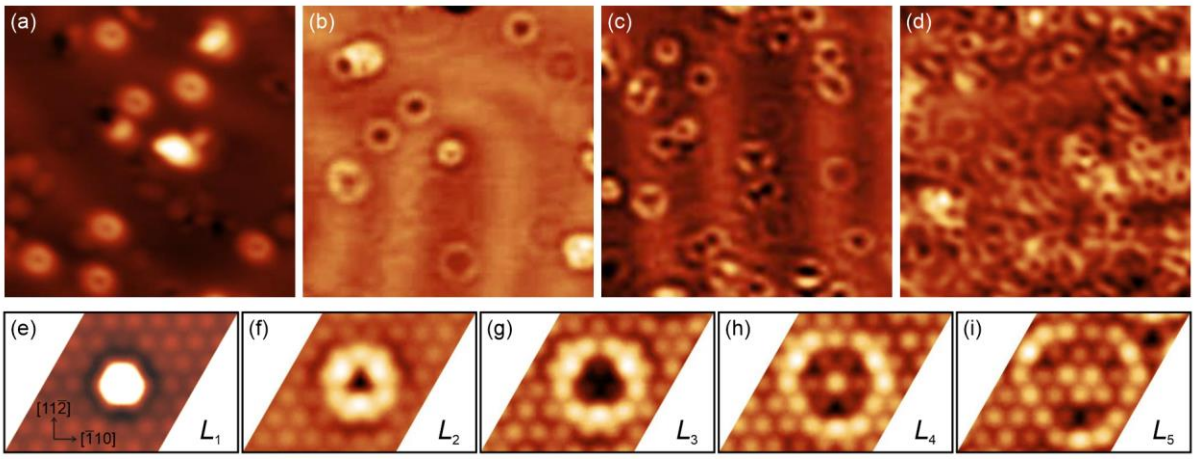

Figure 5-5 (a) STM image of Nb-induced rings formed by annealing at 400 ℃ in UHV (V_s = 1.7 V, I_t = 0.5 nA). (b) – (d) STM images of Nb-induced rings with deposition amount gradually increased. Samples were annealed at 700 ℃ in UHV. (b) V_s = 0.8 V, I_t = 0.3 nA; (c) V_s = 1.0 V, I_t = 0.4 nA; (d) V_s = 1.0 V, I_t = 0.5 nA; image size: 10 nm × 10 nm. (e) – (i) DFT simulated STM images of surface pattern induced by a Nb atom substituting an Au atom at L_1 (surface), L_2, L_3, L_4, and L_5 layers (V_s = 0.5 V).

In the 2D transition metal oxides studies, few papers have reported the interaction between the pure transition metal and the substrate metal because researchers generally pay more attention to the resulting oxide structures and manage to prevent the studied metal from diffusing into deep regions in the substrate. The investigation of Nb oxides on Au(111) in the present work started with the pure Nb metal deposited on Au(111). From Figure 5-1(a) we can see that the Nb-induced ring patterns can be created just after deposition at room temperature. The gaseous Nb atoms generated by the e-beam evaporator possess relatively high kinetic energy, which allows them to impinge on the Au(111) surface. They can substitute Au atoms at the top layers

or be captured by vacancies in the deep layers. The study of Ti-induced rings shows that substitutions can occur at the seventh layer (L_7) after metal deposition at room temperature.

Figure 5-5(a) shows the Au surface with Nb-induced rings after annealing at 400 ℃ in UHV. Compared with the surface condition just after the deposition [Figure 5-1(a)], moderate annealing can stabilize the evaporated Nb atoms on the substrate, so the ring patterns in Figure 5-5(a) have a higher SNR and clearer perimeters. According to the ring size, these rings are results of the Nb-Au substitutions at L_2 as the ring radius is about 1.7 nm (see Section 4.3). The deposition amount was gradually increased in Figure 5-5(b) – (d), and the samples were annealed at 700 ℃ in UHV. We can resolve individual rings with a variety of sizes in Figure 5-5(b). The size of the Nb-induced rings expands with increasing the substitution depth. In other words, a Nb-Au substitution at a deeper layer gives rise to a larger ring pattern on the Au(111) surface. A detailed discussion and the relationship between the ring radius and the substitution layer has been presented in Chapter 4. The DFT simulated STM images of the surface Nb and buried Nb atoms are displayed in Figure 5-5(e) – (i), which confirms that the ring patterns are caused by Nb-Au substitutions in the bulk.

Another significant feature that can be observed from the experimental and simulated STM images is that we can always find three intensity maxima of a ring pattern along $[\bar{1}10]$, $[0\bar{1}1]$, and $[10\bar{1}]$ on the Au(111) surface. This can be explained by the small curvature along <110> directions of the isoenergy surface of the Au fcc crystal in the ***k***-space. We have proved that the directional density of states is reversely proportional to the curvature of the isoenergy surface, so the in-plane directions $[\bar{1}10]$, $[0\bar{1}1]$, and $[10\bar{1}]$ possess a higher density of states due to the impurity scattering. The detailed discussion can be seen in Section 4.4.

In Figure 5-5(c), two close rings can interfere with each other, giving rise to intensity maxima that are not along the $[\bar{1}10]$, $[0\bar{1}1]$, and $[10\bar{1}]$ directions. When the deposition amount was

further increased, abundant rings were generated and superimposed, making the individual ring patterns hard to be discriminated in the STM images [Figure 5-5(d)]. However, such surfaces play a critical role in forming embedded structures. We have found that an ensemble of Nb-induced rings can serve as a precursor structure for the growth of embedded pinwheel (see Section 9.2.4) or embedded honeycomb monolayers (see Section 5.6.2) depending on the oxygen partial pressure during sample preparation.

5.4 NbO_x clusters

White *et al.* reported the first studies of Nb oxide clusters on Cu(111) substrates and Cu_2O [24,224]. They used two-photon photoemission spectroscopy to characterize the niobium oxides regarding the metal oxidation states and cluster sizes. It is shown that the stoichiometries of the clusters are Nb_3O_7 and Nb_4O_{10}, or Nb_3O_5 and Nb_4O_7 for the reduced counterparts. As no direct imaging was done in the real space, they proposed structural models of the Nb_4O_7 and Nb_4O_{10} clusters with 3D Nb atom arrangements and calculated the corresponding formation energy. In our studies, we investigated Nb oxide clusters on Au(111) substrates using STM to characterize various structures in the real space. We found that the Au-supported Nb oxide clusters possess a variety of sizes and configurations. Our collaborators from Paris have done the DFT calculations and simulations that can help elucidate the structures and explain the formation mechanism. Part of the experimental work presented in this section is integrated into an unpublished paper which is currently with a former DPhil student from our group. As a co-author, the DFT results and relevant discussion will be mentioned but not fully displayed here.

This section focuses on the structural diversity of NbO_x clusters. Considering the variety of the cluster morphologies, we classify them into rectangles (Figure 5-6), rings (Figure 5-7), ring-ring bipods (composed of two ring clusters with the same Nb number, Figure 5-8), ring-rectangle bipods (Figure 5-9), and large-sized tripods (Figure 5-10). Many unique patterns are

excluded from the discussion, and some STM results presented in the upcoming paper are organized in a different order. All STM images present in this section were obtained using positive sample bias V_s = 0.5 ~1.5 V with tunneling current I_t = 0.1 ~ 1.2 nA at room temperature.

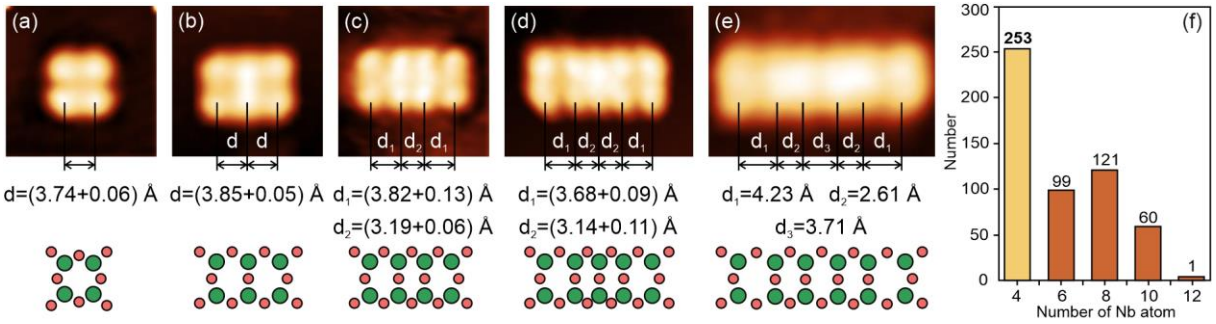

Figure 5-6 (a) – (e) STM images of rectangular clusters and the corresponding structural models for Q4, Q6, Q8, Q10, and Q12. The green and red circles represent the Nb and O atoms, respectively. The distances between columns of the Nb pair in a rectangular cluster are denoted below the STM images. STM image height: 1.85 nm. (f) Statistics of the occurrence of rectangular clusters. Q4 has the largest number.

Figure 5-6(a) – (e) are STM images of the clusters with rectangular structures. The cluster that consists of four protrusions can be seen as a building block for other rectangular clusters with larger sizes. They are named after Q with an even number (4, 6, 8, 10, 12) according to the number of Nb atoms in a rectangular cluster. The bar chart in Figure 5-6(f) shows that Q4 occurred most frequently in our experimental observations, suggesting high structural stability. The distances between the columns of the Nb pair are denoted below the STM images and provide a reference for positioning Nb atoms on the Au(111) surface. Compared with Nb oxide triangles, pinwheel, and honeycomb structures, the clusters' configurations and stoichiometries are much more difficult to be determined due to their diversity and complexity. In theoretical calculations, a few models of Q6 have been proposed and examined in terms of the formation energy. It is shown that, unlike the 3D models supposed by White *et al.*, the Au-supported NbO_x rectangular cluster favours a flat structure with threefold coordinated Nb at surface hollow sites and niobyl groups at the edges, as depicted in the schematic models in Figure 5-6. It is also indicated that the flat morphology and niobyl groups are general characteristics of most clusters.

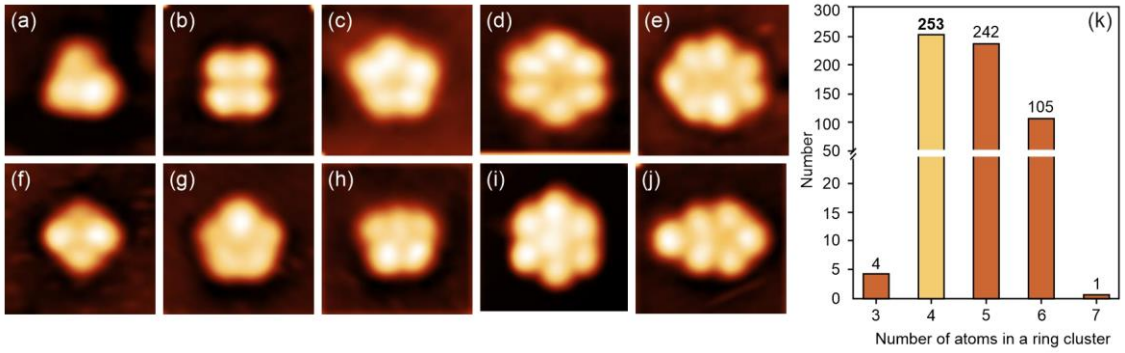

Figure 5-7 STM images of the ring clusters: (a) T3; (b) Q4, the same as Figure 5-6(a); (c) P5; (d) H6; (7) Hp7; (f) variance of Q4; (g) variance of P5; (h) variance of P5; (i) one atom embedded in the central hollow of H6; (j) variance of H6. Image size: 1.85 nm × 1.85 nm. (k) Statistics of the occurrence of ring clusters. Q4 is repeatedly shown for reference.

Figure 5-7(a) – (j) shows the clusters arranged in a ring structure, the Q4 cluster is repeatedly presented as a component of the ring system and for reference in the bar chart in Figure 5-7(k). The number of Nb atoms of observed rings ranges from 3 to 7, which are denoted as T3, Q4, P5, H6, and Hp7. Q4 and P5 predominate in the ring clusters, while T3 and Hp7 are rarely seen. Clusters with an identical Nb atom number may vary in the morphology or the contrast in STM images. Figure 5-7(f) displays a variance of the Q4 cluster, as it remains the square shape but two of the protrusions are much brighter. Besides, we also found some four-membered clusters with a parallelogram shape rather than a near-perfect square. Figure 5-7(g) and (h) present two variances of P5, and Figure 5-7(i) shows a cluster with a central protrusion embedded in the H6. The cluster in Figure 5-7(j) possesses six protrusions, which can be assigned to a variance of H6, a P5 with an adatom, or two joint T3 clusters, depending on the formation process which we are unable to figure out. The DFT calculation proposed a series of atom configurations for Q4, P5, and H6 with stoichiometries Nb_nO_m (n = 2, 4, 6; $m = 2n - 2$, $2n$, $2n + 2$). $m = 2n - 2$ corresponds to a low oxygen content, which results in clusters with twofold coordinated Nb atoms or embedded Nb atoms that substitute the surface Au atoms. $m = 2n + 2$ means a high oxygen content but gives rise to clusters with 3D structures. At moderate oxygen content, namely with a NbO_2 simplified stoichiometry (Nb_4O_8, Nb_5O_{10}, or Nb_6O_{12}), Nb atoms can remain a flat arrangement as well as the threefold coordination. Meantime, it has been proved

that the formation energy of the ring cluster with a NbO_2 simplified stoichiometry is less than that in the former two cases. In addition, the bar chart of the occurrence of ring clusters in Figure 5-7 reveals that the P5 cluster, which has a close occurrence number to Q4, is likely to possess a relatively high structural stability.

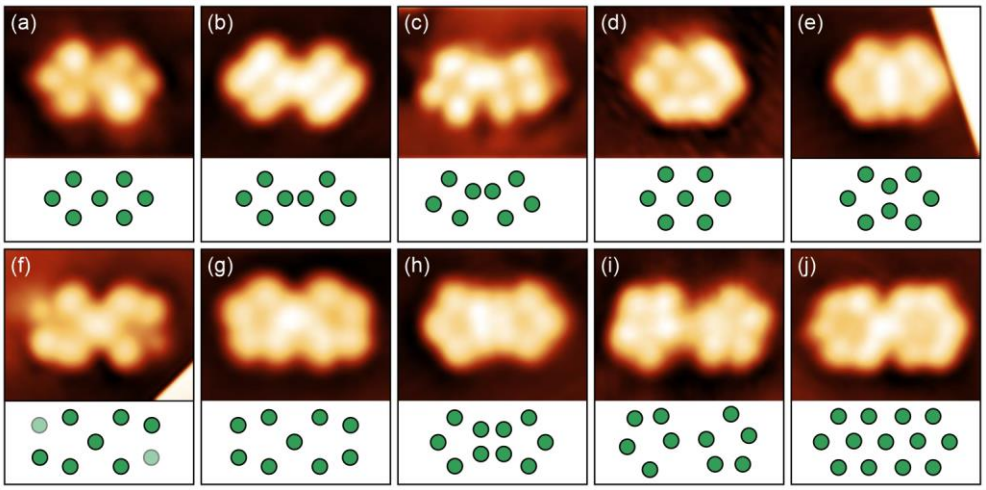

Figure 5-8 STM images of ring-ring bipods and corresponding Nb atom arrangements (2.3 nm × 1.85 nm). (a) Q4-Q4 (n = 7), sharing one atom. (b) Q4-Q4 (n = 8), no shared atom. (c) Q4-Q4 (n = 8) with a tilting angle. (d) compressed Q4-Q4 (n = 7), sharing one atom. (e) P5-P5 (n = 8), sharing two atoms. (f) P5-P5 (n = 9), sharing one atom. Two atoms at the ends are faint. (g) P5-P5 (n = 9), sharing one atom. Two atoms at the ends are brighter than that in (f). (h) P5-P5 (n = 10), no shared atom but compressed. (i) P5-P5 (n = 10), no shared atom. (j) H6-H6, an atom is embedded in the central hollow of the H6 (n = 13), sharing one atom.

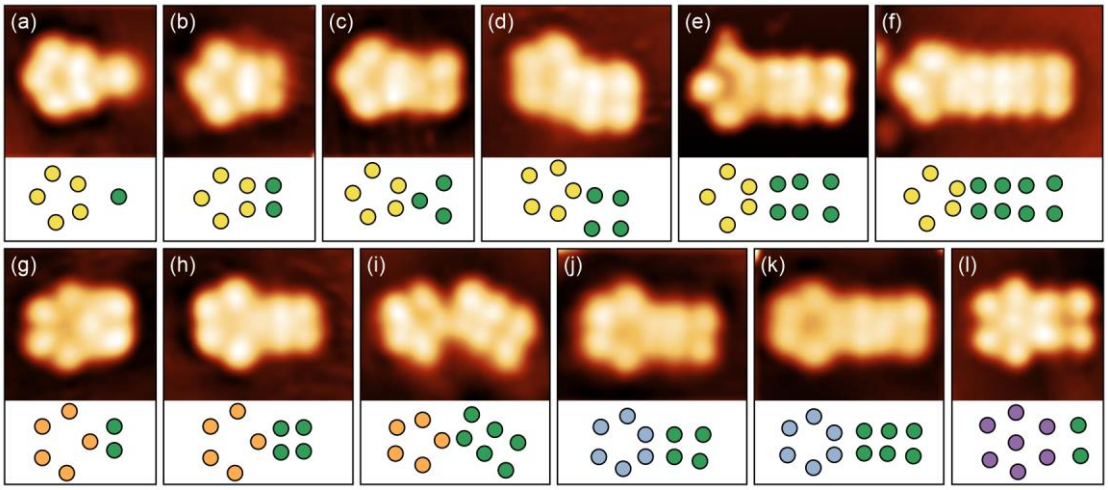

Figure 5-9 STM images of ring-rectangle bipods and corresponding Nb atom arrangements. The images are sorted according to the number of Nb atoms in the ring first (similar arrangements are marked by the same color), and green circles are gradually added to the left part. STM image size: (a) – (c), (g), (l) 1.85 nm × 1.85 nm; (d), (e), (h) – (k) 2.3 nm × 1.85 nm; (f) 2.8 nm × 1.85 nm.

The structural complexity of Nb oxide clusters is also revealed from bipods with a variety of atom configurations, which can be seen as joint clusters of ring-ring or ring-rectangle. For example, two Q4 clusters can form a bipod by sharing one atom [Figure 5-8(a), (d)], or without sharing an atom [Figure 5-8(b), (c)]. Q6 or Q8 can also be seen as two Q4 clusters sharing two atoms or arranging in parallel with no atom shared. Similar scenarios can be found for two P5 clusters: they can share two atoms [Figure 5-8(e)], share one atom[Figure 5-8(f), (g)], or share no atom but arrange differently [Figure 5-8(h), (i)]. Figure 5-8(j) shows two H6 clusters, each of which accommodates an atom in the central hollow site, joining together by sharing one atom.

Figure 5-9 displays a series of STM images of ring-rectangle bipods, which are sorted according to the ring configuration on the left side and the rectangle size on the right side. Noting that we judge them merely from the protrusions in STM images, namely the number of Nb atoms and the arrangement, rather than the actual formation process. We did not give them specific names. Although the DFT calculations suggest that a flat structure with niobyl groups at the edges is favourable, further experimental investigations and theoretical works are required to determine the exact stoichiometry and understand the formation process.

We observed a large number of clusters with triangular shapes, in which the three tripods $Nb_{12}O_{21}$ [Figure 5-10(a)], $Nb_{16}O_{27}$ [Figure 5-11(b)], and $Nb_{15}O_{27}$ [Figure 5-12(b)] occurred more frequently than others and can be seen as based structures for several derivatives. These three tripods are of threefold symmetry, which indicates a strong effect from the Au(111) substrate. The atom configuration in $Nb_{12}O_{21}$ or $Nb_{16}O_{27}$ comprises three four-membered rings (Q4), while in $Nb_{15}O_{27}$, three P5 clusters constitute the tripod. In contrast, clusters that are composed of H6 or H6 derivatives are rare, the bipod in Figure 5-8(j) and the tripod in Figure 5-12(f) are the only two examples we observed in experiments. But they are distinct from the hexagonal unit cell in the (2×2) Nb_2O_3 honeycomb lattice as there is an additional atom in the hexagon hollow site.

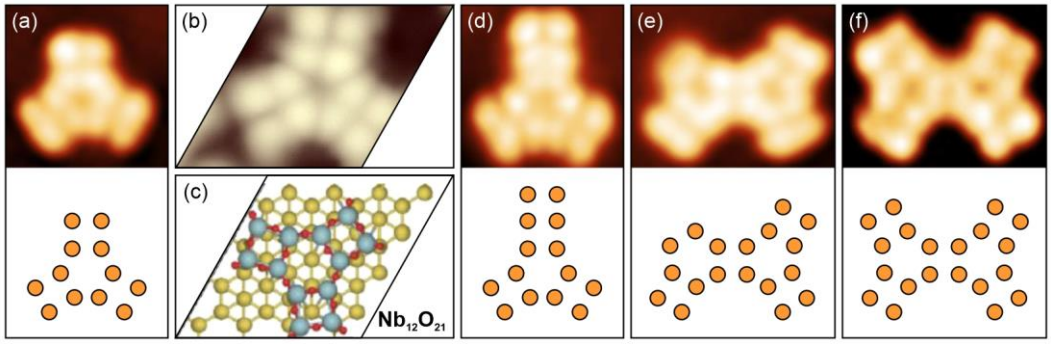

Figure 5-10 STM images of tripods and corresponding Nb atom arrangements based on $Nb_{12}O_{21}$. (a) $Nb_{12}O_{21}$. (b) DFT simulated STM image and (c) complete structural model with Nb (blue) and O (red) atoms. (d) $Nb_{12}O_{21}$ base + two Nb (n = 14). (e) Two joint $Nb_{12}O_{12}$ bases with a pair of central Nb atoms degenerated, and a pair of Nb atoms missing at the top left (n = 18). (f) Two joint $Nb_{12}O_{21}$ with a pair of central Nb degenerated (n = 20). STM image size: (a), (d) 2.0 nm × 2.0 nm; (e), (f) 2.5 nm × 2.0 nm.

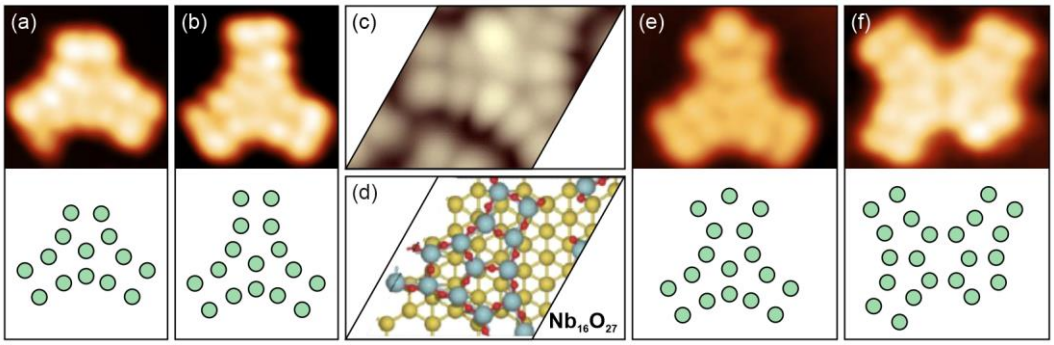

Figure 5-11 STM images of tripods and corresponding Nb atom arrangement based on $Nb_{16}O_{27}$. (a) $Nb_{16}O_{27}$ – two Nb (n = 14). (b) $Nb_{16}O_{27}$. (c) DFT simulated STM image and (d) complete structural model. (e) $Nb_{16}O_{27}$ base + one Nb (n = 17). (f) Two joint $Nb_{16}O_{27}$ bases with a paired of Nb atoms missing at the bottom right (n = 22). STM image size: (a), (b) 2.0 nm × 2.0 nm; (e), (f) 2.5 nm × 2.0 nm.

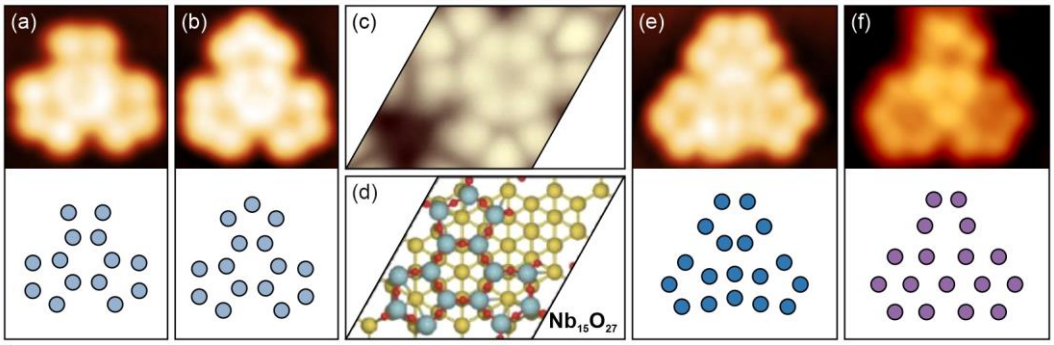

Figure 5-12 (a) – (c) STM images of tripods and corresponding Nb atom arrangement based on $Nb_{15}O_{27}$. (a) $Nb_{15}O_{27}$ – one Nb (n = 14); (b) $Nb_{15}O_{27}$. (c) DFT simulated STM image and (d) complete structural model. (e), (f) Another two examples of tripods with complex Nb atom arrangements. STM image size: (a), (b) 2.0 nm × 2.0 nm; (e), (f) 2.5 nm × 2.0 nm.

There is a discrepancy between experimental observation and theoretical calculation. The DFT calculations show that the formation energy of a cluster based on hexagonal units (H6) is much lower than that of $Nb_{12}O_{21}$, $Nb_{15}O_{27}$, or $Nb_{16}O_{27}$. We have also proved that the (2 × 2) Nb_2O_3 honeycomb structure is most thermodynamically stable compared with other structures. However, we did not see any bipod or tripod composed of typical H6 clusters. Such discrepancy suggests that a kinetic effect may play a role in the cluster growth, by which clusters with smaller building blocks like Q4 or P5 are more predominant than H6.

To sum up, the NbO_x clusters exhibit a variety of configurations, including rectangular, ring, bipod-like, and tripod-like structures, with the stoichiometry $x > 1.5$. The Q4 clusters appeared most frequently and can act as building blocks for other complex permutations. Theoretical calculations have examined various models and proved that flat configurations with threefold coordinated Nb atoms and niobyl groups at the edges are optimal structural solutions. In addition, the Au(111) substrate can stabilize the clusters through charge transfer from Nb to Au, with the Nb atoms approaching the substrate while the oxygen atoms relaxing outward, which is similar to the rumpled structure of the Nb_2O_3 honeycomb. Finally, the discrepancy between experimental observations and DFT calculations for large-sized clusters indicates that their growth is a complex result of the interplay between thermodynamics and kinetics.

5.5 NbO_y triangle and pinwheel structures

Among all the niobium oxide structures that we have identified, the triangle structure is the only one that is always present in the oxygen chemical range we can achieve in the experiments. In a NbO_x cluster sample, single triangles can always be found with small clusters decorating at the corners. In a Nb_2O_3 HC sample, triangles can incorporate into the honeycomb lattice in various ways. It is hard to get rid of triangles in honeycomb monolayers even though the sample was annealed in O_2 up to 10^{-4} Pa.

However, the morphologies of the triangle structures are sensitive to the substrate temperature and evolve significantly from a low to a high coverage. The STM images in Figure 5-13(a) and (b) display a few independently-standing triangles prepared by annealing in 1×10^{-7} Pa O_2 at 500°C. We named these subjects according to the number of triangle elements, such as single triangle (Single-T), double triangle (Double-T), triple triangle (Triple-T), and hexagonal triangle island (Hex-T). The triangle elements can be coupled with neighbours by altering the vertical gap and lateral shift (see Section 9.2.2).

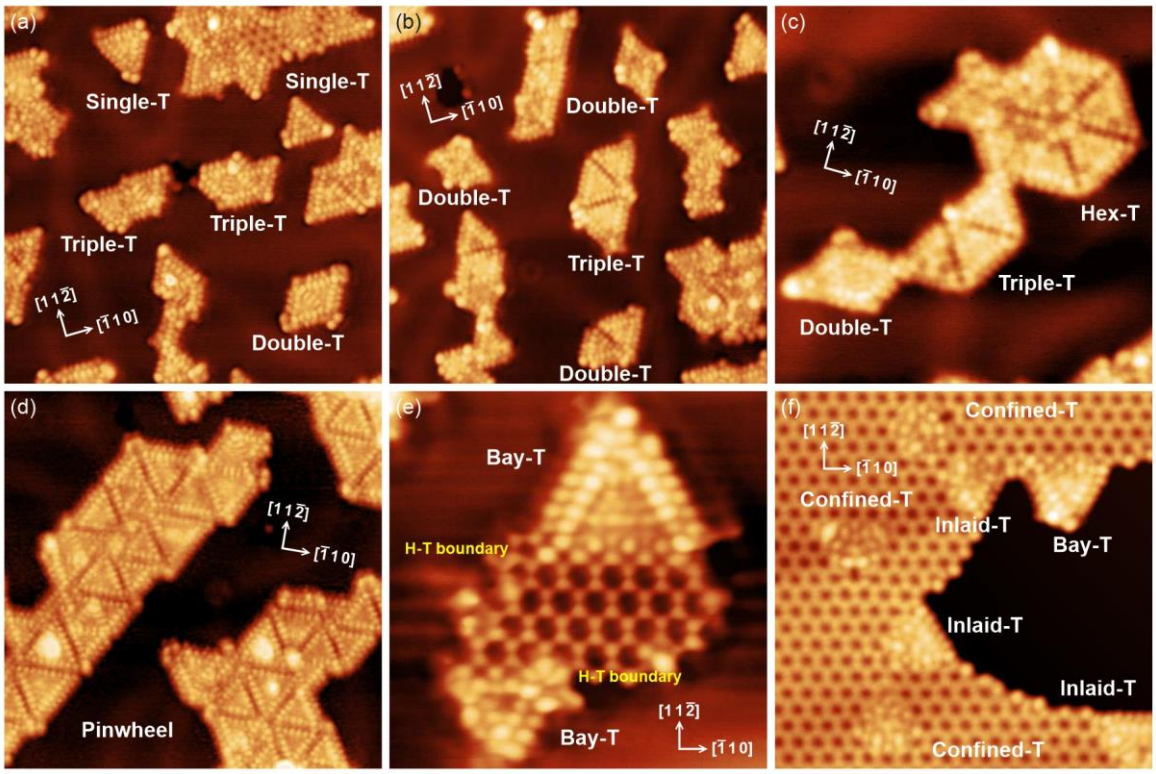

Figure 5-13 STM images of triangles, triangle continuous thin films, pinwheel, and triangles incorporated into the Nb_2O_3 HC structures. (a), (b) Independently-standing single and multiple triangles (17 nm × 17 nm, a: V_s = 1.0 V, I_t = 0.4 nA; b: V_s = 0.8 V, I_t = 0.8 nA). (c) Triangles grown jointly forming a continuous thin film (12 nm × 12 nm, V_s = 2.0 V, I_t = 0.2 nA). (d) Pinwheel structure formed by increasing the coverage (17 nm × 17 nm, V_s = 0.7 V, I_t = 0.5 nA). (e) Triangles incorporated at edges of a small HC island; honeycomb-triangle (H-T) boundaries are resolved at the atomic level (6.7 nm × 6.7 nm, V_s = 0.7 V, I_t = 0.3 nA). (f) Triangles are incorporated into the HC in various ways (10.5 nm × 10.5 nm, V_s = 0.7 V, I_t = 0.5 nA).

The contrast difference of a single triangle allows us to describe its structure as “double triangle rims with a core”. The brightness of the outside rim is comparable with the core but is less than

the inside rim. It can be explained by the atom positions in the structural models that we proposed in Chapter 9: the Nb atoms of outside rims or cores are seated at the hollow sites of Au(111), while the atoms of inside rims are at the on-top sites. Besides, the outside rims, especially their corners, are easily damaged or decorated by NbO_x clusters or adatoms. It is rare to find a single or multiple triangle nanostructure with intact edges. Therefore, in order to indicate the size of a triangle element, we count the number of atoms (n) along an edge of the inside triangle rim which is usually more preserved and straighter.

The continuous film in Figure 5-13(c) comprises a Hex-T, a Triple-T, a Double-T, and a small Single-T on the top. They are interconnected by sharing several atoms at the corner or an edge. The continuous films were usually obtained by annealing at a high temperature (i.e., 700℃), probably resulting from the ripening of independently-standing triangles. The ripening also gives rise to large-sized triangles, the biggest one observed from a continuous film possesses an inside triangle rim with $n = 10$. We proposed a few complete structural models with both Nb and O atoms and presumed that the O/Nb atom ratio y is between 1 and 2.

Moreover, we found that pinwheel monolayers started to grow on Au(111) when increasing the coverage of triangle nanostructures, as shown in Figure 5-13(d). Triangle elements can be seen as building blocks for the pinwheel structure, but the sizes of the elements in a pinwheel monolayer are usually suppressed. The building blocks are concentrated in $n = 4 \sim 7$, and the large-sized triangle elements are less frequently seen in the triangle continuous thin films.

The triangle structure can also incorporate into the (2×2) Nb_2O_3 honeycomb lattice, forming HC-connected triangles. The incorporation can be realized in three ways depending on the number of degenerated edges of the outside triangle rim. Firstly, a H-T boundary is formed when a triangle shares one edge with a honeycomb island and extends outward, as shown in Figure 5-13(e). It is common to see HC islands decorated by bay triangles (Bay-Ts), and the

atom configuration at the boundary is worth exploring and comparing with the Ti counterpart (see Chapter 9). Secondly, a triangle can have two edges integrated into a HC lattice at the border between the film and the Au substrate, forming an inlaid triangle (Inlaid-T). We can see three Inlaid-Ts in Figure 5-13(f), of which the remaining edges constitute parts of the HC edge with a higher atom density than regular HC edges (i.e., zigzag and armchair). Thirdly, a triangle can be entirely confined in the HC lattice with three edges of inside rims surrounded by HC hexagons. A confined triangle (Confined-T) possesses threefold symmetry and can play an important role in the triple junction of three domain boundaries (see Section 9.3.3).

To sum up, Nb oxide triangle nanostructures can exhibit various forms including independently-standing triangles, triangle continuous films, pinwheel monolayers, and HC-connected triangles. Their structures do not follow a strict (1 × 1) epitaxial relationship with the surface, considering Nb atoms of outside and inside rims are located at hollow sites and on-top sites of Au(111), respectively. In the present work, we also studied free and embedded triangles of Ti oxides, which have not yet been reported, as well as the pinwheel structure. In addition, we investigated V oxide free and embedded pinwheel structure on Au(111). A comparative analysis between Nb, Ti, and V oxides will be presented in Chapter 9.

5.6 The (2 × 2) Nb_2O_3 honeycomb structure

5.6.1 General description of the honeycomb structure

Experimental results have shown that the Nb_2O_3 honeycomb is the most thermodynamically stable structure under the conditions $p(O_2)$ =10^{-7} – 10^{-4} Pa, T = 300 – 900 °C, roughly corresponding to an oxygen chemical potential $\mu(O_2)$ between -2.68 ~ -1.12 eV. We have demonstrated the structure evolutions from Nb-induced ring structure (Figure 5-2), NbO_x clusters (Figure 5-3), and triangle and pinwheel structure (Figure 5-4) to the Nb_2O_3 honeycomb structure by successive annealing in oxygen.

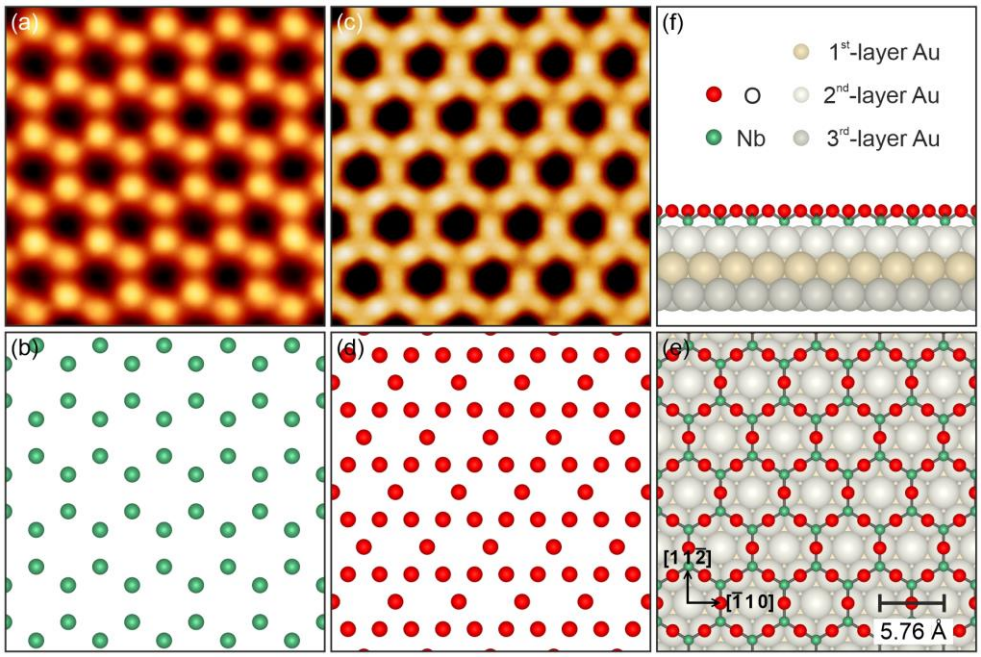

Figure 5-14 (a) STM image of the (2 × 2) Nb_2O_3 honeycomb structure at a positive sample bias, showing Nb atoms as protrusions (V_s = 0.7 V, I_t = 0.8 nA). (b) The corresponding Nb lattice model. (c) STM image at a negative sample bias showing O atoms as protrusions (V_s = -1.8 V, I_t = 0.8 nA). (d) The corresponding O lattice model. (e) Schematic model of the Nb_2O_3 honeycomb structure on Au(111) (top view). Frame size: 2.86 nm × 2.86 nm. The beige balls represent Au atoms of the surface layer; the green and red balls represent Nb and O atoms, respectively. (f) Side view of the rumpled Nb_2O_3 honeycomb on the substrate with three Au layers shown in the schematic.

The freestanding modelled Nb_2O_3 is a Mott-Hubbard semiconductor and possesses a planar honeycomb structure with lattice parameter $a_{Nb_2O_3} \approx 6.67$ Å. By contrast, the Au-supported Nb_2O_3 honeycomb monolayer undergoes striking changes in the structural properties and electronic characteristics due to the substrate effect. Nb_2O_3 has a (2 × 2) epitaxial growth on the Au(111) surface, forming a rumpled honeycomb structure with a lattice parameter $a_{Nb_2O_3} \approx$ 5.77 Å, as shown in Figure 5-14(a) – (e). Nb atoms locate at the fcc and hcp hollow sites of the Au(111) surface layer, while O atoms are at on-top sites and protrude outwards to relax the compression due to the lattice mismatch [Figure 5-14(f)]. The height difference between the Nb layer and O layer δz_{Nb-O} is about 0.93 Å. The (2 × 2) Nb_2O_3 honeycomb monolayer interacts strongly with the Au substrate and has a large electron transfer (Q_{Au} = -1.28e per Nb_2O_3 unit) from Nb cations to Au atoms [27].

5.6.2 Two growth modes of honeycomb islands

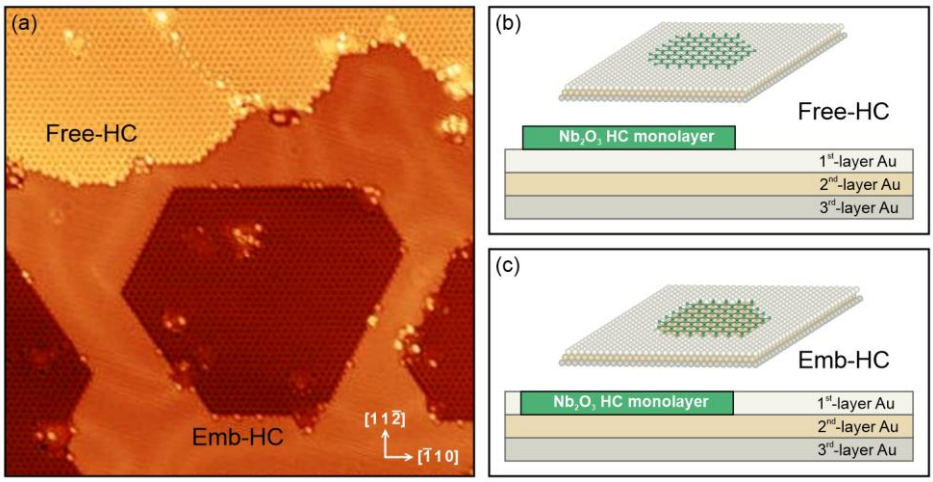

Figure 5-15 (a) STM image showing the coexistence of free-HC and emb-HC (37.5 nm × 37.5 nm, V_s = 0.8 V, I_t = 0.5 nA). (b) and (c) Schematic diagrams showing two growth modes of a Nb_2O_3 honeycomb monolayer.

Recent experimental results show that the (2 × 2) Nb_2O_3 HC can adopt two growth modes on the Au(111) substrate, as shown in Figure 5-15(a). One is growing on the top of the surface layer (L_1), thus forming a free honeycomb monolayer (free-HC) [Figure 5-15(b)]. The other is growing on the second Au layer (L_2), and therefore, the honeycomb monolayer is embedded in L_1, so-called emb-HC [Figure 5-15(c)]. The major difference between a free-HC monolayer and an emb-HC monolayer is the edge structure (see Chapter 7), while other features such as the honeycomb lattice, defects, domain boundaries, and interactions with triangles are essentially the same. The free-HC usually has curved edges with various reconstructions as no "barrier" impede the expansion of the monolayer. By contrast, the emb-HC islands constrained in the surface layer generally possess very straight edges and a 120° angle between neighbouring sides, which indicates a strong effect from the Au(111) substrate.

The growth mode mainly depends on the Nb diffusion (or Nb-Au substitution) and oxidation rates. It is challenging to quantitatively describe or compare the rates of these two processes at the atomic level. Intuitively, if the oxidation rate is higher than the substitution rate, more Nb atoms are transformed to Nb_2O_3 and stay on the surface. The protruding O atoms prevent the

Nb atoms from diffusing into the substrate due to the chemical bonding ($\delta z_{\mathrm{Nb-O}} = 0.93$ Å). If the diffusion rate is higher, a large number of Nb atoms can rapidly diffuse into deep layers, which gives rise to ring patterns with a set of different sizes on the surface. It is worth noting that the majority of Nb atoms should substitute Au atoms at shallow layers. When the oxygen is introduced into the system, the free Nb atoms on the surface are oxidized and reduced in quantity. Due to a concentration gradient, the thermally-activated Nb atoms in the bulk can diffuse upwards to the surface layer and then are gradually oxidized. As the L_1 Au atoms have been substituted before the oxidation, the Nb_2O_3 honeycomb islands are formed on the second layer and surrounded by L_1 Au atoms that are not yet substituted.

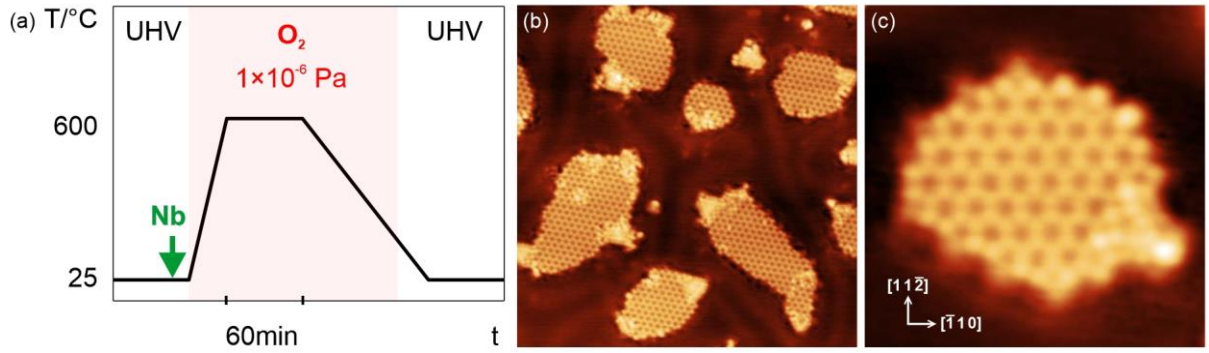

Figure 5-16 (a) Route 1 for the preparation of free-HC monolayers. (b) STM image of free-HC islands (27 nm × 27 nm, V_s = 1.0 V, I_t = 0.8 nA). (c) STM image of a typical free-HC island with edge completely reconstructed (6.5 nm × 6.5 nm, V_s = 1.1 V, I_t = 0.2 nA).

The growth mode can be controlled by the substrate temperature and the sequence of depositing Nb and introducing the O_2 into the chamber. Figure 5-16 – Figure 5-18 demonstrate three synthesis routes that lead to different growth results. In Route 1 [Figure 5-16 (a)], Nb is deposited on the Au(111) substrate at room temperature (indicated by the green arrow). Oxygen is introduced into the chamber once after the deposition, so the chamber is O_2-rich during the heating-up stage. It has been found that annealing at 300 ~ 700 ℃ for 30 ~ 60 mins results in the free-HC and has little effect on the growth mode, as shown in Figure 5-16(b). However, the annealing temperature and duration make a big difference to the free-HC edge structure. A lower temperature with a shorter time (i.e., 350℃ for 30 mins) gives rise to entirely

reconstructed edges. For example, a small free-HC island with reconstructed edges is shown in Figure 5-16(c). The edge reconstruction content is presented in Chapter 7.

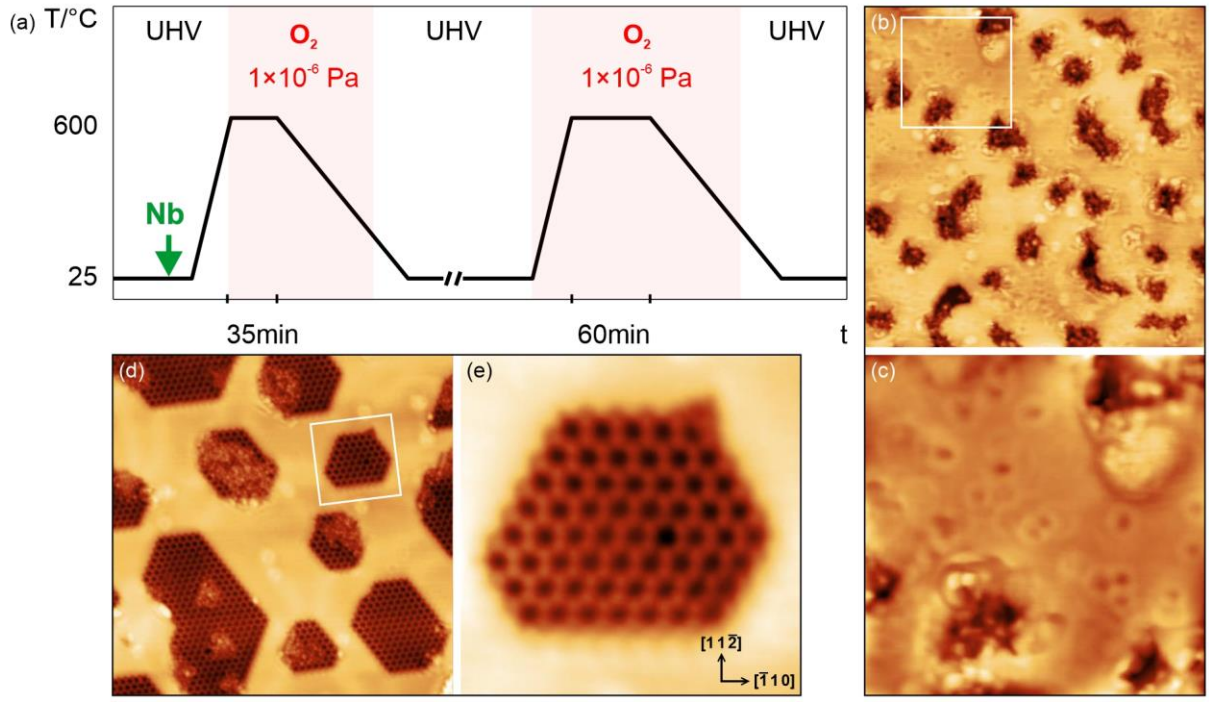

Figure 5-17 (a) Route 2 for the preparation of emb-HC monolayers, two annealing stages are required. (b) STM image of the surface with abundant Nb-induced rings and dark pits after the first annealing stage (35 nm × 35 nm, V_s = 1.0 V, I_t = 0.6 nA). (c) Close-up of the region in the white box in (b) (12 nm × 12 nm). (d) STM image of the surface after the second annealing stage. Nb_2O_3 honeycomb islands are embedded in the surface (27 nm × 27 nm, V_s = 1.0 V, I_t = 0.3 nA). (e) Close-up of the emb-HC island in the white box in (d) (6.5 nm × 6.5 nm).

Figure 5-17(a) shows the preparation of emb-HC islands through Route 2, which contains two annealing stages. Compared with Route 1, the critical difference in the first stage is that the oxygen valve is not open until the substrate has reached a high temperature. Nb atoms can diffuse into the bulk during the heating-up stage in UHV, creating a large number of rings and dark "pits" on the surface, as shown in Figure 5-17(b) and (c). The dark pits were probably formed by removing a lot of L_1 Au atoms, while the distinguishable rings were caused by relatively discrete Nb-Au substitutions at deeper layers below the surface. A large number of Nb-induced rings can be seen as a precursor structure for forming an embedded structure, either the embedded pinwheel or the emb-HC. Annealing the Nb-induced rings in oxygen at low

pressure ($5 \times 10^{-8} \sim 1 \times 10^{-7}$ Pa) results in the pinwheel structure, while annealing in 10^{-6} Pa O_2 (e.g., the second stage of Route 2) leads to emb-HC islands. Figure 5-17(e) displays a hexagonal emb-HC island with few defects except an extending atom at the upper right corner. Generally, the edges of the emb-HC islands are straight, forming 120° internal angles.

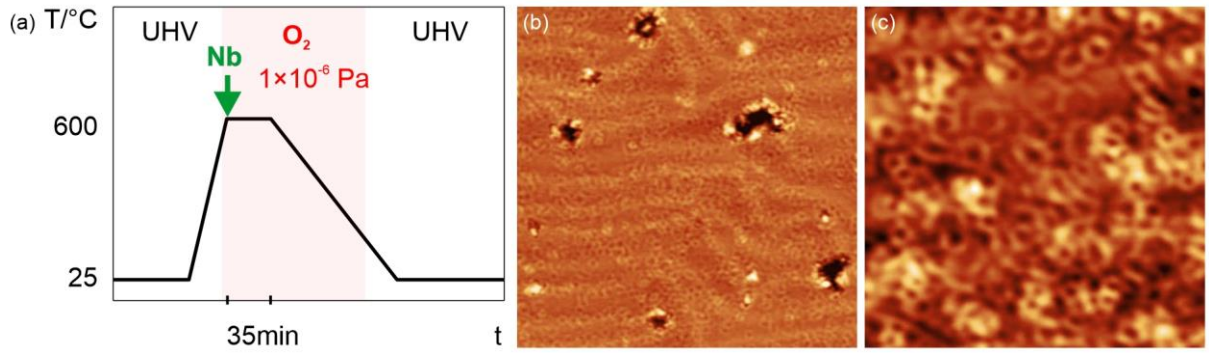

Figure 5-18 (a) Route 3, reactive deposition. (b) and (c) STM images of the sample surface with countless Nb-induced rings. (b) 35 nm × 35 nm, V_s = 1.0 V, I_t = 0.8 nA; (c) 12 nm × 12 nm, V_s = 1.0 V, I_t = 0.5 nA.

We also adopted reactive deposition in sample preparation. As shown in Figure 5-18(a), Nb was deposited in 1×10^{-6} Pa O_2 on Au(111) at 600°C. The evaporated Nb atoms with high kinetic energy can diffuse more rapidly and homogeneously into a hot substrate even in an O_2-rich environment. Figure 5-18(b) and (c) show the STM images of the surface that contains numerous Nb-inducted rings with a variety of sizes. Most of them overlap with each other so the individual rings are hardly distinguished. These rings can turn into emb-pinwheel or emb-HC islands depending on the oxygen pressure that we would use in the following step.

5.6.3 Key features of honeycomb monolayers

The structural analysis of the pristine HC has been done by Wang *et al*. [27], but features on the HC monolayers, including reconstructed edges, defects, domain boundaries, and interactions with triangle structures (Bay-T, Inlaid-T, and Confined-T), have not yet been studied systematically. Figure 5-19 shows two STM images of a free-HC monolayer and an emb-HC monolayer, on which the key features are indicated.

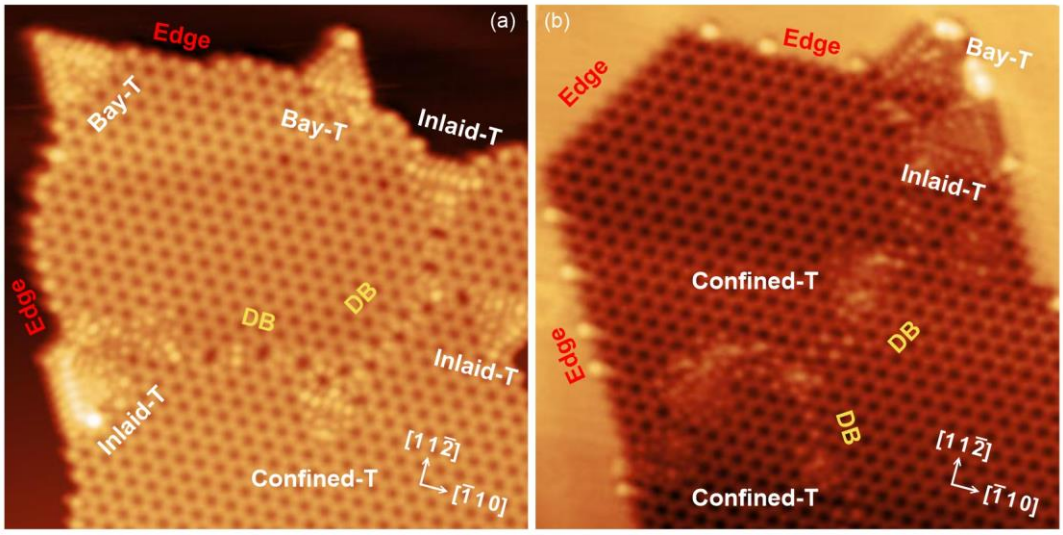

Figure 5-19 STM images showing the key features of honeycomb monolayers. (a) A free-HC island (15 nm × 15 nm, V_s = 0.7 V, I_t = 0.5 nA). (b) An emb-HC island (15 nm × 15 nm, V_s = 0.8 V, I_t = 0.5 nA).

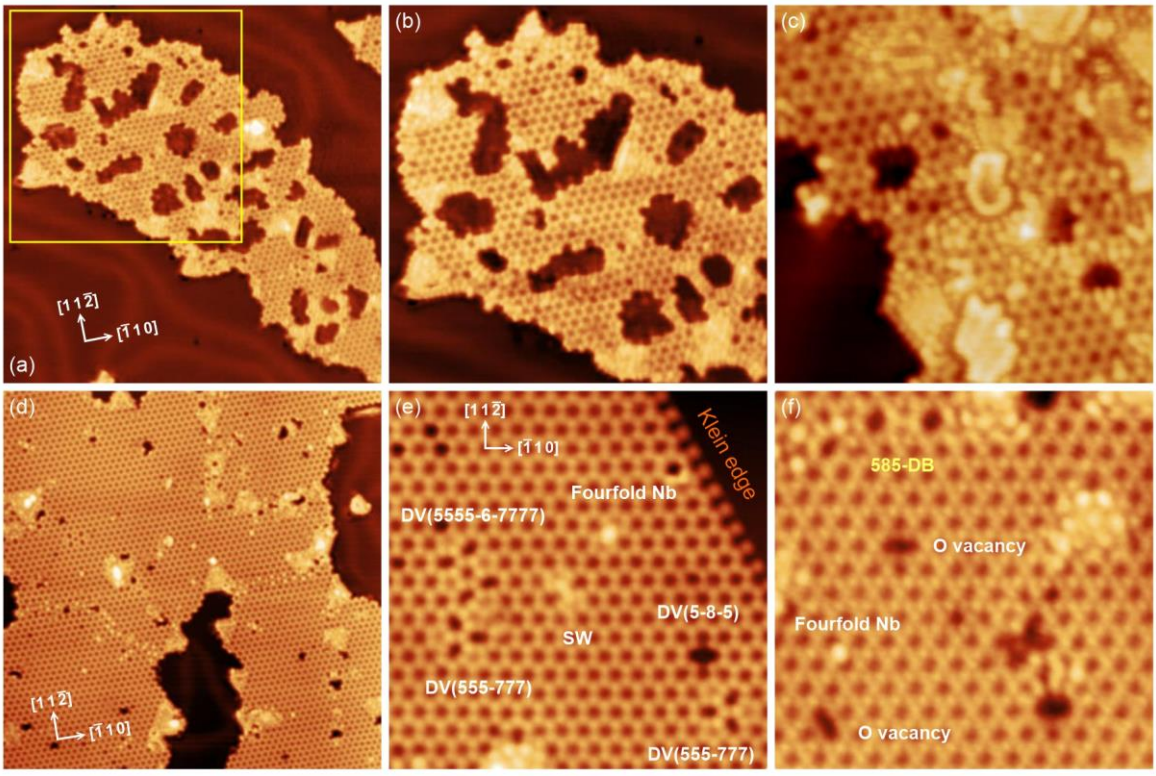

Figure 5-20 STM images of the (2 × 2) Nb_2O_3 honeycomb monolayers after Ar^+ ion bombardment at (a) – (e) 100 eV and (d) – (f) 50 eV, and a sequent annealing at 350°C for 8 mins. (a) A large number of defect structures due to the high-energy bombardment (30 nm × 30 nm, V_s = 0.8 V, I_t = 0.2 nA). (b) Close-up of region in the yellow box in (a) (18 nm × 18 nm, V_s = 0.8 V, I_t = 0.2 nA). (c) Excess Nb atoms accumulate in a region (10 nm × 10 nm, V_s = 1.0 V, I_t = 1.5 nA). (d) A large Nb_2O_3 honeycomb monolayer with appropriate number of defective sites (30 nm × 30 nm, V_s = 0.8 V, I_t = 0.4 nA). (e) A region contains various point defects denoted on the image (10 nm × 10 nm, V_s = 0.8 V, I_t = 0.4 nA). (f) Image taken at a negative bias with the defects denoted (8 nm × 8 nm, V_s = -1.0 V, I_t = 1.0 nA).

As mentioned at the beginning of this section, the (2 × 2) Nb_2O_3 honeycomb structure is very stable over a wide range of oxygen chemical potential, and the density of point defects is very low in a pristine HC monolayer. In order to investigate defect structures, we used low-energy Ar^+ ions to bombard the as-prepared Nb_2O_3 HC monolayers, and then annealed the sample moderately to recover the damaged surface. Figure 5-20(a) – (c) show the sample surface after Ar^+ ion bombardment at 100 eV and annealing at 350 ℃ for 8 mins. The Ar^+ ion energy was relatively high, which resulted in some breakage of the HC lattice and some accumulation regions with excessive Nb atoms [Figure 5-20(c)]. Therefore, a lower accelerating energy (50 eV) was applied to a sample with higher coverage of the (2 × 2) Nb_2O_3 honeycomb monolayer. Recovery was done with the same annealing treatment. Results are displayed in Figure 5-20(d) – (e), from which we can see that the density of defects is quite reasonable. A few point defects such as the SW defect and divacancies (5-8-5, 555-777, 555-6-7777) can be identified at the atomic level under both positive and negative sample biases (see Section 8.3).

In summary, this section is a general demonstration of the (2 × 2) Nb_2O_3 honeycomb structure and relevant features. Two growth modes and the corresponding synthesis routes have been described in detail. The key features of the Nb_2O_3 honeycomb monolayer are introduced without in-depth analysis, more STM results and detailed discussions will be presented in Chapter 7 (edge reconstruction), Chapter 8 (point defects and domain boundaries), and Chapter 9 (HC-connected triangles).

Chapter 6 Fourfold coordinated Nb atoms in Nb_2O_3 honeycomb monolayers

6.1 Introduction

Atom configuration and chemical bonding determine many properties of materials, so it is significant to simultaneously acquire the structural, chemical, and electronic state information at atomic resolution [225]. Annular dark-field (ADF) imaging in scanning transmission electron microscope (STEM) can provide the Z-contrast and atom position information. Energy-dispersive X-ray spectroscopy (EDS) and electron energy loss spectroscopy (EELS) can be used to clarify atom species as well as analyze the electronic states [226]. Many studies have proved that combining ADF STEM with EDS and/or EELS is an effective way to acquire structural and chemical information at atomic resolution in the real space [227–230].

Suenaga *et al*. demonstrated the discrimination between Ce^{3+} and Ce^{4+} in metallofullerene molecules by measuring the energy shift using EELS single atom spectroscopy [229]. He also investigated graphene edges and distinguished the single-, double-, and triple-coordinated carbon atoms with atomic resolution in an ADF STEM image combing the analysis of energy-loss near-edge fin structure (ELNES) spectra [225]. Zhou *et al*. directly observed threefold and fourfold coordinated Si impurities in monolayer graphene by ADF STEM imaging and deduced the chemical bonding of individual impurity atoms by analyzing the ELNES spectra [231]. In recent years, these techniques have also been applied to the studies of transition metal oxides, specifically, imaging the oxidation states of transition metal atoms at atomic resolution. Manganites, such as $La_xCa_{1-x}MnO_3$ and $Pr_{1-x}Ca_xMnO_3$, are good test materials. The Mn oxidation states, which strongly affect their ferromagnetic properties, can be extracted from Mn $L_{2,3}$ edges in STEM-EELS measurement [227,232]. Besides, mixed-valence compounds Mn_3O_4 [227] and Fe_3O_4 [233] have also been investigated by atomic EELS imaging, in which

the cation sites with different oxidation states can be marked on the STEM images. However, this method can only be applied to a known crystalline structure along a specific growth direction. In other words, mapping the oxidation state is achieved by applying a structural grid on the STEM images so that one can assign different oxidation states according to the intensity of the spots.

Oxidation states of oxide materials can also be derived from STM images according to the contrast difference. A good example is using STM to observe the Si(111)-(7×7) surface [234–236]. A Si atom with a dangling oxygen atom absorbed on the top appears much brighter in STM images. This feature can be utilized to distinguish Si atoms with different oxidation states and directly identify the atomic position at which redox happened. Yim *et al*. demonstrated how to establish a spatial distribution of Ti polarons bound to the oxygen vacancies by STM, in which Ti ions could be either Ti^{3+} or Ti^{4+} depending on the excess electrons associated with oxygen vacancies [237]. Compared with STEM-EELS measurement, STM can non-destructively reveal the atomic structure and bonding characteristics. Electron beam irradiation in the TEM/STEM may change the chemical bonding and cannot reflect the stability of individual atoms under electron bombardment. Therefore, a low accelerating voltage (60 kV) is usually applied in the STEM-EELS measurements despite the extremely weak signal [225,229,231].

In this chapter, we demonstrate how to directly determine Nb oxidation states in an Au-supported Nb_2O_3 honeycomb monolayer based on the contrast difference in STM images. Nb oxides are an interesting class of materials which have been reviewed in Section 2.1.1 [23,24,223,238–240]. Nb can form a (2 × 2) Nb_2O_3 honeycomb monolayer on the Au(111) surface with threefold coordinated Nb atoms sitting at fcc and hcp hollow sites [27]. We found that a Nb atom with fourfold coordination exhibits much higher intensity than its threefold coordinated counterpart in the STM images, indicating a higher oxidation state and substantial

changes in the local density of states (ΔLDOS). We conducted DFT calculations to examine the local structure and charge redistribution of fourfold coordinated Nb atoms, which can help us give a better interpretation of those bright protrusions in STM images. In addition, fourfold coordinated Nb atoms play a pivotal role in the defect and edge reconstruction as well as the domain boundary formation. A single fourfold coordinated Nb atom can give rise to a defect domain composed of multiple rings, which can be seen as a locally disordered structure. This suggests a new way to tune the crystalline order of Nb oxide thin films by the amount of Nb atoms with a higher oxidation state, which may, in turn, affect the absorption behavior and catalytic properties.

6.2 Experimental methods

The preparation of the (2 × 2) Nb_2O_3 HC monolayers on Au(111) has been described in Section 5.6.2. In short, (2 × 2) Nb_2O_3 HC monolayers with a very low density of point defects and domain boundaries can be obtained by annealing in 10^{-6} Pa O_2 at 500 ~ 700 ℃ for 45 ~ 90 mins. In order to improve the defect density, we used low-energy (50 eV) Ar^+ ions to bombard the as-prepared samples, followed by moderate annealing at 100 ~ 200 ℃ for surface recovery (see Section 5.6.3). STM images were acquired with tungsten tips by applying a sample bias in constant tunneling current mode at room temperature. DFT calculations and simulations were carried out by a group member who will be a co-author in the forthcoming paper based on this chapter, so the calculation methods and details are not shown here.

6.3 Fourfold-coordinated Nb atoms in point defects

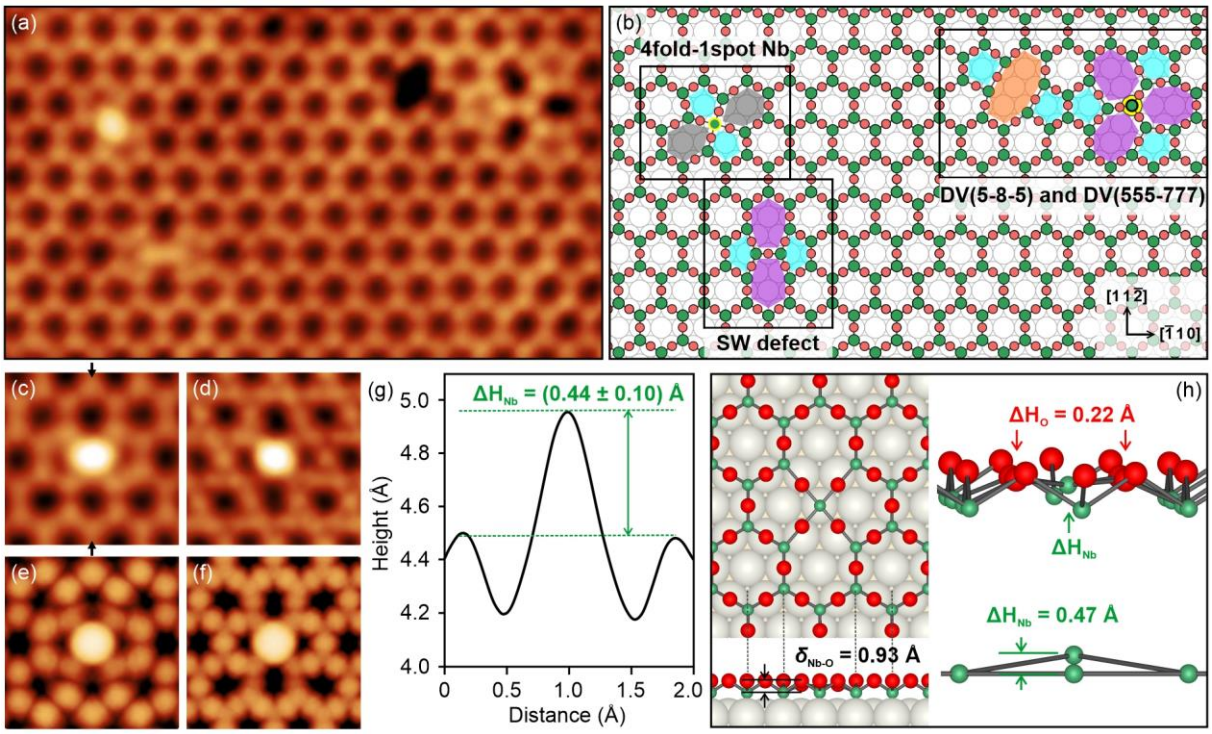

Figure 6-1 (a) STM image of a Nb_2O_3 honeycomb monolayer with different types of defects (8 nm × 4.7 nm, V_s = 0.8 V, I_t = 0.4 nA). (b) Schematic corresponding to (a). The green circles represent Nb atoms, and the red circles represent O atoms. For clarity, the four defect domains are boxed in which the polygon components are filled with different colors: pentagons: cyan; distorted hexagons: grey; heptagons: purple; octagon: orange. The green circle with a yellow perimeter in the 4fold-1spot defect domain represents the fourfold coordinated Nb. The bright green circle with a bold black perimeter indicates the center Nb of DV(555-777) sitting on the top of an Au atom (in yellow). (c) STM image (2 nm × 2 nm) of a close-up of the 4fold-1spot defect at positive sample bias (V_s = 0.8 V, I_t = 0.4 nA) and (d) at negative bias (V_s = -1 V, I_t = 1.0 nA). (e), (f) DFT simulated STM images at positive (V_s = 0.8 V) and negative (V_s = -0.8 V) sample biases. (g) A profile measured between two arrows in (c) and presented in the height unit. (h) 3D structural model of the 4fold-1spot defect.

Figure 6-1(a) shows the coexistence of different defects in a small region of a (2 × 2) Nb_2O_3 honeycomb monolayer. The bright protrusions in the empty-state STM image can be assigned to Nb atoms. Figure 6-1(b) is the schematic corresponding to frame (a), in which the oxygen atoms are inserted at the bridge sites of two adjacent Nb atoms. On the top right of the image, there are two divacancy defects, which are denoted as DV(5-8-5) and DV(555-777). They are formed by the defect domain re-arranging the local atoms after losing a Nb_2O_3 unit. The remaining atoms can keep the stoichiometry unchanged, and therefore, the Nb atoms retain the

threefold coordination. We can observe a small variance in the brightness of the protrusions in these defect domains. This is because some Nb atoms are no longer sitting at the hollow sites of the Au(111) surface after the lattice re-arrangement. For example, the center Nb atom of DV(555-777), depicted in the bright green circle in Figure 6-1(b), should be slightly lifted as it locates on the top of an Au atom. Besides, additional stress caused by the atom re-arrangement can release the compressive strain of the original (2 × 2) Nb_2O_3 honeycomb monolayer and affects the LDOS [88]. A Stone-Wales (SW) defect can be seen at the bottom left of the image. Unlike the divacancy defects, no atom is lost in the SW defect, but a pair of adjacent Nb atoms in a hexagon has a rotation by 90°, creating two pentagons and two heptagons [83]. We can clearly distinguish two Nb atoms from the "bar" in the center of the SW defect domain. A detailed discussion of the point defects in Nb_2O_3 honeycomb will be presented in Section 8.3.

Apart from that, the most prominent feature in the STM image is the large spot with much higher brightness above the SW defect. The defect domain around the bright spot is similar to the SW defect, but it is composed of two pentagons and two stretched hexagons rather than heptagons. The bright spot is surrounded by four nearest atoms, namely possessing the fourfold coordination, so we called it the 4fold-1spot defect. The SW defect has no atom lost, while the 4fold-1spot defect was deprived of a NbO unit. Because of this, the central Nb has to bond to four oxygen atoms, thus forming a higher oxidation state. Figure 6-1(c) and (d) are close-ups of the 4fold-1spot defect at positive and negative bias. The STM image at a negative bias reflects the filled states of oxygen atoms, but we can still see the bright spot in the center. This suggests that the fourfold coordinated Nb atom undergoes a substantial change of the LDOS when it is oxidized to a higher state, leading to an elevated brightness in the STM image.

Figure 6-1(e) and (f) are DFT-simulated STM images, in which the central Nb atom was set to be coordinated to four oxygen atoms, and the monolayer has been fully relaxed. We can see that the simulated images can well reproduce the experimental results, which confirms that the

bright spot is caused by a fourfold coordinated Nb with a higher oxidation state. It should be noted that STM images cannot reveal the 3D structure or the charge redistribution. For example, the entire Au-supported (2 × 2) Nb_2O_3 HC monolayer has a rumpled structure with Nb atoms close to the Au surface and O atoms extended outward by 0.93 Å [27]. Therefore, DFT calculations are irreplaceable for interpreting the contrast difference in the STM images, which can provide insights into the 3D structural properties and film-substrate interaction.

Figure 6-1(g) shows the profile measured between the two arrows in Figure 6-1(c). Although the profile is presented in height difference, the contrast difference (0.44 Å) should be attributed to the change of the atom position and the ΔLDOS, which is not a simple linear superposition. The location of the fourfold coordinated Nb atom is lifted as it is brought to the top of an Au atom. DFT calculations show that the height of the central Nb atom is promoted by 0.47 Å, and the four bonding O atoms are slightly pulled down by 0.22 Å with respect to the original sites. Based on these results, we are able to produce the 3D structural model in Figure 6-1(h). The charge redistribution allows us to evaluate the interaction between the fourfold Nb atom and the substrate. Presumably, the charge transfer from Nb to Au is reduced (less than 1.28*e* per formula unit [27]) because it is now bonding to four O atoms and further away from the surface. The exact value of the charge redistribution is being calculated by my colleague.

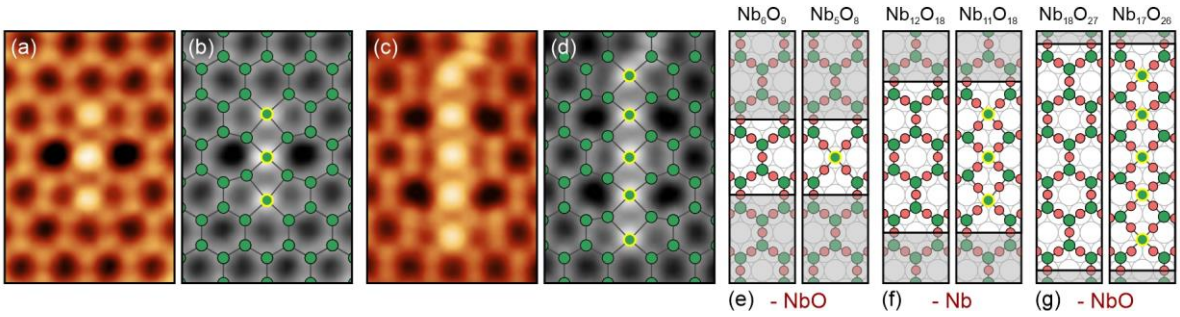

Figure 6-2 (a) STM image of 4fold-3spot defect (2.2 nm × 3.3 nm, V_s = 2.0 V, I_t = 0.5 nA). (b) Nb lattice superimposed on (a) in grayscale. (c) STM image of 4fold-5spot defect (2.2 nm × 3.3 nm, V_s = 1.5 V, I_t = 0.6 nA). (b) Nb lattice superimposed on (c) in grayscale. (e) – (g) Calculation of the atom deficiency in the 4fold-1spot, 4fold-3spot, and 4fold-5spot defects. The left part of each frame is an ideal honeycomb structure for reference. The stoichiometries of local regions are marked on the top. The atom deficiencies are shown in red at the bottom.

Table 6-1 Atom deficiency and number of occurrences of different types of defects

Defect type	Atom deficiency	Total occurrence
SW	0	28
4fold-1spot	NbO	48
4fold-3spot	Nb	14
4fold-5spot	NbO	2
DV(5-8-5)	Nb_2O_3	18
DV(555-777)	Nb_2O_3	77

We also observed the fourfold coordinated Nb atoms in defect domains with three bright spots (4fold-3spot) and five spots (4fold-5spot), as shown in Figure 6-2(a) – (d). Each bright spot is fourfold coordinated, forming a configuration in which four-membered rings and two stretched hexagons are in the middle; five-membered rings and seven-membered rings are arranged alternatively at two sides. In order to clarify the atom deficiency and the local stoichiometry, we counted the atoms and compared them with a defect-free honeycomb lattice [Figure 6-2(e) – (g)]. The 4fold-1spot and the 4fold-5spot lose a non-stoichiometric NbO unit, whereas only one Nb atom is missing in the 4fold-3spot. A summary of defect type, atom deficiency, and the number of occurrences is displayed in Table 6-1. It can be seen that the number of the 4fold-1spot is much more than the 4fold-5spot, which indicates that reconstructing a defect domain with a deficiency of NbO is more inclined to involve just one fourfold coordinated Nb atom rather than five atoms. Intuitively, the formation energy of the 4fold-5spot is relatively high, and the defective structure is less stable. Besides, it is not surprising to see that the DV(555-777) occurred most frequently. A similar result can also be found in the Au-supported Ti_2O_3 honeycomb [88]. Both Nb_2O_3 and Ti_2O_3 HC monolayers grown on the Au(111) substrates are in a state of in-plane compressive strain. Theoretical calculations have shown that forming a DV(555-777) can effectively release the local strain and lower the defect energy [27,88]. In addition, although the atom deficiencies are different, the shape of the defect domain of the SW defect, the DV(5-8-5), and the 4fold-1spot are in common. It has been reported that the DV(5-8-5) possesses high defect energy due to a significant bond distortion in graphene [87] and other graphene-like 2D thin films with a HC structure, including silicene [241], h-BN [242], bilayer

silica [243], and Ti_2O_3 [88]. In Au-supported Ti_2O_3, the formation energy of the SW defect is comparable with the DV(5-8-5) and much higher than the DV(555-777) [88]. Therefore, we assume that the defect energy of the 4fold-1spot is between the DV(555-777) and the SW defect.

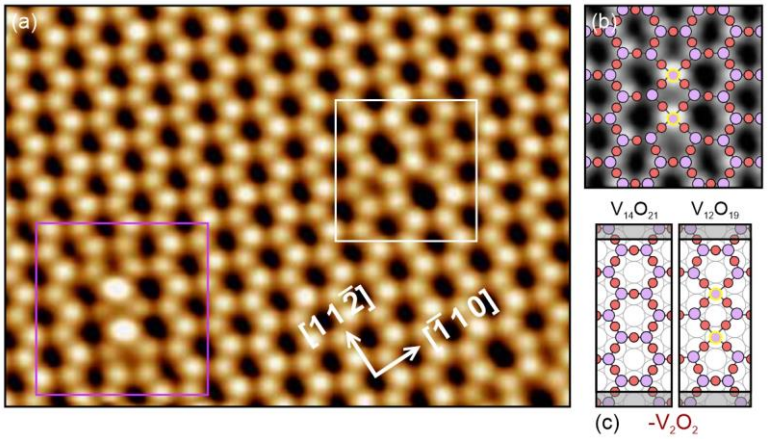

Figure 6-3 (a) STM images of a (2 × 2) V_2O_3 honeycomb monolayer on the Pd(111) substrate [32]. The purple box marks a defect domain with two fourfold coordinated V atoms with much higher intensity. The white box marks the SW defect. (b) A structural model superimposed onto the defect domain in the purple box in (a). The purple circles represent the V atoms; The purple circles with a yellow perimeter represent the fourfold coordinated V atoms. The red circles represent O atoms. (c) Schematic diagrams of (left) defect-free (2 × 2) V_2O_3 honeycomb structure for reference and (right) the defect domain. The local stoichiometries are marked on the top, and the atom deficiency is shown in red at the bottom.

Similar structures with fourfold coordinated metal atoms and much higher intensity in the STM images were also found in vanadium oxide thin films. Surnev *et al*. investigated the (2 × 2) V_2O_3 honeycomb monolayer on Pd(111) and observed two bright spots with fourfold coordination [32], as shown in Figure 6-3(a). They also saw structures with three bright spots but did not provide the STM images with atomic resolution [58]. However, they did not give a detailed description or analysis of these structures but simply attributed the higher intensity to an adatom, possibly O or V, from the second layer. We believe that the two bright spots are caused by fourfold coordinated V atoms with a higher oxidation state rather than adatoms. In Figure 6-3(b), a lattice model composed of V (purple) and O (red) atoms is superimposed on the defect domain with the two bright spots. Compared with the defect-free (2 × 2) V_2O_3 honeycomb structure, the atom deficiency of the defect domain is V_2O_2 [Figure 6-3(c)].

V and Nb are Group VB elements and are capable of oxidation state up to +5. We also studied the Au-supported Ti_2O_3 HC monolayers, however, we did not observe any fourfold coordinated Ti atoms or find any report on similar structures in the existing literature. Compared with Nb or V, a Ti atom has four valence electrons, limiting its highest oxidation state to +4. Theoretical calculations have shown that the charge distribution of a metal oxide M_2O_3 monolayer epitaxially grown on a noble metal substrate is quite different from the freestanding flat monolayer [27,88,244,245]. The significant charge transfer between the oxide thin film and the substrate induces a structural polarization, which can release the compressive strain due to the lattice mismatch. For example, the charge transfer from Nb and Ti in the corresponding (2 × 2) honeycomb monolayers to the Au substrate is $Q_{Nb\rightarrow Au} = 1.28e$ per Nb_2O_3 [27], and $Q_{Ti\rightarrow Au} = 0.94e$ per Ti_2O_3 [88]. Consequently, the actual oxidation state of Nb or Ti is higher than +3 in the Au-supported honeycomb monolayer. Considering the charge transfer with the substrate, when a metal atom bonds to four O atoms, its oxidation state should be higher than +4. This explains why we can observe the fourfold coordinated Nb and V but did not see any fourfold coordinated Ti in the corresponding honeycomb monolayers grown on noble metal substrates.

Figure 6-4 shows STM images and corresponding structural models of two defect domains in Nb_2O_3 HC. All Nb atoms in the lattice are threefold coordinated except for the fourfold Nb, so the complete structures can be determined without any concern about the dangling O atoms [Figure 6-4(c), (f)]. For an arbitrary defect domain in Nb_2O_3 HC, the Nb atom with a higher oxidation state can be discriminated in the STM images according to two features: the fourfold coordination and the elevated brightness. In other words, we can map the oxidation state of Nb atoms at atomic resolution through the contrast difference. This is hardly achieved by other characterization techniques (e.g., STEM-EELS) because, first of all, the oxidation state is substrate-related due to the charge transfer; secondly, the electron bombardment in the STEM-EELS may affect the chemical bonding even if using a low accelerating voltage [225].

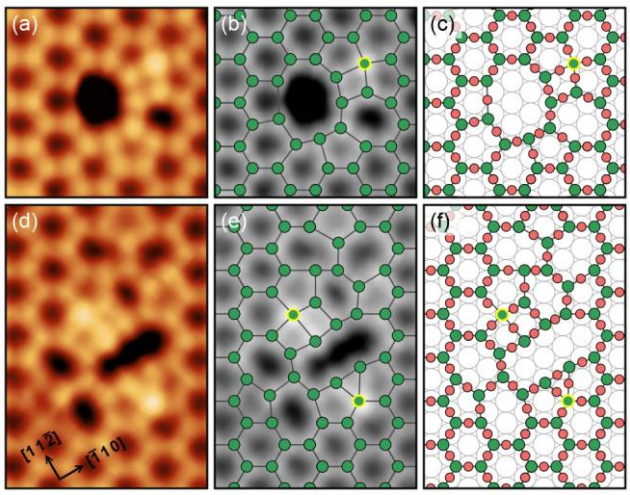

Figure 6-4 STM images and corresponding structural models of two defect domains. An agglomeration of multiple-membered rings was obtained due to fourfold coordinated Nb atoms. (a) 2.7 nm × 2.5 nm, V_s = 0.8 V, I_t = 0.4 nA. (d) 2.7 nm × 3.5 nm, V_s = 0.8 V, I_t = 0.4 nA.

In addition, a single fourfold coordinated Nb atom involved in the atom re-arrangement of a defect domain can give rise to an agglomeration of multiple-membered rings. The defect domain is locally amorphous, which suggests a new way to tune the crystalline order of an oxide thin film. It has been demonstrated that the crystalline order can affect thermal stability [246], absorption [247,248], and catalytic properties of nanomaterials [249,250]. We have demonstrated that threefold coordinated Nb atoms can form a (2 × 2) honeycomb lattice on Au(111) with low defect density. Ideally, an oxide thin film constructed by fourfold coordinated Nb atoms should have a square lattice. Therefore, the crystalline order of a Nb oxide thin film can reach a minimum at a particular concentration of the fourfold coordinated Nb atoms, probably at 50%. In this way, the crystalline structure of the Nb oxide thin film can be regulated, which is similar to the crystalline-vitreous interface in the 2D silica [251].

6.4 Fourfold coordinated Nb atoms in large vacancies and reconstructed edges

It is common for a 2D thin film with a honeycomb structure to have its vacancy sites and edges reconstructed [78,87,90]. DV(5-8-5) and DV(555-777) are two solutions to the reconstruction of stoichiometric divacancy (e.g., Nb_2O_3). Fourfold coordinated Nb atoms provide alternative

ways for the defect reconstruction in Nb_2O_3 HC. The 4fold-1spot (and 4fold-5spot) or 4fold-3spot results from the defect reconstruction after the local lattice lost a NbO unit or a Nb atom. This section will discuss the circumstances in large-vacancy and edge reconstructions.

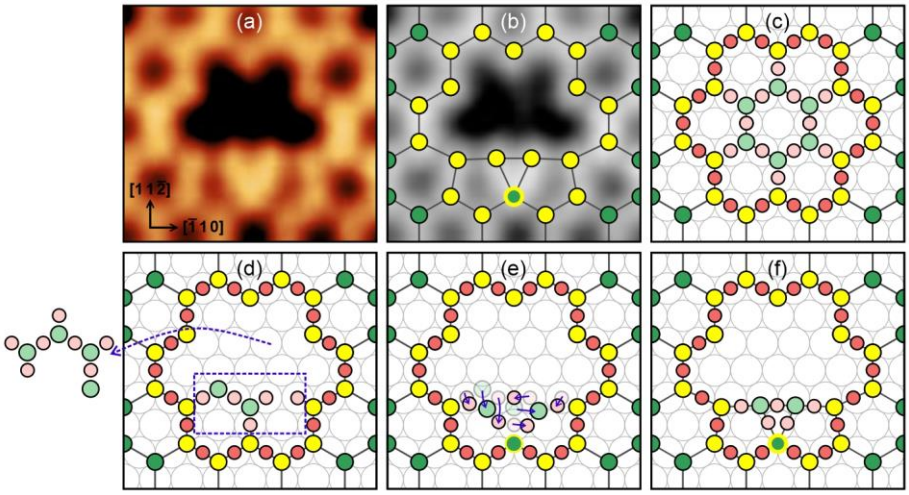

Figure 6-5 (a) STM image of a reconstructed 6-vac defect (2.3 nm × 2.2 nm, V_s = 0.8 V, I_t = 0.7 nA). (b) Nb lattice model superimposed on the STM image in grayscale. (c) Nb_2O_3 HC structural model. The yellow circles (Nb atoms) mark the border of the defect domain. For simplicity, O atoms beyond the defect domain are omitted. O atoms at the border are represented by the red circles. The 6-vac defect is formed by removing the six internal Nb atoms (light green circles). O atoms that bond to these Nb atoms are marked by circles in pink. (d) – (f) Schematics of the defect reconstruction by re-arranging atoms and forming a fourfold coordinated Nb (the green circle with a yellow perimeter).

Figure 6-5 shows an example of the 6-vacancy (6-vac) defect reconstruction achieved by forming a fourfold coordinated Nb atom. We can quickly identify the fourfold coordinated Nb in the STM image according to the brightness and the number of the nearest atoms. In the structural model in Figure 6-5(c), the border of the 6-vac defect domain is depicted by yellow circles. Once the six internal Nb atoms (light green circles) are removed by Ar^+ ion bombardment, a large vacancy site will form a so-called 6-vac defect. Such defect domain undergoes reconstruction, resulting in various reconstrued structures, see Figure 8.11. A reconstructed domain usually involves five- and seven-membered rings with twofold coordinated Nb atoms, which may carry dangling oxygen atoms. Apart from that, defect reconstruction can also be realized by re-arranging the local Nb and O atoms and forming a

fourfold coordinated Nb, as shown in Figure 6-5(d) – (f). A non-stoichiometric Nb_4O_7 unit was removed from the domain, leaving two Nb atoms and five oxygen atoms inside. The Nb atom at the domain border in the middle of the frame can bond to four neighboring O atoms, by which it can be converted from a three coordinated atom to a fourfold coordinated atom with no external O atom involved in this process. It should be noted that this is a tentative model proposed to describe the reconstruction of a large defect domain and the formation of a fourfold coordinated Nb atom. The actual situation could be more complex. For example, a residual oxygen molecule in the chamber may engage in this process.

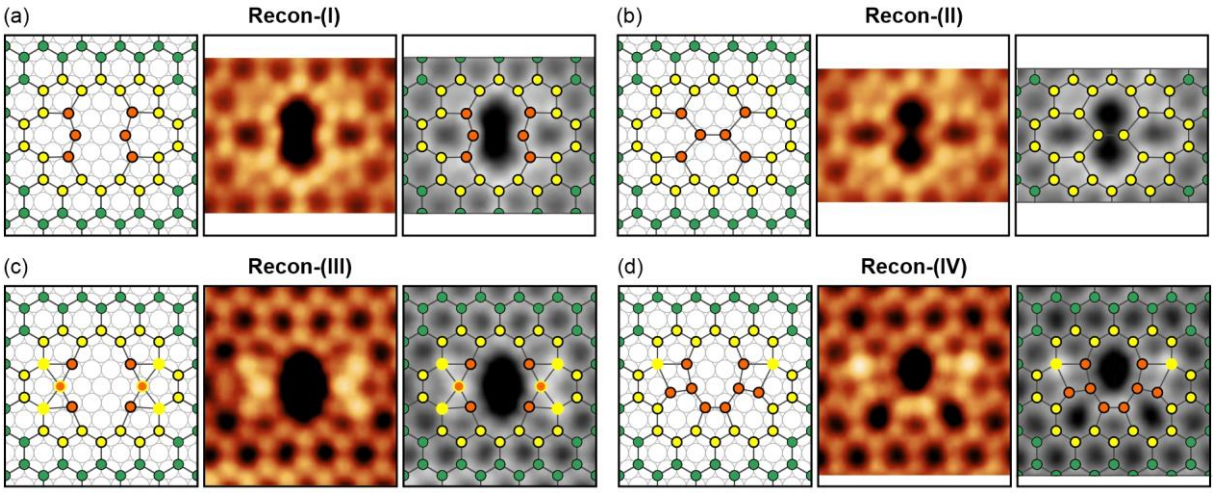

Figure 6-6 Reconstruction of the 10-vac defect domain. (a) Remedied by six Nb atoms forming four five-membered rings and two seven-membered rings (2.9 nm × 2.3 nm, V_s = 0.8 V, I_t = 0.2 nA). (b) Remedied by six Nb atoms forming a tetravacancy defect TV(5555-7777) (2.9 nm × 2.0 nm, V_s = 0.8 V, I_t = 0.2 nA). (c) Remedied by six Nb atoms and four fourfold coordinated Nb atoms converted from threefold coordinated border atoms (2.9 nm × 3.0 nm, V_s = 0.8 V, I_t = 0.4 nA). (d) Remedied by eight Nb atoms and two fourfold coordinated Nb atoms converted from threefold coordinated border atoms (2.9 nm × 2.8 nm, V_s = 0.8 V, I_t = 0.4 nA). The yellow circles mark the border of the 10-vac defect domain; The orange circles represent the remedied Nb atoms; The circles with a yellow perimeter represent fourfold coordinated Nb atoms.

Figure 6-6 shows four reconstruction examples of the 10-vacancy (10-vac) defect domain. The reconstruction way becomes more diverse with the number of vacant sites increasing. We have collected 12 different reconstructed structures with certain symmetric features for the 10-vac defect domain, and the rest eight examples can be seen in Figure 8-14. Similar to the 6-vac defect reconstruction, we can quickly judge whether fourfold coordinated Nb atoms participate

in the reconstruction by the brightness and the coordination number of the protrusions. Figure 6-6(a) and (b) are two reconstructions without the engagement of fourfold coordinated Nb atoms. The critical difference can be seen at the image center. In Recon-(I), the gap between two central protrusions is too wide to sustain the Nb-O-Nb bonding. The reconstructed structure cannot be settled as we are unsure whether dangling oxygen atoms are involved. In Recon-(II), the two central Nb atoms are much closer, which allows an oxygen atom to bridge them and thus becomes threefold coordinated. Interestingly, the atom deficiency is Nb_4O_6, which means this defect is a tetravacancy. A detailed discussion of this structure can be seen in Section 8.3.2. Figure 6-6(c) and (d) show two reconstructions with fourfold coordinated Nb atoms. The reconstructed structures can be well-determined and possess central symmetry.

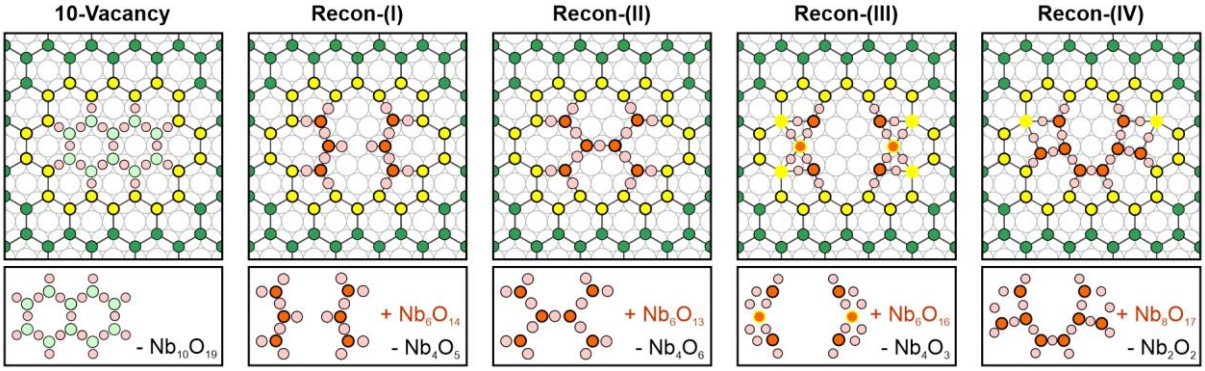

Figure 6-7 Comparison of the atom deficiency of different reconstruction ways. The rightmost frame is an intact honeycomb structure for reference. The yellow circles mark the border of the defect domain; The 10-vac defect results from removing 10 Nb atoms (light green) and 19 O atoms (pink). The other four frames correspond to four reconstructions in Figure 6-6. The remedied Nb and O atoms are represented by orange and pink circles, and the numbers are denoted in orange with a plus sign. The atom deficiency is indicated in black with a minus sign.

We calculated the atom deficiencies of Recon-(I) – (IV), as shown in Figure 6-7. Only the atoms within the yellow border were considered for simplicity. The twofold coordinated Nb atoms in Recon-(I) were assumed to carry dangling oxygen atoms. The atom deficiency was calculated by the number of remedied Nb and O atoms (indicated in orange with a plus sign) subtracting the 10-vac deficiency ($Nb_{10}O_{19}$). The number of remedied Nb atoms in Recon-(I), (II), and (III) are equal, but more remedied O atoms are brought to the defect domain in Recon-(III) as the

fourfold coordinated Nb can bond to more oxygen atoms. The defect domain can be either Nb-deficient or O-deficient with respect to a stoichiometric deficiency ($NbO_{1.5}$). The tetravacancy in Recon-(II) is a stoichiometric defect, while Recon-(I) ($NbO_{1.25}$), Recon-(III) ($NbO_{0.75}$), and Recon-(IV) (NbO) all lead to Nb-deficient defect domains. Figure 6-8 shows a reconstruction with threefold symmetry of a 13-vacancy (13-vac) defect domain. Three Nb atoms at the border became fourfold coordinated. In contrast, the atom deficiency, which can be simplified as $NbO_{2.5}$, shows that this reconstructed defect domain is O-deficient.

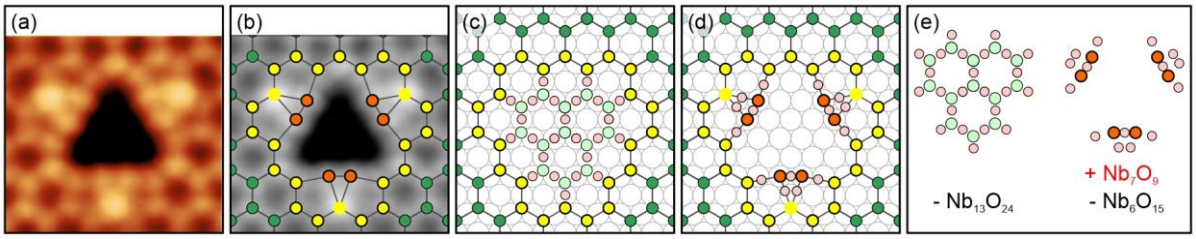

Figure 6-8 (a) STM image of a reconstructed 13-vac defect domain (2.9 nm × 2.6 nm, V_s = 1.0 V, I_t = 0.2 nA). (b) Nb lattice superimposed on the STM image in grayscale. (c) Intact HC lattice with the yellow circles marked the border of the defect domain. 13 Nb atoms (light green) and 24 O atoms (pink) are removed, forming the 13-vac defect. (d) Simplified structural model for the reconstructed defect domain. (e) The calculation for the atom deficiency.

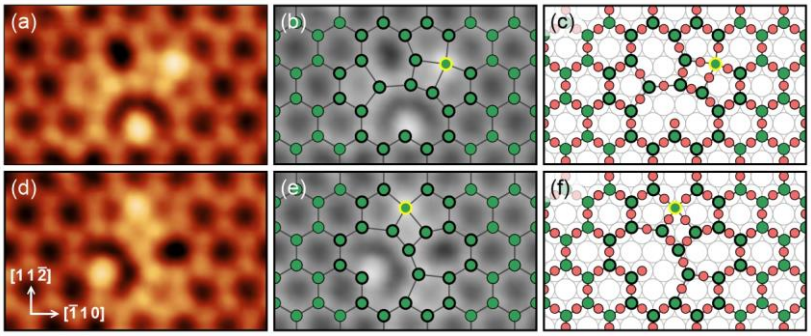

Figure 6-9 STM images of a fourfold coordinated Nb atom flipping inside the HC lattice and corresponding structural models (3.5 nm × 2.1 nm, V_s = 0.8 V, I_t = 0.2 nA).

We observed flipping phenomena of fourfold coordinated Nb atoms during STM imaging at room temperature. Figure 6-9 shows two frames of a fourfold coordinated Nb that flipped back and forth inside the HC lattice. The local Nb-O bonds can open and re-form, followed by a position shift of the fourfold coordinated Nb atom. We can also see a second spot as bright as

the fourfold Nb atom, but it is twofold coordinated in the STM image. The high intensity is probably due to a dangling O atom or an adatom. Here we attributed this phenomenon to a dangling O atom protruding inwards in the structural model [Figure 6-9(c), (f)].

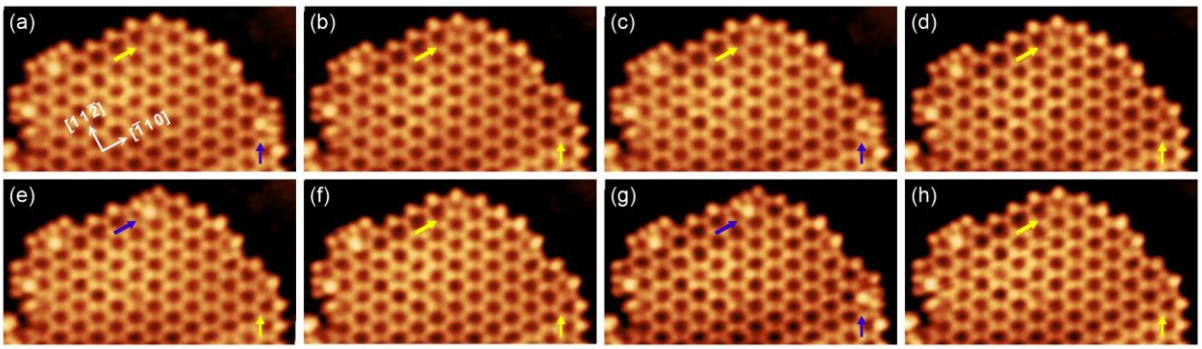

Figure 6-10 STM image series of a Nb_2O_3 HC edge (8.0 nm × 4.5 nm, V_s = 1.0 V, I_t = 0.6 nA). The arrows indicate two sites with flipping fourfold coordinated Nb atoms. The yellow arrows indicate the normal sites with threefold coordinated Nb atoms; the blue arrows indicate the occurrence of a fourfold coordinated Nb atom.

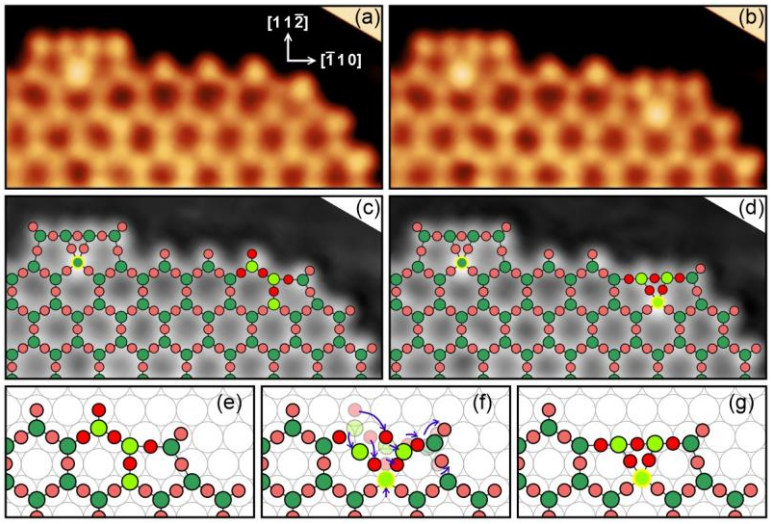

Figure 6-11 (a), (b) Close-ups of the top-left side of Figure 6-10(a), (e) (frame size: 5.0 nm × 2.4 nm). (c), (d) Structural models superimposed on (a), (b) in grayscale. Twofold coordinated Nb atoms are assumed to carry dangling oxygen atoms. (e) – (g) Schematics of a local structure transition achieved by atom re-arrangement.

The fourfold coordinated Nb atom can also participate in the Nb_2O_3 HC edge reconstruction by forming individual 535-6 units without a periodic arrangement. A detailed description and comparison with the three-membered rings in Ti_2O_3 HC edge reconstruction can be seen in Section 7.3.3. Figure 6-10 shows successive STM images of a Nb_2O_3 HC edge, among which

we can observe four fourfold coordinated Nb atoms at most in frame (g): two are on the right side of the image and remain unchanged; the third one is on the top and the fourth one is on the left side. The bright spots at these two sites disappeared (marked by yellow arrows) and re-appeared (marked by blue arrows) in the image series, indicating the transition between the fourfold coordination and the threefold coordination. This is quite different from Figure 6-9, in which the fourfold coordinated Nb just flipped but did not disappear.

The flipping phenomenon at the edge allows us to propose a transition model, as shown in Figure 6-11. It is assumed that all the terminal Nb atoms at the honeycomb edge bond to three O atoms, so dangling O atoms are attached to the twofold coordinated Nb atoms in Figure 6-11(c) – (g). Similar to the analysis in the defect reconstruction in Figure 6-5, the transition at the edge can be achieved by atom re-arrangement without involving any external Nb or O atoms. This is more convincing than the scenario in the defect reconstruction because of the flipping phenomena in the STM image series. It can be concluded that the elastic Nb-O bonding can open and form at room temperature, and the formation of a fourfold coordinated Nb at the edge costs relatively low energy. We speculated that the flipping was induced by tip scanning, which could affect the atom configuration but did not introduce new atoms or destroy the surface.

6.5 Fourfold coordinated Nb atoms in domain boundaries

We have presented single fourfold coordinated Nb atoms observed from defect domains and the HC edge. In this section, we will show a collection of fourfold coordinated Nb atoms that participated in domain boundaries (DB) of Nb_2O_3 HC. A detailed discussion of DB can be seen in Section 8.4. Basically, Nb_2O_3 HC possesses a variety of structural solutions to zigzag-oriented (Z1, Z2) and armchair-oriented (A1, A2) domain boundaries. The number “1” or “2” means two domains without or with a lateral shift along the boundary extension direction. Due

to the capability of forming fourfold coordinated Nb atoms, Nb_2O_3 HC has alternative ways to fill the boundary gaps compared with Ti_2O_3 HC, thus having some unique structural solutions.

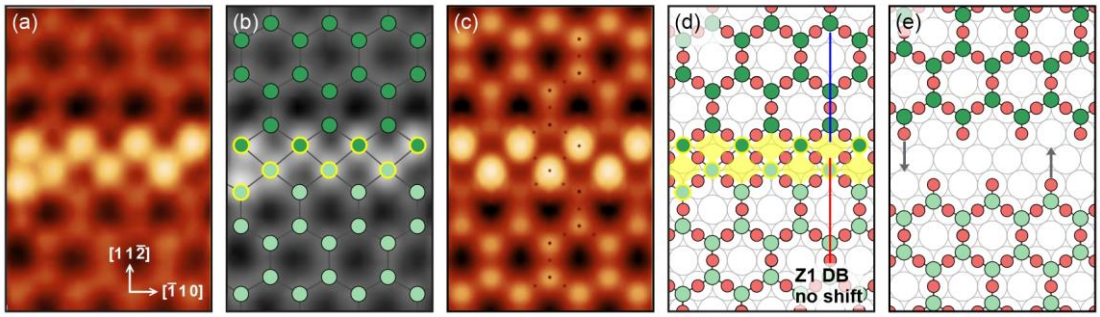

Figure 6-12 (a) Experimental STM image of a Z1-44 DB (V_s = 1.0 V, I_t = 0.2 nA). (b) Nb lattice superimposed on (a) in grayscale. (c) DFT-simulated STM image (V_s = 0.8 V). (d) Structural model of the Z1-44 DB. Green: Nb atoms; red: O atoms. The repeated units are highlighted in yellow. The blue and red lines indicate that it is a Z1 DB with no lateral shift. (e) Schematic of two HC domains with dangling O atoms approaching each other. Frame size: 2.0 nm × 3.0 nm.

Figure 6-12 displays a Z1 DB with a repeating unit of 4-4 (four-membered ring), so-called the Z1-44 DB (see Section 8.4.2). The fourfold coordinated Nb atoms at the boundary are arranged up and down alternatively. The leftmost bright spot in Figure 6-12(a) breaks the periodicity and can be seen as a point defect. Figure 6-12(c) is a DFT-simulated STM image of the Z1-44 DB, which can well reproduce the experimental observation. We proposed a scenario for the Z1-44 DB formation: when two domains with dangling O atoms are approaching each other due to ripening [Figure 6-12(e)], two oxygen rows are the first batch of atoms to arrive at the boundary. The giant repulsion could lead to a position shift of the oxygen atom, resulting in a configuration of -Nb-O-Nb-O- by forming new bonding. Nb atoms at the boundary may adjust their positions to minimize the lattice strain, and each of them is surrounded by four O atoms thus becoming the fourfold coordinated Nb with a higher oxidation state. Finally, the rhombus-shaped repeated units are created and extended along the [$\bar{1}$10] direction. It should be noted that the Au-supported Nb_2O_3 HC monolayer has a rumpled structure with the O layer extended outwards. The proposed model is just a tentative model in order to correlate the structural feature with the chemical bonding. Similar to the tentative models for edge and defect reconstructions in

Chapter 7 and Chapter 8, it is challenging to determine O atom behaviors and elucidate the real formation mechanisms. They could be simpler than the proposed models, or much more sophisticated if our assumption of the dangling bond is invalid or adatoms are involved.

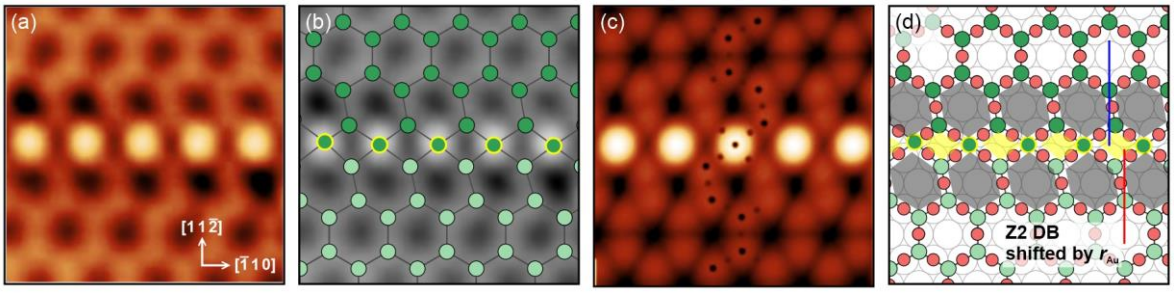

Figure 6-13 (a) Experimental STM image of a Z2-646 DB (V_s = 0.8 V, I_t = 0.5 nA). (b) Nb lattice superimposed on (a) in grayscale. (c) DFT-Simulated STM image (V_s = 0.8 V). (d) Structural model of the Z2-646 DB. The repeated units are highlighted in grey (distorted hexagons) and yellow (four-membered rings). The blue and red lines indicate that it is a Z2 DB with a lateral shift by r_{Au} = 1.44 nm. Frame size: 2.7 nm × 2.7 nm.

Figure 6-13 shows the Z2-646 DB with fourfold coordinated Nb atoms arranged in a line and distorted hexagons at both sides. The two domains have a lateral shift by half of the Au-Au distance (2.88 nm) along the [1$\bar{1}$0] direction in (111) plane [Figure 6-13(d)]. This STM image is also displayed in Figure 8-22 when discussing the DB solutions. Figure 6-13(c) is a DFT-simulated STM image of the Z2-646 DB. The resulting distortion in the vicinity of the fourfold coordinated Nb atom row matches the experimental observation to a good degree. Such brightly protruding domain boundaries were observed in silicene on Ag(111) as well [107]. However, the silicene domain boundaries showed strong dependence on tunneling bias. They appeared as protrusions at a sample bias (1.5 ~ 2 V) but converted to depressions at a negative bias. In contrast, fourfold coordinated Nb atoms always appear as protrusions with elevated brightness at both positive and negative biases, see Figure 6-1(c), (d).

6.6 Conclusion

To sum up, we are able to map the oxidation state of Nb atoms in Nb_2O_3 HC monolayers at the atomic level according to the contrast difference and the coordination number in STM images. A Nb atom with fourfold coordination to O atoms appears much brighter than a threefold HC lattice Nb, and does not show a sample bias dependence. Considering the charge transfer to the Au substrate, its actual oxidation state is higher than +4.

The exact value of the charge redistribution was not given in this chapter as the relevant theoretical calculations are still in progress. Similar bright spots with fourfold coordination were also observed in Pd-supported (2 × 2) V_2O_3 honeycomb monolayer but not found in Au-supported (2 × 2) Ti_2O_3 honeycomb. This can be explained by the electron configuration of the transition metal atoms. V and Nb possess five valence electrons and thus have the highest oxidation state of +5. While a Ti atom only has four valence electrons, limiting its oxidation state to +4. The actual oxidation of a metal atom in the honeycomb lattice should be higher than +3 due to the large charge transfer to the substrates. Therefore, V and Nb can further bond to a fourth oxygen atom, but a Ti atom does not have additional electrons to form new bonding.

In this chapter, we also demonstrated that fourfold coordinated Nb atoms play a significant role in defect and edge reconstructions as well as the domain boundary formation. They give rise to diverse reconstructed structures and alternative solutions to domain boundaries. We proposed several tentative models to correlate structural properties to chemical bonding. However, it is challenging to elucidate the actual reconstruction process or the formation mechanism without support from theoretical studies.

Chapter 7 Edge structures of Nb_2O_3 and Ti_2O_3 honeycomb monolayers

7.1 Introduction

Edge structure has a significant impact on the physical and chemical properties of graphene and graphene-like 2D materials [113]. Extensive studies including experimental characterization and theoretical calculations have been conducted on graphene in terms of the structural nature of edge, edge reconstruction, and edge physical properties [110,114,116,117,225]. In contrast, there are fewer edge studies on metal oxide monolayers with a honeycomb structure as an oxide contains at least two elements, which significantly increases the system complexity.

In the present work, we focus on Au-supported Nb_2O_3 and Ti_2O_3 honeycomb monolayers. Due to the substrate effect, they exhibit good conductance and thermal stability during STM imaging at room temperature. Similar to the graphene edge, the as-cut zigzag edge and the armchair edge of Nb_2O_3 or Ti_2O_3 monolayers will undergo edge reconstruction to form more stable edge structures under certain conditions. We found that the resulting structural properties are distinct from graphene, and the reconstruction is greatly affected by the Au substrate. For example, the zigzag (57) and armchair (677) are two typical reconstructed edges that have been experimentally confirmed and theoretically studied [119]. But neither of the two types was observed on the Au-supported Nb_2O_3 or Ti_2O_3 honeycomb monolayers in our studies. This chapter aims to contribute to the understanding of edge structures of graphene-like 2D oxide materials as well as the film-substrate interaction.

7.2 Nomenclature and model building for the edge structures

In this chapter, the nomenclature rule of the edge structures is as follows. We classify all types of the edge structures into two groups according to the base: pristine zigzag (Z) and armchair (A), using the symbol of Z-XX-X or A-XX-X to refer to the edges of a honeycomb monolayer. The numbers after the first hyphen indicate the edge polygons in an edge unit cell. The pristine zigzag and armchair are denoted by Z-66 and A-66, even if the smallest unit cell of the zigzag edge is a single hexagon. The Klein edge is formed by an array of single atoms extending from a zigzag edge [109,110], thus denoting as Z-K. The extending atoms can form pentagons by two atoms approaching each other, which can be considered as a reconstruction based on the Klein edge. We call it reconstructed Klein edge and denote it as Z-rK.

The symbol after the second hyphen is numbered with Roman numerals to distinguish reconstruction edges with the same repeated unit but different geometric features. For example, we found that the distance between a terminal edge atom and the nearest atom in the Z-646 edge has two values (3.49 Å and 2.25 Å) after careful calibration and calculating the average from several samples. Therefore, we further classify the Z-646 edge into Z-646-I and Z-646-II (see Figure 7-7). For an embedded Nb_2O_3 honeycomb monolayer, the edge structure is essentially the same as the free counterpart. However, due to its growth mode and the fcc stacking sequence of Au(111), the terminal Nb atoms at the edge can occupy two different sites for the same type of edge structure. We classify them according to the relative crystalline orientation denoted as Z1 or Z2, and the detailed description can be seen in Section 7.3.2.

STM images are displayed in the amber lookup table by convention. In order to clarify the edge structure, only Nb or Ti lattice is superimposed on the grayscale STM image taken at positive sample bias. Theoretically, it is feasible to experimentally determine the configuration of O atoms at negative sample bias. Obtaining the STM images of the same site at both positive and

negative bias will help to determine the structure precisely. Successful examples can be seen in Figure 7-11. However, in most cases, changing the sample bias from a positive value to a negative value probably gives rise to changes in the geometry or the electronic structure of the tip. Consequently, the atomic resolution may immediately be lost and can hardly be restored when going back to a positive bias. Therefore, it is still very challenging to determine the arrangement of oxygen atoms by applying negative biases during STM imaging. In particular, the same Nb lattice may possess various O lattices under different oxygen chemical potentials. The inhomogeneity of materials may also lead to the coexistence of multiple O lattices.

In this chapter, oxygen lattice models are proposed to help elucidate possible edge configurations of Nb_2O_3 honeycomb monolayers. Theoretical work that calculates the formation edge energy of different models will tell us which type of atomic configuration is more stable under a specific oxygen chemical potential. We have received some preliminary calculation results from our collaborators, Jacek and Claudine, from CNRS-Sorbonne Université, Paris. The calculations are still proceeding, so the results are not presented in this thesis. Experimental observations can also support arguments regarding edge stability. For example, we found that the Z-K edges appear more abundantly than the Z-66 edge in the Nb_2O_3 emb-HC, and we did not observe any armchair edge. So a general conclusion can be drawn without any doubt that Z-K is a more stable edge structure of the Nb_2O_3 emb-HC.

In short, this chapter discusses various edge structures of Nb_2O_3 and Ti_2O_3 honeycomb monolayers grown on the Au(111) substrates. We also made a comparison between Nb_2O_3 and Ti_2O_3 honeycomb edge in terms of the reconstruction. It is significant to understand the different reconstruction behaviors and structural properties of the two materials with the same epitaxial structure on the Au(111) surface. New parameters *density of edge atoms* and *density difference* δD are introduced to compare the degree of reconstruction quantitatively.

7.3 Results and discussion

7.3.1 Nb_2O_3 free-HC

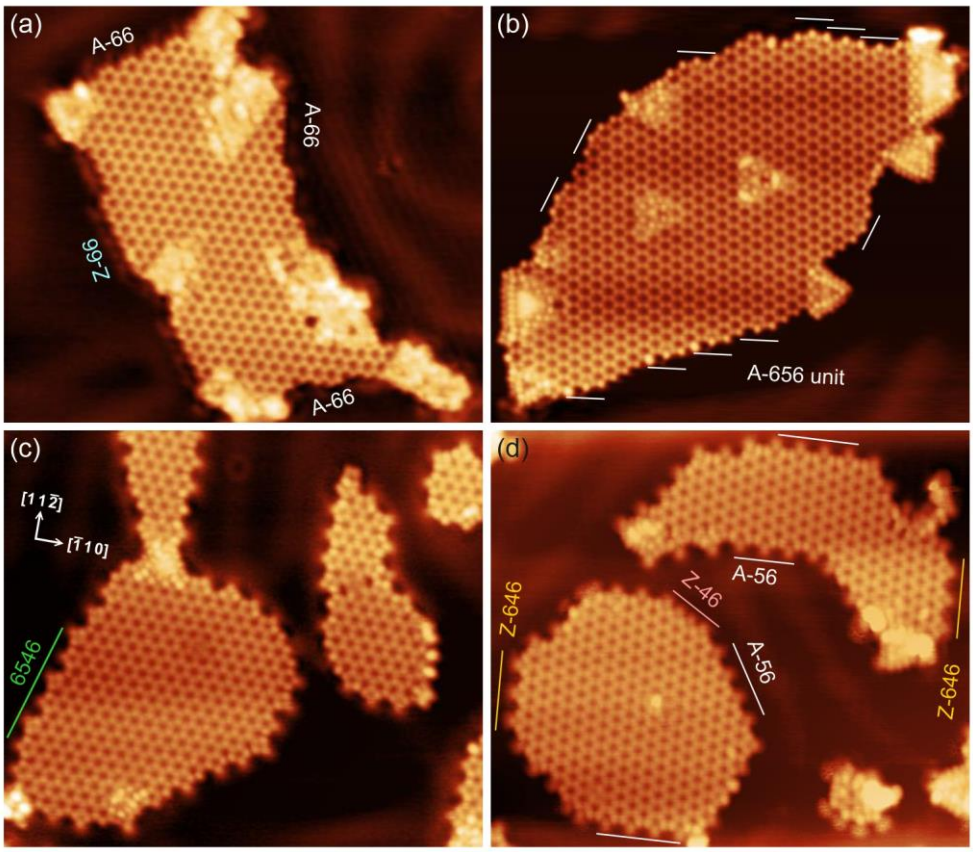

Figure 7-1 STM images (19 nm × 16.5 nm) of Nb_2O_3 free-HC islands prepared by different conditions. (a) 1 × 10^{-6} Pa O_2, annealing at 600 ℃ for 1 h (V_s = 0.9 V, I_t = 0.25 nA). (b) Annealing in UHV at 800 ℃ for 1 h (V_s = 0.7 V, I_t = 0.6 nA). (c), (d) 1 × 10^{-6} Pa O_2 at 350 ℃ for 30 mins. The green line with repeated unit 6546 in (c) is not regarded as a common reconstruction type of Nb_2O_3 free-HC (c: V_s = 1.0 V, I_t = 0.3 nA; d: V_s = 1.05 V, I_t = 0.1 nA).

The preparation of Nb_2O_3 free-HC has been described in Section 5.6.2. Nb_2O_3 free-HC can be obtained by post-oxidation in 1 × 10^{-6} Pa and annealing at a temperature ranging between 300 – 700 ℃. The (2 × 2) Nb_2O_3 honeycomb structure does not decompose after annealing at up to 900 ℃ in UHV, and can remain stable at a high oxygen pressure up to 1 × 10^{-4} Pa. However, the annealing temperature, duration, and oxygen pressure strongly affect the characteristics of the honeycomb islands, one of which is the edge structure. Figure 7-1 shows the STM images of Nb_2O_3 free-HC obtained from different preparation conditions. Figure 7-1(a) was obtained from a sample annealed at 600 ℃. The island edges were composed of regular A-66 and Z-66

without reconstruction. When the sample was annealed at 800 ℃, free-HC could grow into larger islands due to ripening. We can barely see a long A-66 or Z-66 in Figure 7-1(b). Instead, a repeated unit A-656 can be frequently found at the edges without a periodic arrangement along any direction. By contrast, annealing at a lower temperature (350 ℃) gives rise to different types of edge reconstruction. In Figure 7-1(c) and (d), all the free-HC islands were completely reconstructed by forming non-hexagonal rings at the edges with certain periodicities. Reconstructed edges, including A-56, Z-46, and Z-646, are marked in Figure 7-1(d) with their extension directions.

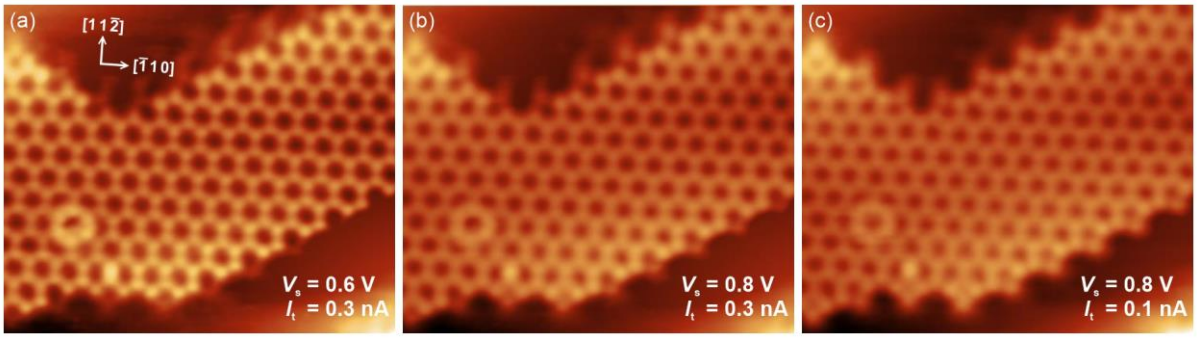

Figure 7-2 STM images (8.4 nm × 7 nm) of the same region using different imaging conditions. Terminal Nb atoms are barely seen in (a), while the edge in (c) can be assigned to A-56.

It is worth noting that the terminal protrusions, which should be Nb atoms as the STM images were taken at positive bias, look faint compared with the HC lattice Nb atoms. We investigated these terminal protrusions by altering imaging conditions, and the results are displayed in Figure 7-2. According to Formula (3-19) – (3-21), the tip-sample distance should be smaller when using a lower sample bias but keeping the current constant, so the tip approaches the surface. This can explain that the resolution in Figure 7-2(a) is much better than that in Figure 7-2(b) as each lattice Nb atom is more clearly resolved with higher contrast. On the contrary, the terminal atoms are almost invisible in Figure 7-2(a), so the edges seem to be regular A-66 edges. When keeping the bias the same but altering the tunneling current, a smaller current will drive the tip away from the sample surface. This can explain why the resolution of lattice Nb atoms becomes

worst in Figure 7-2(c) compared with (b). However, the signal intensity of the terminal atoms is much higher in Figure 7-2(c), so one can easily assign the edge to an A-56 reconstructed edge. Therefore, we can conclude that a relatively higher sample bias and a lower tunneling current is favorable for resolving the terminal atoms of reconstructed edges.

It should be noted that the tunneling current in the STM is proportional to the tip-sample distance as well as the sample's LDOS according to the Tersoff-Hamann Approximation. The dramatic changes in the visibility of terminal atoms point to a significant difference in the electronic structure between terminal Nb atoms and lattice Nb atoms. This phenomenon was not observed when imaging the A-656 repeated units created by high-temperature annealing. Instead, the terminal atoms of the pentagon in A-656 units in Figure 7-1(b) look brighter than the lattice atoms (a close-up can be seen in Figure 7-10). Such discrepancy in the terminal atoms suggests that the reconstruction mechanisms and the atom configurations with O atoms involved are probably different under different oxygen chemical potentials.

Experimental results have confirmed seven common edge structures for Nb_2O_3 free-HC. They can be classified into two groups: the A-based group including A-66 and A-56, and the Z-based group including Z-66, Z-46, Z-646, Z-K, and Z-rK. All of them possess a periodicity either along $[\bar{1}10]$ or $[11\bar{2}]$ on Au(111), or along the equivalent directions with a rotation angle of 60° against the two directions due to the threefold symmetry of the substrate (Figure 2-25). Reconstructed edges with an intermediate orientation, such as the repeated unit 6456 in Figure 7-1(c), were not regarded as common edge types. Figure 7-3 – Figure 7-8 show the STM images and corresponding Nb lattice models for the seven edge structures. The complete Nb_2O_3 honeycomb structures with possible O lattice models are also proposed in these figures.

Figure 7-3 and Figure 7-4 show the A-66 and Z-66 edges, respectively. The Nb lattices for these two basic edge structures are well determined. O lattice models in the second row are presented

by gradually adding dangling O atoms at the terminal Nb atom at the edge until all the Nb atoms bond to dangling O atoms. O lattice models for the reconstructed edges are built in the same way but are not fully presented in the corresponding figures.

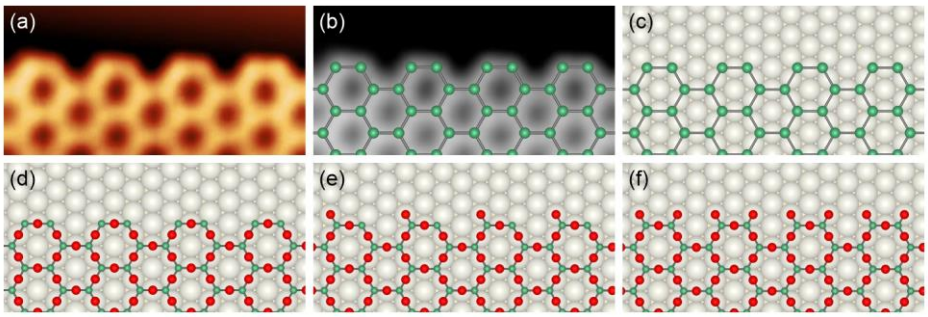

Figure 7-3 (a) STM image of an A-66 edge (4 nm × 2 nm, V_s = 0.75 V, I_t = 0.5 nA). (b) A Nb honeycomb lattice superimposed on the STM image in grayscale. (c) The Nb honeycomb lattice placed on the Au(111) substrate. (d) – (f) Possible models for the O atom configuration at the A-66 edge: (d) no dangling O atom; (e) adding one O atom on a terminal Nb atom in a hexagon; (f) adding two O atoms on both terminal Nb atoms. Green balls represent Nb atoms; red balls represent O atoms; large white balls represent the L_1 Au atoms.

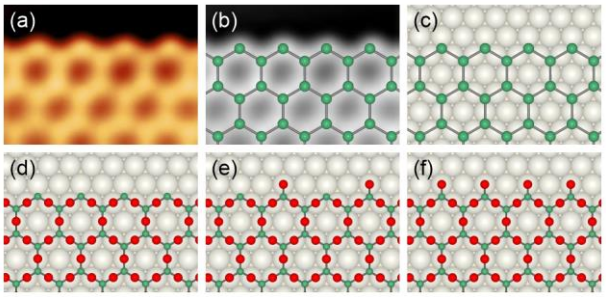

Figure 7-4 (a) STM image of a Z-66 edge (2.6 nm × 1.9 nm, V_s = 0.85 V, I_t = 0.25 nA). (b) A Nb honeycomb lattice superimposed on the STM image in grayscale. (c) The Nb honeycomb lattice placed on the Au(111) substrate. (d) – (f) Possible models for the O atom configuration at the Z-66 edge: (d) no dangling O atom; (e) O atoms are alternatively added on terminal Nb atoms; (f) all terminal Nb atoms carry dangling O atoms.

Figure 7-5 shows the STM image and models for the A-56 edge. The distance between the terminal atoms and the nearest lattice atoms was measured to determine their locations on the substrate. The distance (d = 2.4 Å) indicates that the locations of terminal Nb atoms are almost at on-top sites. If one only considers the height difference, these terminal Nb atoms should be higher than the lattice Nb atoms that sit at the hollow sites, thus being closer to the tip and brighter in the STM images. However, this is in conflict with what we observed in the

experiment. In fact, the terminal atoms look faint, and the visibility depends on the imaging condition (Figure 7-2). In the above discussion, we pointed out that the electronic structure of the terminal edge atoms may differ from that of the lattice atoms. Here we give another proposal: the terminal edge atoms may substitute the L_1 Au atoms below, thus being lower than the honeycomb lattice Nb atoms in the vertical direction. The top view and side view of the new model can be seen in Figure 7-5(f) and (g).

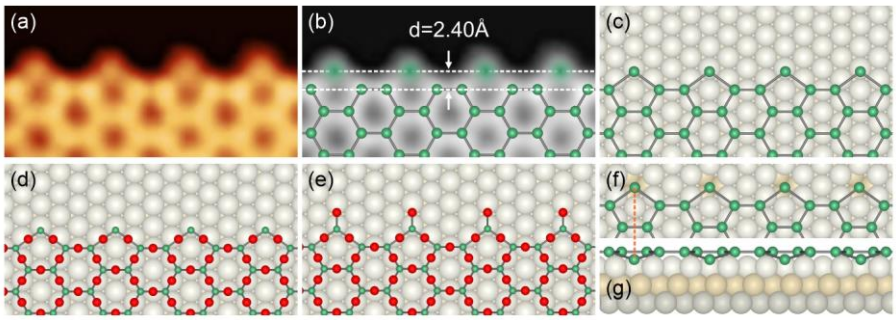

Figure 7-5 (a) STM image of an A-56 edge (3.9 nm × 2 nm, V_s = 1.0 V, I_t = 0.1 nA). (b) A Nb honeycomb lattice superimposed on the STM image in grayscale. (c) The Nb lattice placed on the Au(111) substrate. (d) and (e) Possible models for the O atom configuration at the A-56 edge: (d) no dangling O atom; (e) adding one O atom on terminal Nb atoms; (f) An alternative model of the Nb lattice, in which the terminal atoms substitute the below the L_1 Au atoms (top view). (g) Side view of the model in (f). The Nb lattice forms a rumpled structure.

Furthermore, we assumed two possible geometries for the terminal Nb atoms. One is that the terminal Nb atoms connect to the honeycomb island by Nb-O-Nb bonding and form a rumpled structure. The other is that terminal Nb atoms accumulate and are constrained along the island edge, they do not bind to the honeycomb lattice. The latter circumstance is postulated based on the strong dependence on the imaging condition, which is also found when investigating *M* – induced ring patterns on the Au(111) surface (*M* = Nb, Ti, V, and Mn, see Chapter 4).

We applied this assumption when building the structural models for Z-46 (Figure 7-6) and Z-646 (Figure 7-7). It works particularly well with Z-46. We found that the Z-46 can be classified into two subgroups depending on the distance *d* between the terminal edge atoms and nearest lattice atoms: Z-46-I with a larger *d* (2.96 Å) and Z-46-II with a smaller *d* (2.22 Å). Figure

7-6(e) – (g) show the schematics of the proposed structures, in which the Nb atoms in the second row become fourfold coordinated if the terminal Nb atoms connect to the honeycomb lattice.

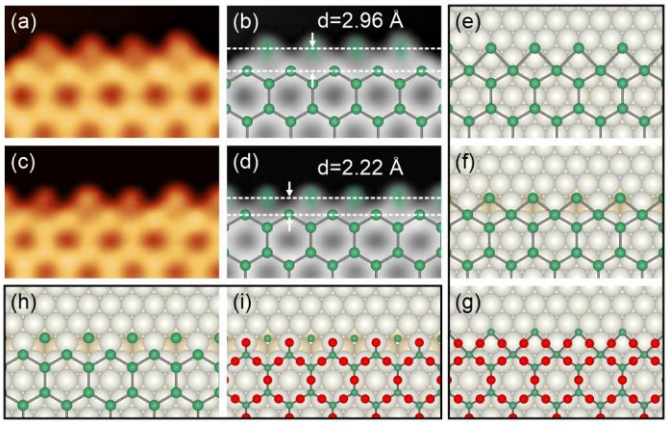

Figure 7-6 (a) STM image of the Z-46-I edge (2.8 nm × 1.8 nm, V_s = 1.0 V, I_t = 0.3 nA). (b) Nb honeycomb lattice superimposed on the STM image in grayscale. (c) STM image of the Z-46-II edge (2.8 nm × 1.8 nm, V_s = 1.05 V, I_t = 0.1 nA). (d) Nb honeycomb lattice superimposed on the STM image in grayscale. (e) and (f) The Nb honeycomb lattice of Z-46-I and Z-46-II (substituted model) on the Au(111) substrate. O atoms are depicted in (g). Noting that the Nb atoms at the second row are fourfold coordinated in the models. (h) The terminal Nb atoms substitute Au atoms below are not bound to the honeycomb lattice. (i) A proposed O lattice model in which O atoms are only possessed by the honeycomb lattice.

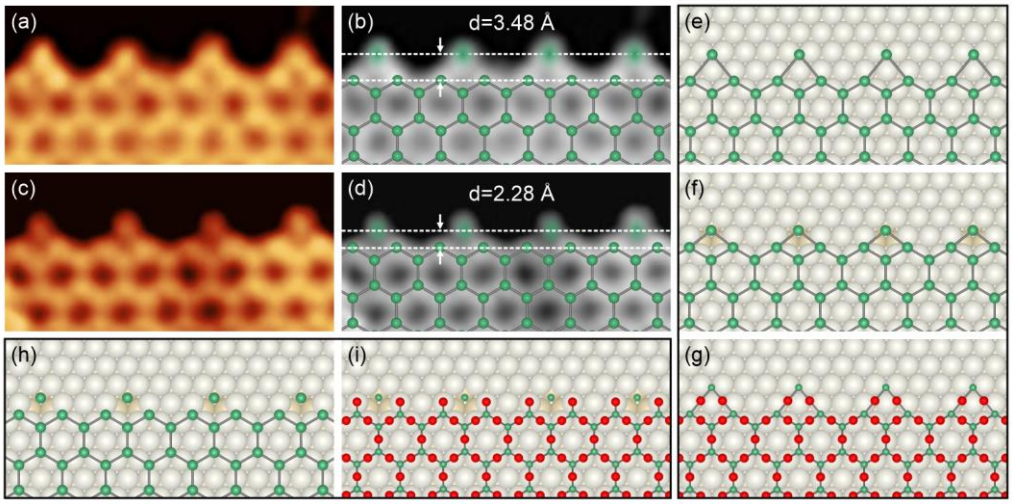

Figure 7-7 (a) – (g) STM images (4.4 nm × 2.1 nm, V_s = 1.0 V, I_t = 0.3 nA) and models of Z-646-I (d = 3.48 Å) and Z-646-II (d = 2.28 Å). Unlike Z-46, the Nb atoms at the second row in the models can remain the threefold coordination. (h) The terminal Nb atoms substitute Au atoms below but are not bound to the honeycomb lattice. (i) A possible O lattice model in which O atoms are only possessed by the honeycomb lattice.

Experimental results show that Nb atoms are able to be fourfold coordinated with a higher oxidation state, which has also been confirmed by theoretical calculation (see Chapter 6). The

typical feature of a fourfold coordinated Nb is a great enhancement of the local intensity compared with the threefold coordinated Nb in the honeycomb lattice. But this feature was not revealed in the STM images in Figure 7-6(a) or (b). Therefore, the proposed models in Figure 7-6(e) – (g) are less likely to be proper structures for Z-46. By contrast, models with terminal Nb atoms that substitute Au atoms below and do not connect to the honeycomb are more in line with the STM images, as shown in Figure 7-6(h) and (i).

Similar STM results were obtained from Z-646 edges [Figure 7-7(a) and (c)]. Z-646 also has two subgroups: Z-646-I and Z-646-II. Compared with Z-46, the main difference is that, when connecting the terminal atoms to the honeycomb lattice, Nb atoms in the second row in the models in Figure 7-7(e) – (g) can remain threefold coordination due to the reduction of half terminal atoms. So the proposed models in (e), (f), and (h) are reasonable.

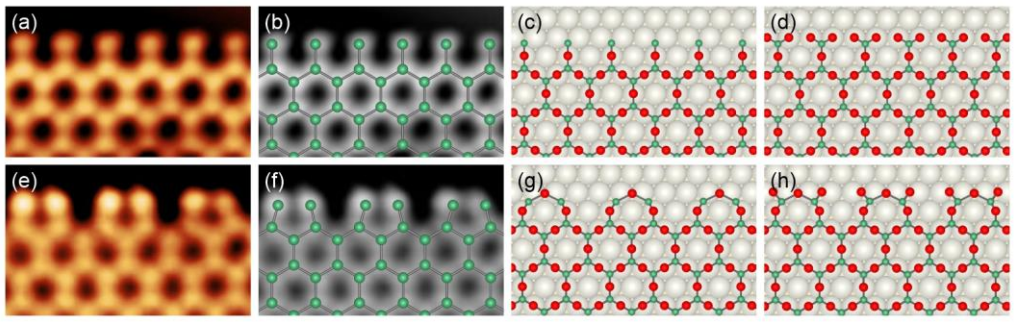

Figure 7-8 (a) STM image of a Klein edge (3.3 nm × 2 nm, V_s = 0.8 V, I_t = 0.4 nA). (b) A Nb honeycomb lattice superimposed on the STM image in grayscale. (c), (d) Possible models for the O configuration at the edge: (c) no dangling O; (d) two dangling O atoms connected to each terminal Nb atom. (e) STM image of a reconstructed Klein edge (3.3 nm × 2 nm, V_s = 0.7 V, I_t = 0.5 nA). (b) A Nb honeycomb lattice superimposed on the STM image in grayscale. (g), (h) Possible models for the O configuration: (g) two terminal Nb atoms are bridged by an O atom without dangling O atom; (d) each terminal Nb carries one dangling O atom.

Klein edge (Z-K) and reconstructed Klein edge (Z-rK) were observed in Nb_2O_3 free-HC, as shown in Figure 7-8(a) and (e). They never showed up in small islands like the other edge structures in the free-HC; they only appeared at the Au substrate steps and extended along the step edges. Terminal Nb atoms in a Z-rK edge no longer remain parallel as that in the Z-K edge.

Instead, every two atoms approach each other by an opposite position shift, which is probably induced by the formation of Nb-O-Nb bonding, see models in Figure 7-8(g) and (h).

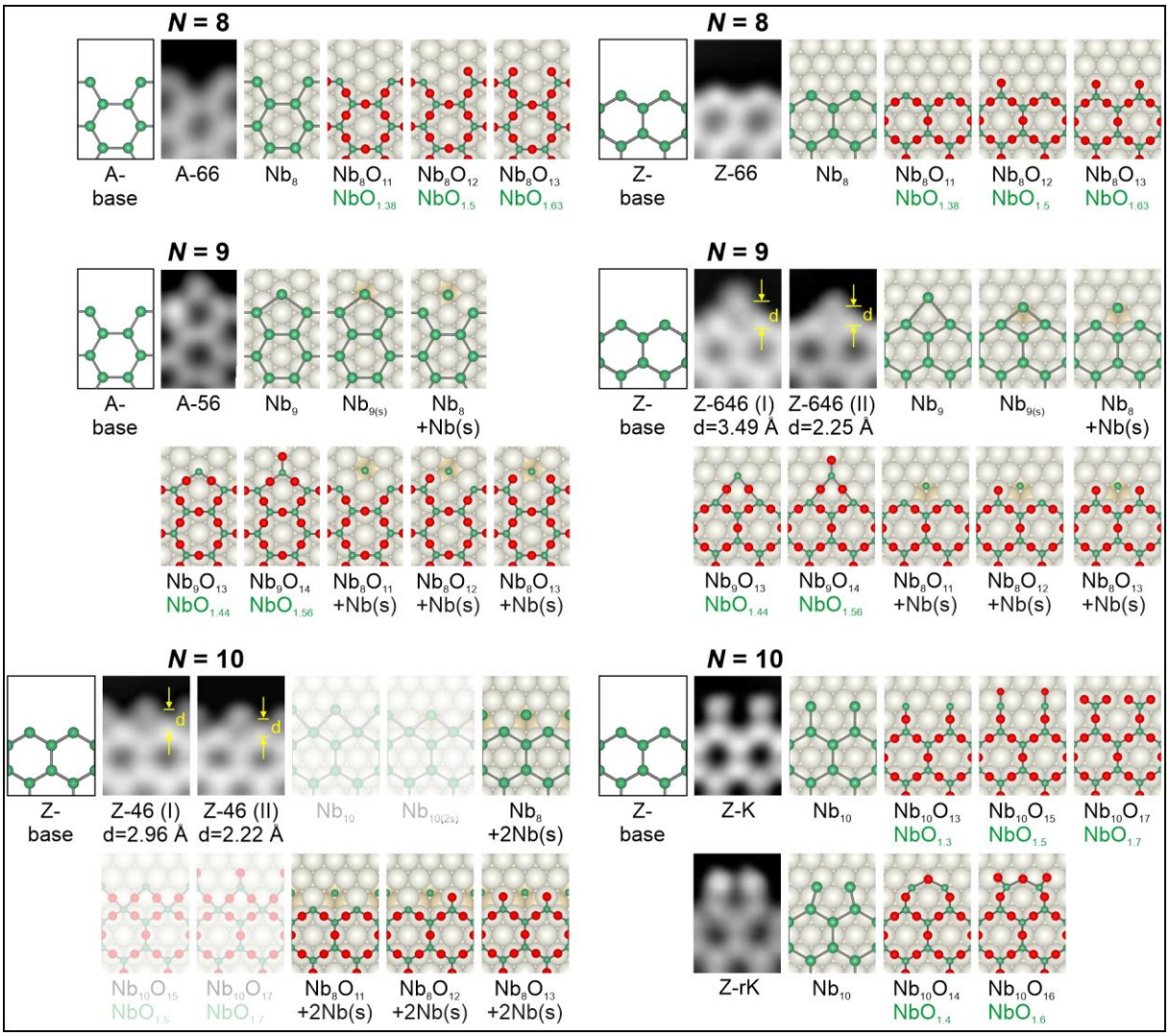

Figure 7-9 Summary of the unit cells of seven common edge structures of the Nb_2O_3 free-HC and corresponding structural models with stoichiometries indicated below.

We summarized the unit cell of the seven common edge structures and arranged them by increasing the total number of the Nb atoms (*N*) in Figure 7-9. As base structures, A-66 and Z-66 should be unified to possess equal Nb atoms in a unit cell. Possible Nb lattice models are listed, except the models with fourfold coordinated Nb in Z-46, which are set to be half-transparent. Complete HC structures with O lattice are also provided below the Nb lattice models, together with the stoichiometries of the unit cells. If the terminal Nb atoms are assumed

to be bound to the HC lattice, no matter they substitute the Au atoms below or not, they have equal O atoms in a unit cell. If the terminal atoms are separated from the HC lattice, they are denoted by, for example, "+Nb(s)" in the unit cell. The corresponding O lattice models and complete HC structures are consistent with A-66 or Z-66.

From the summary we can see that Z-46, Z-K, and Z-rK have the most Nb atoms in a unit cell (N = 10). The local edge stoichiometry can be deviated from $NbO_{1.5}$, ranging between $NbO_{1.3}$ and $NbO_{1.7}$. Both two extrema are found in the structural models of Z-K.

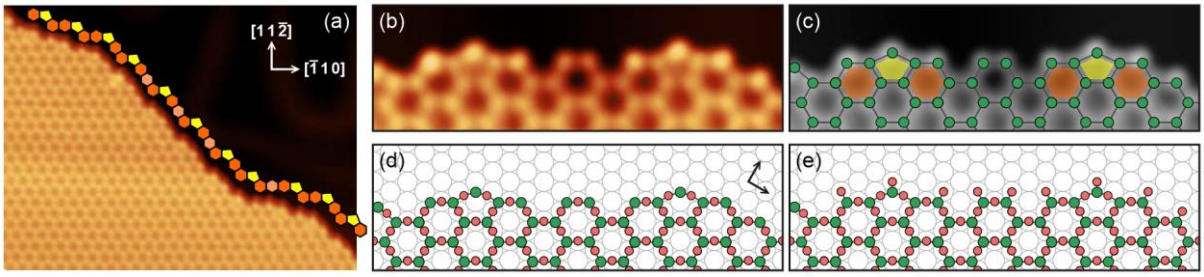

Figure 7-10 (a) STM image of an as-prepared Nb_2O_3 sample further annealed at 900 °C in UHV (16 nm × 12 nm, V_s = 0.75 V, I_t = 0.45 nA). The polygons represent the ring configuration at the edge. The A-656 unit is marked by the orange hexagon-yellow pentagon-orange hexagon. The hexagons in light orange are randomly inserted between the A-656 units. (b) Close-up of the A-656 unit (6 nm × 3 nm, V_s = 0.7 V, I_t = 0.6 nA). (c) Nb lattice superimposed on the STM image in grayscale. (d) and (c) are two possible models for the O configuration at the edge: (d) no dangling O atoms; (e) each terminal Nb atom carries a dangling O atom.

As mentioned above [Figure 7-1(b)], Nb_2O_3 free-HC that undergoes edge reconstruction at high temperatures (800 – 900 °C) can form A-656 repeated units. A long edge composed of a few A-656 units and random hexagons is shown in Figure 7-10(a). Due to its random arrangement, the A-656 can only be regarded as a repeated unit rather than a common edge type. Figure 7-10(b) displays a close-up STM image of the A-656, from which we can see the terminal atoms of two hexagons and the middle pentagon are much brighter than the lattice Nb atoms. Altering the sample bias or tunneling current had little effect on this feature. This suggests that the reconstruction formed at high temperatures (800 – 900 °C) may differ from that formed at low temperatures (300 – 400 °C) in terms of the structural properties and formation mechanism. We

also proposed two structural models in Figure 7-10(d) and (e). Given that the oxygen chemical potential at 900 ℃ in the 10^{-8} Pa chamber is extremely low, the edge is more likely to be O-poor [Figure 7-10(d)] than O-rich [Figure 7-10(e)].

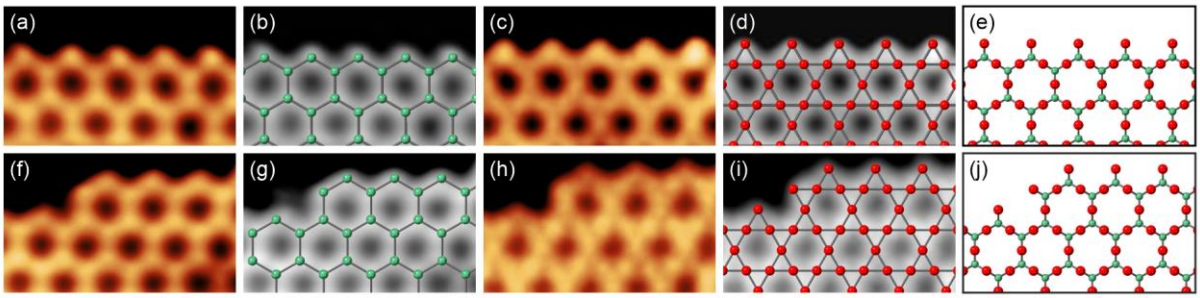

Figure 7-11 (a) – (e) STM images (2.8 nm × 1.7 nm) of a Z-66 edge with its models (a: V_s = 1.0 V, I_t = 0.5 nA; c: V_s = -0.6 V, I_t = 1.2 nA). (f) – (j) STM images (2.8 nm × 1.7 nm) of a corner including both zigzag and armchair with the corresponding models (f: V_s = 0.5 V, I_t = 1.0 nA; e: V_s = -1.0 V, I_t = 1.0 nA).

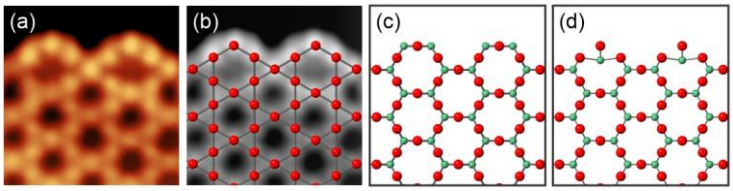

Figure 7-12 (a) STM image of an edge showing the O atom arrangement (2.1 nm × 2.2 nm, V_s = -1.5 V, I_t = 1.5 nA). (b) O lattice superimposed on the STM image in grayscale. (c), (d) Two possible Nb lattice models that can work with the O lattice in (b): (c) A-66 without dangling O; (d) A-56 with one dangling O on each terminal Nb atom.

We proposed quite a few structural models mainly because we lack information on the arrangements of O atoms at the edge. Although technically we can see the oxygen atoms as protrusions using a negative sample bias, it is very challenging to achieve in the experiment. We obtained two sets of STM images taken at the same region under both positive and negative biases, which can help determine the exact structure by superimposing one on the other. Figure 7-11(a) – (e) are STM images and corresponding lattice models for a Z-66 edge. The result after superimposing shows that each terminal Nb atom is threefold coordinated by connecting to a dangling O atom, namely, the proposed model in Figure 7-4(f). Figure 7-11(f) – (j) shows an

edge corner including a zigzag and an armchair unit, from which we can see that all terminal Nb atoms are connected with dangling oxygen atoms.

Figure 7-12(a) is a STM image of an A-based edge taken at a negative sample bias. However, the precise structure cannot be confirmed due to the lack of a positive-biased STM image of the same site. Two possible Nb lattice models are proposed in Figure 7-12(c) and (d), which are an A-66 edge with no dangling oxygen atom, and an A-56 edge with all terminal Nb atoms carried O atoms. At the edge sites of a honeycomb monolayer, the same Nb configuration may correspond to several O configurations depending on the chemical oxygen potential. Similarly, different Nb configurations can also work with a specific O configuration.

7.3.2 Nb_2O_3 emb-HC

The preparation of Nb_2O_3 emb-HC monolayers has been described in detail in Section 5.6.2. The honeycomb lattice of the emb-HC and interior features such as defects, domain boundaries, and triangles are consistent with the free-HC, but edge structures can alter substantially. As the emb-HC islands are grown on the second Au(111) layer and constrained in the surface layer, the island expansion and the edge extension are strongly affected by the threefold symmetry of the Au(111) surface. Consequently, hexagonal emb-HC islands with straight edges were usually generated. Notably, only two common edge types were observed from the emb-HC: the Z-K edge and the Z-66 edge. The Nb lattice should be essentially the same as the free-HC, so lattice models are not presented repeatedly in this section. However, due to the stacking sequence of Au fcc structure along the [111] direction (ABCABC…if not considering the herringbone structure), the positions of terminal Nb and O atoms are worth a categorized discussion.

First of all, it should be noted that the Nb atoms in the (2 × 2) Nb_2O_3 honeycomb monolayer on Au(111) substrates can occupy either the fcc sites or the hcp sites, as shown in Figure 7-13. It gives rise to zigzag edges with two crystalline orientations: one is the Z-66 composed of Nb

atoms at the fcc sites, as indicated by the orange dash line in Figure 7-13(b); the other is the Z-66 composed of Nb atoms at the hcp sites (the blue dash line). For a Nb_2O_3 free-HC, it makes no sense to clarify the crystalline orientation of the Nb atoms in an arbitrary edge. However, three layers are involved in an emb-HC system: the Nb_2O_3 honeycomb monolayer, the L_1 Au(111), and the L_2 Au(111). The relative position shift between the terminal Nb atoms on the L_2 and the nearest Au atoms from the L_1 should be clarified.

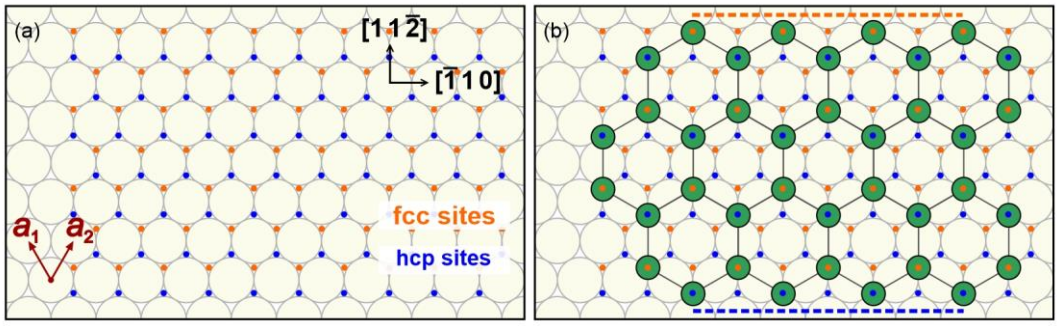

Figure 7-13 Schematic diagrams showing (a) the Au(111) surface with hollow sites denoted; (b) the (2 × 2) Nb_2O_3 honeycomb lattice on the Au(111) surface. The fcc sites are marked by orange dots, and the hcp sites are marked by blue dots. Nb atoms can either occupy the fcc sites or the hcp sites. The dash lines mark two zigzag edges composed of Nb atoms at different sites. The orange dash line indicates the terminal Nb atoms at the fcc sites, while the blue dash line indicates the terminal Nb atoms at the hcp sites.

We draw the schematic models for imaginary emb-HC islands with hexagonal shapes and pure Z-66 or Z-K edges in Figure 7-14. By inserting the Nb lattice between the L_1 and the L_2 Au layers [Figure 7-14 (a), (c)], one can easily assign the location of terminal Nb atoms on six sides. Noting that we take the L_2 Au(111) as the reference layer when assigning the fcc and hcp sites, and let the L_1 Au atoms occupy the hcp hollow sites on the L_2 layer (some are marked by the blue dots). Now it makes sense to clarify the crystalline orientation of the edge terminal Nb atoms with respect to the L_1 layer. We used Z1 to name a Z-based edge with terminal Nb atoms at the hcp sites on the L_2 Au(111). It has the same orientation as the L_1 layer, and therefore, the terminal Nb atoms may substitute half row or the whole row of the nearest Au atoms from the L_1 layer. In schematic models in Figure 7-14(b) and (d), three equivalent Z1 edges are indicated

by the blue dash lines. Similarly, we used Z2 to mark the Z-based edges with terminal Nb atoms at the fcc sites, which are indicated by the orange dash lines in the models.

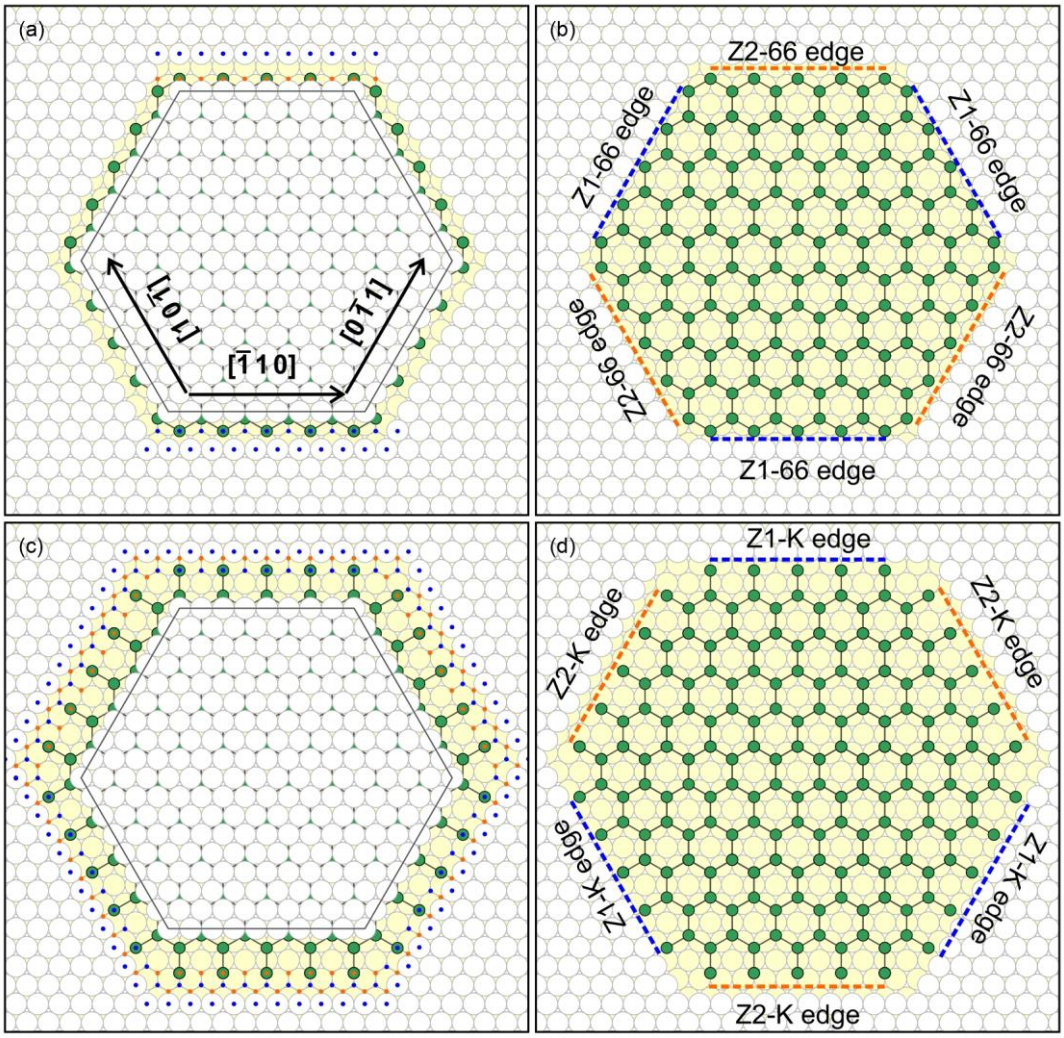

Figure 7-14 Schematic models showing the crystalline orientation of the emb-HC edge structures. White circles represent the L_1 Au atoms; yellow circles represent the L_2 Au atoms. We take the L_2 Au(111) substrate as the reference and let the L_1 Au atoms occupy the hcp sites of the L_2 layer, some L_1 Au atoms are marked by the blue dots. The Nb_2O_3 honeycomb monolayer is grown on the L_2 Au(111) and embedded in the L_1. (a), (b) An imaginary Nb_2O_3 honeycomb monolayer with a hexagonal shape and pure zigzag edges. The Z-66 edges with two crystalline orientations with respect to the L_1 are denoted aside. (c), (d) An imaginary Nb_2O_3 honeycomb monolayer with a hexagonal shape and pure Klein edges. The Z-K edges with two crystalline orientations with respect to the L_1 are denoted aside.

Figure 7-15 shows the STM images of two emb-HC islands with corresponding structural models. In frame (c) and (f), edges with different crystalline orientations were identified and denoted aside. We have examined a number of samples with Nb_2O_3 emb-HC islands but did

not observe any armchair or A-based edge structure. Besides, we also found that the number of K-Z edges is much more than Z-66 edges, which indicates that the K-Z edge is probably the most stable edge structure for the emb-HC. We did not observe a Z1-66 edge in experiments, possibly due to a low occurrence and a limited sample number.

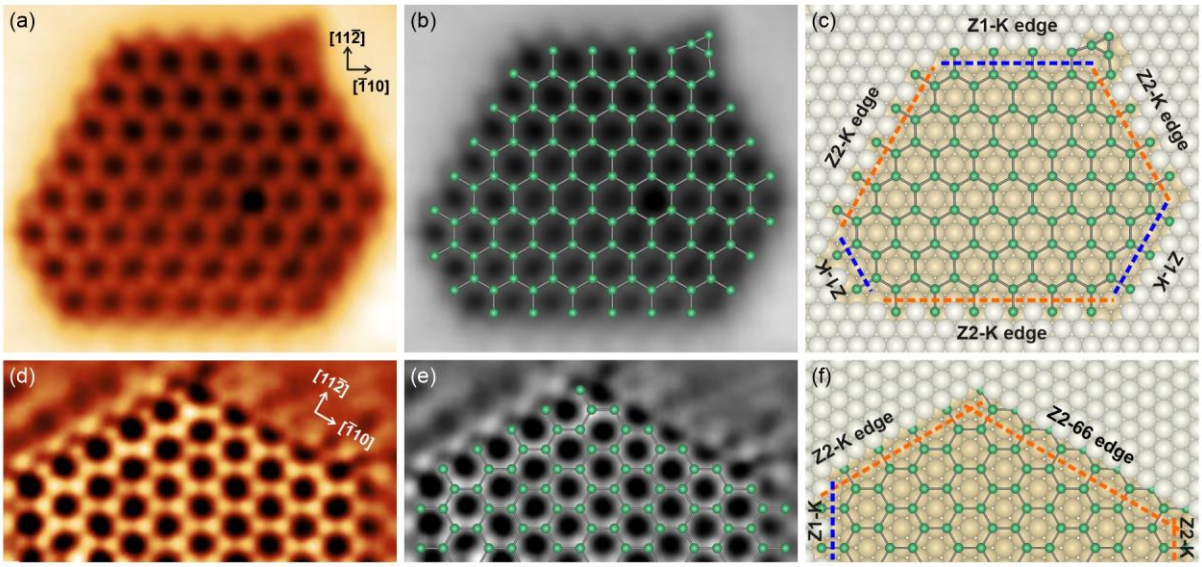

Figure 7-15 (a), (d) STM images of embedded Nb_2O_3 islands (a: 5.7 nm × 5.1 nm, d: 5.8 nm × 2.9 nm, V_s = 1.0 V, I_t = 0.3 nA). The contrast in (d) is enhanced to highlight the edge difference. (b), (d) Nb lattice superimposed on the STM images in grayscale. (c), (f) 3D models for the islands with edge types indicated. White and beige balls represent the L_1 and L_2 Au atoms, respectively. The blue and orange dash lines indicate Z1-K and Z2-66 edges, respectively.

Although the Nb atoms could be atomically resolved in the STM images in Figure 7-15(a) and (d), the Au atoms from the surface are of much stronger signal intensity in the STM images and unable to be characterized at atomic resolution. We cannot determine the exact configuration of the Au atoms next to an emb-HC edge, so a few models are proposed in Figure 7-16. Apart from the relative locations with respect to the L_1 Au atoms, the gap between the terminal Nb atoms and the nearest row of the L_1 Au atoms also leads to various atom configurations. Here we use a hyphen with a number to represent the removal of the nearest row of the L_1 Au atoms. For example, Figure 7-16(d) shows the tightest arrangement of a Z2-66 edge denoted as Z2-66-0. If two Au atoms above the terminal Nb atoms were removed, it would be Z2-66-0.5 (not depicted in the figure); and if the middle Au atom was further removed, it would be Z2-66-1

[Figure 7-16(e)]. It is unnecessary to consider a further removal "larger than 1" because there is no visible gap in the STM images. The same approach can be applied to analyze the possible configurations for the Klein edges. When the terminal Nb atoms occupied the same sites as the surface Au atoms on the L_2 Au(111), the Nb atoms may substitute half of the nearest Au row, thus denoting by -0.5. For example, the Z1-K-0.5 in Figure 7-16(a). The terminal atoms may also substitute the whole row, for example, the Z1-66-1 in Figure 7-16(c). The Z2-K-0 model in Figure 7-16(b) is visibly the most similar to the experimental observation of the Z-K edges in Figure 7-15(a) and (d). However, we cannot judge the existence of the Au atoms located just above the terminal Nb atoms.

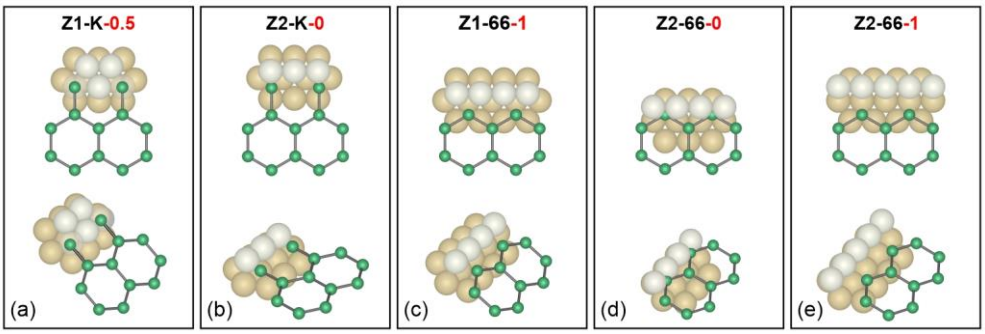

Figure 7-16 Simplified structural models for Z-K and Z-66 edges classified according to the crystalline orientation with respect to the L_1 Au and the gap between the nearest Au atom row from the L_1 layer and the terminal Nb atoms.

It is more difficult to determine the O atom arrangement of an emb-HC edge compared with a free-HC edge. First of all, Nb_2O_3 grown on the Au(111) substrate is a rumpled honeycomb monolayer with O atoms located higher than Nb atoms by 0.93 Å [27]. The distance of Au-Au between the (111) layers is about 2.5 Å (lattice parameter $a_{\mathrm{Au}} = 4.08$ Å, $d_{111} = a_{\mathrm{Au}}/\sqrt{3}$), which means for an emb-HC, O atoms are located on the top of the L_2 Au atoms but still lower than the L_1 Au atoms. When assuming the O atom arrangement at the emb-HC edge, one should consider if there is sufficient space to insert the O atoms between the L_1 and the L_2 Au(111) layers. Secondly, the DFT calculation has predicted a significant charge transfer between Nb atoms and the Au substrate (Q_{Au} = -1.28 e per Nb_2O_3 unit) [27]. If the edge structure adopts the

tightest model, the total charge transfer may remain unchanged but could be allocated with a specific ratio to L_1 and L_2. Therefore, the structural polarization due to the charge transfer can alter, leading to a position shift of the Nb layer or the O layer in the vertical direction.

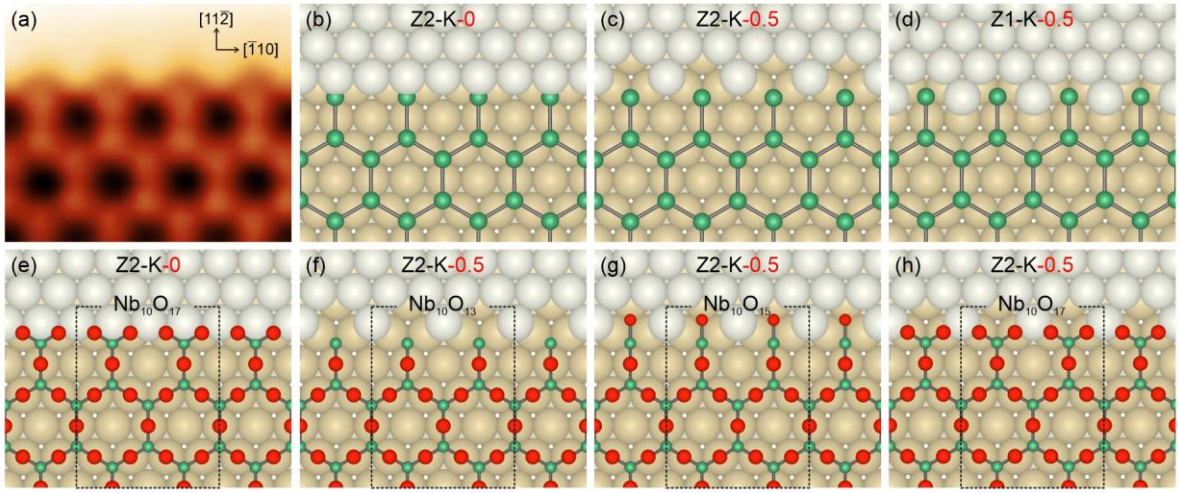

Figure 7-17 (a) STM image of an emb-HC Z-K edge (2.3 nm × 1.9 nm, V_s = 1.0 V, I_t = 0.3 nA). (b) – (d) Different configurations of terminal Nb atoms. (e) – (h) Structural models with O atoms. The rectangles in the dash lines show the repeated units of the Z-K edge.

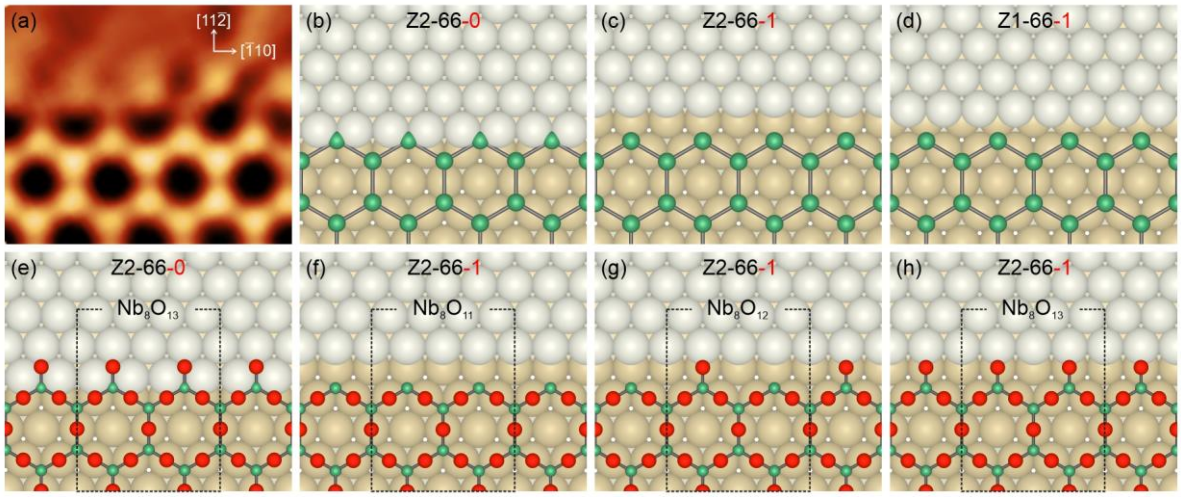

Figure 7-18 (a) STM image of an emb-HC Z-66 edge (2.3 nm × 1.9 nm, V_s = 1.0 V, I_t = 0.3 nA). (b) – (d) Different configurations of terminal Nb atoms. (e) – (h) Structural models with O atoms. The rectangles in the dash lines show the repeated units of the Z-66 edge.

Nevertheless, we still proposed some structural models with O lattice for Z-K and Z-66 edges of the emb-HC, as shown in Figure 7-17 and Figure 7-18. Frame (e) of both figures shows the top view of the tightest models (marked by "-0") with dangling O atoms. It is clear that the

arrangement is too narrow along the $[11\bar{2}]$ direction to accommodate the O atoms between the L_1 and the L_2 layers, so they should be invalid models. Compared with frame (d) of both figures, models in frame (c) visually better reproduce the STM images. Therefore, based on the Nb lattice models in frame (c), complete structural models with O atoms are provided in frame (f) – (h), which are identical to the models proposed for Z-K and Z-66 of the free-HC in Figure 7-8 and Figure 7-4, respectively.

7.3.3 Ti_2O_3 HC

Previous studies have confirmed that Ti_2O_3 also has a (2 × 2) epitaxial growth on the Au(111) surface [42,88]. In the present work, Ti was deposited on the Au(111) substrate by e-beam at room temperature in UHV. Ti_2O_3 honeycomb monolayers were formed by post-oxidation in 3 × 10^{-7} Pa O_2 at 500 ℃ for 0.5 ~ 1 h. Samples prepared in this way result in free honeycomb monolayers grown on the Au(111) surface. Since we did not investigate the embedded growth mode of Ti_2O_3 honeycomb, discussion about the edge structure in this section will be based on the free type.

Figure 7-19(a) and (b) are STM images of two Ti_2O_3 honeycomb islands. It can be seen that the reconstructed edges are composed of a number of polygons, including triangles, squares, pentagons, distorted hexagons, and heptagons, without any periodicity along a specific direction. Figure 7-19(c) shows the STM image of the (2 × 2) Ti honeycomb lattice with atomic resolution. Ti atoms occupy the hcp and fcc hollow sites of the Au(111) surface, while O atoms are at on-top sites, as shown in Figure 7-19(e). Theoretical calculations have proved that the Au-supported Ti_2O_3 honeycomb also forms a rumpled monolayer with O atoms extending outward by 0.7 Å with respect to Ti atoms [88].

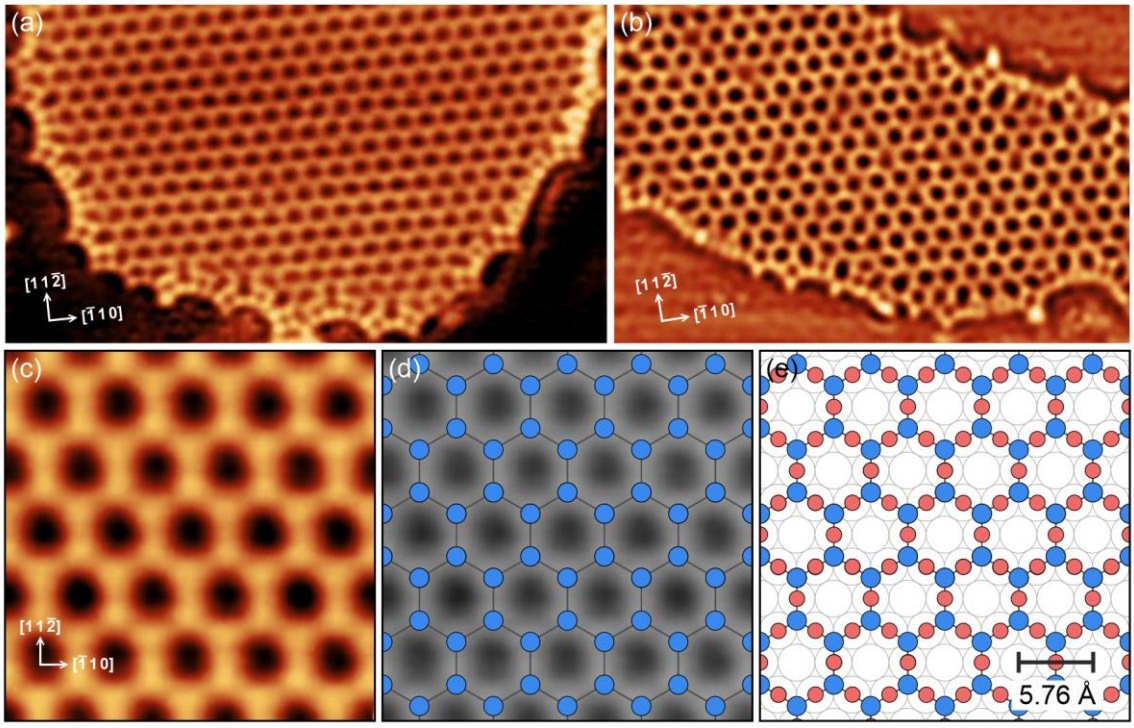

Figure 7-19 (a), (b) STM images of Ti_2O_3 honeycomb islands (a: 14.7 nm × 8.2 nm, b: 12.5 nm × 8.2 nm, V_s = 0.8 V, I_t = 0.3 nA). The edges are curving and reconstructed. (c) Atomically-resolved STM image of the (2 × 2) Ti_2O_3 honeycomb structure (2.9 nm × 2.9 nm, V_s = 1.0 V, I_t = 0.6 nA). (d) Ti lattice superimposed on (c) in grayscale. (e) Structural model of the Ti_2O_3 honeycomb structure. Blue circles represent Ti atoms; red circles represent the O atoms.

Figure 7-20(a) and (b) show two close-up STM images of the curving edges with corresponding schematics presented in (c) and (d). The purple dash line marks the same site in two figures. The cyan circles represent Ti atoms in the vicinity of the edges. Circles with a yellow perimeter represent threefold coordinated terminal Ti atoms. Those with a brown perimeter could be either threefold coordinated Ti atoms or twofold coordinated Ti atoms, depending on whether they carry dangling O atoms.

It is noticeable that many three-membered rings are involved in the edge reconstruction of Ti_2O_3 honeycomb monolayers. The three-membered rings usually pair with distorted heptagons and hold a short periodic arrangement along the $[10\bar{1}]$ direction. The repetition is usually broken by a square or a pentagon, forming bumps extending outward. The termination of the periodic extension is an inevitable result due to severe lattice distortion of neighboring heptagons.

Presumably, the Ti-O-Ti bond will open when the distorted heptagon cannot sustain the tension. Then an extra Ti atom will be introduced into the lattice to form a four-membered ring, which terminates the repetition of the triangle-heptagon (3-7) pair.

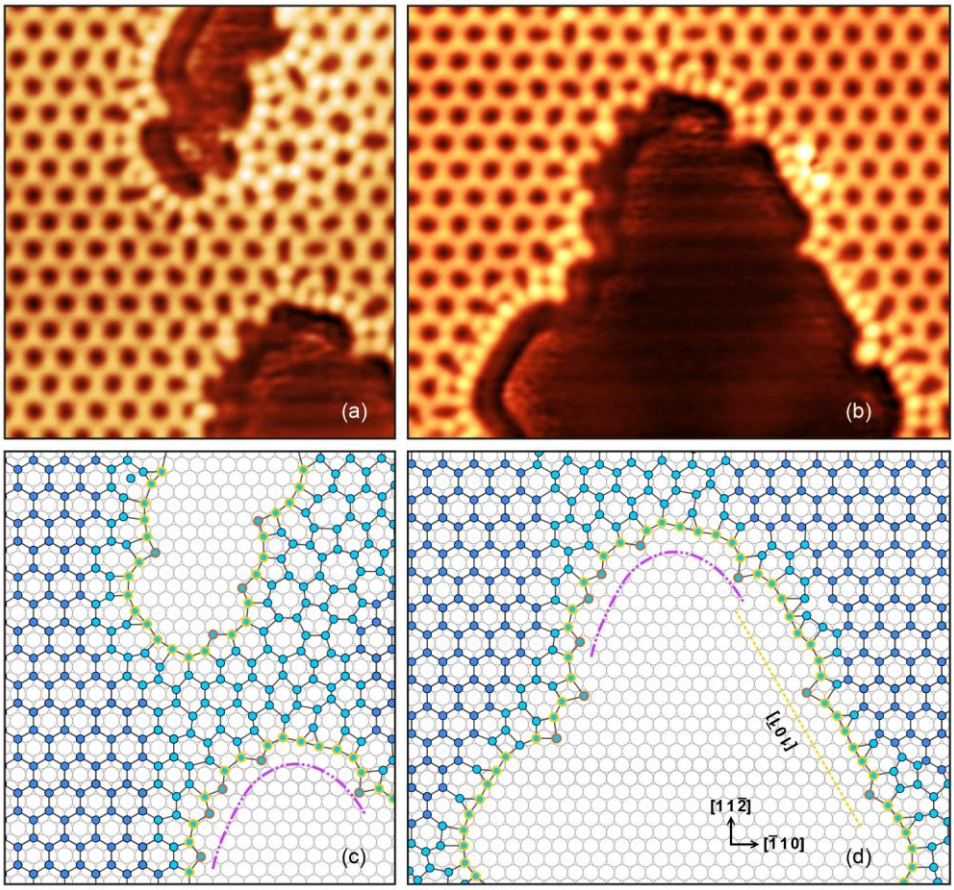

Figure 7-20 (a), (b) STM images of the Ti_2O_3 HC monolayer with curving edges (a: 7.2 nm × 8 nm, b: 10 nm × 8 nm, V_s = 1.0 V, I_t = 0.3 nA). (c) and (d) are schematics corresponding to (a) and (b), respectively.

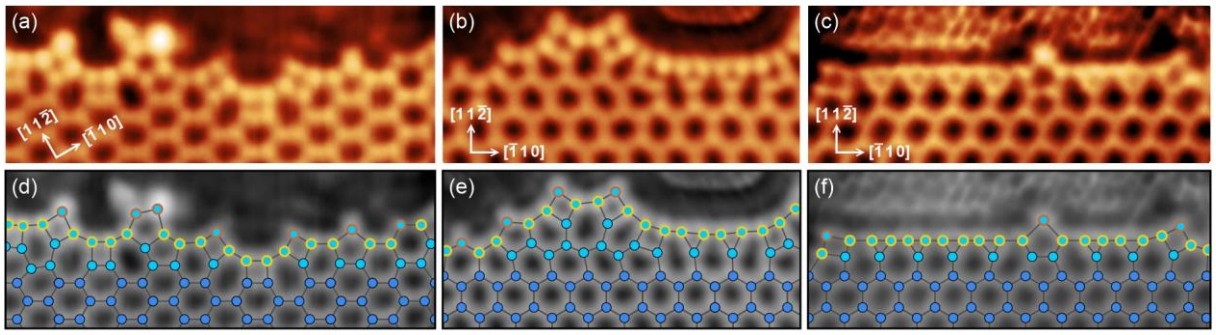

Figure 7-21 STM images of Ti_2O_3 honeycomb edges with corresponding Ti lattice superimposed on the STM images in grayscale. (a) An A-based edge (6.8 nm × 2.5 nm, V_s = 1.0 V, I_t = 0.6 nA). (b), (c) Z-based edges (b: 5.7 nm × 2.5 nm, c: 6.4 nm × 2.5 nm, V_s = 0.7 V, I_t = 0.6 nA).

STM images in Figure 7-21 (a) – (c) display three local edges of Ti_2O_3 honeycomb monolayers. Figure 7-21(a) shows an A-based edge with random polygons. The edge in Figure 7-21(b) is a typical Ti_2O_3 edge structure that exhibits a curving shape due to the triangle-heptagon (3-7) and square-heptagon (4-7) pairs. Figure 7-21(c) shows the longest straight edge that we observed in the experiment. Instead of the 4-7-4 bump, a vertical 5-5 bump acts as a terminator of the triangle-heptagon repetition. The two heptagons next to the middle bump are strongly distorted compared with the heptagons away from the 5-5 terminator. Therefore, breaking the repetition of the 3-7 pair is inevitable because heptagons at the ends are under great tensile stress.

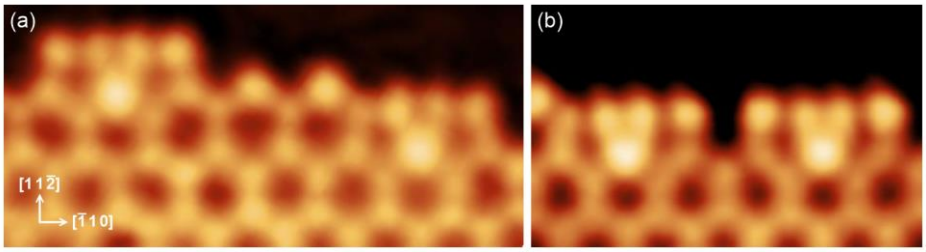

Figure 7-22 Two STM images of Nb_2O_3 free-HC edges comprised by three-membered rings. The bright spots are fourfold coordinated Nb atoms with a higher oxidation state (a: 4.6 nm × 2.1 nm, V_s = 1.0 V, I_t = 0.6 nA; b: 3.4 nm × 2.1 nm, V_s = 0.7 V, I_t = 0.5 nA).

The engagement of three-membered rings in the Ti_2O_3 edge reconstruction allows terminal Ti atoms to keep the threefold coordination. We also observed three-membered rings from Nb_2O_3 honeycomb edges, as shown in Figure 7-22. They usually appear as 535-6 units, which are composed of two pentagons (on top) and one hexagon (in the lattice) sharing a central Nb atom. Therefore, the central Nb atom becomes fourfold coordinated with a significant intensity enhancement in the STM images. Schematic models for the Nb_2O_3 535-6 unit and the Ti_2O_3 3-7 pairs are shown in Figure 7-23. Both Nb_2O_3 and Ti_2O_3 edges possess three-membered rings from a geometric perspective, but the formation mechanisms should be completely different. In the Nb_2O_3 edge, the three-membered ring is achieved by a fourfold coordinated Nb atom with a higher oxidation state. In contrast, in the Ti_2O_3 edge, three-membered rings are always accompanied by distorted heptagons with all the terminal Ti atoms being threefold coordinated.

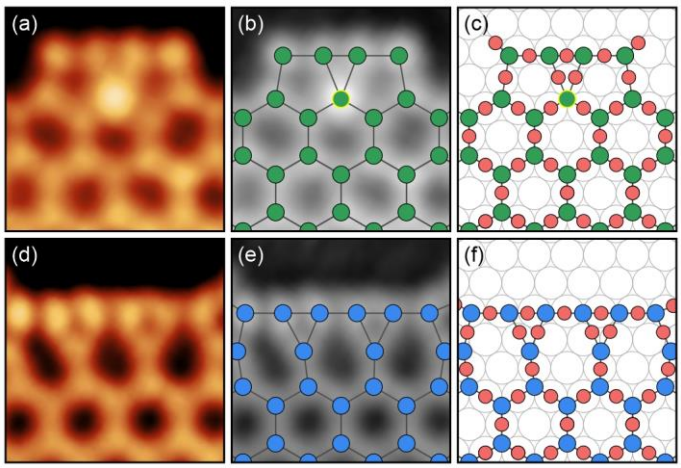

Figure 7-23 Comparison of the three-membered rings at the edge between Nb_2O_3 and Ti_2O_3. (a) – (c) STM image and corresponding lattice model of the Nb_2O_3 edge (1.9 nm × 2 nm, V_s = 1.0 V, I_t = 0.6 nA). The green circle with a yellow perimeter represents the fourfold coordinated Nb. The terminal Nb atoms are assumed to carry dangling O atoms. (d) – (f) STM image and corresponding lattice model of the Ti_2O_3 edge (1.9 nm × 2 nm, V_s = 0.7 V, I_t = 0.6 nA). All the terminal Ti atoms at the edge are three-fold coordinated. Green: Nb; blue: Ti; red: O atoms.

7.3.4 Density of the edge atoms

In the last three sections, we have shown various edge structures of Nb_2O_3 and Ti_2O_3 honeycomb monolayers. Nb_2O_3 edges are reconstructed in a more organized way compared with Ti_2O_3. Ti_2O_3 edge reconstruction usually gives rise to a random arrangement of polygons and involves 3-7 and 4-7 pairs, making the edge look more dense-packed.

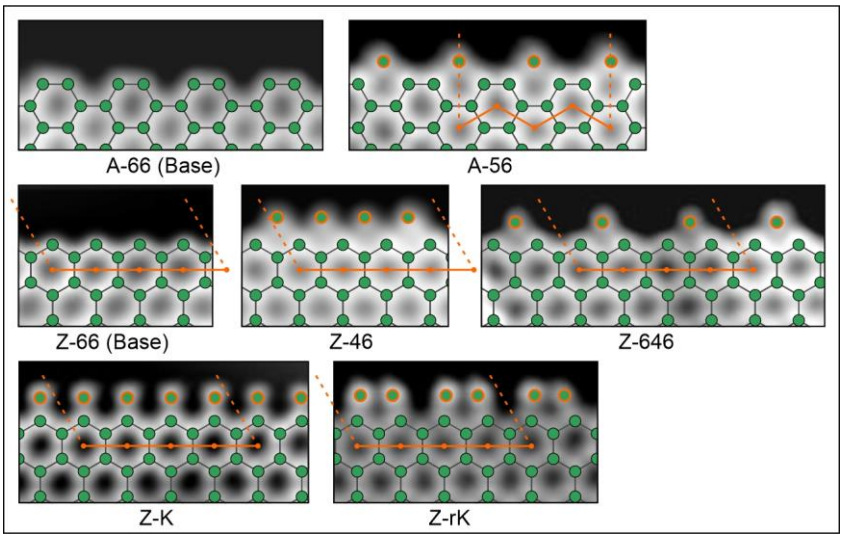

Figure 7-24 Nb lattices superimposed on different edge types to show the ROIs and edge paths. The solid orange lines indicate the edge paths; the orange dash lines show the border of the ROI.

In order to compare the edge reconstruction of the two materials quantitatively, a new parameter *D* is introduced to describe the density of the edge atoms. It should reveal the number of terminal Nb or Ti atoms at the edge of a specific region and be independent of the edge length and extension direction. We define the *density of edge atoms D* as the number of edge atoms per edge path unit L_p. Due to the (2 × 2) epitaxial relationship, the value of the edge path unit is set to be twice the Au-Au distance (2.88 Å) in the (111) plane. An edge path with two borders is required to be constructed before counting the number of edge atoms. Besides, the density should be unified for the two bases: A-66 and Z-66. Figure 7-24 shows the seven common edge types of Nb_2O_3 with the edge paths and borders indicated on each image. An edge path is required to pass through the centers of terminal lattice hexagons and be normal to the sides that it breaks. For a Ti_2O_3 edge, due to the lattice distortion, "the centers of terminal lattice hexagons" will be modified into high-index polygons' centers (polygon = hexagon, heptagon, octagon….) next to the undistorted lattice hexagons. The length of the edge path can be expressed as nL_p. It is unnecessary to calculate the absolute value of the path length. The edge path with two borders defines the region of interest (ROI), from which we count the number of the edge atoms *N*. By calculating N/n, we can obtain the density of the edge atom in the ROI.

For the seven common edge types of Nb_2O_3, the edge paths are all set to be $4L_p$. In order to unify the density for two bases, an edge path with a "M" shape is built for the A-66, while a horizontal line is used for the Z-66. In this way, the total number of Nb atoms in the ROI of the A-66 is identical to that of the Z-66 ($N = 8$). The density of the edge atoms of the two bases can now be unified as two atoms per L_p. Furthermore, the *density difference* δD between an arbitrary edge and corresponding standard hexagonal lattice reveals the degree of reconstruction. A larger δD means more extra atoms can be found beyond the honeycomb lattice. In addition, using δD to assess the reconstruction degree can reduce the effect of path selection, in particular for curving edges with strong lattice distortion.

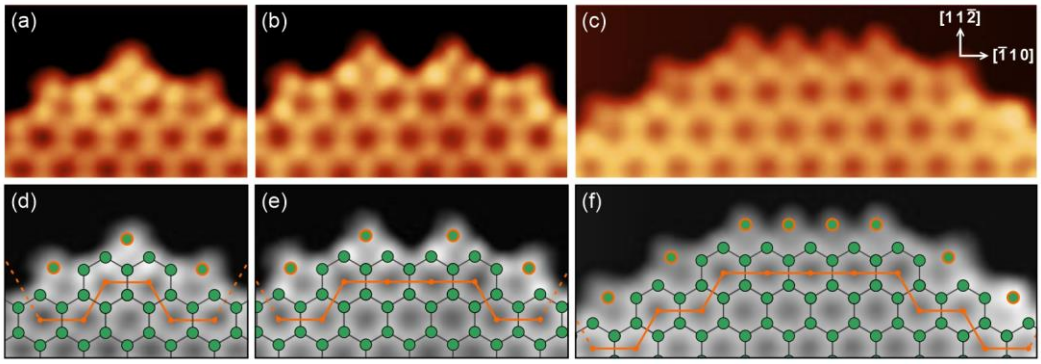

Figure 7-25 (a) – (c) STM images of three Nb_2O_3 free-HC edge examples. (d) – (f) Nb lattices superimposed on the grayscale STM images with edge paths and the ROI borders indicated (a: 3.2 nm × 2.3 nm, V_s = 1.05 V, I_t = 0.1 nA; b: 4.1 nm × 2.3 nm, V_s = 1.0 V, I_t = 0.3 nA; c: 6.1 nm × 2.3 nm, V_s = 1.0 V, I_t = 0.3 nA).

Calculation results of D and δD of the seven common edges are displayed in Table 7-1. For an arbitrary Nb_2O_3 reconstructed edge that comprises a mixture of the seven common types (see three examples in Figure 7-25), the edge path can be quickly drawn by passing through the terminal hexagons with a polyline. The extra atoms can be recognized without much difficulty because they are either located in the middle of an A-base forming a pentagon, or in the middle of a Z-base forming a four-membered ring bump. They usually look faint compared with the lattice atoms. Calculation results of D and δD of the three examples are presented in Table 7-1.

Regarding the Ti_2O_3 reconstruction edge, it is challenging to identify the edge atoms which should be counted for density calculation due to severe lattice distortion. Two examples are shown in Figure 7-26 (a) and (b). The way to construct the edge path now should be modified into connecting terminal polygons, including distorted hexagons and heptagons, as illustrated in Figure 7-26(c) and (d). All the Ti atoms represented by cyan circles should be regarded as edge atoms that engaged in the reconstruction. In order to clarify the extra atoms, equivalent honeycomb lattices with perfect hexagons are provided for reference [Figure 7-26(e), (f)]. Then the number of extra atoms can be obtained by the actual model subtracting the reference model in the ROI. For example, the number of edge atoms in Figure 7-26(c) is 35, and in (e) is 24; the

edge path is $12L_p$. So the density difference $\delta D = \frac{35-24}{12} = 0.92$ atoms/L_p. Calculation results for the Ti_2O_3 edge examples are shown in Table 7-1.

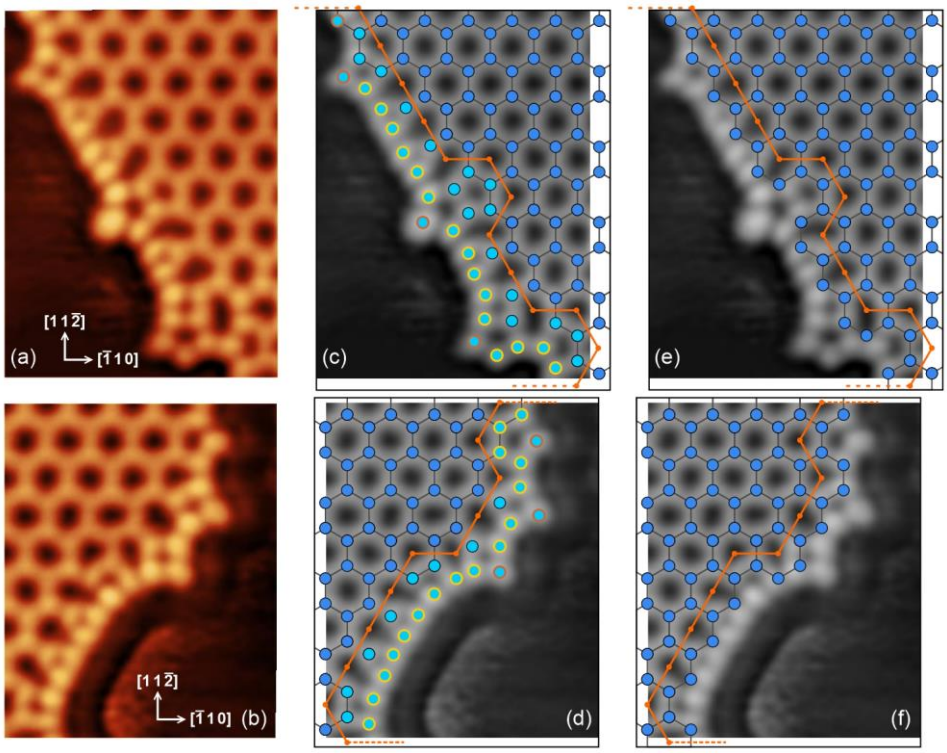

Figure 7-26 (a) and (b) STM images (a: 3.6 nm × 4.9 nm, b: 3.6 nm × 4.4 nm, V_s = 0.7 V, I_t = 0.6 nA) of two curving edge examples of Ti_2O_3 honeycomb with corresponding structural models in (c) and (d), respectively. (e) and (f) are reference models with perfect hexagonal lattices that aid the calculation of the density difference.

Table 7-1 Density of edge atoms from the examples shown in Figure 7-24, 7-25, and 7-26.

Figure	Name	Path Length nL_p	N (atoms)	$D = \frac{N}{\text{Path}}$ (atom/L_p)	$\delta D = \frac{N - N_{ref}}{\text{Path}}$ (atom/L_p)
7-24	Nb A-66 (Base)	4	8	2	0
7-24	Nb A-56	4	10	2.5	0.5
7-24	Nb Z-66 (Base)	4	8	2	0
7-24	Nb Z-46	4	12	3	1
7-24	Nb Z-646	4	10	2.5	0.5
7-24	Nb Z-K	4	12	3	1
7-24	Nb Z-rK	4	12	2	1
7-25	Nb edge-a	5	14	2.8	0.6
7-25	Nb edge-b	7	15	2.14	0.57
7-25	Nb edge-c	12	25	2.08	0.67
7-26	Ti edge-a	12	35	2.92	0.92
7-26	Ti edge-b	10	27	2.7	0.7

Table 7-1 shows the calculation results of the density of edge atoms and density difference from the examples in Figure 7-24, Figure 7-25, and Figure 7-26. For the Nb_2O_3 honeycomb edge structure, Z-46, Z-K, and Z-rK possess the highest density of edge atoms. Z-K should not be technically counted as a reconstructed edge because no new polygon was formed. Therefore, Z-46 and Z-rK are the two edge types that undergo the strongest reconstruction. In fact, we found that both of them could not retain the extension for a long distance. They appeared less frequently than A-56 and Z-646, which also means that A-56 and Z-646 are more energetically favorable in the Nb_2O_3 edge reconstruction. For an arbitrary reconstructed edge of Nb_2O_3, the density difference is between 0.5 and 1 as a result of a mixture of different edge types. Generally, this value is around 0.6 because A-56 and Z-646 are more dominant in occurrence.

The density difference δD can be used to assess the reconstruction degree when comparing Nb_2O_3 with Ti_2O_3. We can see that δD of Ti_2O_3 is usually higher than that of Nb_2O_3. This is why the edges of Ti_2O_3 look more densely packed in the STM images. As mentioned above, this can be attributed to the 3-7 and 4-7 pairs engaged in the Ti_2O_3 edge reconstruction, which are not the characteristics of Nb_2O_3 edges.

7.4 Conclusion

In the chapter, we discuss the edge structure of Nb_2O_3 and Ti_2O_3 honeycomb monolayers. Both of them can form reconstructed edge structures by creating non-hexagonal rings. Seven common edge structures have been identified for Nb_2O_3, including A-66, A-56, Z-66, Z-46, Z-646, Z-K, and Z-rK. All of them can be found in Nb_2O_3 free-HC, but only Z-K and Z-66 appear in Nb_2O_3 emb-HC. From the discussion above, we can make conclusions as follows.

(1) Annealing temperature strongly affects the edge reconstruction of Nb_2O_3 honeycomb monolayers. Low-temperature annealing (300 – 400 ℃) leads to a variety of reconstructed

edges with long-range order, while high-temperature annealing (800 – 900 ℃) gives rise to A-656 repeated units without any periodicity along a specific extension direction. (2) The intensity of terminal atoms that form the non-hexagonal polygons at the edge is much weaker in the low-temperature reconstruction than in the high-temperature reconstruction, which suggests that the structural properties and the reconstruction mechanisms should be different. (3) We also proposed a few O lattice models to construct the complete structures at the edges. Different models may work with different preparation conditions as the oxygen chemical potential plays a critical role in the number of dangling O atoms at the edge. (4) Z-K and Z-66 edge of the Nb_2O_3 emb-HC are essentially the same as the free-HC. But due to the stacking sequence of Au(111) layers, they can be further classified according to the location of terminal Nb atoms with respect to the surface layer. (5) In addition, the location is also relevant to the arrangement of O atoms due to the space and charge transfer from Nb atoms to the Au substrate. Hence the configuration of a Nb_2O_3 emb-HC edge is much more complex than the free-HC, and it requires further experimental and theoretical investigations.

(6) The edge reconstruction in Ti_2O_3 honeycomb monolayers leads to a random arrangement of polygons and a curving shape. Compared with Nb_2O_3 free-HC, Ti_2O_3 reconstructed edges contain more three-membered rings that can form triangle-heptagon (3-7) pairs. Terminal Ti atoms in the 3-7 pairs maintain the threefold coordination. (7) Three-membered rings were also observed in the Nb_2O_3 honeycomb edge in the form of individual 535-6 units. The Nb atom at the node is fourfold coordinated with a higher oxidation state and much higher intensity in the STM images. (8) In order to compare the degree of edge reconstruction, we calculated the density of edge atoms and density difference with respect to the unreconstructed edge with perfect hexagons. For an arbitrary reconstructed edge of Nb_2O_3 and Ti_2O_3 HC monolayers, Ti_2O_3 usually possesses a higher density difference, which indicates that the Ti_2O_3 honeycomb monolayer undergoes a stronger edge reconstruction.

Chapter 8 Defect structures of Nb_2O_3 and Ti_2O_3 honeycomb monolayers

8.1 Introduction

It is common to find defects in 2D materials, including point defects and line defects [81,87]. It has been reported that these defects can strongly affect the properties of the 2D materials and their performance in nanodevices. For example, vacancies, adatom impurities, and boundaries can act as scattering centers that impede the carrier mobility and prolong the response time of electronic devices [85,99,252]. Therefore, it is significant to have an understanding of the defect structures and then utilize preferable defects, which is also the aim of defect engineering [76,77,89]. In defect engineering, the desired structure can be obtained by e-beam or ion bombardment and some chemical treatments [76].

Local defects in the 2D materials with a honeycomb structure usually appear as the breaking of perfect hexagons. Polygons such as three-, four-, five-(pentagons), seven-(heptagons), eight-(octagons) membered rings, as well as distorted hexagons and multiple-membered rings with a higher number, may involve in a defect domain. Previous studies have shown that the substrate for a supported honeycomb monolayer plays a critical role in forming and stabilizing the point defect structures [88,94,104,253]. A study of domain boundary structures of the (2 × 2) Ti_2O_3 honeycomb monolayer on the Au(111) substrate has just been published by our research group together with our collaborators Jacek and Claudine from CNRS-Sorbonne Université, Paris, who undertook the theoretical calculation work [254].

In the present work, we focus on the defect structures of the (2 × 2) Nb_2O_3 honeycomb monolayer on the Au(111) substrate. A small amount of work was also done on Ti_2O_3, which has shown a good agreement with the previous research [88,254]. Theoretical calculations of

the Nb_2O_3 defects are in progress. They are not presented in this thesis but will be integrated into upcoming research papers. The comparison between Nb_2O_3 and Ti_2O_3 may help us better understand the structural properties of defects and the cation's role in the defect behavior.

This chapter discusses point defects first in Section 8.3 and then line defects in Section 8.4. We will show STM images of tetravacancy (TV) defects in the Nb_2O_3 honeycomb, which have not been experimentally observed in Ti_2O_3 honeycomb. Besides, a variety of defect reconstructions of large vacancies will be presented without much in-depth analysis due to the uncertainty of dangling oxygen. Regarding the line defects, Nb_2O_3 and Ti_2O_3 share some common types of domain boundaries. However, Nb_2O_3 possesses two distinct features that significantly affect defect reconstruction and domain boundary formation. Firstly, fourfold coordinated Nb atoms, which have been discussed in Chapter 6, provide alternative ways to reconstruct defect domains and expand the structural solutions. Secondly, the triangle structure incorporated in a Nb_2O_3 honeycomb monolayer can act as a DB termination or a triple junction for three honeycomb domains. In addition, we also observed a few grain boundaries of Nb_2O_3 honeycomb monolayers caused by a small tilting angle of two Au(111) substrates. In other words, the grain boundary of the honeycomb monolayer is a reflection of substrate discontinuity. At the end of this chapter, elementary work on Ti_2O_3 defects is presented. The similarities and differences of the defect behaviors between Nb_2O_3 and Ti_2O_3 are briefly discussed.

8.2 Experimental methods

The Nb_2O_3 domain boundaries can form naturally during the preparation of the honeycomb structure described in Section 5.6.2. It is more convenient to collect DBs from large monolayers with a high coverage on the substrate. However, the density of point defects in the Nb_2O_3 honeycomb monolayer under the present conditions was extremely low. Therefore, we used Ar^+ ions with a low accelerating voltage (50 eV) to cause defects. Detailed description can be

found in Section 5.6.3. The defect-induced treatment affects the density and the size of defect domains, but the structural properties of the point defects are determined by the thin film and influenced by the substrate.

8.3 Point defects in Nb_2O_3 honeycomb monolayers

8.3.1 Simple vacancy

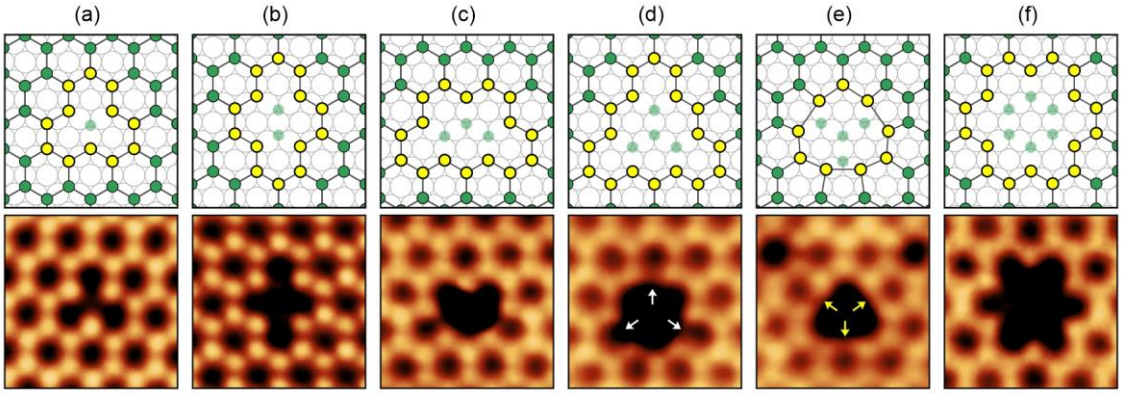

Figure 8-1 Simple vacancies with increasing the number of missing Nb atoms. The top row shows the structural models, and the bottom row shows the STM images. The yellow circles mark the Nb atoms at the border of the defect domains. The half-transparent green circles indicate the positions of the missing Nb atoms. The white arrows in (d) indicate the Nb atoms at the border retain their position at the hollow sites, while the yellow arrows in (e) indicate the Nb atoms approaching each other, forming three pentagons. STM image size: 2.3 nm × 2.3 nm. (a) V_s = 1.0 V, I_t = 0.8 nA. (b) V_s = 0.7 V, I_t = 0.8 nA; (c) V_s = 2.0 V, I_t = 0.2 nA; (d) V_s = 2.0 V, I_t = 0.2 nA; (e) V_s = 1.0 V, I_t = 0.8 nA; (f) V_s = 0.8 V, I_t = 0.7 nA.

Figure 8-1 displays a series of simple vacancies arranged according to the number of missing Nb atoms. The simplest point defect is a single Nb vacancy in the frame (a). Without any defect-induced treatment, the as-prepared Nb_2O_3 honeycomb monolayer was so stable and well-arranged that even the single vacancy was barely seen. The STM images were taken at positive sample biases, so we can identify the missing Nb atoms without doubt but hardly determine the missing oxygen atoms. The Nb-O deficiency can be either stoichiometric ($NbO_{1.5}$) or non-stoichiometric. For example, a single vacancy can be created by losing a Nb atom, a NbO unit, a NbO_2 unit, or a NbO_3 unit. Figure 8-1(b) shows the STM image of the honeycomb lattice with two missing Nb atoms. It is evident that the border Nb atoms maintained their positions at the

hollow sites without any displacement or distortion. This defect domain can act as a base for the structural analysis of the SW defect, DV(5-8-5), and 4fold-1sp defect. Figure 8-1(c) and (d) show the lattice with three and four Nb vacancies. The transition from (c) to (d) can be achieved by losing the Nb atom at the upper middle. Although the resolution of these two images is not as good as (a) and (b), we can see that the atoms at the defect border can still retain their original positions. By contrast, the border Nb atoms in Figure 8-1(e) slightly shifted and made the border look like a closed triangle. The two Nb atoms indicated by the yellow arrows approached each other, leading to the formation of three pentagons.

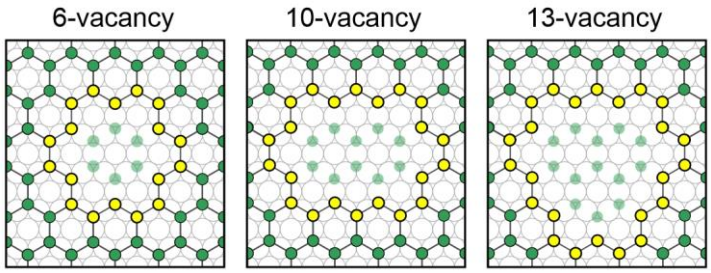

Figure 8-2 Structural models of 6-, 10-, and 13-vacancy. The half-transparent green circles indicate the positions of the missing Nb atoms.

Figure 8-1(f) shows a vacancy site that looks like a hexapetalous flower. It is the largest non-reconstructed vacancy that was observed in the experiment. Vacancies with more missing Nb atoms usually undergo reconstruction or carry adatoms. In this work, we only discuss the 6-vacancy (6-vac), the 10-vacancy (10-vac), and the 13-vacancy (13-vac) defect domains, as shown in Figure 8-2. Reconstructions based on the three large vacancies will be displayed later. Local defects with more missing Nb atoms were also observed, as shown in Figure 5-20(a) and (b) when using a higher accelerating voltage of Ar^+ ions. But it is difficult to analyze these vacancy sites with irregular shapes. The borders of the large vacancies are inclined to reconstruct, which can be regarded as a short-range edge reconstruction.

We can see oxygen atoms in STM images due to their contributions to the filled states at negative biases. We were able to obtain some images of the 2- and 3-vacancy in the same region

at both positive and negative sample biases. As shown in Figure 8-3, a Nb atom and two neighbouring oxygen atoms are missing in the 2-vacancy defect. The surrounded four oxygen atoms retain their positions in the HC lattice, thus becoming dangling oxygen with lower intensity in the STM image. A similar situation can be observed in the 3-vacancy defect domain (Figure 8-4), where five dangling oxygen atoms are located at the domain border.

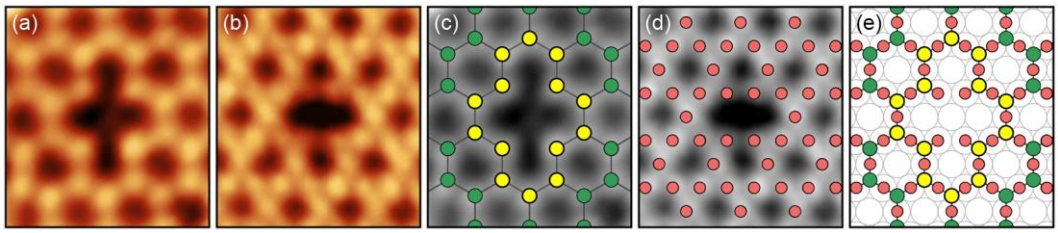

Figure 8-3 STM images (2.2 nm × 2.3 nm) of the 2-vacancy defect at (a) a positive sample bias (V_s = 0.8 V, I_t = 0.5 nA); and at (b) a negative sample bias (V_s = -1.0 V, I_t = 1.0 nA). (c) Nb lattice model superimposed on (a) in grayscale. (d) O lattice model superimposed on (b) in grayscale. (e) Complete honeycomb lattice with Nb and O atoms.

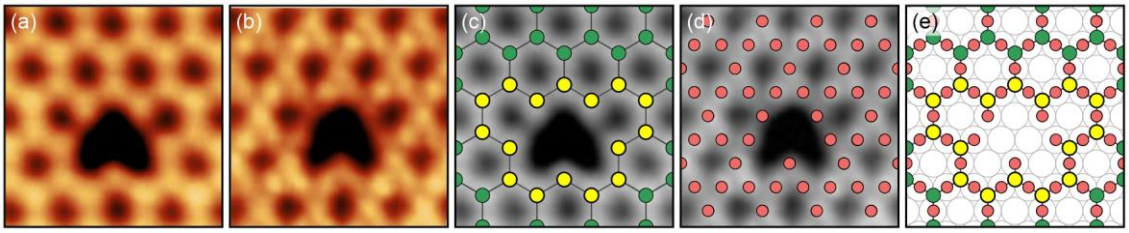

Figure 8-4 STM images (2.3 nm × 2.3 nm) of the 3-vacancy defect at (a) a positive sample bias (V_s = 1.0 V, I_t = 0.5 nA); and at (b) a negative sample bias (V_s = -1.0 V, I_t = 1.0 nA). (c) Nb lattice model superimposed on (a) in grayscale. (d) O lattice model superimposed on (b) in grayscale. (e) Complete honeycomb lattice with Nb and O atoms.

Figure 8-5 shows the schematic models of the SW defect and the DV(5-8-5) with the same defect domain as the 2-vacancy. Figure 8-5(a) – (d) are pristine (2 × 2) Nb_2O_3 honeycomb structures for reference. The SW defect is formed by the central Nb-O-Nb unit rotating by 90° with no atom lost from the domain. The two Nb atoms no longer stayed at the hollow sites, and the central area of the defect domain was probably lifted by small atom displacements perpendicular to the substrate surface. Therefore, Nb atoms at the center look brighter than others in the vicinity of the defect domain.

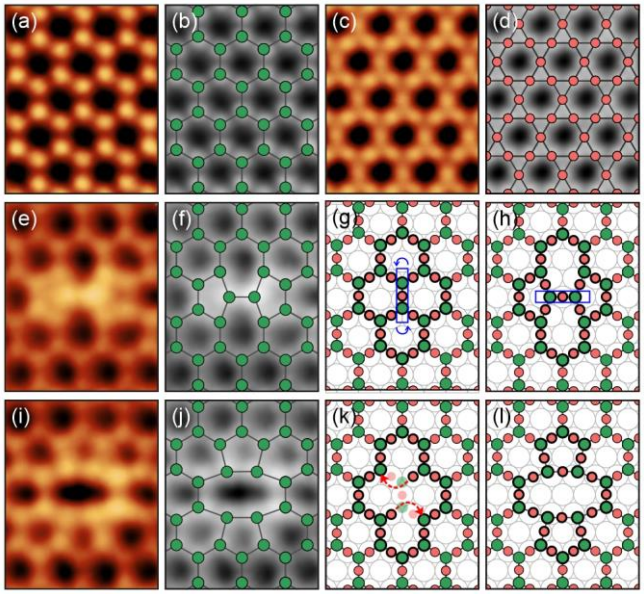

Figure 8-5 (a) – (d) STM images and structural models of a pristine (2 × 2) Nb_2O_3 honeycomb for reference (a: V_s = 0.7 V, I_t = 0.8 nA; c: V_s = -1.8 V, I_t = 0.8 nA). (e) STM image of a SW defect (V_s = 2.0 V, I_t = 0.2 nA). (f) Nb lattice model superimposed on (e) in grayscale. (g), (h) Structural models showing the formation of a SW defect by rotating the Nb-O-Nb unit marked in the blue rectangle. (i) STM image of a DV(5-8-5) defect (V_s = 2.0 V, I_t = 0.2 nA). (j) Nb lattice model superimposed on (i) in grayscale. (k), (l) Structural models showing the formation of a DV(5-8-5) defect by losing a Nb_2O_3 unit and reconstructing. Image size: 2.0 nm × 2.5 nm.

The number of Nb atoms in a 2-vacancy [Figure 8-1(b) or Figure 8-3(a)] is identical to that in a DV(5-8-5) [Figure 8-5(i)]. But it is manifest that the central four Nb atoms of the DV(5-8-5) are looped by lattice distortion. The atom deficiency of the 2-vacancy is non-stoichiometric, which can be Nb_2O (Figure 8-3) or $Nb_2O_{2\text{-}5}$ depending on the number of dangling oxygen atoms. In contrast, a divacancy defect is formed by losing a Nb_2O_3 unit and then connecting the dangling oxygen atoms with the twofold coordinated Nb atoms [Figure 8-5(k), (l)]. As a result, all the Nb in the divacancy defect domain can retain the threefold coordination.

8.3.2 Divacancy (DV) and tetravacancy (TV)

Apart from the DV(5-8-5), we also observed two divacancy defects at both positive and negative sample biases, as shown in Figure 8-6 and Figure 8-7. We follow the nomenclature in Ref. [88], calling them DV(555-777) and DV(5555-6-7777). The numbers indicate the ring size of the building blocks and are arranged according to symmetry. The blue circles in frames (h)

show the Nb atom positions in a pristine honeycomb structure. By counting the number of green circles that deviated from the pristine positions and then subtracting the number of the blue circles, one can quickly figure out the Nb atom deficiency. The O deficiency can then be calculated by multiplying 1.5. This rapid method is particularly convenient for analyzing a tetravacancy with a much larger defect domain.

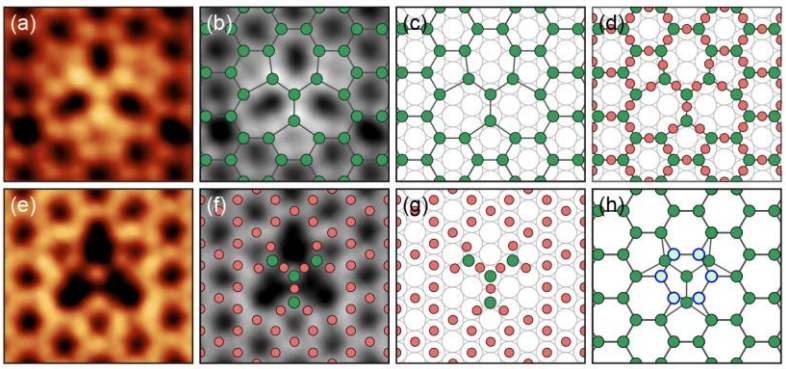

Figure 8-6 (a) STM image of the DV(555-777) at a positive sample bias (V_s = 0.8 V, I_t = 0.2 nA). (b) Nb lattice model superimposed on (a) in grayscale. (c) Nb lattice on Au(111). (d) Complete structural model. (e) STM image of the DV(555-777) at a negative sample bias (V_s = -0.5 V, I_t = 1.0 nA). (f) O lattice model superimposed on (e) in grayscale; the Nb atoms at the defect core are still visible at the negative bias. (g) O lattice model with visible Nb atoms on Au(111). (h) Schematic diagram that aids the calculation of the Nb deficiency. The blue circles mark the Nb atom positions in a pristine honeycomb. The number of the blue circles: 6; the number of the green circles deviated from the pristine positions: 4; therefore, the Nb deficiency is 2. Frame size: 2.5 nm × 2.3 nm.

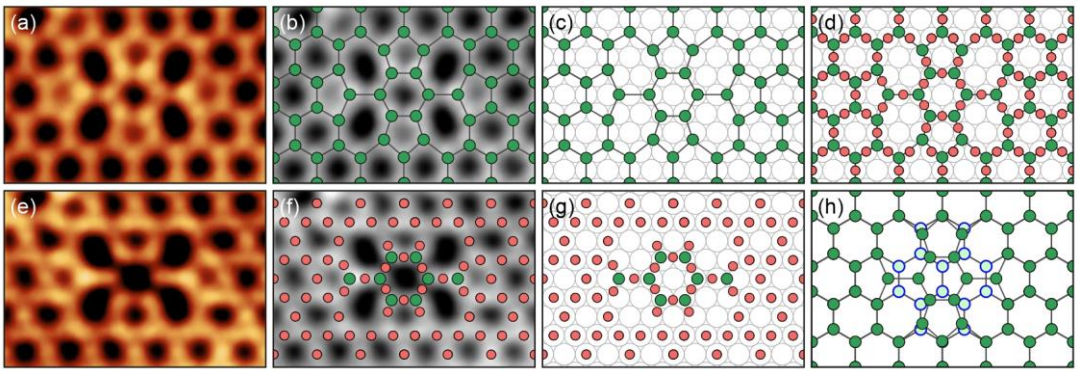

Figure 8-7 (a) STM image of the DV(5555-6-7777) at a positive sample bias (V_s = 0.5 V, I_t = 1.0 nA). (b) Nb lattice model superimposed on (a) in grayscale. (c) Nb lattice on Au(111). (d) Complete structural model. (e) STM image of the defect at a negative sample bias (V_s = -1.0 V, I_t = 1.0 nA). (f) O lattice model superimposed on (e) in grayscale. (g) O lattice model with visible Nb atoms on Au(111). (h) The number of the blue circles: 14; the number of the green circles deviated from the pristine positions: 12; Nb deficiency: 2. Frame size: 3.5 nm × 2.3 nm.

Empty-state STM images of the DV(555-777) and the DV(5555-6-7777) in Ti_2O_3 are shown in Ref. [88]. There is no discrepancy between Nb_2O_3 and Ti_2O_3 in the cation arrangement. In this work, STM images showing the filled states of the DV(555-777) and DV(5555-6-7777) in Nb_2O_3 honeycomb were obtained as well [Figure 8-6(e), Figure 8-7(e)]. It is interesting to visualize the central Nb atoms in the two STM images at negative sample biases. These Nb atoms in the defect cores deviated from the hollow sites to are involved in the defect domain reconstruction. The atom displacement may induce an anisotropic strain field, which lifts the locations of the central Nb atoms as well as the LDOS [88].

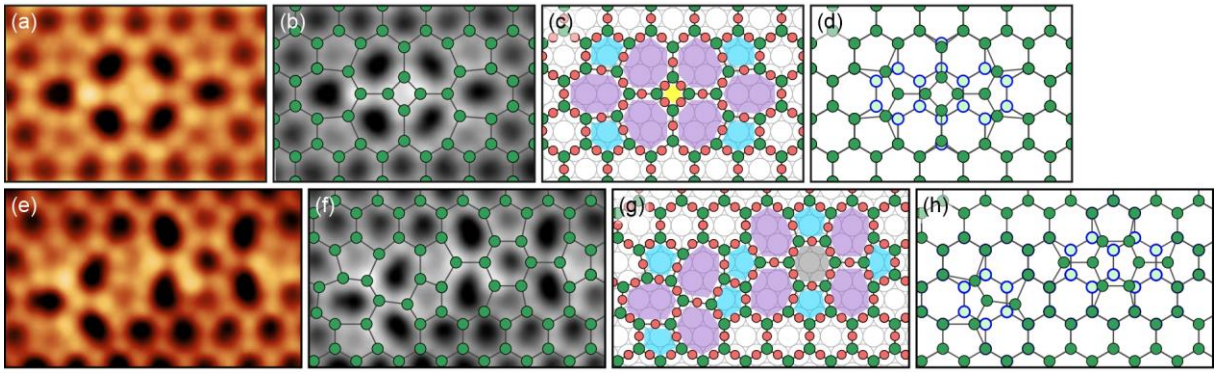

Figure 8-8 (a) STM image of the TV(55777-4-55777) defect (3.5 nm × 2.3 nm, V_s = 1.0 V, I_t = 0.2 nA). (b) Nb lattice model superimposed on (a) in grayscale. (c) Complete structural model with polygons marked in different colors in the defect domain. (d) Schematic diagram that aids the calculation of the Nb deficiency. The number of the blue circles: 16; the number of the green circles that deviated from the pristine positions: 12; therefore, the Nb deficiency is 4. (e) STM image of the TV[(555-777)-(5555-6-7777)] defect (4.2 nm × 2.4 nm, V_s = 2.0 V, I_t = 0.2 nA). (f) Nb lattice model superimposed on (e) in grayscale. (g) Complete structural model. (h) The number of the blue circles: 16; the number of the green circles that deviated from the pristine positions: 12; therefore, the Nb deficiency is 4.

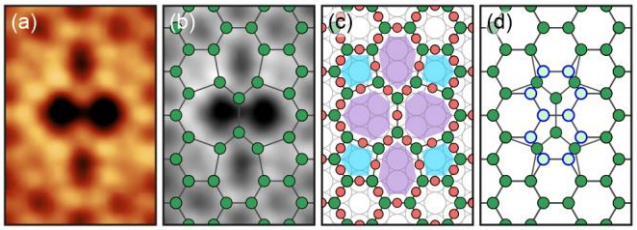

Figure 8-9 (a) STM image of the newly-found TV(5555-7777) defect (2.0 nm × 2.9 nm, V_s = 0.8 V, I_t = 0.2 nA). (b) Nb lattice model superimposed on (a) in grayscale. (c) Complete structural model. (d) The number of the blue circles: 10; the number of the green circles that deviated from the pristine positions: 6; therefore, the Nb deficiency is 4.

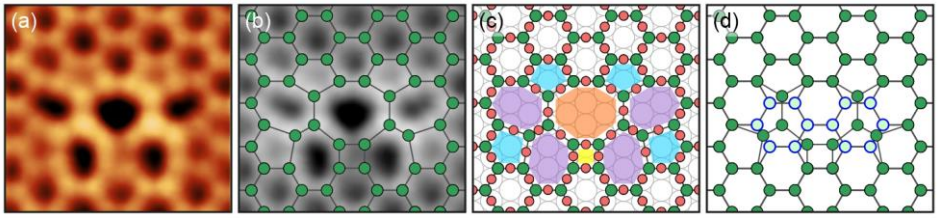

Figure 8-10 (a) STM image of the newly-found TV(5757-48-5757) defect (3.0 nm × 2.7 nm, V_s = 2.0 V, I_t = 0.2 nA). (b) Nb lattice model superimposed on (a) in grayscale. (c) Complete structural model. (d) The number of the blue circles: 12; the number of the green circles that deviated from the pristine positions: 8; therefore, the Nb deficiency is 4.

We have observed four tetravacancy defects in the Nb_2O_3 honeycomb monolayers. The tetravacancies have an atom deficiency of Nb_4O_6, with all the Nb atoms retaining the threefold coordination in the defect domains. They have been theoretically predicted and experimentally confirmed in graphene [255,256]. Robertson *et al*. used a high-energy electron beam to create the defects and characterized their structures by TEM at atomic resolution. A series of structural models with the naming scheme is listed in Ref. [255].

The most straightforward way to construct a tetravacancy is to connect two divacancies and meanwhile retain the threefold coordination of all the node atoms. Figure 8-8 shows two examples of tetravacancy defects formed by double divacancies. Polygons in structural models are filled with different colors to represent the sizes: yellow for the square, light blue for the pentagon, grey for the hexagon, purple for the heptagon, and orange for the octagon. In Figure 8-8(a) two DV(555-777) defects with a mirror symmetry (or rotated by 60°) grew together by degenerating the five-membered ring into a four-membered ring at the center. We did not adopt the naming scheme that focuses on the orientation and defect shape in Ref. [255]. Instead, we named this tetravacancy defect according to the ring size and symmetry as we did for the divacancy defect. So the defect in Figure 8-8(a) is called TV(55777-4-55777). This tetravacancy permutation has also been observed in graphene [255]. Figure 8-8(e) shows a tetravacancy formed by a DV(555-777) and a DV(5555-6-7777) that shared the borders of the central pentagon, so we name it TV[(555-777)-(5555-6-7777)]. A set of similar structures has

been found in graphene, in which the two divacancies either share partial borders or entire rings. Figure 8-9 and Figure 8-10 display two novel TV defects which are named TV(5555-7777) and TV(5757-48-5757), respectively. These two permutations have not yet been experimentally observed or theoretically predicted in any 2D thin film with a honeycomb lattice.

Table 8-1 A summary of atom deficiency and the occurrence of the Stone-Wales defect, divacancies, and tetravacancies.

Defect type	Atom deficiency	Total occurrence
SW	0	28
DV(5-8-5)	Nb_2O_3	18
DV(555-777)	Nb_2O_3	77
DV(5555-6-7777)	Nb_2O_3	13
TV(55777-4-55777)	Nb_4O_6	1
TV[(555-777)-(5555-6-7777)]	Nb_4O_6	1
TV(5555-7777)	Nb_4O_6	1
TV(5757-48-5757)	Nb_4O_6	1

Table 8-1 summarizes the SW, DV, and TV defects in terms of the atom deficiency and the occurrence. The statistics have been partially presented in Table 6-1 when discussing the 4fold-1sp/3sp/5sp. Each TV defect only appeared once in our experiment, which suggests the high formation energy of a tetravacancy. It is not surprising to see that the number of DV(555-777) is far more than the other defects, and the same phenomenon was also observed in Ti_2O_3 [88]. Given that there are quite a few commonalities between the Nb_2O_3 and Ti_2O_3 systems, we can apply the explanation in Ref. [88] here. Compared with the freestanding counterpart, the Au-supported Nb_2O_3 honeycomb monolayer is in a state of in-plane compressive strain. The removal of a Nb_2O_3 unit gives rise to a tensile strain in the freestanding film while a release of compressive strain in the Au-supported film. Besides, the alternative arrangement of the five- and seven-membered rings is the most efficient way to release the compressive strain among various permutations. Therefore, the DV(555-777) can possess the lowest defect formation energy and highest frequency of occurrence.

8.3.3 Vacancy reconstruction

The DV and TV defects discussed in the last section are essentially vacancy reconstruction, through which the remaining Nb atoms retain the threefold coordination in the defect domains. This section will discuss the reconstruction of large vacancy sites, including 6-, 10-, and 13-vacancy. Most of the resulting structures are not fully reconstructed, which means: (i) the number of remedied Nb atoms is less than that of the missing Nb atoms; (ii) there are twofold coordinated Nb atoms. Whether they carry dangling oxygen atoms cannot be determined, so we are not able to present the complete structural models with both Nb and O atoms. Nevertheless, we can solve the structures of some particular permutations that involve the fourfold coordinated Nb atoms in the reconstruction, as shown in Figure 6-6.

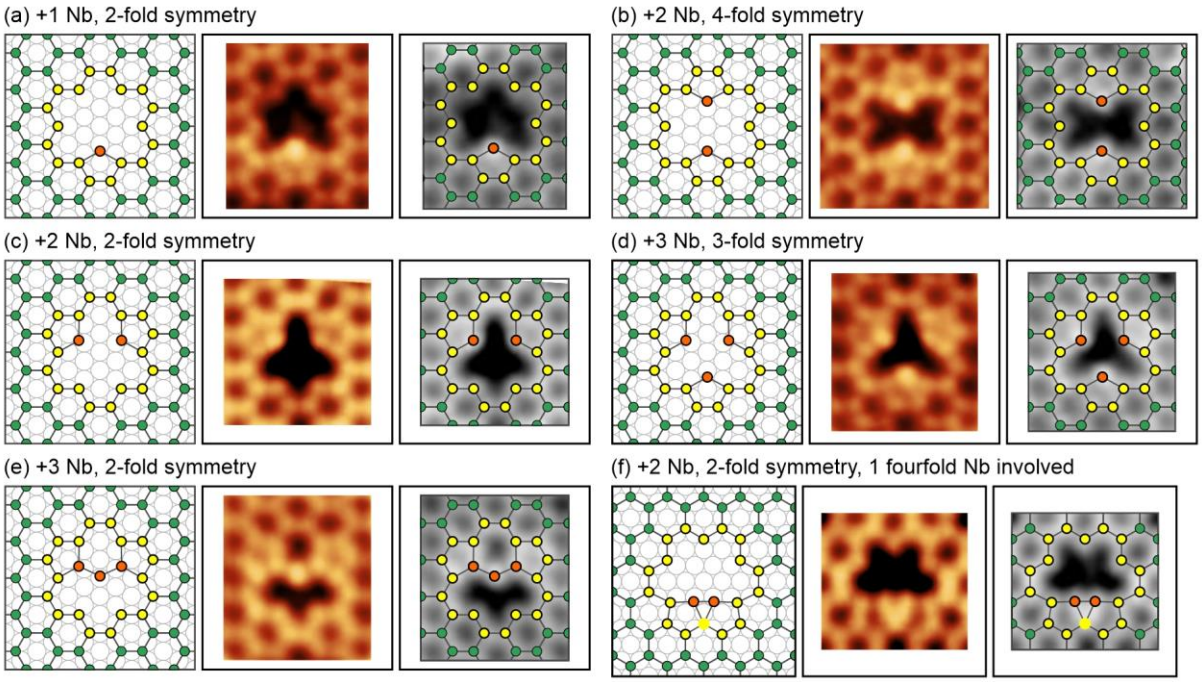

Figure 8-11 Reconstructions of the 6-vac defect. The number of remedied Nb atoms and symmetry are denoted on the top of each reconstruction. The orange circles represent the remedied Nb atoms. The circles with a yellow perimeter in (f) mark the fourfold coordinated Nb atoms. (f) has been analyzed in Figure 6-5. Frame size: 3.0 nm × 2.9 nm. Imaging conditions: (a) V_s = 0.8 V, I_t = 0.8 nA; (b) V_s = 0.8 V, I_t = 0.8 nA; (c) V_s = 1.0 V, I_t = 0.2 nA; (d) V_s = 0.8 V, I_t = 0.2 nA; (e) V_s = 1.0 V, I_t = 0.3 nA; (f) V_s = 0.8 V, I_t = 0.7 nA.

Figure 8-11 shows six reconstructed structures of the 6-vac defect, sorted by the number of remedied Nb atoms. Due to the substrate effect, both the vacancy site and the resulting reconstructions exhibit distinctly symmetrical structures. A 6-vac defect that undergoes a non-stoichiometric reconstruction can accommodate up to 3 remedied Nb atoms, as shown in Figure 8-11(d) and (e). Once it gets the fourth Nb atom, it can become the DV(555-777) with a stoichiometric atom configuration. Figure 8-11(f) shows a reconstructed structure with a Nb atom at the border becoming fourfold coordinated. An intuitive model for the transition has been proposed in Section 6.4.

The remedied Nb atoms usually lead to five- and/or seven-membered rings. Some become the terminal Nb atoms with twofold coordination and may look brighter than other Nb atoms at the border or in the honeycomb lattice outside the defect domain. For example, Figure 8-11(a) shows the simplest reconstruction (+ 1 Nb), in which the intensity of the remedied Nb atom is much higher than the others. Such contrast difference cannot be attributed to the same reason for the fourfold coordinated Nb atom. Presumably, this was caused by an atom displacement perpendicular to the surface or an enhancement of the LDOS due to the lattice strain. However, the remedied Nb atoms are not always brighter than the others. For instance, the brightness of the remedied Nb atom at the right pentagon in Figure 8-11(c) is approximate to the surrounding Nb atoms. One possible explanation is that the dangling oxygen may influence the LDOS of Nb atoms.

We take the simplest reconstruction in Figure 8-11(a) as an example and propose three models for the dangling oxygen configurations in Figure 8-12. Frame (a) depicts the most O-rich model, in which all twofold coordinated Nb atoms at the defect domain border bond to dangling oxygen atoms. In contrast, frame (b) shows the model with no dangling oxygen. Figure 8-11(c) shows a case between the two extreme states, in which some twofold coordinated Nb atoms carry dangling oxygen, but some do not.

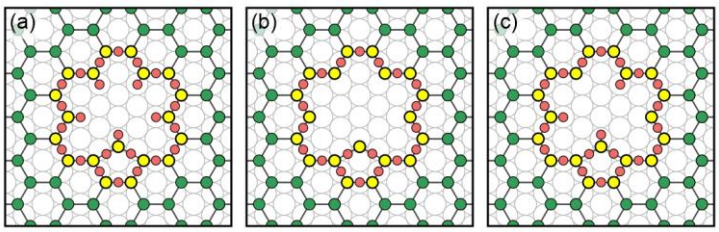

Figure 8-12 Possible models for the dangling oxygen configurations. (a) All the twofold coordinated Nb atoms in the defect domain carry dangling oxygen atoms. (b) No dangling oxygen. (c) A part of the twofold coordinated Nb atoms carries dangling oxygen.

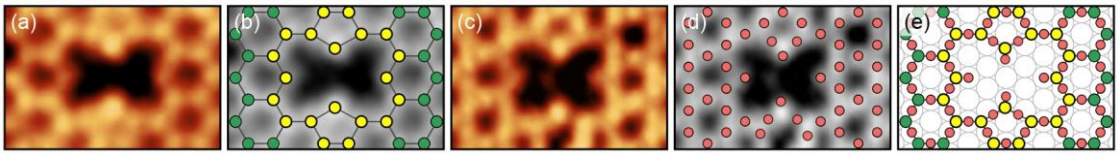

Figure 8-13 (a) STM image of a reconstructed structure of the 6-vac defect at a positive sample bias (V_s = 0.8 V, I_t = 0.8 nA). (b) Nb lattice model superimposed on (a) in grayscale. (c) STM image at a negative sample bias (V_s = -1.0 V, I_t = 1.0 nA). (d) A proposed O lattice model superimposed on (c) in grayscale. (e) Complete structural model. Image size: 2.9 nm × 1.9 nm.

Figure 8-13(a) shows the same reconstructed structure as Figure 8-11(b), but we simultaneously obtained the filled-state STM image of the defect domain [Figure 8-13(c)]. The two border Nb atoms in the horizontal direction carry dangling oxygen, whereas the situation for the two terminal Nb atoms in the vertical direction cannot be confirmed. The high intensity of the two terminal Nb atoms in the vertical direction may obscure the signal coming from oxygen, so we can only assume that they carry dangling oxygen in the proposed model [Figure 8-13(d), (e)].

Figure 8-14 displays a variety of the 10-vac defect reconstructions. As the 10-vac defect has more vacancy sites that can be filled with remedied Nb atoms, the reconstruction permutations are diverse and exhibit new traits. The simplest reconstruction in our experimental observation starts from two remedied Nb atoms with a central symmetry [Figure 8-14(a)]. Frame (b) – (g) demonstrate reconstructions from three remedied Nb atoms to six atoms. The reconstructed structure in Figure 8-14(g) and the TV(5555-7777) in Figure 8-9(a) can be differentiated by the gap between two central Nb atoms. In the TV(5555-7777), they are closed enough to be bridged by an oxygen atom; in Figure 8-14(g), they are separated by a larger gap and become twofold

coordinated Nb atoms that possibly carry two dangling oxygen atoms. Besides, Figure 8-14(h) can be seen as a derivative with a protrusion at the center. The core of the defect domain is able to accommodate an additional twofold coordinated Nb atom, which suggests that the TV(5555-7777) is in a state of large tensile strain. Figure 8-14(i) and (j) show two reconstructions with fourfold and twofold coordinated Nb atoms, so the structure cannot be solved due to the uncertainty of dangling oxygen. In contrast, the two reconstructed defect domains displayed in Figure 6-6(c) and (d), which also belong to 10-vac reconstructions, can be well-determined.

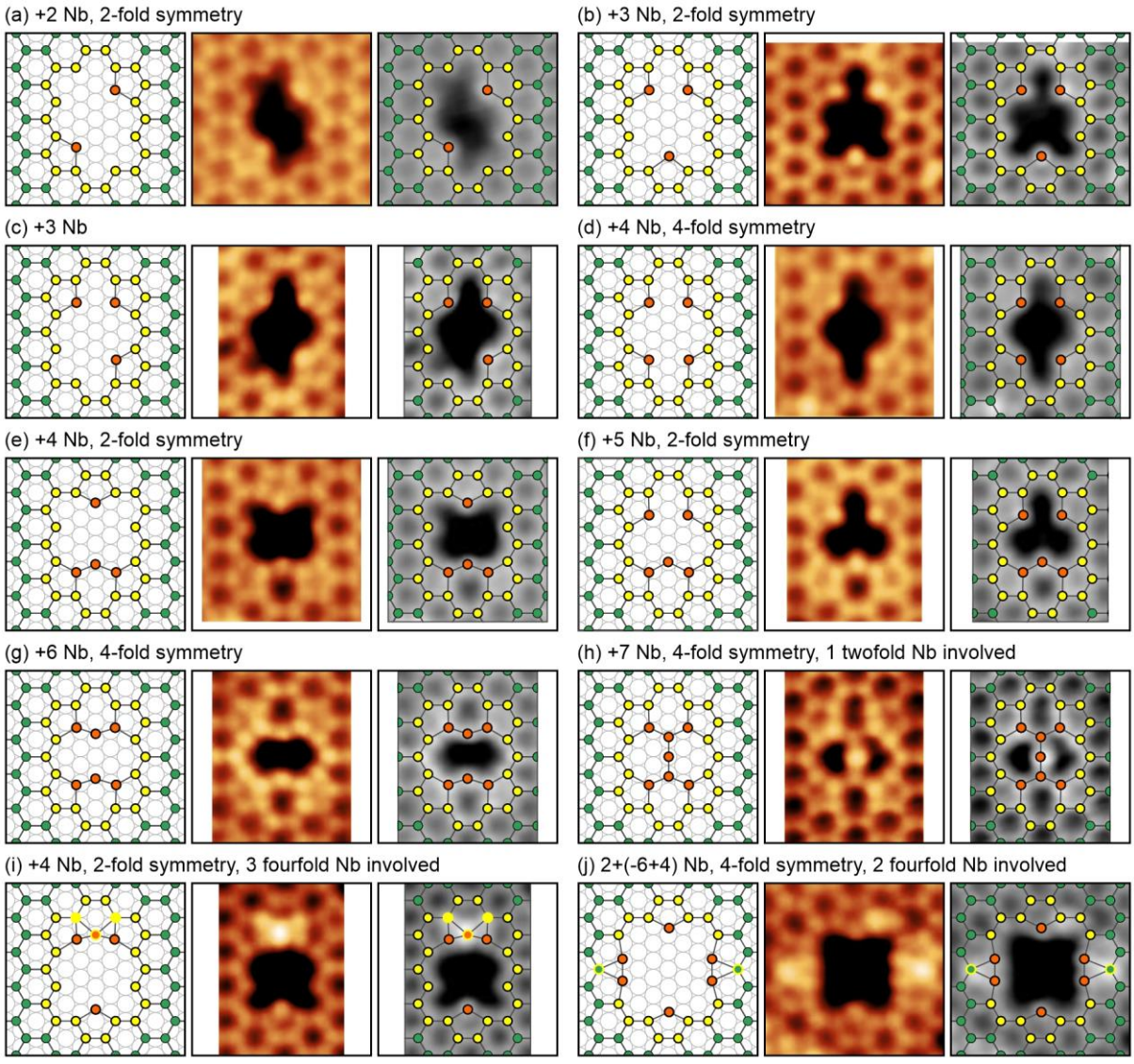

Figure 8-14 Reconstructions of the 10-vac defect. The fourfold coordinated Nb atoms are marked by circles with yellow perimeters. The reconstruction at one side in (j) can be seen as missing three Nb atoms first and then compensating by two atoms. So the change of Nb atom number at both sides is (-6+4); considering the two remedied Nb atoms in the vertical direction,

the total number of the remedied Nb atoms can be expressed as 2+(-6+4), namely 0. Frame size: 3.0 nm × 2.9 nm. Imaging conditions: (a) V_s = 0.8 V, I_t = 0.8 nA; (b) V_s = 1.0 V, I_t = 0.5 nA; (c) V_s = 0.8 V, I_t = 0.2 nA; (d) V_s = 1.0 V, I_t = 0.2 nA; (e) V_s = 0.8 V, I_t = 0.2 nA; (f) V_s = 0.8 V, I_t = 0.7 nA; (g) V_s = 0.8 V, I_t = 0.2 nA; (h) V_s = 2.0 V, I_t = 0.2 nA; (i) V_s = 1.0 V, I_t = 0.5 nA; (j) V_s = 0.8 V, I_t = 0.2 nA. Another two reconstructed structures of the 10-vac defect can been seen in Figure 6-6(c), (d).

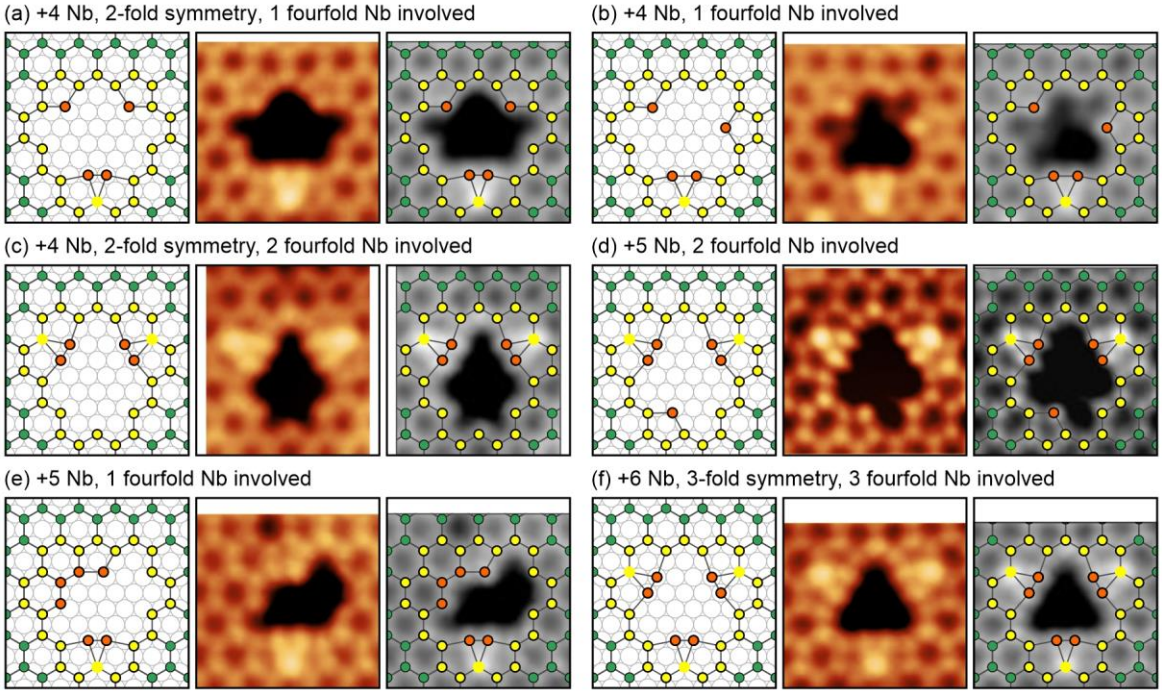

Figure 8-15 Reconstructions of the 13-vac defect. The defect domain is so large that almost all the reconstructions involved fourfold coordinated Nb atoms. (f) has been demonstrated in Figure 6-8. The structure can be determined as no twofold Nb involved. Frame size: 2.9 nm × 3.0 nm. Imaging conditions: (a) V_s = 1.0 V, I_t = 0.2 nA; (b) V_s = 0.8 V, I_t = 0.7 nA; (c) V_s = 0.8 V, I_t = 0.2 nA; (d) V_s = 1.0 V, I_t = 0.5 nA; (e) V_s = 0.8 V, I_t = 0.2 nA; (f) V_s = 1.0 V, I_t = 0.2 nA.

When the defect domain further expands to have 13 vacancy sites, almost all the reconstructed structures contain fourfold coordinated Nb atoms, as shown in Figure 8-15. The transition from a threefold coordinated Nb to a fourfold coordinated Nb enables the compensation with more oxygen atoms. We have discussed the reconstructed structure in Figure 8-14(f) in Figure 6-8 and claimed that it is more O-deficient compared with Recon-(III) and Recon-(IV) in Figure 6-7. This does not conflict with the statement here because defect domains in Figure 6-7 (10-vac) and Figure 6-8 (13-vac) are different. For a specific domain with several solvable structures, a fourfold coordinated Nb atom in the lattice can bond to four oxygen atoms, which means the local chemical environment is more oxidized.

8.4 Line defects in Nb_2O_3 honeycomb monolayers

A line defect is usually found at a boundary where two monolayers with the same structure are grown together. Such defect is generally described as a 2D grain boundary with a rotational misalignment. A domain boundary is a particular case of the grain boundary in which the tilting angle between two monolayers is zero. The lattices of these two monolayers usually have translational offsets with respect to each other in vertical and/or lateral directions, giving rise to several structural solutions to the gap. The atom permutation in a boundary gap can be periodic or non-periodic and is strongly affected by the substrate. The 2D honeycomb monolayers that are epitaxially grown on a substrate exhibit unique domain boundaries [94,105,107,253,254]. It has been shown that the substrate plays a critical role in atom arrangement and formation energy of the domain boundary.

In this section, we will present a variety of domain boundaries in the (2 × 2) Nb_2O_3 honeycomb monolayers. As the Au(111) substrate blocks the position of the (2 × 2) HC lattice, the lateral offset and vertical gap between the two domains are discrete values. The frequency of occurrence can be used to roughly compare the formation energies of different domain boundaries, but DFT calculations are still required in order to have an accurate evaluation. The theoretical work is underway with our collaborators from Paris, so here we focus on the structural characterization of the DBs and propose the corresponding lattice models. Some of them may not be very satisfying but are the optimal solutions that we could develop. Apart from the domain boundaries, we will show two compelling experimental observations: the triple junction of three DBs and the small-angle grain boundary caused by the substrate discontinuity.

8.4.1 DB classification and nomenclature

We follow the nomenclature rule for the (2 × 2) Ti_2O_3 honeycomb in Ref. [254]. The honeycomb edge can be zigzag-oriented (Z) along $[\bar{1}10]$, $[0\bar{1}1]$, and $[10\bar{1}]$, or armchair-

oriented along $[11\bar{2}]$ and its threefold equivalents, or an intermediate edge. Two domains with zigzag-oriented edges and the same crystallographic orientation form a Z1 boundary. The same orientation means the lateral shift along $[\bar{1}10]$ is zero, as shown in Figure 8-16(a). By contrast, A Z2 boundary is formed when there is a lateral shift of r_{Au} = 1.44 nm, which is half of the Au-Au distance (d_{Au} = 2.88 nm) in the (111) plane, as shown in Figure 8-16(b). Similarly, two domains with armchair-oriented edges will create either an A1 boundary with no later shift [Figure 8-16(c)] or an A2 boundary with a shift of $\sqrt{3}r_{Au}$ along the $[11\bar{2}]$ direction [Figure 8-16(d)]. The gap distance between two domains can be varied but has to adopt discrete values due to the requirement of the epitaxial relationship. Boundary gaps are clarified by two orange dash lines with gap distances denoted in the following figures. A boundary may correspond to several structural solutions, either ordered or disordered. In the following section, we will summarize the ordered solutions and display a few disordered domain boundaries of Nb_2O_3 HC monolayers. Relevant content for Ti_2O_3 HC will be presented in Section 8.5.2.

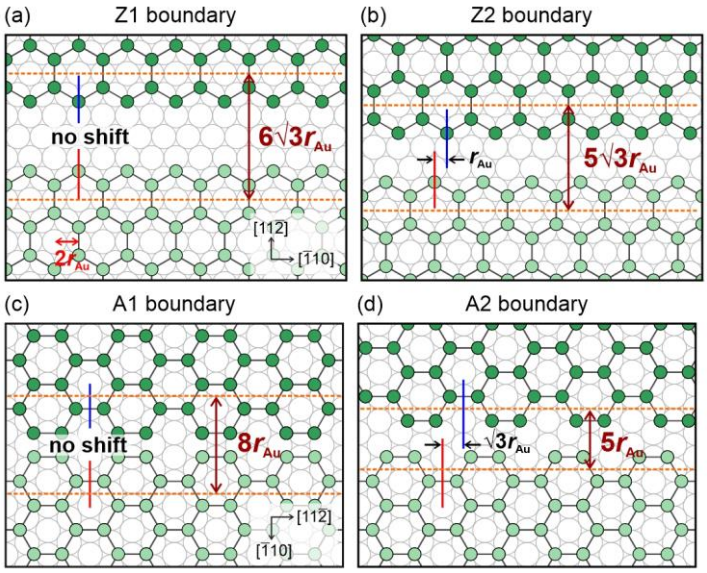

Figure 8-16 Domain boundary classification. Lattices with dark green circles and light green circles represent two Nb_2O_3 HC domains. Blue and red lines indicate the lateral shift. The gap between two domains in the vertical direction is clarified by two orange dash lines; the red arrow marked the gap distance. (a) Z1 boundary, no lateral shift, gap distance in this schematic is $6\sqrt{3}r_{Au}$. (b) Z2 boundary, lateral shift: r_{Au}, gap in the schematic: $5\sqrt{3}r_{Au}$. (c) A1 boundary, no lateral shift, gap in the schematic: $8r_{Au}$ (d) A2 boundary, lateral shift: $\sqrt{3}r_{Au}$, gap in the schematic: $5r_{Au}$.

8.4.2 Ordered solutions to Z1, Z2, and A1 boundaries

Figure 8-17 presents two structural solutions to the Z1 domain boundary with a gap of $4\sqrt{3}r_{Au}$. The first structural solution to the gap comprises a set of distorted hexagons and is called the Z1-distorted 6 DB [Figure 8-17(b) – (d)]. The Nb atoms within the gap are threefold coordinated and slightly shifted from their original hollow sites. In contrast, the second solution involves fourfold coordinated Nb atoms [Figure 8-17(e) – (g)]. This domain boundary has been discussed in Section 6.5. The repeated unit comprises two rhombuses, so we call it the Z1-44 DB.

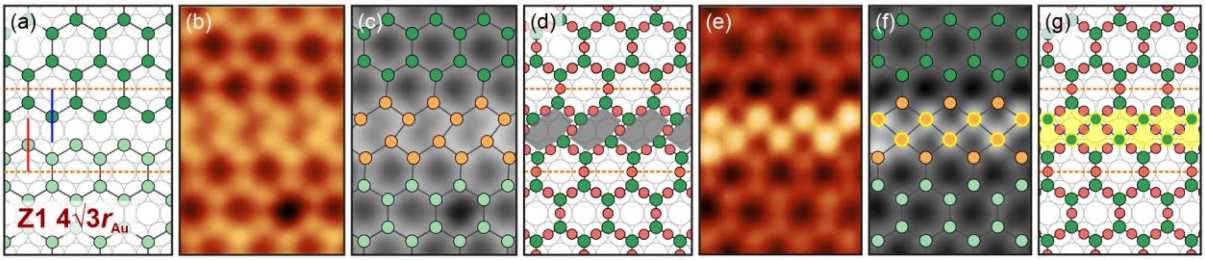

Figure 8-17 Two structural solutions to the Z1 DB with a gap of $4\sqrt{3}r_{Au}$. Frame size: 2.0 nm × 3.0 nm. (a) Schematic of two domains forming a Z1 boundary with a gap of $4\sqrt{3}r_{Au}$. (b) STM image of the Z1-distorted 6 DB (V_s = 0.8 V, I_t = 0.8 nA). (b) Nb lattice model superimposed on (b) in grayscale. (d) Complete structural model with Nb (green) and O atoms (red). The repeated units are marked in grey. (e) STM image of the Z1-44 DB (V_s = 1.0 V, I_t = 0.2 nA). (f) Nb lattice model superimposed on (e) in grayscale. The fourfold coordinated Nb atoms are marked by circles with a yellow perimeter. (g) Complete structural model with repeated units in yellow.

Three DB structures have been identified as solutions to the gap of $6\sqrt{3}r_{Au.}$ The structure of the Z1-5775 DB shown in Figure 8-18 is well-determined according to the empty-state and filled-state STM images in the same region. All the Nb atoms within the boundary maintain the threefold coordination, but those from the middle row in Figure 8-18(b), (c) are located at bridge sites of Au atoms, thus appearing slightly brighter than the lattice Nb at hollow sites. Figure 8-19 shows the second solution with fourfold coordinated Nb atoms involved. The repeated unit is composed of a square at the center and six surrounding pentagons, so we call it the Z1-5554555 DB. In addition, two bright protrusions are clearly visible in the STM image, which are probably due to adatoms from the second layer.

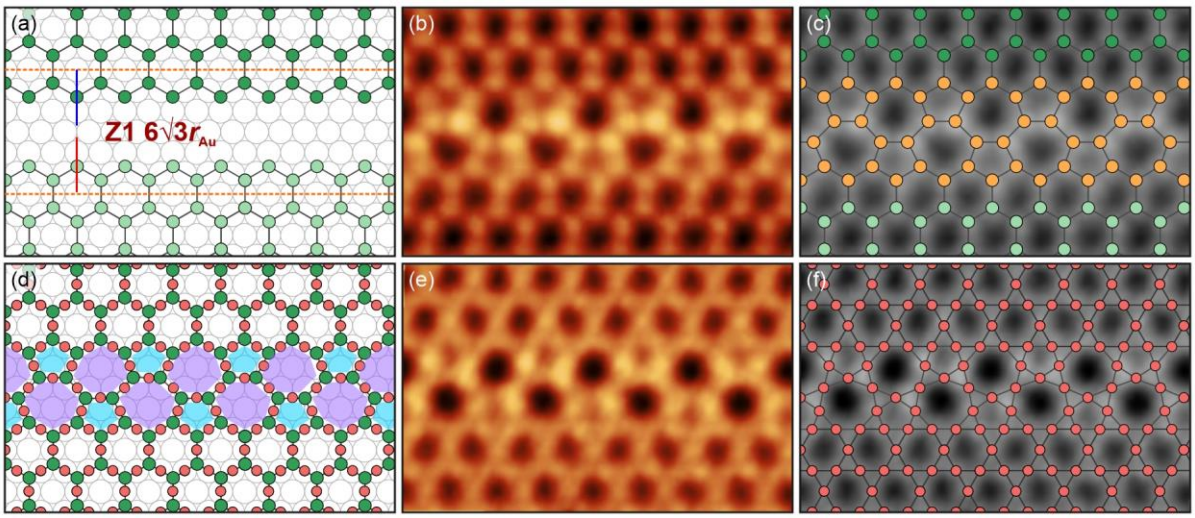

Figure 8-18 Structural solution to the Z1 DB with a gap of $6\sqrt{3}r_{Au}$. Frame size: 4.7 nm × 3.0 nm. (a) Schematic of two domains forming a Z1 boundary with a gap of $6\sqrt{3}r_{Au}$. (b) Empty-state STM image of the Z1-5775 DB (V_s = 1.0 V, I_t = 0.2 nA). (c) Nb lattice model superimposed on (b) in grayscale. (d) Complete structural model. Repeated units are filled with colors: pentagons: cyan; heptagons: purple. (e) Filled-state STM image of the Z1-5775 DB (V_s = -1.7 V, I_t = 1.0 nA). (f) O lattice model superimposed on (e) in grayscale.

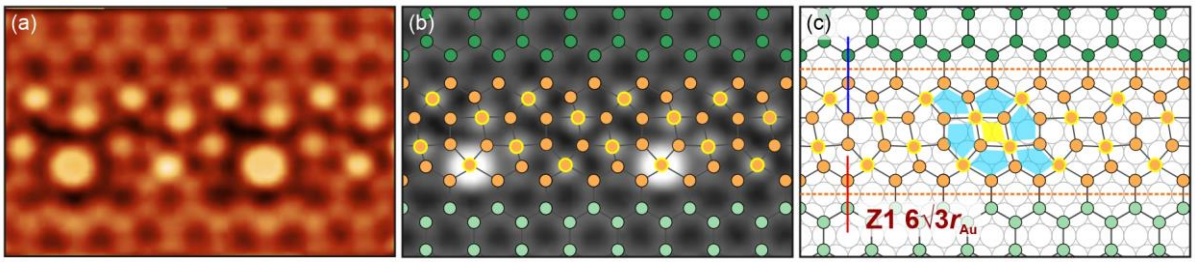

Figure 8-19 Structural solution to the Z1 DB with a gap of $6\sqrt{3}r_{Au}$. Frame size: 4.7 nm × 3.0 nm. (a) STM image of the Z1-5554555 DB (V_s = 1.0 V, I_t = 0.2 nA). (b) Nb lattice model superimposed on (a) in grayscale. (c) Structural model on Au(111) with a repeated unit 555-4-555 marked in colors: square: yellow; pentagons: cyan.

We also observed the third solution to the $6\sqrt{3}r_{Au}$ gap and named it the Z1-S1 DB, as shown in Figure 8-20. Although it possesses a clear periodicity, we got in trouble when solving the structure. The model we proposed in Figure 8-20(b), (c) contains both fourfold and twofold coordinated Nb atoms. The eight brightest protrusions hinder the observation of other atoms in the vicinity, so we are unable to resolve the atom arrangement. The structural model is not very convincing, but it is the most reasonable solution we could devise.

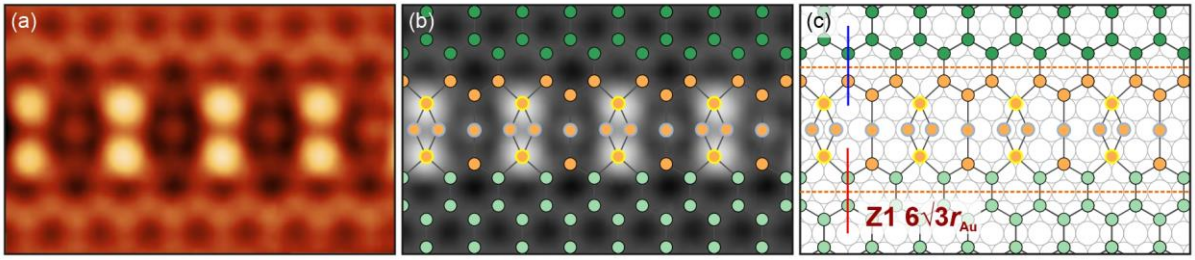

Figure 8-20 Structural solution to the Z1 DB with a gap of $6\sqrt{3}r_{Au}$. Frame size: 4.7 nm × 3.0 nm. (a) STM image of the Z1-S1 (V_s = 0.8 V, I_t = 0.5 nA). (b) Proposed Nb lattice model superimposed on (a) in grayscale. (c) Proposed model on Au(111), the coordination number of the Nb atoms in the middle row cannot be well-determined. Orange circles with a grey perimeter represent Nb atoms that are supposed to be twofold coordinated.

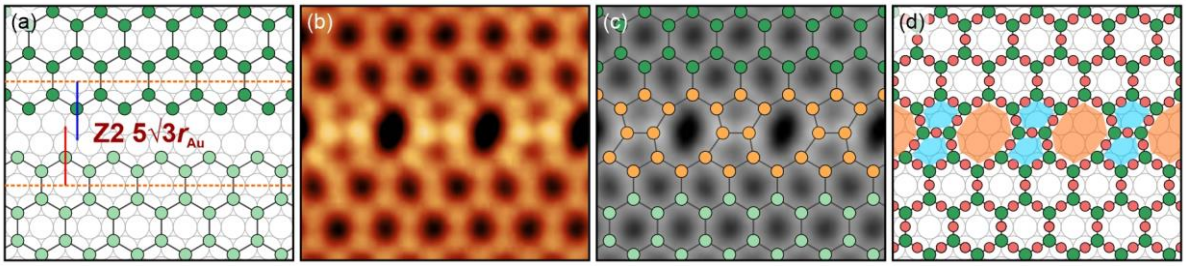

Figure 8-21 Structural solution to the Z2 DB with a gap of $5\sqrt{3}r_{Au}$. Frame size: 3.6 nm × 3.0 nm. (a) Schematic of two domains forming a Z2 boundary with a gap of $5\sqrt{3}r_{Au}$. (b) STM image of the Z2-558 DB (V_s = 0.7 V, I_t = 0.5 nA). (c) Nb lattice model superimposed on (b) in grayscale. (d) Structural model on Au(111) with a repeated unit 558 marked in colors: pentagons: cyan; octagons: orange.

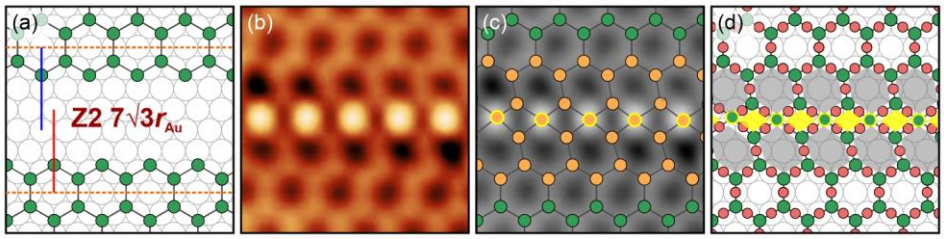

Figure 8-22 Structural solution to the Z2 DB with a gap of $7\sqrt{3}r_{Au}$. Frame size: 2.7 nm × 2.7 nm. (a) Schematic of two domains forming a Z2 boundary with a gap of $7\sqrt{3}r_{Au}$. (b) STM image of the Z2-646 DB (V_s = 0.8 V, I_t = 0.5 nA). (c) Nb lattice model superimposed on (b) in grayscale. (d) Complete structural model on Au(111) with a repeated unit 646 marked in colors: rhombus: yellow; distorted hexagons: grey.

Regarding the Z2 domain boundary, Figure 8-21 shows the STM image and corresponding structural model of the Z2-558, which is a common solution to the gap of $5\sqrt{3}r_{Au}$. Figure 8-22 gives a solution to the gap of $7\sqrt{3}r_{Au}$, which has been demonstrated in Figure 6-13.

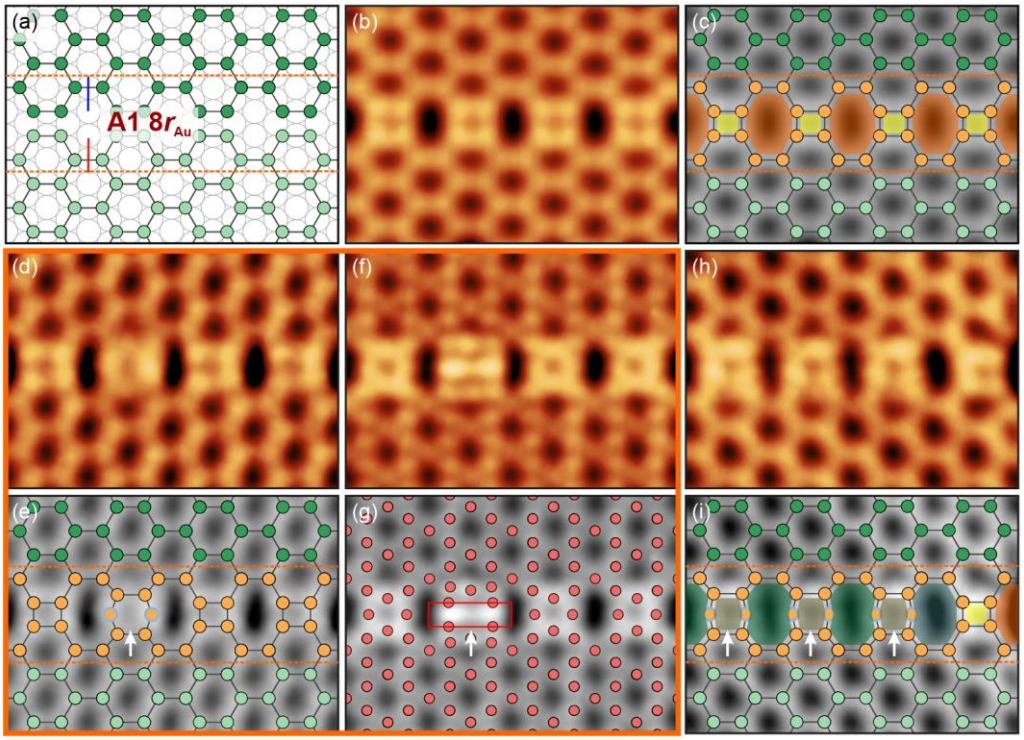

Figure 8-23 (a) Schematic of two domains forming an A1 boundary with the gap of $8r_{Au}$. (b) STM image of the A1-48 DB (V_s = 0.7 V, I_t = 0.5 nA). (c) Nb lattice model superimposed on (b) in grayscale with repeated units filled with different colors. (d) – (g) STM images and corresponding models for the same region. The white arrows indicate a special unit. (d) Empty-state STM image of an A1 DB mainly based on the 48 units but with a squeezed unit (V_s = 0.7 V, I_t = 1.0 nA). (e) Proposed Nb lattice model, two circles with a grey perimeter are twofold coordinated. (f) Filled-state STM image (V_s = -0.6 V, I_t = 1.0 nA). (d) Proposed O lattice model. Region in the red box is supposed to comprise four O atoms. (h) STM image of the A1-6(10) DB mainly based on the special unit but with a 48 unit at the tail (V_s = 0.8 V, I_t = 0.5 nA). (i) Proposed Nb lattice model superimposed on (h) in grayscale. Frame size: 4.0 nm × 2.9 nm.

The structural solutions to the armchair-oriented DB are not as diverse as the zigzag-oriented DB. The A1-48 is a solution to an A1 DB with a gap of $8r_{Au}$ [Figure 8-23(b), (c)]. The complete structure can be well determined based on the filled-state STM image in Figure 8-23(f). However, a special unit can be seen in Figure 8-23(d) – (g) where the white arrows indicate. It seems that more Nb atoms are squeezed into the region that should initially accommodate four atoms. We cannot determine the exact atom arrangement in the squeezed unit due to insufficient resolution, so we speculate that two additional Nb atoms with twofold coordination (marked by circles with a grey perimeter) are included. The difference to the common AC-48 is more obvious in the filled-state STM image [Figure 8-23(f)], which is convincing evidence that it is

a new configuration, although we are not sure about the O atom arrangement in the red box. Moreover, this special unit can arrange periodically, thus becoming a second solution to the gap of $8r_{Au}$, as shown in Figure 8-23(h). The four-membered ring at the right end of the boundary is in sharp contrast to the special unit. According to the repeated unit in the proposed model, we call it A1-6(10) DB.

8.4.3 Disordered solutions to Z2 and A1 boundaries

Non-hexagonal polygons can fill domain boundary gaps with a relatively flexible combination, which can be regarded as disordered solutions. They do not exhibit a well-defined periodicity along specific directions and appear less frequently. Therefore, it is hard to do any theoretical calculations to examine the formation energy.

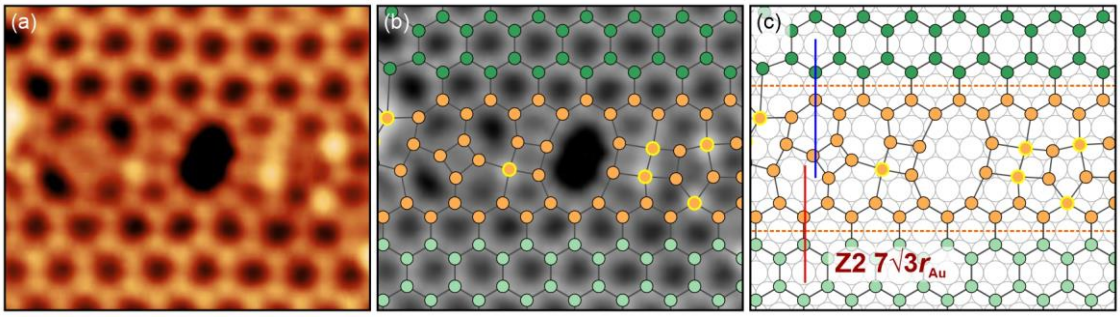

Figure 8-24 Disordered solution to the Z2 DB with a gap of $7\sqrt{3}r_{Au}$. Frame size: 4.8 nm × 4.0 nm. (a) STM image of the DB (V_s = 0.8 V, I_t = 0.3 nA). (b) Nb lattice model superimposed on (a) in grayscale. (c) Structural model on Au(111).

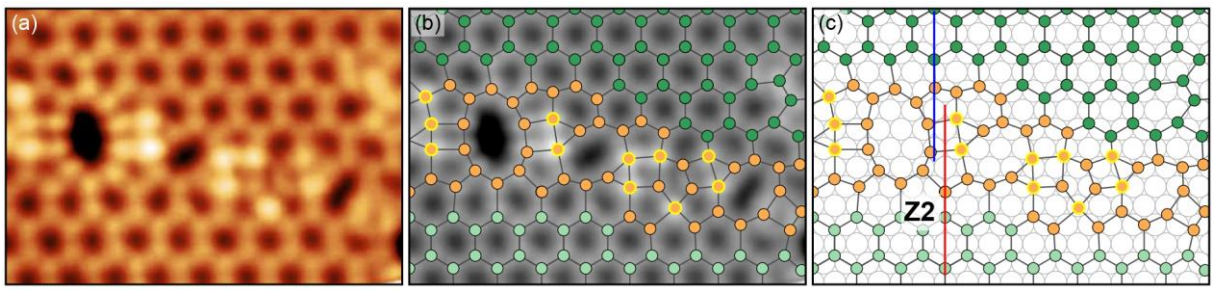

Figure 8-25 Disordered solution to a local Z2 DB. Frame size: 5.2 nm × 3.6 nm. (a) STM image of the local Z2 DB (V_s = 1.0 V, I_t = 0.5 nA). (b) Nb lattice model superimposed on (a) in grayscale. (c) Structural model on Au(111) indicating the local Z2 relationship.

Figure 8-24 shows a solution to the Z2 DB with a gap of $7\sqrt{3}r_{Au}$, which has a unique atom permutation. A decagon is located at the image center; Two pairs of heptagons and compressed hexagons are distributed alternatively on the right side, forming an internal square. In contrast, the extension direction of the domain boundary in Figure 8-25 is no longer along $[\bar{1}10]$, it can still be seen as a local Z2 DB as indicated in Figure 8-25(c). The Nb configuration at the left side in Figure 8-25(b) exhibits a mirror symmetry with the middle part in Figure 8-24(b).

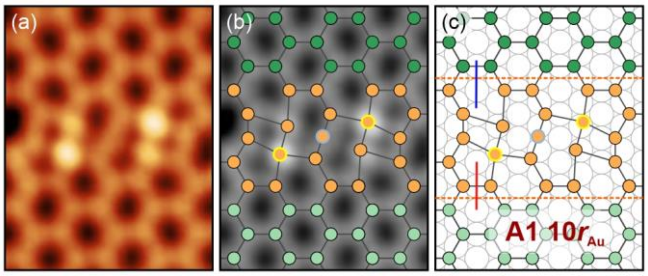

Figure 8-26 Disordered solution to the A1 DB with a gap of $10r_{Au}$. Frame size: 2.5 nm × 3.2 nm. (a) STM image of the A1-S1 DB (V_s = 0.7 V, I_t = 0.5 nA). (b) Nb lattice model superimposed on (a) in grayscale. (d) Structural model on Au(111) showing the central symmetry. The central Nb atom is supposed to be twofold coordinated.

The domain boundary in Figure 8-26 displays a central symmetry. It is a solution to a local A1 DB with a gap of $10r_{Au}$. We speculated that the protrusion at the center was due to a twofold coordinated Nb atom. Although a fourfold coordinated Nb atom is more reasonable in geometry, it does not possess a high brightness, which is a critical feature of the fourfold coordinated Nb atom. In short, these three examples all contain fourfold coordinated Nb atoms that allow the Nb_2O_3 HC monolayer to form non-hexagonal polygons with a random arrangement.

8.4.4 Solutions to A2 boundaries

DFT calculations have shown that the A2 DB possesses much higher formation energy than the Z1, Z2, or A1 DB in Ti_2O_3 HC monolayers [254]. This can also be reflected from Nb_2O_3 HC monolayers as we did not observe any A2 boundary solution with a periodic atom arrangement along the [112] direction. However, inspired by the two examples in Figure 8-27 and Figure

8-28, we presume that a boundary declination is required to overcome the high formation energy, leading to a stepped A2 DB.

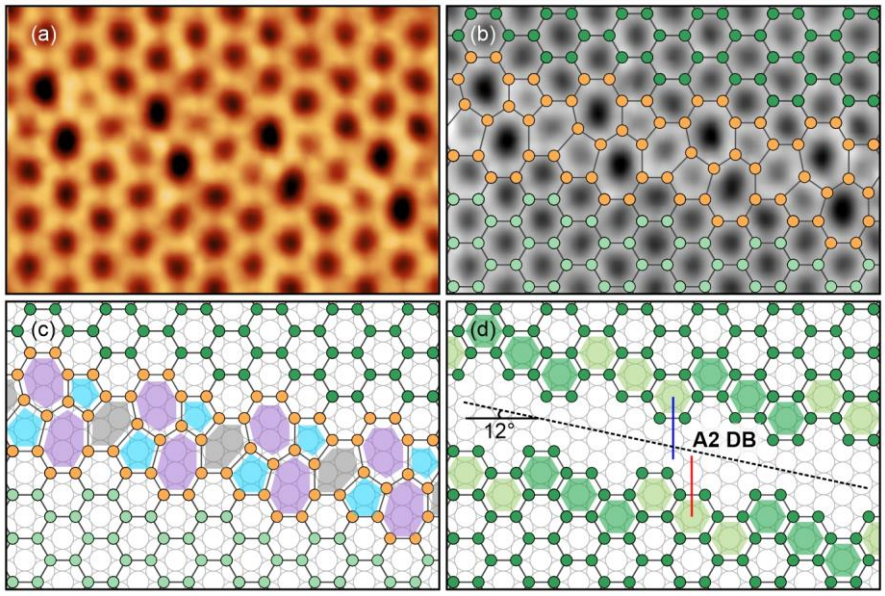

Figure 8-27 Stepped A2 DB with a repeated unit of 65775 in Nb_2O_3 HC. Frame size: 5.7 nm × 3.8 nm. (a) STM image of the stepped A2 DB (V_s = 0.75 V, I_t = 0.6 nA). (b) Nb lattice model superimposed on (a) in grayscale. (c) Nb lattice model on Au(111) with repeated units marked in different colors: pentagons: cyan; distorted hexagons: grey; heptagons: purple. (d) Schematic of the two domains with stepped edges. The extension direction of the boundary, indicated by the black dash line, has a tilting angle of 12° with respect to [112].

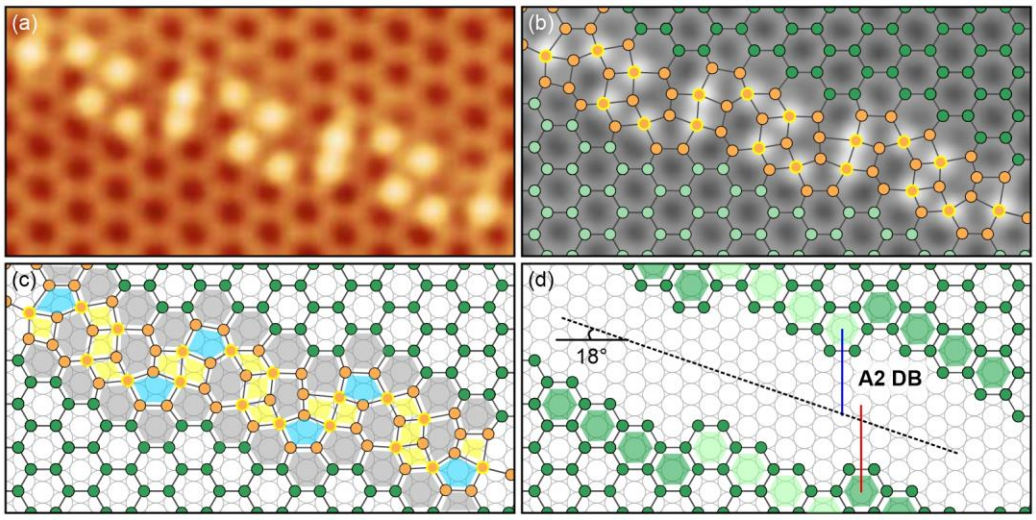

Figure 8-28 Stepped A2 DB composed of fourfold coordinated Nb atoms in Nb_2O_3 HC. Frame size: 6.7 nm × 3.3 nm. (a) STM image of the stepped (V_s = 1.0 V, I_t = 0.5 nA). (b) Nb lattice model superimposed on (a) in grayscale. (c) Nb lattice model on Au(111) with repeated units marked in different colors: squares: yellow; pentagons: cyan; distorted hexagons: grey. (d) Schematic of the two domains with stepped edges. The extension direction of the boundary, indicated by the black dash line, has a tilting angle of 18° with respect to [112].

The stepped DB in Figure 8-27(a) is constituted by repeated units of 65775. It can be assigned to an A2 DB if only considering the local crystallographic relationship of the two domains. However, the extension direction of the whole domain boundary has a tilting angle of around 12° with respect to the [112] direction, as indicated by the black dashed line in Figure 8-27(d). Similarly, Figure 8-28 shows a stepped DB with a tilting angle of 18° and a more complicated atom configuration due to the engagement of fourfold coordinated Nb atoms.

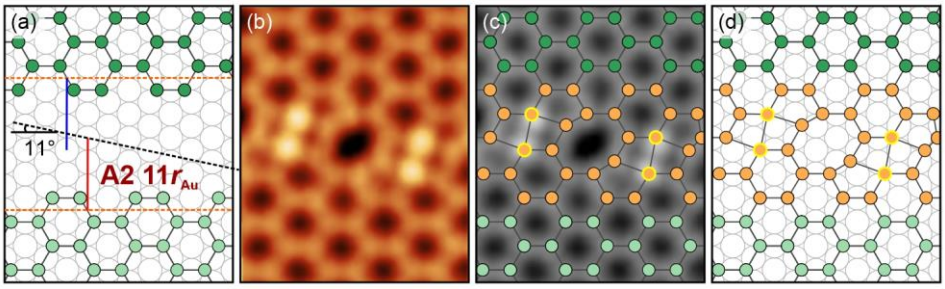

Figure 8-29 A local A2 DB with central symmetry. Frame size: 2.7 nm × 3.3 nm. (a) Schematic of two domains forming an A2 boundary with a gap of $11r_{Au}$. The extension direction of the A2 DB is indicated by the black dash line, passing through the center of symmetry. The tilting angle of this A2 DB is around 11° with respect to [112]. (b) STM image of the local A2 DB (V_s = 0.7 V, I_t = 0.5 nA). (c) Nb lattice model superimposed on (a) in grayscale. (d) Structural model on Au(111).

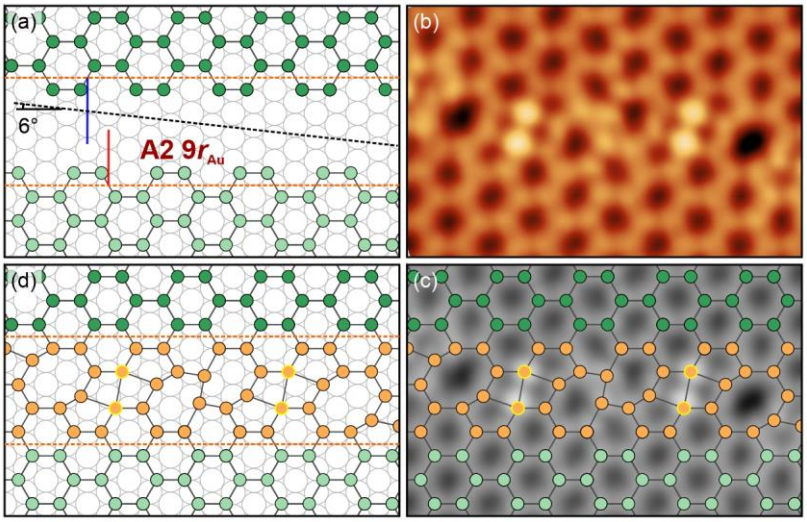

Figure 8-30 A local A2 DB with central symmetry. Frame size: 4.7 nm × 3.0 nm. (a) Schematic of two domains forming an A2 boundary with a gap of $9r_{Au}$. The tilting angle of the A2 DB is indicated by the black dashed line, around 6° with respect to [112]. (b) STM image of the A2 DB (V_s = 0.7 V, I_t = 0.5 nA). (c) Nb lattice model superimposed on (b) in grayscale. (d) Structural model on Au(111).

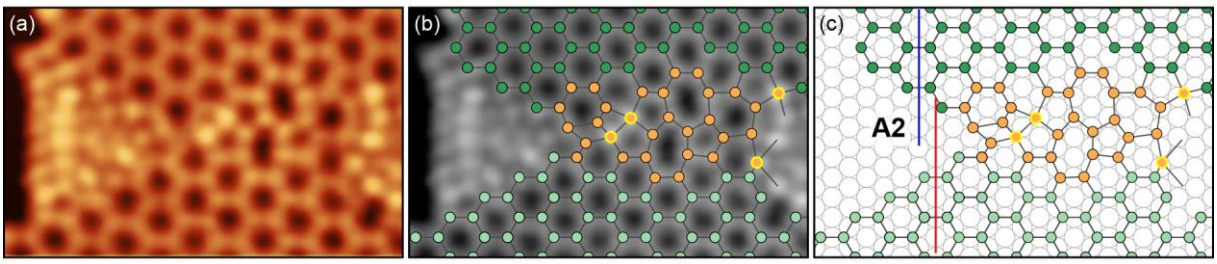

Figure 8-31 (a) STM image of a local A2 DB terminated by a triangle structure (Inlaid-T) (5.8 nm × 3.6 nm, V_s = 0.7 V, I_t = 0.5 nA). (b) Nb lattice model superimposed on (a) in grayscale. Atom arrangement at the inlaid-T is omitted here; the structure is elucidated in Section 9.3.2, see Figure 9-37. (c) Nb lattice model on Au(111).

Besides, we observed some short-ranged DBs that locally comply with the A2 characteristic. The two domain boundaries in Figure 8-29 and Figure 8-30 exhibit central symmetry. Although the parallel orange dash lines mark the boundary gap, the black dash line that passes through the center of symmetry indicates the real extension direction. The tilting angle is 11° and 6°, respectively, which confirms our assumption that the boundary declination is a requirement for forming an A2 DB. Figure 8-31 also shows a local A2 DB with a random arrangement of the polygons. The interesting feature is that there is an inlaid-T acting as a DB termination at the right end. The HC-connected triangle structure will be discussed in detail in Chapter 9. This DB structure implies that apart from a boundary declination, the random arrangement of polygons is an alternative way to overcome the high formation energy of an A2 boundary.

8.4.5 Triple junction formed by three DBs

We have observed triple junctions in the study of Nb_2O_3 domain boundaries. In a 3D polycrystalline material, a triple junction is a line defect where three grain boundaries meet; while in a 2D material, a triple junction can be seen as a point defect [257]. Studies concerning the triple junction of the 2D materials with a honeycomb structure have been carried out on graphene [257] and silicon [258]. It is predicted that the triple junction can strongly affect the mechanical and electronic properties of materials [257,259].

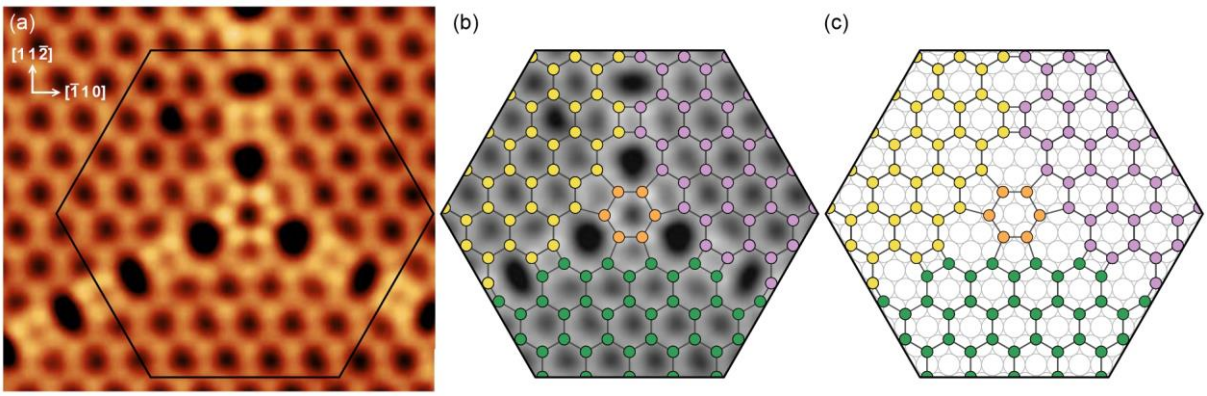

Figure 8-32 (a) STM image of a triple junction formed by three A1-48 DBs (6.4 nm × 5.1 nm, V_s = 0.7 V, I_t = 0.5 nA). (b) Nb lattice model superimposed on the region in the hexagonal box in (a). Three domains are depicted in different colors. (c) Nb lattice model on Au(111).

The intersection of three A1-48 domain boundaries results in a triple junction with threefold symmetry in Figure 8-32. It consists of a central hexagon, which is rotated by 30° with respect to the lattice honeycomb, and three surrounding pentagons and octagons that are alternatively arranged. The three Nb_2O_3 domains have the same crystallographic orientation and are depicted in different colors in the model in Figure 8-32(b), (c). This triple junction was not observed or predicted in graphene in Ref. [257], which suggests that the Au(111) substrate has a significant impact on the triple junction of the Nb_2O_3 DBs.

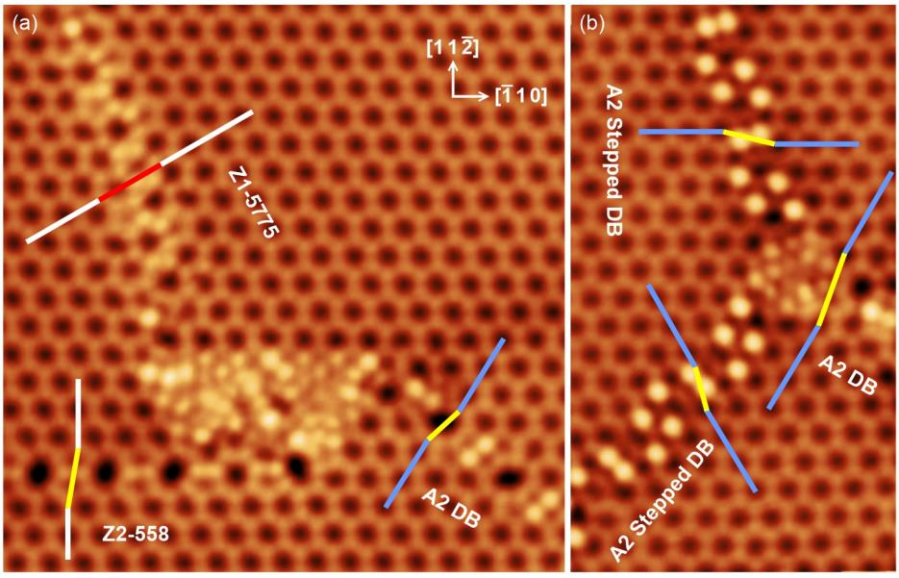

Figure 8-33 Two examples of the Confined-T acting as a triple junctions. The zigzag-oriented and armchair-oriented DBs are represented by white and blue lines, respectively. (a) 10.0 nm × 10.1 nm, V_s = 0.7 V, I_t = 0.5 nA; (b) 5.8 nm × 10.1 nm, V_s = 0.5 V, I_t = 0.5 nA.

The confined triangle (Confined-T) structures in the Nb_2O_3 honeycomb can also act as triple junctions of three DBs, two examples are presented in Figure 8-33. The domain shifts are indicated by polylines, and boundary types are denoted on the STM images. A regular Confined-T has threefold symmetry (see Section 9.3.3), which makes it have the potential for being an intersection of three DBs. Compared with the simple atom arrangement in Figure 8-32, Confined-Ts are able to accommodate excessive Nb atoms in a limited area.

8.4.6 Grain boundary

Domain boundaries with a zero tilting angle are exceptional cases of grain boundaries, which can be attributed to the epitaxial relationship between the (2 × 2) honeycomb monolayer and the single-crystalline Au(111) substrate. However, the Au substrate can be discontinuous, for example, a polycrystalline region composed of two grains with a small tilting angle. When two Nb_2O_3 honeycomb monolayers met at such a defective region on the Au(111) substrate, a grain boundary would be formed instead of a domain boundary.

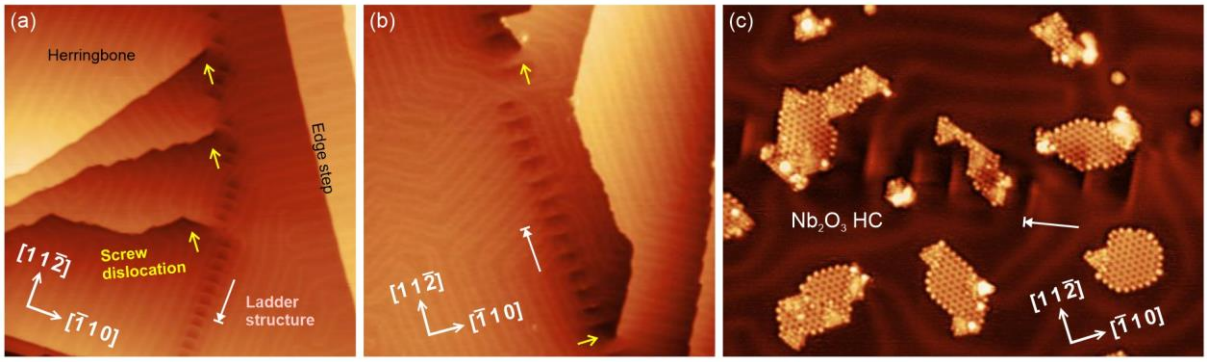

Figure 8-34 (a), (b) STM images of the Au(111) substrates (75 nm × 75 nm, a: V_s = 2.0 V, I_t = 0.15 nA; b: V_s = 2.0 V, I_t = 0.16 nA). The screw dislocations and the ladder structures are indicated by yellow and white arrows, respectively. (c) Small Nb_2O_3 honeycomb islands on the Au(111) substrate with a ladder structure (38.2 nm × 27.9 nm, V_s = 0.8 V, I_t = 0.6 nA).

Figure 8-34(a) and (b) show two STM images of the pristine Au(111) surfaces. The yellow arrows indicate the screw dislocation of the Au substrates, which can influence the nucleation and crystal growth of thin films [260]. We can also see a periodic defect structure on the surface,

which looks like a ladder (marked by the white arrow). Figure 8-34(c) shows some small Nb_2O_3 HC islands on Au(111). Their growth is barely affected by the ladder structure as the islands' sizes are pretty small. However, the substrate effect is pronounced when the film expands. For example, the three depression sites in Figure 8-35 are caused by the ladder structure. The grain boundary at the left side of the middle depression can also be attributed to the substrate defect.

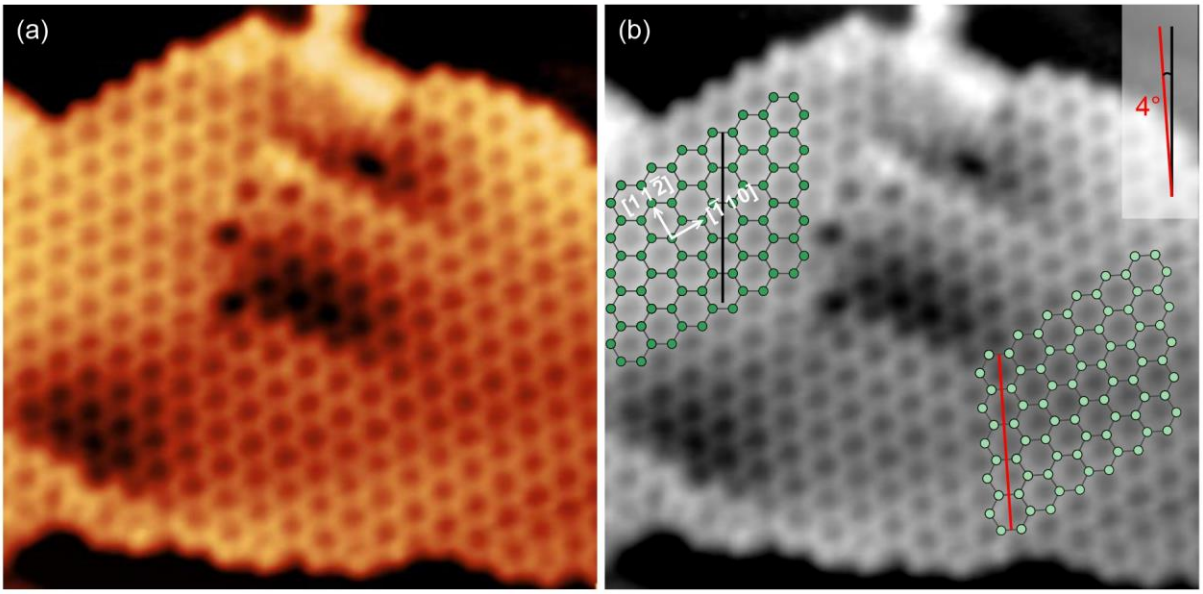

Figure 8-35 (a) STM image of a Nb_2O_3 honeycomb monolayer grown on the ladder structure of the Au(111) surface (7.9 nm × 7.7 nm, V_s = 0.7 V, I_t = 0.5 nA). Three depression sites and a grain boundary in the vicinity of the middle depression can be seen in the image. (b) Nb lattices superimposed on two domains showing a tilting angle of 4°.

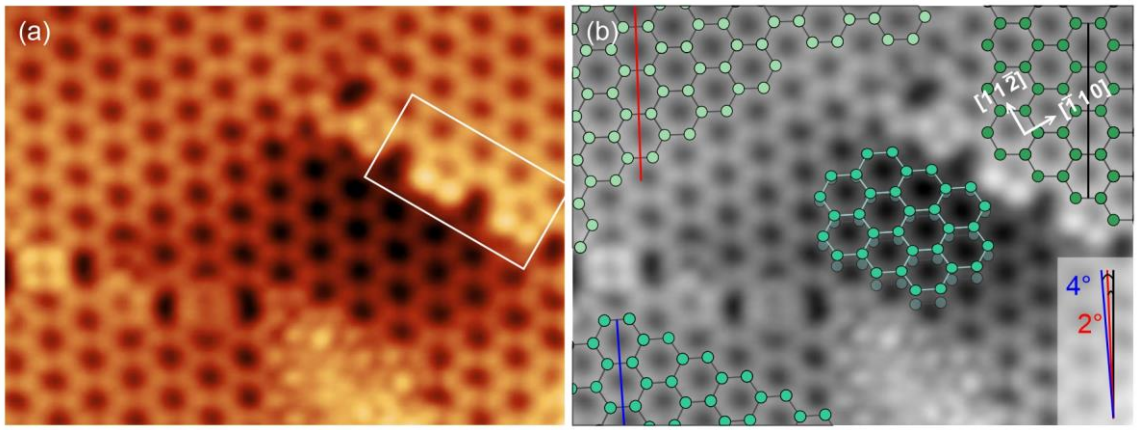

Figure 8-36 (a) STM image of a Nb_2O_3 honeycomb monolayer grown on a screw dislocation site of the Au(111) surface (7.4 nm × 5.5 nm, V_s = 0.7 V, I_t = 0.5 nA). The depression in the center is due to the screw dislocation. A Z-rK edge can be seen in the white rectangle. The screw dislocation gives rise to three Nb_2O_3 honeycomb domains. Nb lattice masks are superimposed on the three domains at the corners and the depressed region in frame (b).

In Figure 8-36, the Z-rK edge indicated by the white rectangle results from the screw dislocation of the substrate. The screw dislocation also gives rise to three Nb_2O_3 domains with a small tilting angle of 2° between two adjacent domains. Grain boundaries are formed to remedy the misalignment of two Nb_2O_3 domains. Similar morphology that has a depressed region can be seen from two examples in Figure 8-37. The tilting angles are usually 2° ~ 4°.

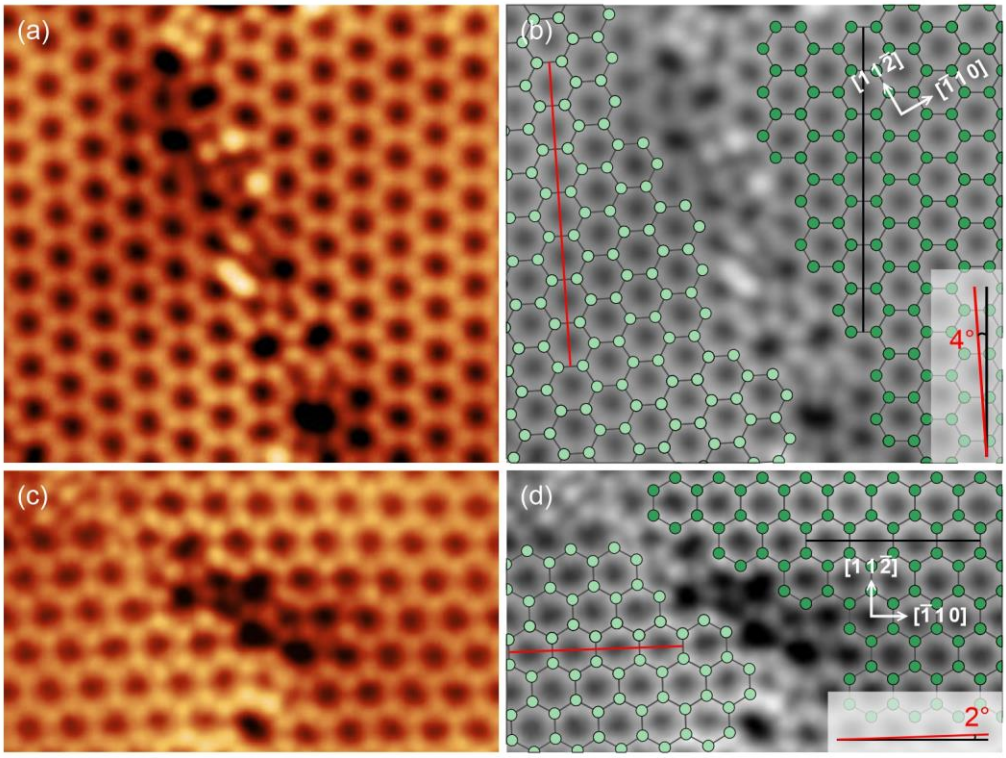

Figure 8-37 Two examples of Nb_2O_3 grain boundaries caused by the discontinuity of Au substrates. The small tilting angle between the two Nb_2O_3 domains is 2° ~ 4°. (a) 6.5 nm × 6.1 nm, V_s = 0.7 V, I_t = 0.5 nA; (c) 6.5 nm × 3.7 nm, V_s = 0.7 V, I_t = 0.5 nA.

8.5 Comparison between Nb_2O_3 and Ti_2O_3 defects

8.5.1 Defect domain in Ti_2O_3 HC

We also studied the defect structures of the (2 × 2) Ti_2O_3 honeycomb monolayer on Au(111), and the results are in good agreement with previous reports [88,254]. Figure 8-38 shows a defect domain mainly composed of pentagons, heptagons, and distorted hexagons. The edge structure of this region has been discussed in Section 7.3.3. The theoretical work on the

DV(555-777) defect in Ref. [88] has shown that the 5-7 rings are an optimal arrangement as they can efficiently release the compressive strain of the Au-supported Ti_2O_3 thin films.

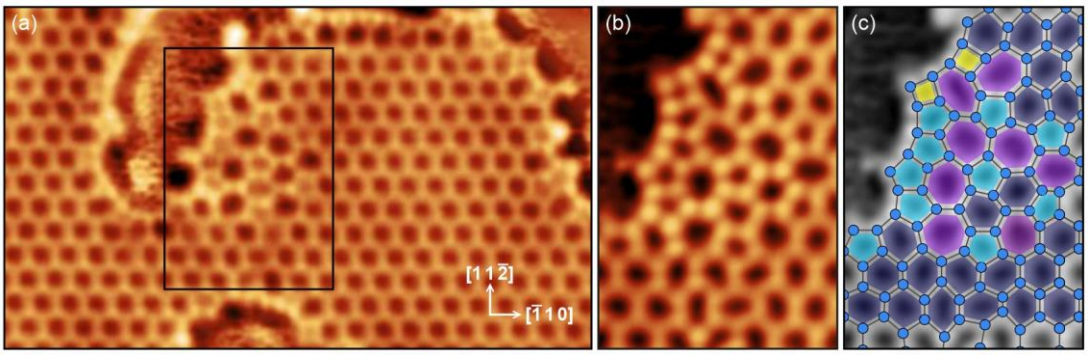

Figure 8-38 (a) STM image of a large defect domain in the Ti_2O_3 honeycomb monolayer (14.4 nm × 7.1 nm, V_s = 0.7 V, I_t = 0.35 nA). (b) Close-up of the defect domain in the black box in (a) (3.5 nm × 5.0 nm, V_s = 0.7 V, I_t = 0.6 nA). (c) Ti (blue circles) lattice model superimposed on (b). Squares: yellow; pentagons: cyan; distorted hexagons: dark blue; heptagons: purple.

8.5.2 Domain boundary solutions in Ti_2O_3 HC

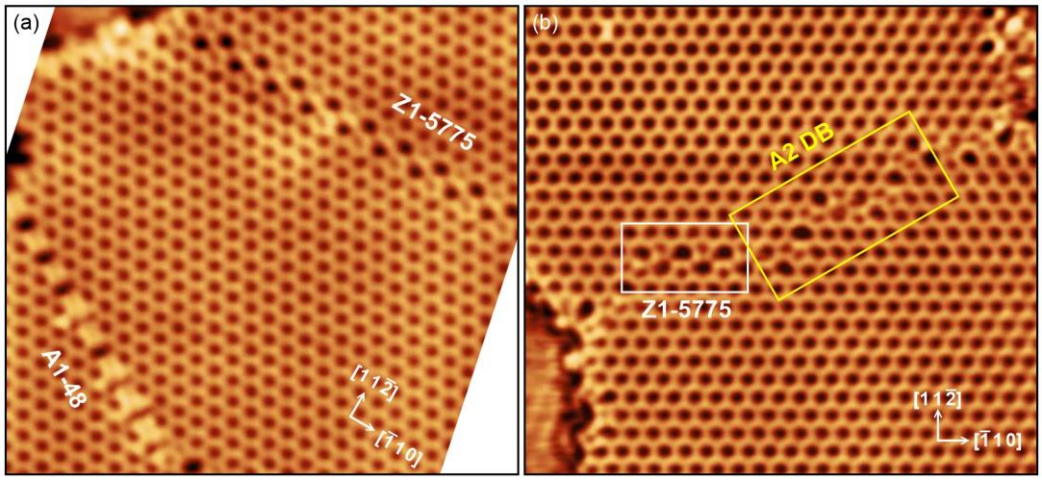

Figure 8-39 Two STM images (frame size: 14.0 nm × 12.8 nm) of large Ti_2O_3 honeycomb monolayers with different domain boundaries. The DB types are denoted on the images. (a) V_s = 1.0 V, I_t = 0.5 nA; (b) V_s = 0.6 V, I_t = 1.0 nA.

Figure 8-39 shows two STM images of large Ti_2O_3 honeycomb monolayers with relatively long domain boundaries. Ti atoms of these DBs are threefold coordinated, generally forming 4-8 or 5-7 pairs and sometimes creating octagons. The DBs in Figure 8-39(a) can be easily identified as A1-48 and Z1-5775. Figure 8-40 reproduces the results of the three most common DBs in Ti_2O_3: A1-48, Z1-5775, and Z2-558. A detailed discussion can be found in Ref. [254].

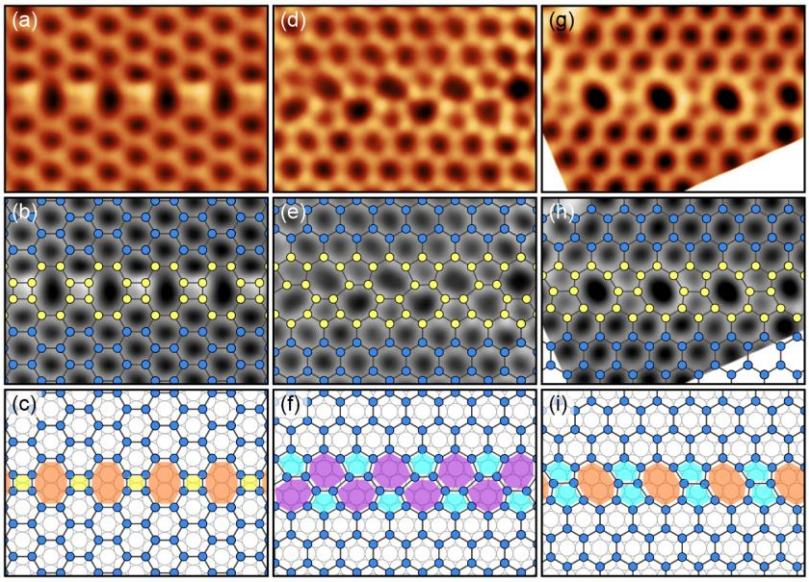

Figure 8-40 Three common domain boundaries in Ti_2O_3 honeycombs and the corresponding Ti lattice models. (a) – (c) A1-48. (d) – (f) Z1-5775. (g) – (i) Z2-558. Frame size: 4.6 nm × 3.3 nm. (a) V_s = 0.8 V, I_t = 0.6 nA; (d) V_s = 0.6 V, I_t = 0.6 nA; (g) V_s = 0.8 V, I_t = 0.8 nA. Squares: yellow; pentagons: cyan; heptagons: purple; octagons: orange.

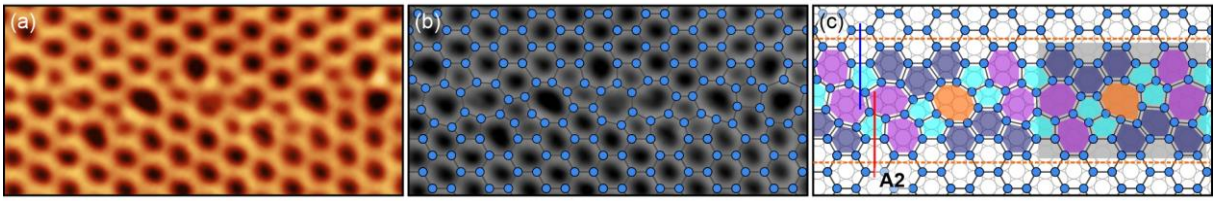

Figure 8-41 Close-up of the A2 DB in the yellow box in Figure 8-39(b). Frame size: 7.0 nm × 3.3 nm. (a) STM image of the A2 DB. (b) Ti lattice superimposed on (a). (c) Ti lattice put on Au(111) with polygons filled with different colors. Distorted hexagons are in dark blue.

The DB in the white box in Figure 8-39(b) is also a short Z1-5775, whereas the polygons in the yellow box exhibit a complex combination and seem disordered. Interestingly, it can be assigned to an A2 DB, and the close-up of this region is shown in Figure 8-41. In fact, there are two complete repeated units in Figure 8-41(c), but the unit (in the shade) is relatively large. It comprises four pentagons, four heptagons, six hexagons, and an octagon, showing a central symmetry. An A2 DB demands high formation energy, so generally, we cannot see a long A2 DB with a good periodicity along [112]. Instead, a mixed combination of polygons with central symmetry (boundary declination) is often observed, which has been demonstrated in Nb_2O_3 A2 DB in Section 8.4.4.

8.5.3 Comparison of the defect structures between Nb_2O_3 and Ti_2O_3

The Au-supported Nb_2O_3 or Ti_2O_3 monolayer has a (2 × 2) epitaxial relationship with the (111) surface and is compressively strained (Nb_2O_3: 5.7%, Ti_2O_3: 2.3%) [27,88]. Here we summarize the similarities and differences between these two materials in terms of the defect behaviors.

(1) Under the experimental conditions [Nb_2O_3: $p(O_2)$ ~ 1 × 10^{-6} Pa, T ~ 500 – 600 ℃; Ti_2O_3: $p(O_2)$ = 3 × 10^{-7} Pa, T = 500 ℃] the point defect density of Nb_2O_3 is extremely low, while Ti_2O_3 can form a few defect domains mainly composed of pentagons, distorted hexagons, and heptagons. This indicates that Nb_2O_3 HC is more stable than Ti_2O_3 HC on Au(111), which can be explained by higher adhesion energy and stronger interaction with the substrate. The DFT calculated adhesion energy is 4.2 eV per Nb_2O_3 formula unit (fu) [27] and 3.5 eV per Ti_2O_3 fu [244]. The charge transfer from the film to the Au substrate is 1.28*e* per Nb_2O_3 [27] while 0.94*e* per Ti_2O_3 [88]. Therefore, in order to investigate the Nb_2O_3 defect behaviors, it is necessary to create point defects by external interferences, for instance, the Ar^+ ion bombardment in the present work.

(2) The SW defects and divacancies, including DV(5-8-5), DV(555-777), and DV(5555-6-7777), have been observed in both materials. The Au substrate plays an important role in stabilizing these defect structures. DFT studies have shown that the defect formation energy in the Au-supported thin film is much lower than that in the freestanding counterparts [88]. The DV(555-777) is a predominant defect in both honeycomb monolayers. DFT calculations have shown that 5-7 rings can effectively release the compressive strain in the thin film.

(3) We observed tetravacancy defects in Nb_2O_3 but did not see them in Ti_2O_3 due to the low occurrence of TVs and small Ti_2O_3 sample number. The non-stoichiometric point vacancy defects in Nb_2O_3 can be found around the fourfold coordinated Nb atoms. The reconstruction of defective sites usually involves the fourfold coordinated Nb atoms as well. In contrast, Ti

atoms cannot possess fourfold coordination in HC monolayers on Au(111), so they are usually threefold coordinated and sometimes twofold coordinated at the edges.

(4) Regarding the line defects, both Nb_2O_3 and Ti_2O_3 HC possess A1-48, Z1-5775, and Z2-558. These three DBs are frequently observed and have all the cations retaining threefold coordination. DFT calculations have shown that the formation energy of an A2 DB is much higher than the other three types. We did not observe an A2 boundary with a long-range periodicity along [112]. However, the stepped A2 DBs and local A2 segments with central symmetry imply that a boundary declination or a mixed polygon arrangement could be two effective ways to overcome the high formation energy.

(5) Nb_2O_3 has more structural solutions to boundary gaps and shows diverse permutations due to the engagement of fourfold coordinated Nb atoms. In contrast, domain boundaries in Ti_2O_3 are achieved by forming polygons with all Ti atoms retaining the threefold coordination.

8.6 Conclusion

This chapter discusses the defect structures of the (2 × 2) Nb_2O_3 and Ti_2O_3 HC monolayers on Au(111). Regarding the Nb_2O_3 point defects, we have demonstrated simple vacancy sites, the SW defect, divacancies, tetravacancies, and defect reconstructions of the 6-vac, 10-vac, and 13-vac. Regarding the Nb_2O_3 line defects, we present a few structural solutions to the domain boundaries with discrete gap values. The fourfold coordinated Nb atoms provide alternative ways for defect reconstruction and domain boundary formation. Besides, we also show triple junctions of three Nb_2O_3 DBs and small-angle grain boundaries due to the Au substrate discontinuity. Furthermore, a comparative study of the defect structures between Nb_2O_3 HC and Ti_2O_3 HC has been conducted in the last section of the chapter, which gives us a better understanding of the defect behaviors of the two oxides.

Chapter 9 Triangle and pinwheel structures

9.1 Introduction

Pinwheel structures are common in many 2D materials. A review of the pinwheel structures of Cr/Pt surface alloy, Ti oxides on Au/Pt/Rh, V oxides on Rh/Pd, Fe oxides on Pt, $MoTe_2$/$MoSe_2$ on MoS_2 has been presented in Section 2.3. Three models are generally used to elucidate the formation of the pinwheel patterns: the alloy model, the Moiré pattern model, and the domain boundary model. The Moiré pattern model has been widely applied to transition metal oxide thin films supported on metal substrates. A lattice mismatch and a tilting angle between the film and the substrate are usually found. In the alloy model, which is derived from the Cr/Pt surface, the contrast is due to a local variation of chemical composition. The surface Cr lattice showed no rotation with respect to the Pt(111) surface. The domain boundary model is used to explain the pinwheel structures formed by $MoTe_2$/$MoSe_2$ on MoS_2. The spokes of the pinwheel network are attributed to the film domain boundaries and are irrelevant to the substrate.

Here we propose a new model called the triangle building block model to describe the pinwheel structures of Nb oxide and Ti oxide monolayers on the Au(111) substrates. In the previous models, although the triangle elements of a pinwheel pattern have been discussed regarding the size and atom arrangement, they were not treated as "building blocks" that constitute the network. The triangle building block model possesses two distinct features: (i) the triangle elements follow a strict epitaxial registry with respect to the substrate with no rotation, which means the cations are located either at fcc/hcp hollow sites or on-top sites of the Au(111) surface; (ii) the pinwheel network is usually composed of triangles with various sizes ranging from n = 2 to n = 10 (n is the number of cations of one side), that is why they are regarded as "building

blocks" due to the size flexibility. Besides, we have observed many single Nb/Ti oxide triangles that can independently stand on the substrates, which are the inspiration for the new model.

This chapter focuses on the triangle and pinwheel structures of three transition metal oxides: Nb, Ti, and V. In the Nb and Ti sections, single triangles with various sizes and multiple triangles with different position arrangements will be shown before discussing the pinwheel structures. However, we did not find any V oxide triangles that can independently stand on Au(111). By altering the preparation routes, Nb/Ti/V oxide pinwheel can be grown on the substrate surface (L_1 layer) or the L_2 layer, forming free or embedded monolayers. Moreover, Nb and Ti show distinct characteristics regarding the boundaries between the triangle/pinwheel and the honeycomb lattice.

It should be noted that all the structural models we proposed in this chapter were based on the experimental STM images. As there is no support from theoretical calculations or simulations, the interpretation of the STM images and the proposed models are tentative. Many fine details due to the electronic structures of oxide materials cannot be well explained.

9.2 Nb oxide triangle and pinwheel structures

Sample preparations for Nb oxide triangles, triangle continuous films, and pinwheel monolayers have been introduced in Section 5.5. A triangle continuous film usually comprises a few triangle building blocks and was formed at a higher annealing temperature (700 ℃) than triangles (500 ℃). Pinwheel monolayers were obtained at high coverages and can be converted to the (2 × 2) Nb_2O_3 honeycomb monolayers by further oxidation (see Figure 5-4). Besides, it is frequently observed that the honeycomb islands can carry triangles at the corners and accommodate triangles inside the lattice.

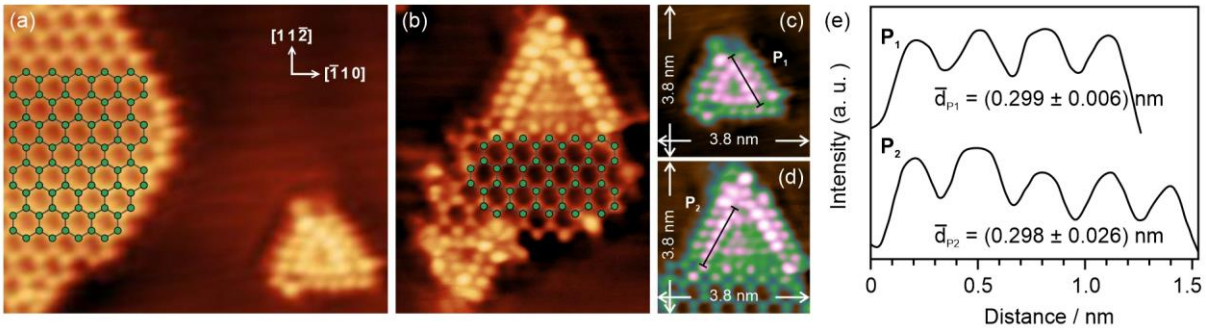

Figure 9-1 STM image of (a) a Single-T with the (2 × 2) Nb_2O_3 honeycomb lattice acting as a good crystallographic marker (8.5 nm × 6.8 nm, V_s = 1.5 V, I_t = 0.75 nA). (b) A (2 × 2) Nb_2O_3 honeycomb island with two Bay-Ts (5.6 nm × 6.8 nm, V_s = 0.7 V, I_t = 0.3 nA).

Figure 9-1 shows the measurement of the periodicity of triangle structures before building the structural models. The Nb oxide triangles, either standing independently on the surface or connecting to the Nb_2O_3 HC islands at the corners, always exhibit double rims. It is filled with more atoms at the core when the size is enlarged. The STM images were taken at positive biases, so protrusions of the triangles in these empty-state images are attributed to Nb atoms.

The outside triangle rim is generally defective, so the periodicity measurement and size determination are based on the inside triangle rim. The (2 × 2) Nb_2O_3 honeycomb island is excellent for precise calibration in terms of crystallographic orientation and distance. From the profiles in Figure 9-1(e) we can see that distance of adjacent Nb atoms from the same side is around 0.299 nm, approximate to the (1 × 1) periodicity of Au(111) (0.289 nm). Figure 9-1(c) and (d) are cropped from frames (a) and (b), using a green-pink lookup table to highlight the contrast difference. Obviously, atoms from the inside triangle rims possess higher signal intensities, which suggests that they are at a more elevated location than atoms from the outside triangle rims and the cores if only considering the topographical effect.

9.2.1 Single triangle (Single-T)

Figure 9-2 gives two examples for building the single triangle models. According to the number of Nb atoms from the inside triangle rims, they can be denoted as T_4 and T_6, respectively. In a

single Nb oxide triangle, we located Nb atoms from the inside rim at on-top sites of the Au(111) surfaces, using circles with a bold perimeter. Nb atoms from the outside rim and the core are supposed to occupy hollow sites, as shown in frame (b) and (g). We also put atoms from the outside rim at on-top sites for comparison [frame (d), (i)]. By superimposing the model masks on the STM images, we can see that the former model matches much better and particularly works well for bigger triangles.

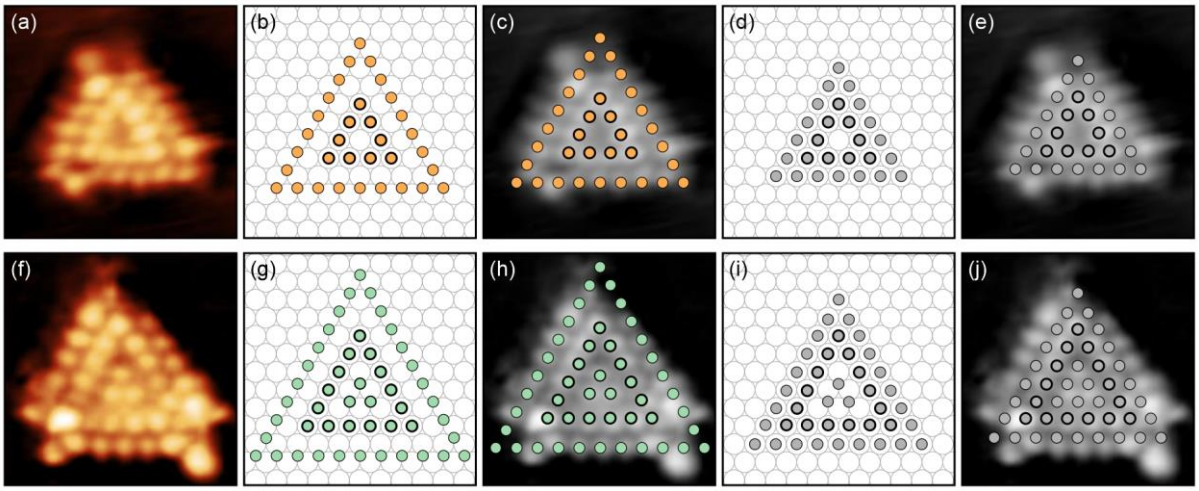

Figure 9-2 (a) STM image of a Single-T_4 (3.2 nm × 3.2 nm, V_s = 1.5 V, I_t = 0.75 nA). (b) Schematic of a proposed structure with atoms from the outside triangle at hollow sites. (c) Structural model in (b) superimposed on (a) in grayscale. (d) Schematic of a proposed structure with atoms from the outside triangle at on-top sites. (e) Structural model in (d) superimposed on (a) in grayscale. (f) – (j): STM image of a Single-T_6 (3.2 nm × 3.2 nm, V_s = 0.7 V, I_t = 0.3 nA) and proposed models.

Schematics of single triangle models from n = 2 to n = 10 (T_2 ~ T_{10}) are displayed in Figure 9-3, and the STM images of some single triangle examples are shown in Figure 9-4. The biggest single triangle observed in the experiment is T_8 if assuming the nanostructure is complete and free from defects. We did not find independently-standing T_9 and T_{10} but observed two in triangle continuous films, as shown in Figure 9-5(b) – (g). The bar chart in Figure 9-5(a) shows the occurrence of single triangles according to the size. T_4 and T_5 are the most common single triangles, which implies that the Nb oxide triangles with sizes of n = 4 and n = 5 are more thermodynamically stable on the Au(111) substrates.

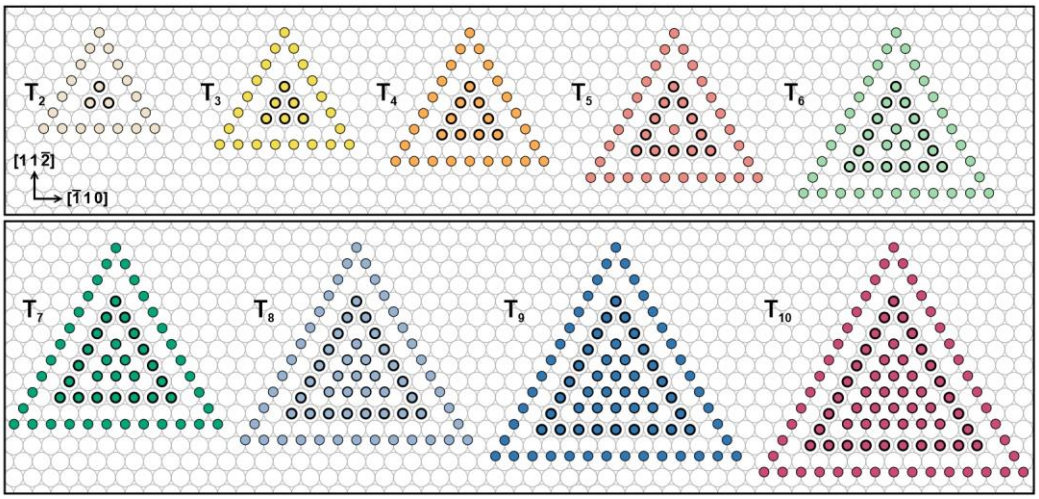

Figure 9-3 Schematics of Nb oxide single triangle models from T_2 to T_{10}. Atoms from the outside triangle rim, inside triangle rim, and the core are put at hollow sites, on-top sites, and hollow sites, respectively. Different colors correspond to specific triangle sizes *n*, namely the number of side atoms from the inside triangle rim. The colors will keep consistent in all triangle structures, including Nb oxide Sing-T, building blocks for Double-T, Triple-T, Hex-T, continuous thin film, pinwheel, Bay-T, Inlaid-T, Confined-T; and Ti oxide free-triangles, emb-triangles, and pinwheel. (Beige: $n = 2$; yellow: $n = 3$; orange: $n = 4$; light red: $n = 5$; light green: $n = 6$; dark green: $n = 7$; light blue: $n = 8$; dark blue: $n = 9$; plum: $n = 10$. Sometimes grey is also used for $n = 5$ when proposing complete structural models with O atoms in light red.

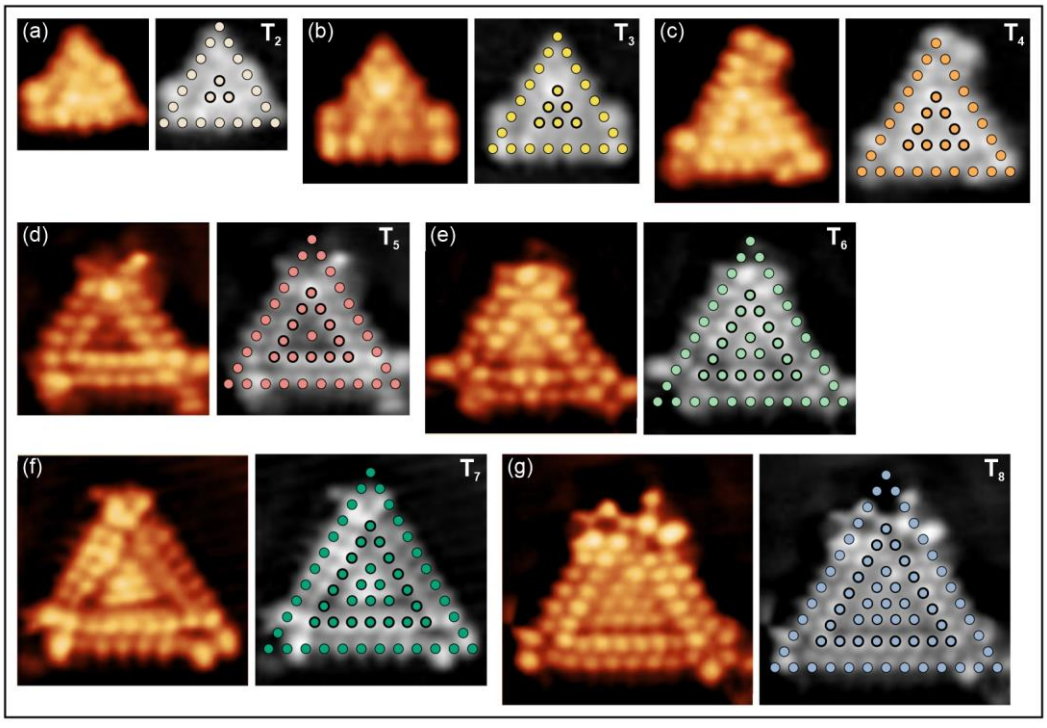

Figure 9-4 STM images of Nb oxide single triangles from T_2 to T_8. (a) T_2 (2.0 nm × 2.0 nm, V_s = 0.7 V, I_t = 0.2 nA). (b) T_3 (2.6 nm × 2.6 nm, V_s = 0.8 V, I_t = 0.8 nA). (c) T_4 (2.9 nm × 2.9 nm, V_s = 0.8 V, I_t = 1.0 nA). (d) T_5 (3.0 nm × 3.0 nm, V_s = 0.7 V, I_t = 0.3 nA). (e) T_6 (3.3 nm × 3.3 nm, V_s = 0.7 V, I_t = 0.3 nA). (f) T_7 (3.6 nm × 3.6 nm, V_s = 1.0 V, I_t = 0.3 nA). (g) T_8 (3.9 nm × 3.9 nm, V_s = 0.7 V, I_t = 0.3 nA). Model masks are superimposed on the STM images in grayscale if assuming the nanostructures are free from defects.

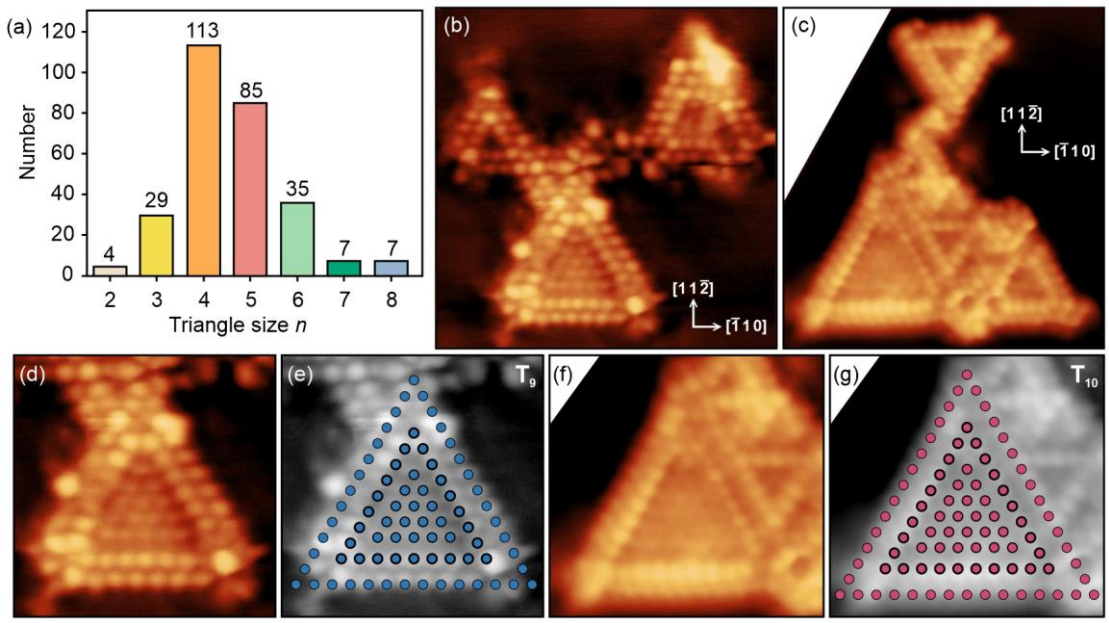

Figure 9-5 (a) The occurrence of Nb oxide single triangles according to the size *n*. STM images of triangle continuous films with (b) a T_9 element (7.5 nm × 7.5 nm, V_s = 0.7 V, I_t = 0.3 nA); (c) a T_{10} element (frame size: 7.0 nm × 7.5 nm, V_s = 1.1 V, I_t = 0.1 nA). (d) Cropped image showing the T_9 with model mask superimposed in (e). (f) Cropped image showing the T_{10} with model mask superimposed in (g). (d) – (g) Frame size: 4.2 nm × 4.2 nm.

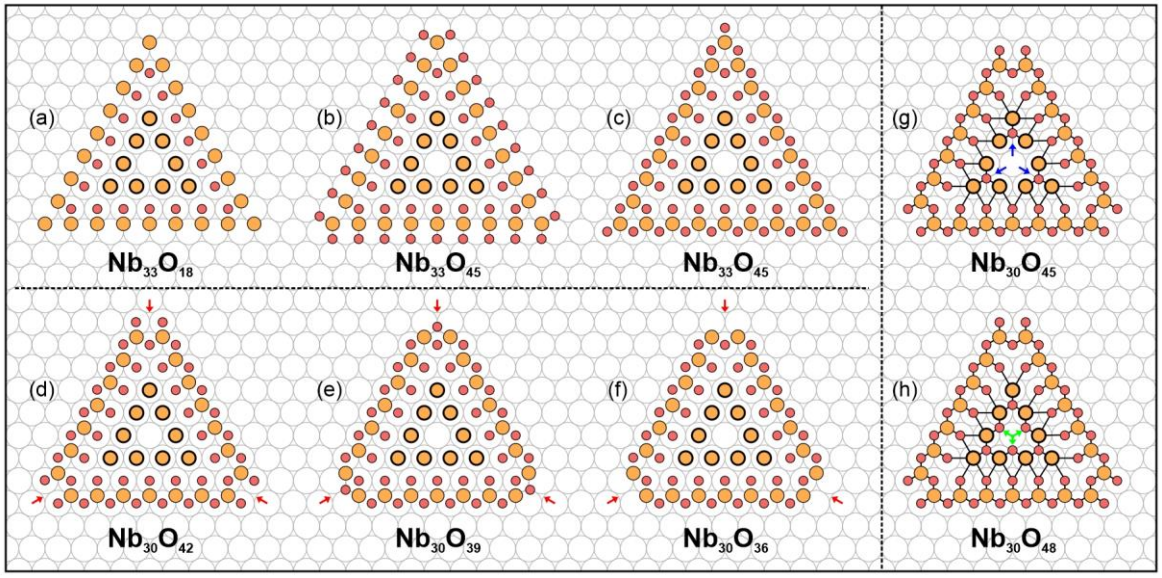

Figure 9-6 Structural models for Single-T_4 with O atoms. Orange: Nb; light red: O. (a) O atoms are added between the inside and outside triangle rims. More O atoms are added to the outside triangle rim, occupying (b) hollow sites or (c) on-top sites. (d) – (f) Truncated triangles with the three Nb atoms at the vertices removed. The red arrows indicate the varied O atoms at the vertices. (g), (f) Three additional O atoms are inserted in the triangle core. The blue arrows and green arrows indicate the O positions. Solid lines are drawn between Nb and O atoms to see the Nb atoms' coordination with surrounded O, but they do not represent the actual Nb-O bonding. The stoichiometry of each proposed atom configuration is denoted below.

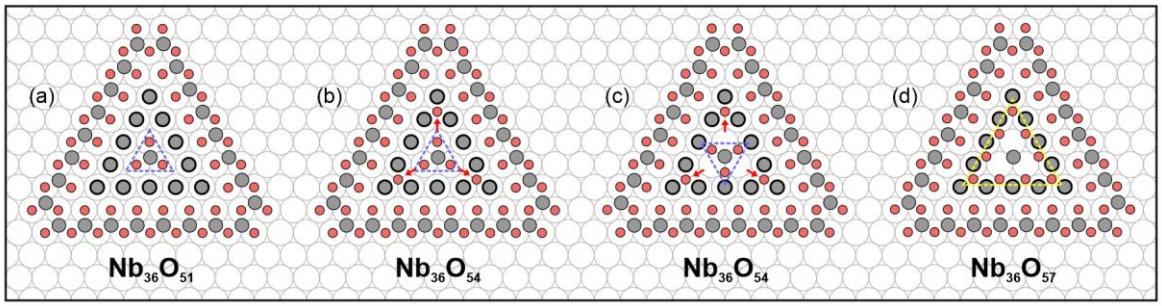

Figure 9-7 Structural models for Single-T_5 with O atoms. Grey: Nb; light red: O. (a) – (d) A truncated triangle of Nb outside rim with adjacent O atoms at on-top sites is adopted as a base. O atoms in the triangle cores are varied and highlighted by blue/yellow dash lines and red arrows. Stoichiometries are denoted below.

Although O atoms are invisible in the empty-state STM images, a few structural models with O atoms are proposed in Figure 9-6 and Figure 9-7, taking T_4 and T_5 as examples. O atoms were inserted between Nb atoms along a side with a (1 × 1) periodicity as well. This arrangement is similar to the models of FeO(111) on Pt(111) [138], but the difference is: in a FeO triangular nanostructure, Fe atoms are closed-packed with a rhombic unit cell; while a Nb oxide triangle can be divided into three components: the outside rim (Nb at hollow sites), the inside rims (Nb at on-top sites), and the core (Nb at hollow sites). The gap distance between components is not identical to the periodicity along a triangle side. Therefore, the O atom configuration and the Nb-O bonding could be diverse and complicated.

In Figure 9-6(a), O atoms are located between the outside and inside rims occupying on-top sites. This configuration gives rise to a stoichiometry of $Nb_{33}O_{18}$. Based on the experience from other Nb oxide nanostructures (e.g., clusters, honeycomb), O atoms are supposed to protrude outwards, and Nb atoms approach the substrate due to the electron transfer to the Au substrate. The models only display the 2D projection of the rumpled structures. In addition, theoretical calculations have shown that an oxygen-terminated edge possesses lower energy in the (2 × 2) Nb_2O_3 honeycomb edges. Therefore, we proposed two models in frame (b) and (c) where additional O atoms are attached at the edges of the triangle outside rims, sitting at hollow sites or on-top sites with an equal stoichiometry of $Nb_{33}O_{45}$.

Theoretical calculations of rectangular NbO_x clusters reveal that niobyl groups at the edges are energetically more favorable. So we believe that the O atom configuration in frame (c) should be more reasonable than that in frame (b). Given that the three corners of a single triangle are often damaged, a truncated shape with the three Nb atoms at the vertices removed is proposed based on the configuration in frame (c). Figure 9-6(d) – (f) gives three models with various O atoms at the truncated corners. The scheme is quite similar to the discussion of O configurations in Nb_2O_3 HC edge structures (see Section 7.3.1).

Compared with the outside rim, it is more challenging to speculate the O arrangement of the inside rim and at the triangle core. In Figure 9-6(g) three O atoms are added at the corners of the inside triangle, while in frame (h), six O atoms are inserted within the inside rim showing a (1 × 1) periodicity. This nanostructure has a stoichiometry of $Nb_{30}O_{48}$ with the O/Nb ratio reaching 1.6. The solid lines that connect O and Nb atoms are used to surmise the Nb-O bonding conditions. As discussed in Chapter 6, a fourfold coordinated Nb atom appears much brighter in STM images. The Nb atoms from the inside triangle rim in frame (h) are fourfold coordinated (side atoms) or even fivefold coordinated (three Nb atoms at the vertices), which means they may possess higher oxidation states. This could be another explanation for why they look brighter than the outside triangle rim apart from the height difference.

Figure 9-7 displays four possible models for a Single-T_5. A truncated shape with all O atoms at on-top sites is used as a "base" for the discussion. The number of O atoms and their locations in the triangle core are varied in frame (a) – (d). The models proposed for T_4 and T_5 imply that for a Nb oxide single triangle, the stoichiometry NbO_y usually has $1 < y < 2$.

9.2.2 Double triangle (Double-T)

Many double triangles with various size combinations have been observed in the experiment. Two triangles can exhibit four arrangements: side-to-side (A), stack (B), corner-to-corner (C),

and abreast (D), as depicted in Figure 9-8. Type A is dominant in Nb oxide double triangles and can be classified according to the vertical gap d_g [i.e., (i), (ii), (iii) in frame (a)] and lateral shift d_s between two triangles. Double-T is earmarked for double triangles with a Type A arrangement. Type B, C, and D occurred less frequently than Type A, three examples are presented in Figure 9-9. Model masks can be quickly selected and superimposed on the STM images to assess the size of the triangle elements. They do not represent the actual Nb atom arrangements, particularly at the corners where adatoms or defects are usually found.

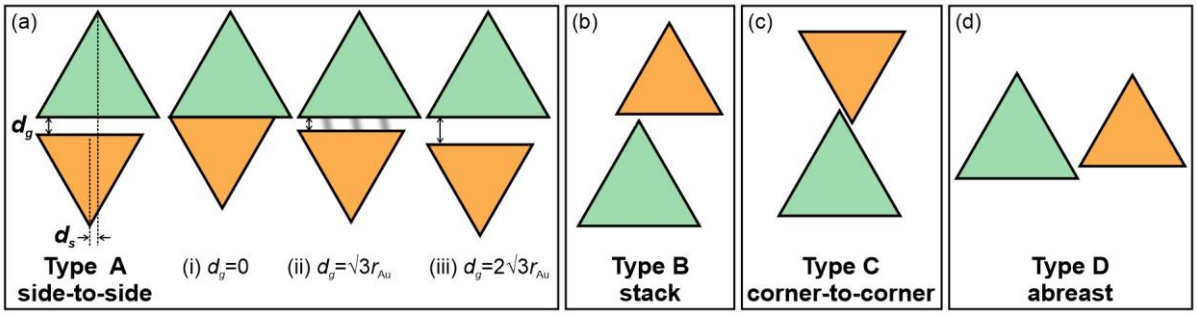

Figure 9-8 Schematics of different arrangements of two Nb oxide triangles. (a) Type A, side-to-side. It is referred to as Double-T or T_m-T_n ($2 < m, n < 8$), and can be classified into (i), (ii), and (iii) according to the vertical gap d_g between two triangles. Lateral shift d_s depends on the size parity. (b) Type B, stack arrangement. (c) Type C, corner-to-corner. (d) Type D, abreast.

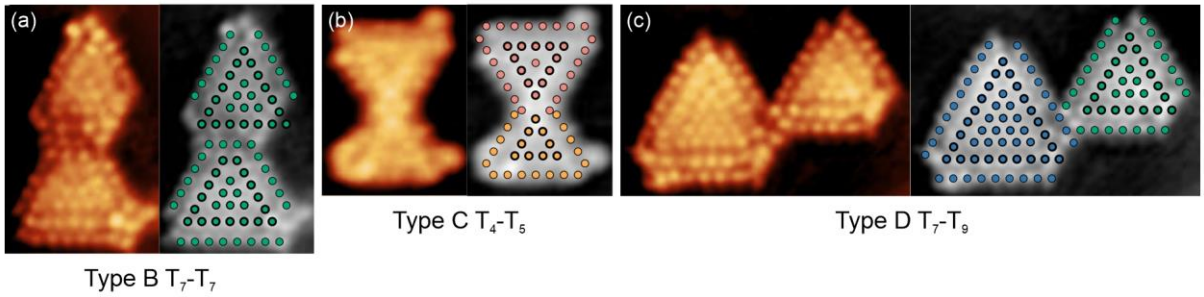

Figure 9-9 Three examples for Type B, C, D arrangements. (a) Type B, stack (3.2 nm × 5.1 nm, V_s = 0.6 V, I_t = 0.6 nA). (b) Type C, corner-to-corner (3.2 nm × 3.9 nm, V_s = 0.45 V, I_t = 0.65 nA). (c) Type D, abreast (5.9 nm × 4.1 nm, V_s = 0.6 V, I_t = 0.6 nA).

Figure 9-10 takes a Double-T (T_5-T_5) as an example to elucidate the relative positions of two triangles. The corners of the triangles are usually defective, so the top and bottom corners are omitted in the schematics. The epitaxial registry limits the location because Nb atoms from the inside triangle rim are always at on-top sites. In the vertical direction, two inside triangles can

(i) share the side with no gap distance ($d_g = 0$), or are separated by a gap of (ii) $d_g = \sqrt{3}r_{\mathrm{Au}}$ or (iii) $d_g = 2\sqrt{3}r_{\mathrm{Au}}$ (r_{Au} is the radius of an Au atom). A larger gap distance makes no sense to a Double-T structure. In the lateral direction, the two triangles may have a relative shift, generally not exceeding $4r_{\mathrm{Au}}$ and restricted by the epitaxial registry. Figure 9-11 shows four STM images of T_5-T_5. Frame (a) and (b) correspond to chiral arrangements of model (a) in Figure 9-10. Model (b) and (c) in Figure 9-10 well reproduce the triangle arrangements in experimental observations in Figure 9-11(c) and (d), from which wider gaps can be seen.

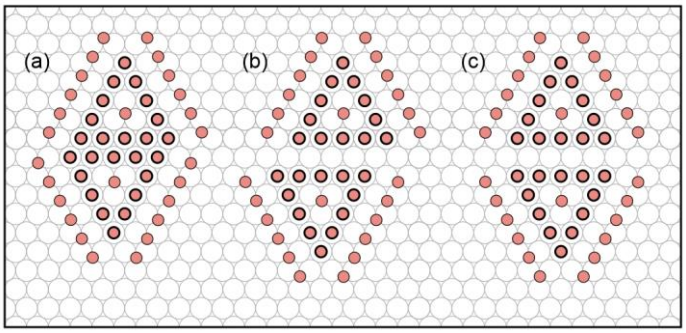

Figure 9-10 Schematics of different arrangements of T_5-T_5. (a) Gap (ii) with a lateral shift of half Au atom. (b) Gap (iii) with a lateral shift by one Au atom. (c) Gap (iii) with no lateral shift.

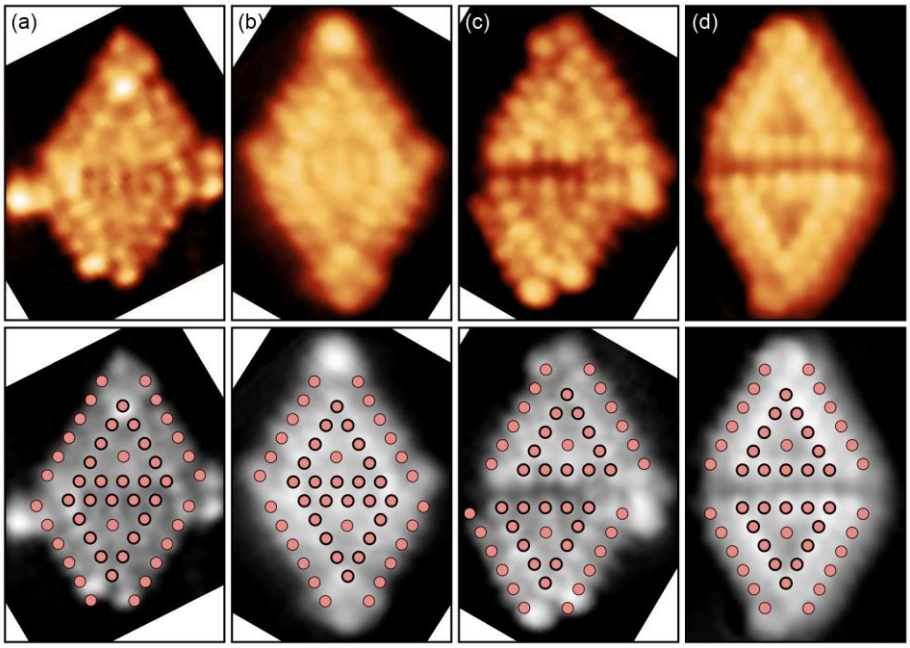

Figure 9-11 STM images of Nb oxide Double-T (T_5-T_5) with different triangle arrangements, frame size: 2.9 nm × 4.2 nm. (a) V_s = 1.0 V, I_t = 0.2 nA; (b) V_s = 1.0 V, I_t = 0.3 nA; (c) V_s = 1.0 V, I_t = 0.4 nA; (d) V_s = 1.1 V, I_t = 0.1 nA.

Figure 9-12 demonstrates the schematics of T_5-T_6 with different arrangements. The STM results are displayed in Figure 9-13, corresponding to models (a) – (d) in Figure 9-12. Figure 9-13(d) and (e) are chiral arrangements of model (d). Model (e) was not experimentally observed and thus being covered in a grey rectangle. In the following text, only experimentally-observed Doubt-Ts will be presented with corresponding structural models.

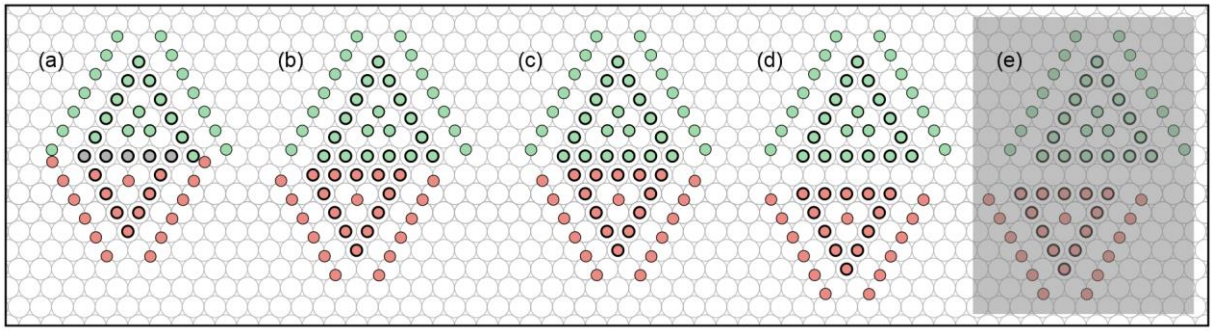

Figure 9-12 Schematics of different arrangements of T_5-T_6. (a) Shared edge. (b) Gap (ii) with a lateral shift of one Au atom. (c) Gap (ii) with no lateral shift. (d) Gap (iii) with a lateral shift of half Au atom. (e) Gap (iii) with a lateral shift of one and a half Au atoms. The grey covering indicates that it was not experimentally observed.

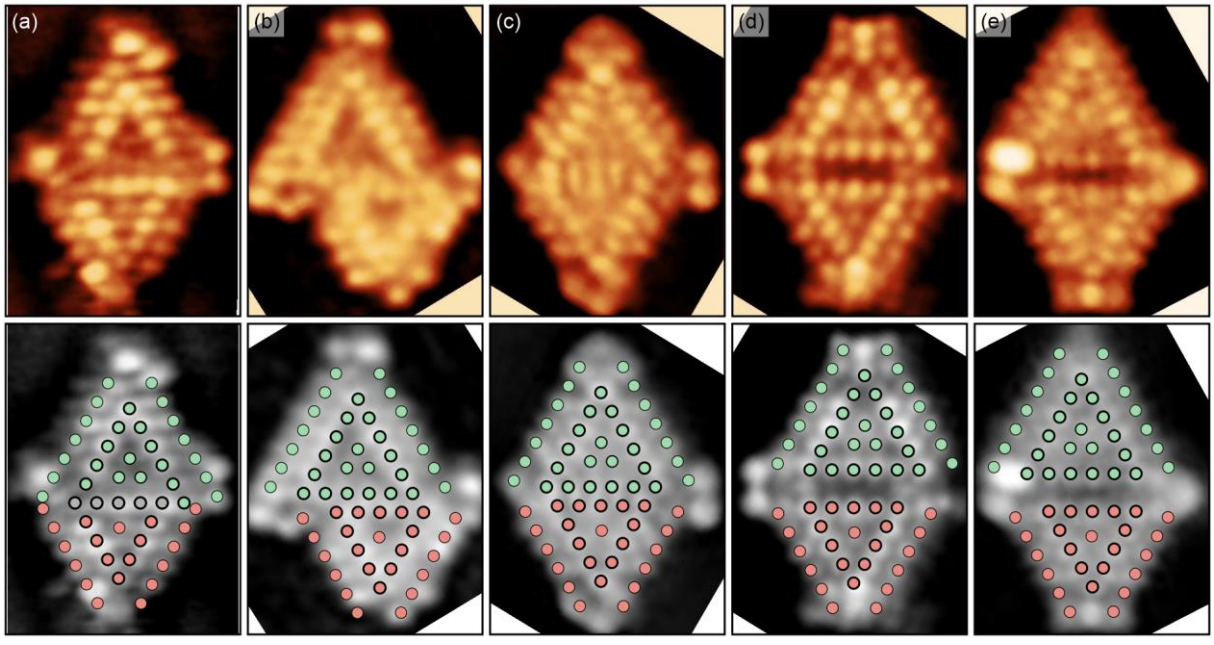

Figure 9-13 STM images of Nb oxide Double-T (T_5-T_6) with different arrangements, frame size: 3.1 nm × 4.1 nm. (a) Shared edge (V_s = 0.7 V, I_t = 0.3 nA). (b) Gap (ii) with a lateral shift of one Au atom (V_s = 0.7 V, I_t = 0.3 nA). (c) Gap (ii) with no lateral shift (V_s = 0.8 V, I_t = 0.8 nA). (d) Gap (iii) with a lateral shift of half Au atom (V_s = 0.7 V, I_t = 0.3 nA). (e) Gap (iii) with a lateral shift of half Au atom (V_s = 0.8 V, I_t = 0.8 nA).

Figure 9-14 – Figure 9-17 display Nb oxide double triangles with a variety of size combinations and position arrangements, including T_3-T_4, T_3-T_5, T_4-T_4, T_4-T_5, T_4-T_6, T_5-T_7, T_6-T_6, and T_7-T_8. The models given in these figures are tentative models which can only help to clarify the triangle sizes and relative positions. O atom configurations and corner decorations are so complex that they are beyond the scope of the discussion here.

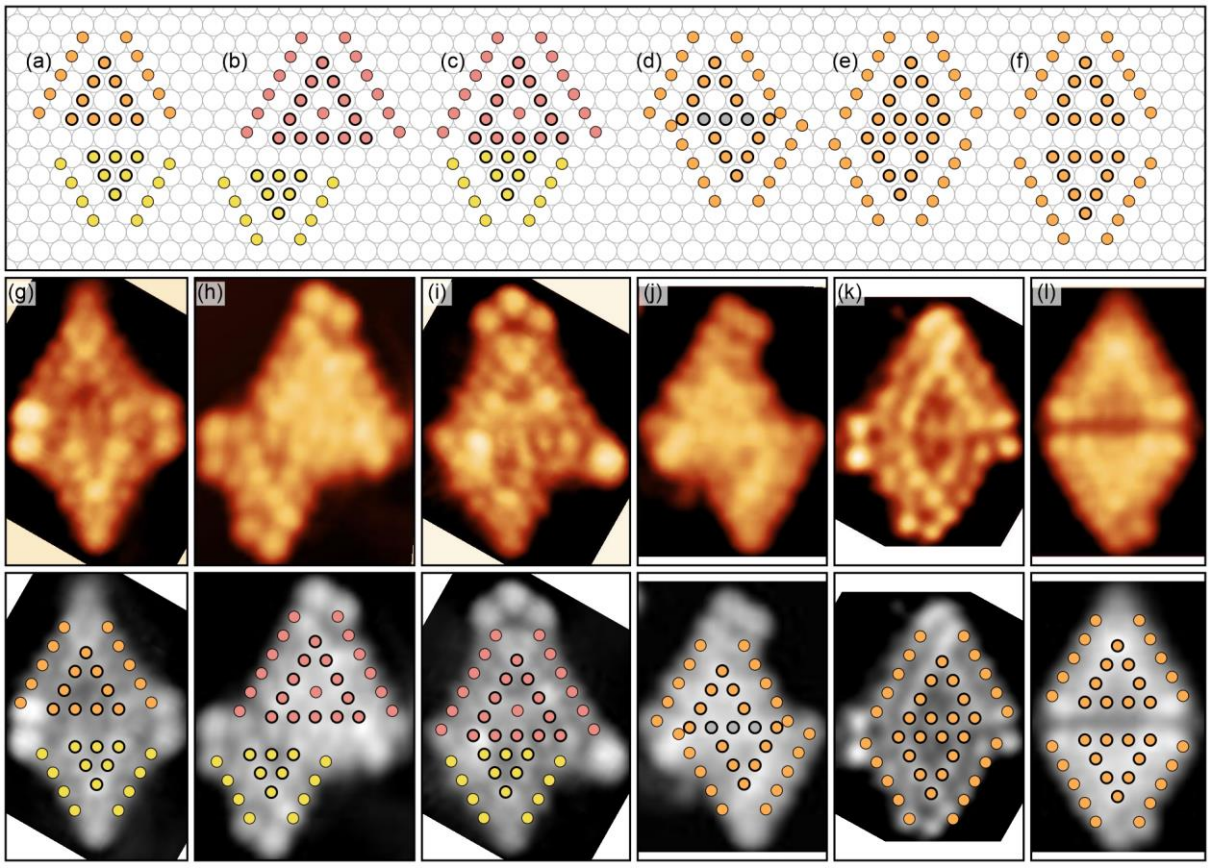

Figure 9-14 (a) – (f) Schematics and (g) – (l) STM images of Nb oxide Double-Ts (T_3-T_4, T_3-T_5, T_4-T_4) with different arrangements. Frame height: 3.8 nm. (g) V_s = 1.0 V, I_t = 0.4 nA; (h) V_s = 0.9 V, I_t = 0.45 nA; (i) V_s = 1.0 V, I_t = 0.4 nA; (j) V_s = 0.7 V, I_t = 0.3 nA; (k) V_s = 0.7 V, I_t = 0.3 nA; (l) V_s = 1.0 V, I_t = 0.35 nA.

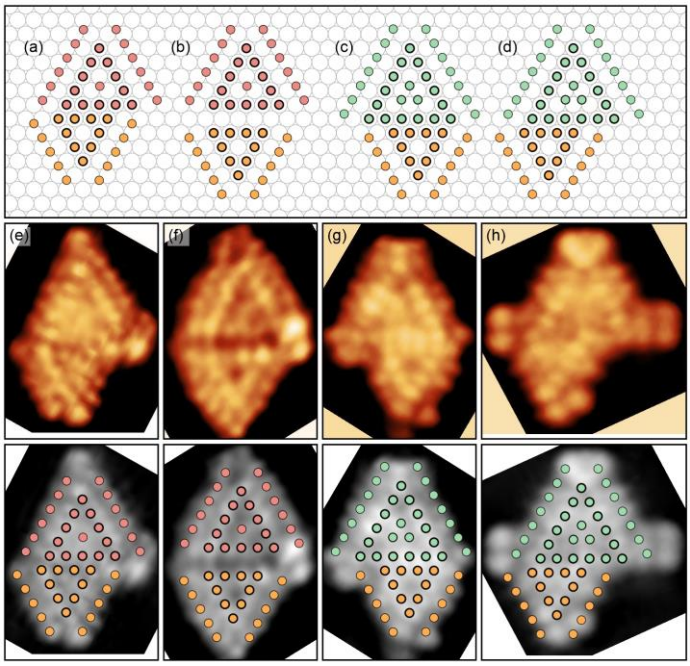

Figure 9-15 (a) – (d) Schematics and (e) – (h) STM images of Double-Ts (T_4-T_5, T_4-T_6). Frame height: 3.8 nm. (e) V_s = 0.8 V, I_t = 0.6 nA; (f) V_s = 0.7 V, I_t = 0.8 nA; (g) V_s = 0.56 V, I_t = 0.6 nA; (h) V_s = 1.0 V, I_t = 0.4 nA. (Figure was reduced to 75% for layout.)

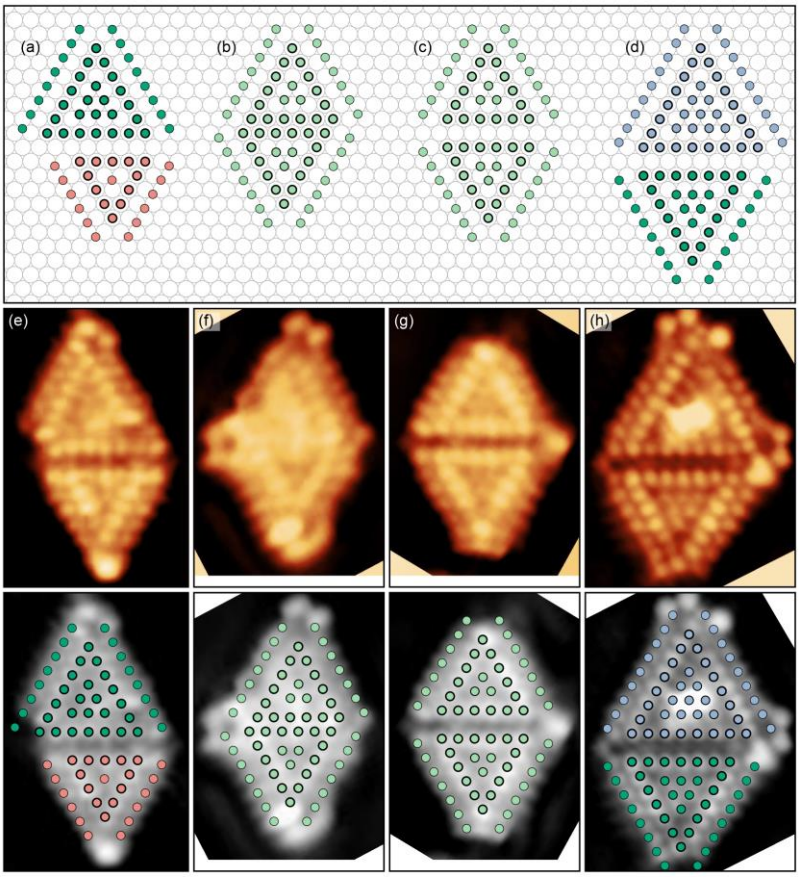

Figure 9-16 (a) – (d) Schematics and (e) – (h) STM images of Double-Ts (T_5-T_7, T_6-T_6, T_7-T_8). Frame height: 4.9 nm. (a) V_s = 0.7 V, I_t = 0.5 nA; (b) V_s = 0.56 V, I_t = 0.65 nA; (c) V_s = 0.56 V, I_t = 0.65 nA; (d) V_s = 0.7 V, I_t = 0.3 nA. (Figure was reduced to 75% for layout.)

9.2.3 Multiple triangles and triangle continuous films

A Triple-T comprises three triangle building blocks usually arranged in a trapezoid-like shape. The connections between adjacent triangles are consistent with Double-Ts. We found that T_5 is the most common building block that constitutes Triple-Ts, hexagonal patterns, and triangle continuous films. Figure 9-17 presents three Triple-T examples with close or equal sizes, which are T_4-T_5-T_5, T_5-T_5-T_5, and T_5-T_6-T_5. It is also quite common to find Triple-Ts with three different triangle building blocks, for example, T_6-T_4-T_3, T_4-T_5-T_6, and T_6-T_7-T_5 in Figure 9-18.

A hexagonal pattern (Hex-T) is formed by six triangles that are arranged around a central point. It meets the geometric definition of a pinwheel pattern, and we can quickly identify its "hub" and "spokes". It is worth noting that in the triangle building block model, the triangle size and the gap distance between adjacent triangles can be varied. This is in sharp contrast to the previous models, especially the identical triangular elements in a Moiré pattern. Interestingly, two unique Hex-Ts that only consist of T_5 building blocks were observed in experiments and presented in Figure 9-19. We have demonstrated a series of T_5-T_5 structural models in Figure 9-10. The pinwheel pattern in Figure 9-19(a) is consistent with model (a) in Figure 9-10 where the triangles are separated by the gap (ii) $d_g = \sqrt{3}r_{\mathrm{Au}}$ and a lateral shift of half Au atom. While the pinwheel pattern in Figure 9-19(b) corresponds to model (c) in Figure 9-10 with the gap (iii) $d_g = 2\sqrt{3}r_{\mathrm{Au}}$ and no lateral shift.

In addition, we also observed some pinwheel patterns that comprise triangle building blocks with unequal sizes and gaps. Small triangles separated by short gaps make the whole hexagonal pattern look more "compact" with a high atom density, as the example $3T_4$-$3T_5$ shown in Figure 9-20. Lager triangle elements with the gap (iii) in Figure 9-21 formed a much bigger pinwheel which can be described as T_5-$4T_6$-T_7.

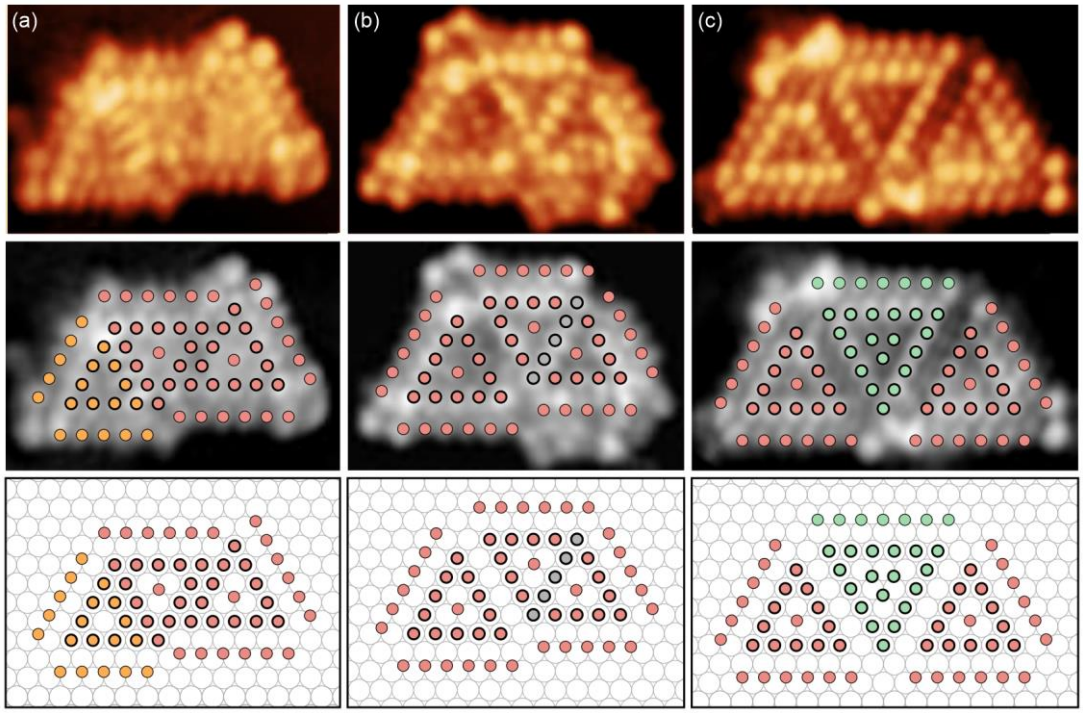

Figure 9-17 STM images of Nb oxide Triple-Ts mainly composed of T_5; corresponding triangle building blocks are superimposed on the STM images in grayscale and put on the Au(111) substrates to see the relative positions. (a) 4.4 nm × 3.0 nm, V_s = 0.8 V, I_t = 0.8 nA; (b) 4.5 nm × 3.0 nm, V_s = 0.7 V, I_t = 0.3 nA; (c) 5.1 nm × 3.0 nm, V_s = 1.0 V, I_t = 0.35 nA.

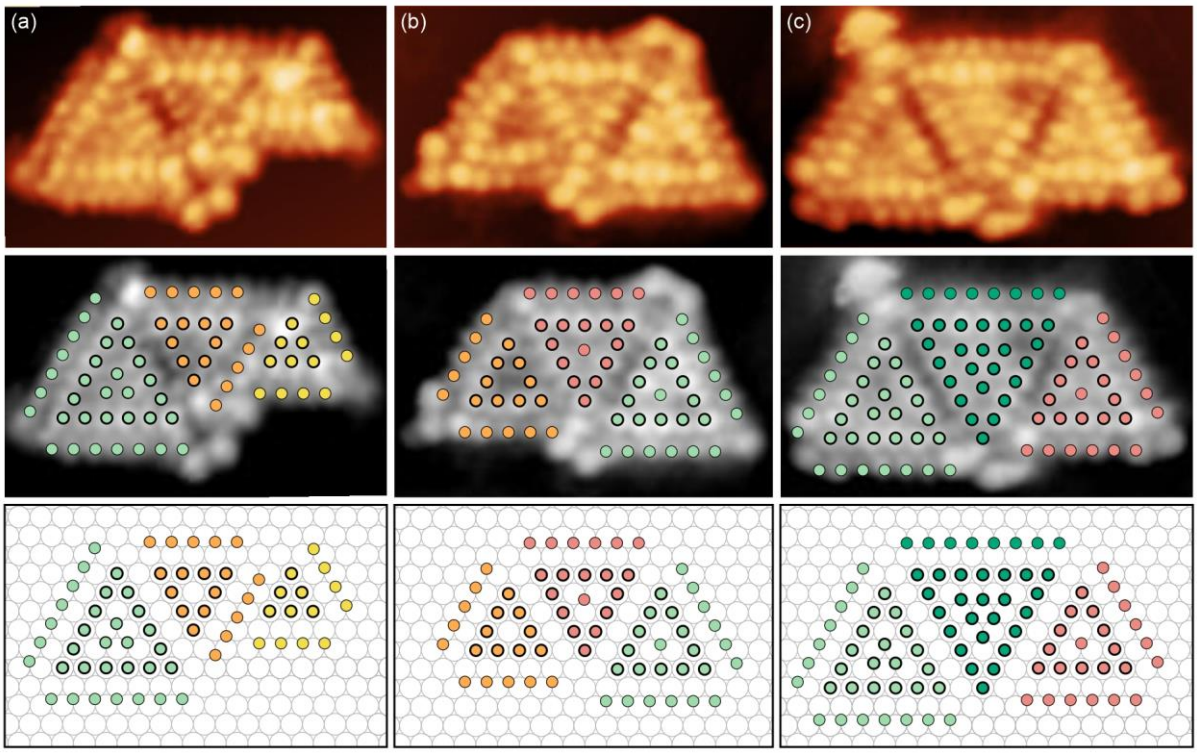

Figure 9-18 STM images of Nb oxide Triple-Ts composed of triangle elements in different sizes. (a) T_6-T_4-T_3, 5.1 nm × 3.2 nm, V_s = 1.0 V, I_t = 0.3 nA; (b) T_4-T_5-T_6, 5.0 nm × 3.2 nm, V_s = 1.0 V, I_t = 0.2 nA; (c) T_6-T_7-T_5, 5.5 nm × 3.2 nm, V_s = 1.0 V, I_t = 0.2 nA.

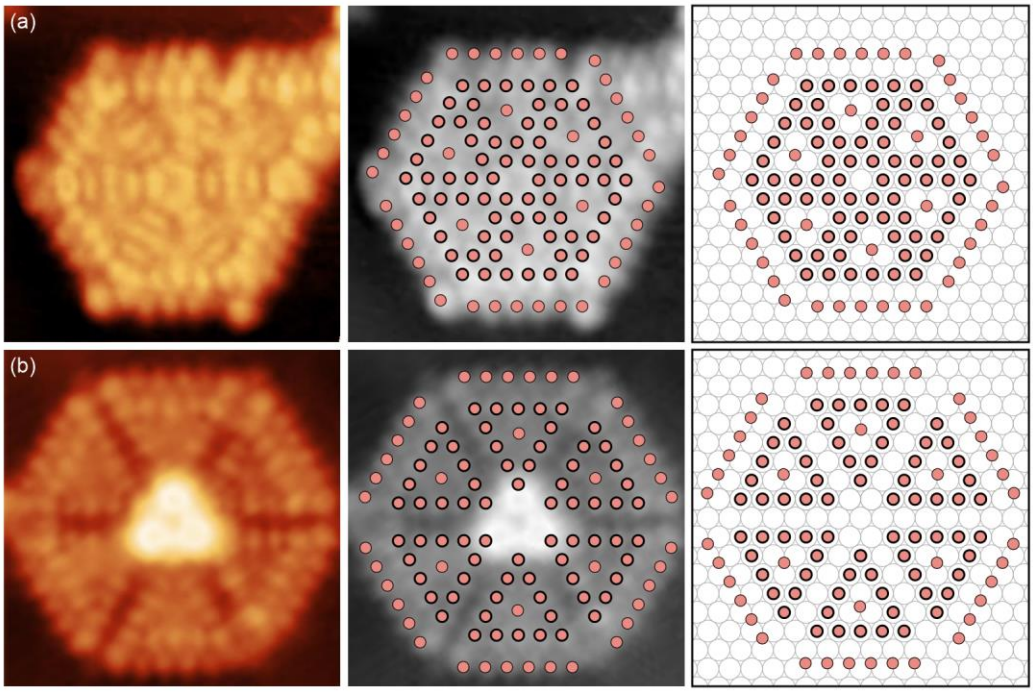

Figure 9-19 Two types of Hex-T composed of T_5 elements, image size: 4.5 nm × 4.5 nm. T_5 elements separated by (a) gap (ii), V_s = 0.8 V, I_t = 0.6 nA; (b) gap (iii), V_s = 1.0 V, I_t = 0.2 nA.

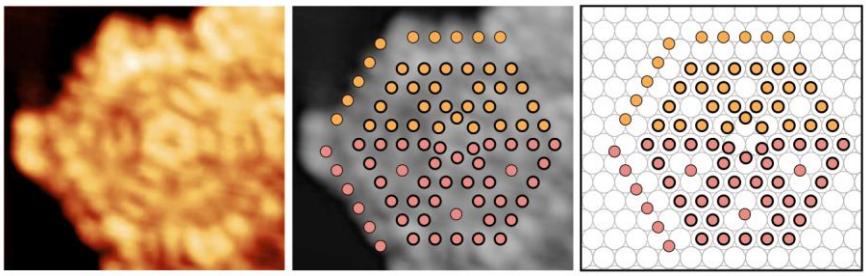

Figure 9-20 A small Hex-T, described as $3T_4$-$3T_5$ (3.7 nm × 3.5 nm, V_s = 0.7 V, I_t = 0.6 nA).

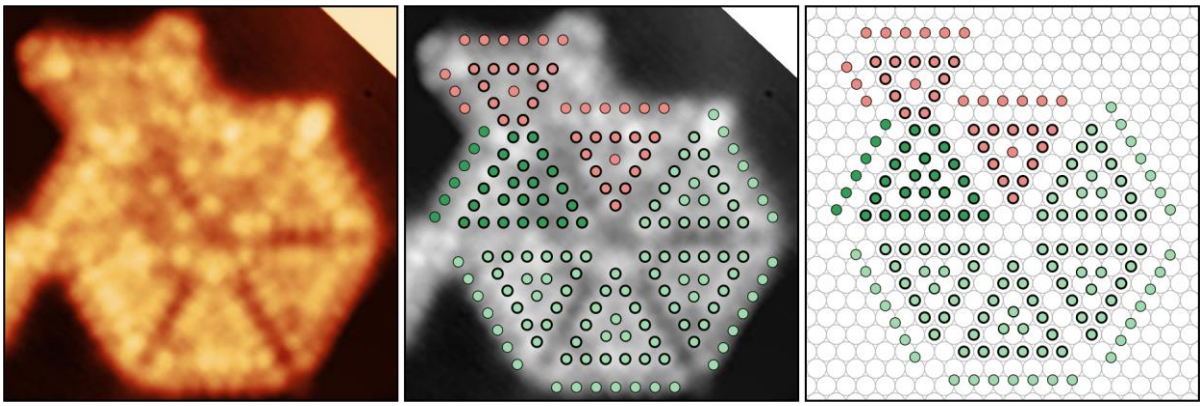

Figure 9-21 A large Hex-T, described as T_5-$4T_6$-T_7 (5.8 nm × 5.8 nm, V_s = 2.0 V, I_t = 0.2 nA).

As presented above, the triangle building block model works very well with Nb oxide triangular nanostructures including Single-T, Double-T, Triple-T, and Hex-T. The model is also valid for continuous films that comprise a number of triangle components. Figure 9-22 shows three examples of triangle continuous films with all the triangle components identified and covered by model masks. The combination of the triangle building blocks is very flexible. We can quickly reproduce the structural features of the films based on atomically-resolved STM images.

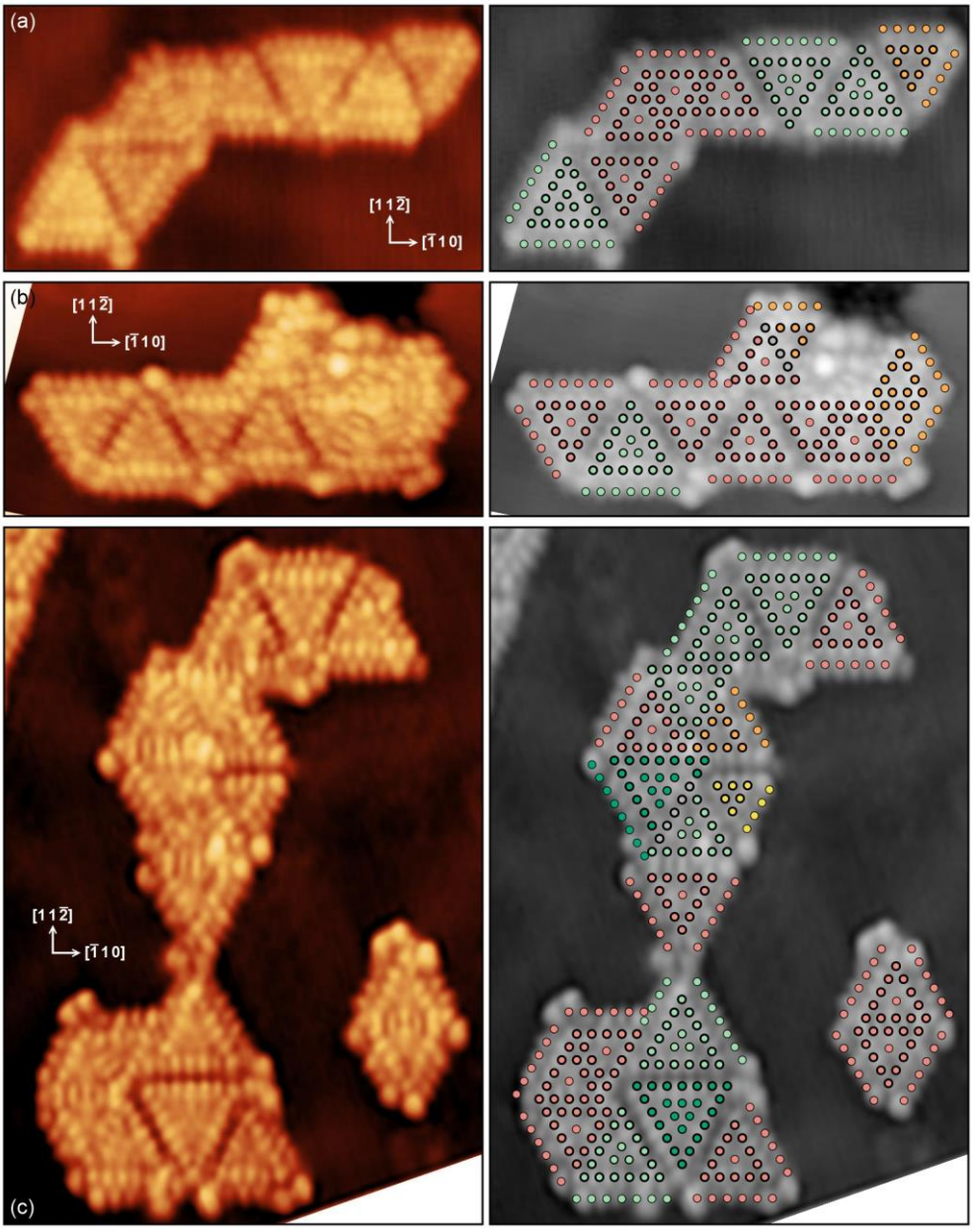

Figure 9-22 Three examples of Nb oxide triangle continuous film with triangle building blocks superimposed on the STM images in grayscale. (a) 9.2 nm × 5.3 nm, V_s = 0.7 V, I_t = 0.6 nA; (b) 9.2 nm × 4.5 nm, V_s = 0.7 V, I_t = 0.6 nA; (c) 9.2 nm × 13.3 nm, V_s = 0.7 V, I_t = 0.6 nA.

9.2.4 Nb oxide pinwheel structure

The Nb oxide pinwheel structure can be obtained using the same preparation condition as the triangle continuous films but with more metal deposition. Same as the HC structure, the pinwheel structure can adopt two growth modes: the free pinwheel (free-pinwheel) grown on the surface and the embedded pinwheel (emb-pinwheel) formed on the L_2 layer. Figure 9-23(a) shows the coexistence of free-pinwheel and emb-pinwheel, similar to the coexistence of free-HC and emb-HC in Figure 5-15.

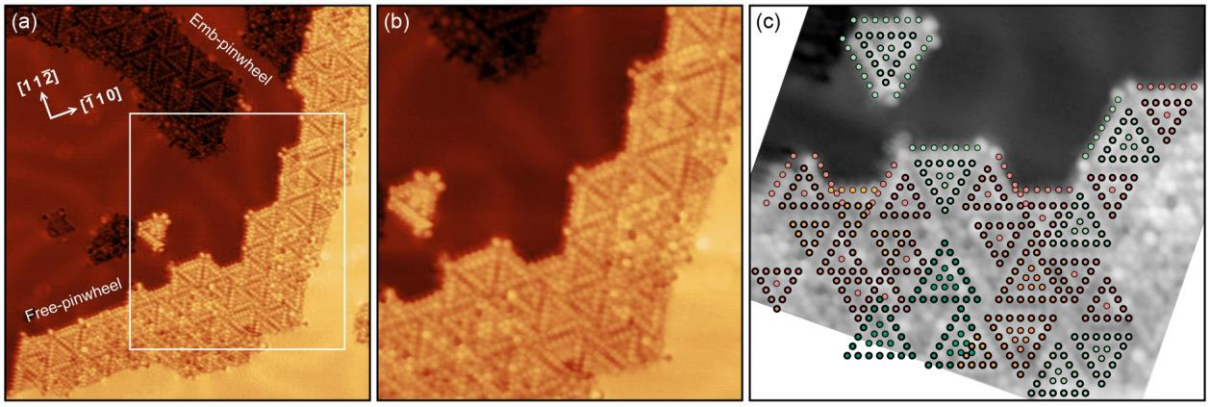

Figure 9-23 (a) STM images of Nb oxide pinwheel monolayers (25.5 nm × 27.6 nm, V_s = 1.0 V, I_t = 0.2 nA). (b) A close-up of the region in the white box in (a) (16.2 nm × 17.5 nm, V_s = 1.0 V, I_t = 0.2 nA). (c) Triangle building blocks are superimposed on the rotated (b) in grayscale.

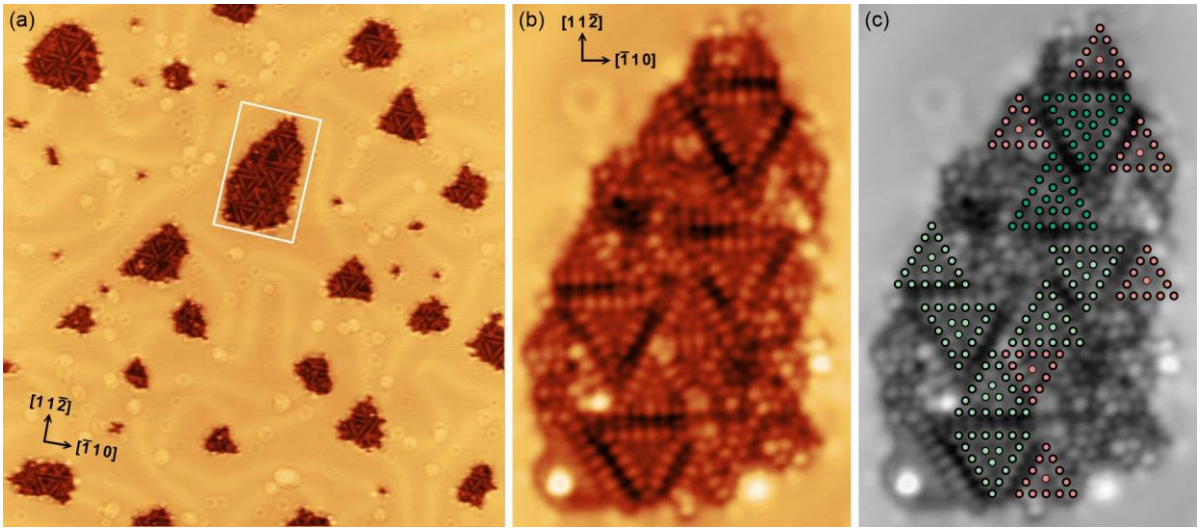

Figure 9-24 (a) STM images of an Au(111) surface with a number of Nb oxide emb-pinwheel islands (46 nm × 48 nm, V_s = 0.8 V, I_t = 0.3 nA). (b) A close-up of the region in the white rectangle in (a) (7.3 nm × 11.2 nm, V_s = 0.8 V, I_t = 0.3 nA). (c) Triangle building blocks are superimposed on (b) in grayscale.

It has been shown that the Nb-induced rings due to Nb-Au substitutions can act as a precursor structure for Nb oxide embedded monolayers. Similar to the preparation route in Figure 5-17, the critical step for acquiring emb-pinwheel monolayers is to deposit Nb on a hot substrate, which can accelerate the diffusion and the substitution process. In Figure 9-24(a), a few Nb oxide pinwheel islands are embedded in the Au(111) surface accompanied by lots of Nb-induced rings, which implies an inadequate oxidation. There is no discrepancy between the free-pinwheel and the emb-pinwheel regarding the structural characteristics. The triangle building block model performs well on examples shown in Figure 9-23(c) and Figure 9-24(c). Although the Moiré pattern model has been successfully applied to the Ti oxide pinwheel on Pt(111) [33] and the V oxide pinwheel on Rh (111) [69], it is not compatible with the Nb oxide pinwheel where the triangle elements exhibit a variety of sizes, gap distances, and lateral shifts.

Zhang [128] and Sedona [39] separately reported that the STM images of the pinwheel network showed a strong bias dependence [Figure 2-29(a) – (d), Figure 2-30(b)]. Zhang attributed this phenomenon to the electronic structure of Cr atoms. Sedona adopted the Moiré pattern model and she pointed out that the bias dependence could not be explained if only considering the topographical difference. We also observed that the Nb oxide pinwheel structure was sensitive to the sample bias. In Figure 9-25(a), the inside triangle rims were manifest, and the contrast difference between the inside rims and the triangle cores was greater when using a smaller sample bias. In contrast, though the inside triangle rims were still brighter in Figure 9-25(b), the contrast difference was reduced. Since the tunneling current remained unchanged, according to Formula (3-19) – (3-21), a higher sample bias means the tip will be slightly withdrawn, moving away from the sample surface. As a result, the sensitivity to a local height variation will be decreased during the tip scanning the sample surface. In the triangle building block model, the Nb atoms from the inside triangle rims are at on-top sites, higher than the core Nb atoms that occupy hollow sites. Therefore, increasing the sample bias reduces the contrast

difference between the inside triangle rims and the core. It should be noted that the electronic structure of the pinwheel network may also alter with the sample bias, which can contribute to the bias dependence phenomenon as well. Theoretical calculations are required to examine the assumptions, but they are beyond the scope of discussion in this work.

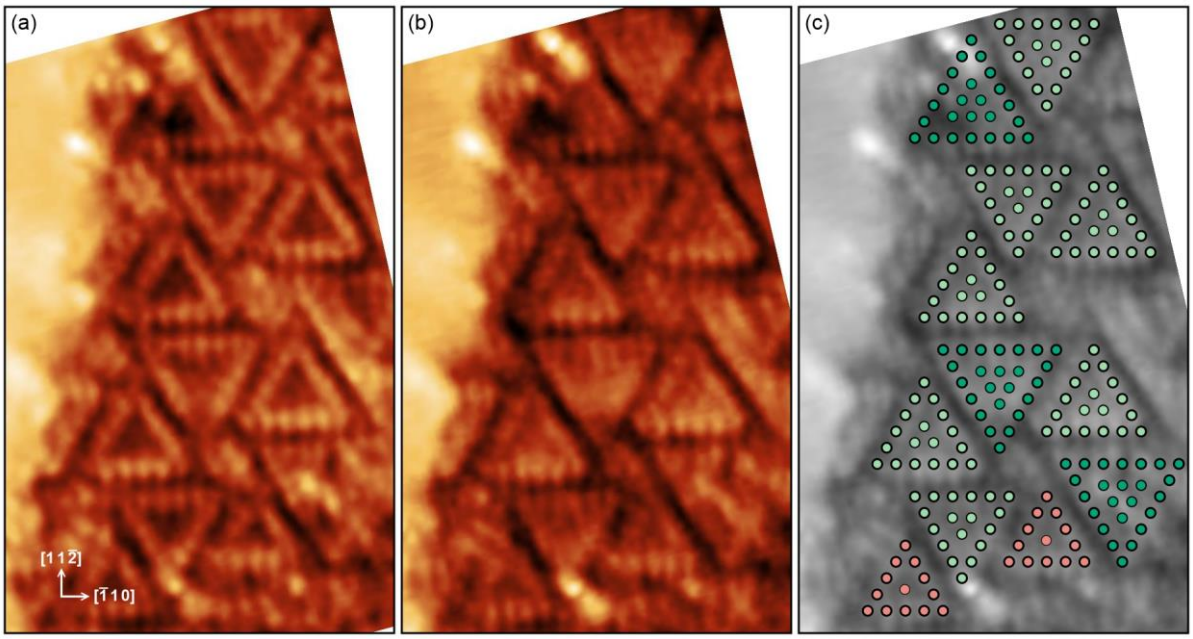

Figure 9-25 STM images showing that the Nb oxide pinwheel structure is sensitive to the sample bias. Frame size: 5.9 nm × 9.6 nm. (a) V_s = 0.5 V, I_t = 0.9 nA; (b) V_s = 0.6 V, I_t = 0.9 nA. (c) Triangle building blocks are superimposed on (b) in grayscale.

9.3 Nb oxide HC-connected triangles

It has been shown that the (2 × 2) Nb_2O_3 honeycomb structure is the most thermodynamically stable structure on Au(111) under the experimental conditions in this work. However, it is hard to get rid of triangle structures on Nb_2O_3 honeycomb islands by prolonged annealing or high-pressure oxygen (10^{-5} ~ 10^{-4} Pa). As shown in Figure 5-13(f), the HC-connected triangles exhibit three forms on Au(111): (i) Bay-T, which is usually found at the corners of HC islands and shares one side with the HC zigzag edge; (ii) Inlaid-T, which has two edges of the outside triangle rim degenerated and the remaining one became a part of the HC island's edge; (iii) Confined-T, which means the whole structure is enclosed by the hexagons of the HC lattice

with the outside triangle rim completely disappeared. The triangle size *n* is still determined by the inside triangle rim because the outside triangle rim would degenerate depending on the incorporation way. The core atoms ($n > 4$) are not reduced or seriously interrupted.

The HC-connected triangles have distinct structural properties from the independently-standing Nb oxide triangles. Firstly, the junction between a Bay-T and the HC lattice can be seen as a boundary (H-T boundary) where the Nb atom configuration depends on the parity of the triangle size *n*. Secondly, regarding the Inlaid-T and the Confined-T, Nb atoms from the inside triangle rims are no longer at on-top sites but hollow sites when integrated into the HC lattice. Meanwhile, Nb atoms at the triangle corners may have complex interactions with the HC lattice atom, and Nb atoms at the sides would deviate from the original sites. As a result, the triangle sides do not retain the straight lines but show a wavy feature.

Nb atom positions can be identified according to the protrusions on the empty-state STM images, but exact O atom configurations remain unknown. It is challenging to presume the complete structures of the HC-connected triangles with both Nb and O atoms. Therefore, the proposed models can only reflect possible Nb locations and focus on the permutation features. At the end of this section, we take T_5 as an example and speculate the O atom arrangements of Bay-T_5, Inlaid-T_5, and Confined-T_5.

9.3.1 Bay-T

Bay-Ts usually appear at the corners or short edges of HC islands. Assuming the HC edge is sufficiently long to sustain the Bay-T, the triangle bottom side connects with the HC edge in a unique way. For Bay-T_n, n = 4, 6, 8, 10, there are two equivalent permutations with chirality characteristics. Figure 9-26(a), (b) take Bay-T_4 as an example and show the chiral arrangements at the H-T boundary, denoted as Type A and Type A'. For n = 3, 5, 7, 9, 11 (the biggest Bay-T observed in the experiment), there are two different permutations. Taking Bay-T_5 as an example,

in Figure 9-26(c), the 1st, 3rd, and 5th atoms from the bottom side of the inside triangle rim are sitting above the terminal Nb atoms from the HC edge Z-66 (Type A); while in Figure 9-26(d), it is the 2nd and 4th atoms that locate directly above terminal edge atoms (Type B). These two types have a bilateral symmetry if the Z-66 edge is long and continuous.

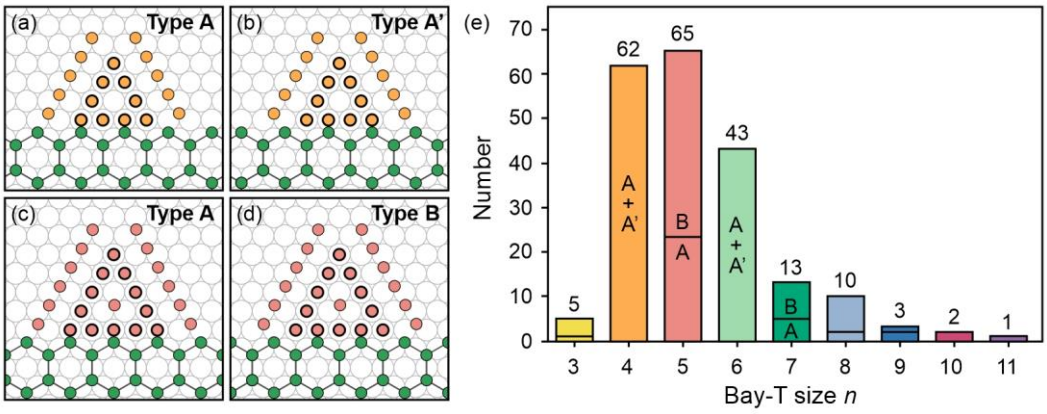

Figure 9-26 (a) – (d) Schematics of atom configurations of Bay-T_4 and Bay-T_5. The yellow, light red, and green circles all represent Nb atoms. (a) Type A of Bay-T_4, the triangle's 1st and 3rd side atoms are above the terminal atoms of the Z-66. (b) Type A', chiral to Type A; the triangle's 2nd and 4th side atoms are above the edge terminal atoms. (c) Type A of Bay-T_5, the triangle's 1st, 3rd, and 5th side atoms are above the edge terminal atoms. (d) Type B of Bay-T_5, the triangle's 2nd and 4th side atoms are above the edge terminal atoms. (e) The occurrence of Nb oxide Bay-Ts according to the triangle size *n*.

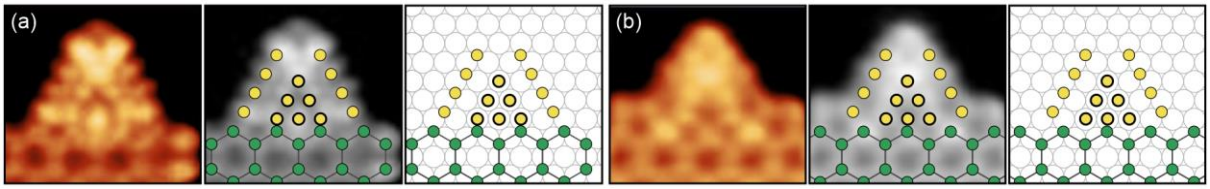

Figure 9-27 STM images of two types of Bay-T_3; model masks are superimposed on the STM images in grayscale and put on Au(111). The schematics focus on the relative positions and do not bother with the slight position deviation of the boundary atoms or defective sites. Image size: 2.6 nm × 2.3 nm. (a) V_s = 1.0 V, I_t = 0.4 nA; (b) V_s = 1.0 V, I_t = 0.8 nA.

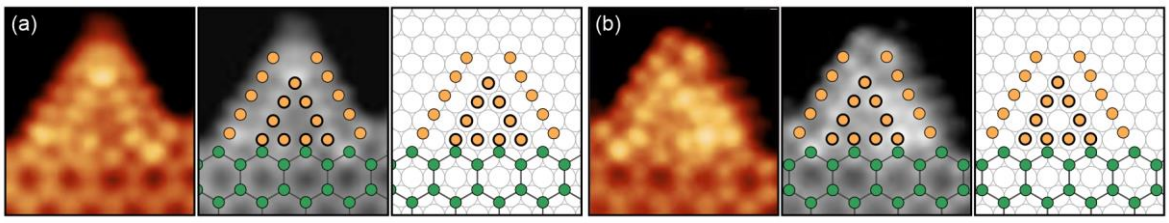

Figure 9-28 STM images and structural models of two types of Bay-T_4. Image size: 2.5 nm × 2.7 nm. (a) V_s = 0.8 V, I_t = 0.8 nA; (b) V_s = 1.0 V, I_t = 0.8 nA.

It is worth noting that the actual atom positions at the H-T boundary have slightly deviated from the original sites. The degree of the deviation is relevant to the lattice strain or Nb-O chemical bonding. Figure 9-27 – Figure 9-33 display two types of Bay-Ts from n =3 to n = 9. Figure 9-34 shows one permutation of Bay-T_{10} and Bay-T_{11}, we did not observe the other permutation because large Bay-Ts occurred less frequently, which leads to a small sample number.

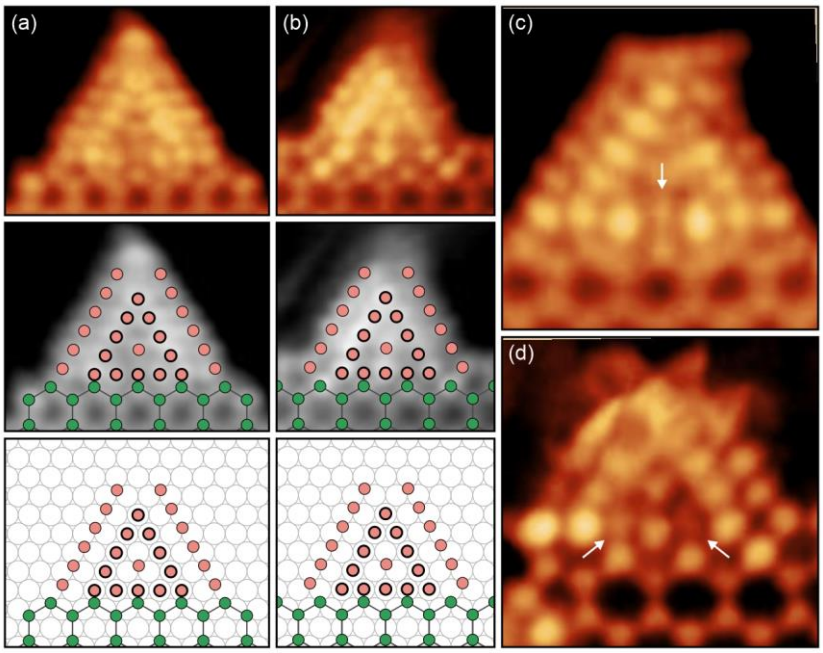

Figure 9-29 STM images of two types of Bay-T_5 with structural models. (a) 3.5 nm × 2.7 nm, V_s = 0.7 V, I_t = 0.5 nA; (b) 2.9 nm × 2.7 nm, V_s = 1.0 V, I_t = 0.3 nA. (c), (d) are another two examples in which atoms with lower contrast at the boundary are better resolved, as indicated by the white arrows (2.5 nm × 2.6 nm, c: V_s = 0.7 V, I_t = 0.5 nA; d: V_s = 0.7 V, I_t = 0.3 nA).

Atoms at the H-T boundaries show significant contrast variation in the STM images. Sometimes the resolution was not high enough to identify the atoms with lower brightness, so Figure 9-29(c) and (d) give another two examples of Bay-T_5, in which the boundary atoms are better resolved. It is evident that the triangle side atoms at the dent sites and the terminal atoms of the Z-66 exhibit higher brightness in the STM images [e.g., Figure 9-29(d)]. As these Nb atoms are surrounded by five or even six nearest atoms, the elevated brightness cannot be attributed to fourfold coordinated Nb atoms with a higher oxidation state. Presumably, the unique atom interaction and electronic structures lead to an increase of the LDOS. In addition, the highest

occurrence of Bay-T_5 in the bar chart in Figure 9-26(e) is consistent with the independently-standing triangles, indicating that T_5 is the most stable triangle structure.

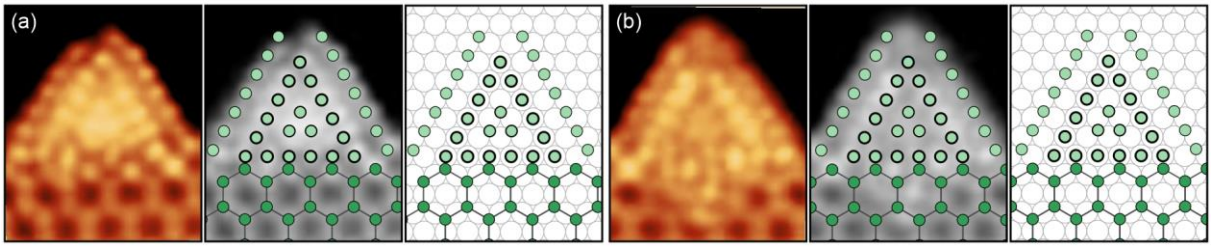

Figure 9-30 STM images of two types of Bay-T_6 with structural models. Image size: 2.6 nm × 3.1 nm. (a) V_s = 1.0 V, I_t = 0.16 nA; (b) V_s = 0.7 V, I_t = 0.5 nA.

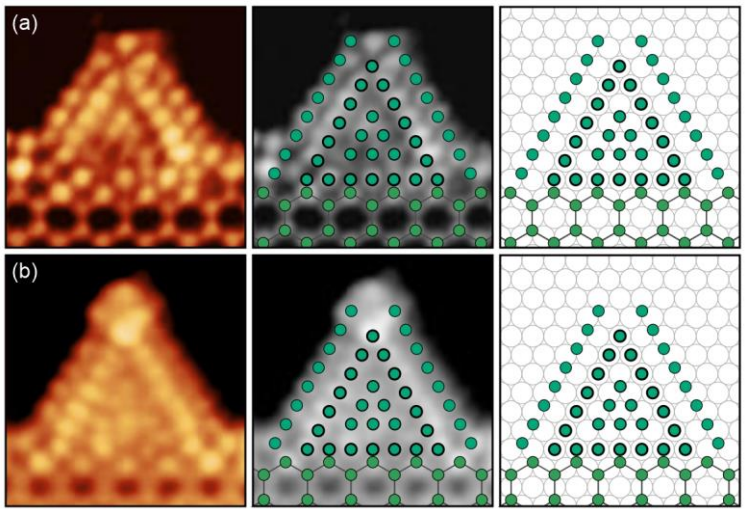

Figure 9-31 STM images of two types of Bay-T_7 with structural models. Image size: 3.2 nm × 3.2 nm. (a) V_s = 0.7 V, I_t = 0.3 nA; (b) V_s = 0.7 V, I_t = 0.5 nA.

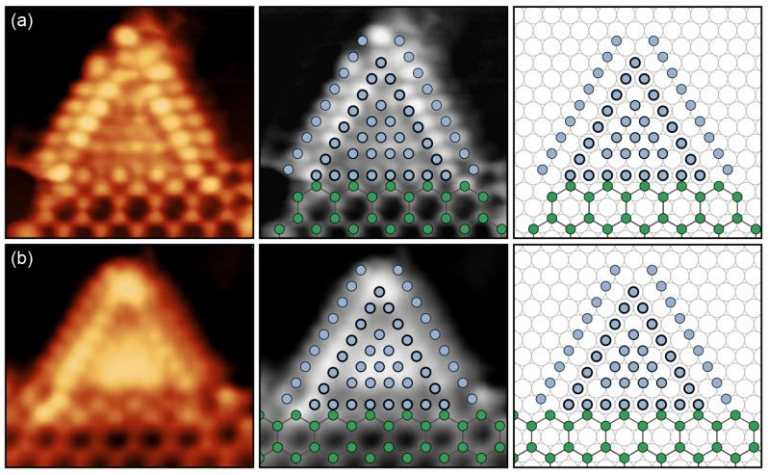

Figure 9-32 STM images of two types of Bay-T_8 with structural models. Image size: 3.9 nm × 3.6 nm. (a) V_s = 0.7 V, I_t = 0.3 nA; (b) V_s = 0.8 V, I_t = 0.4 nA.

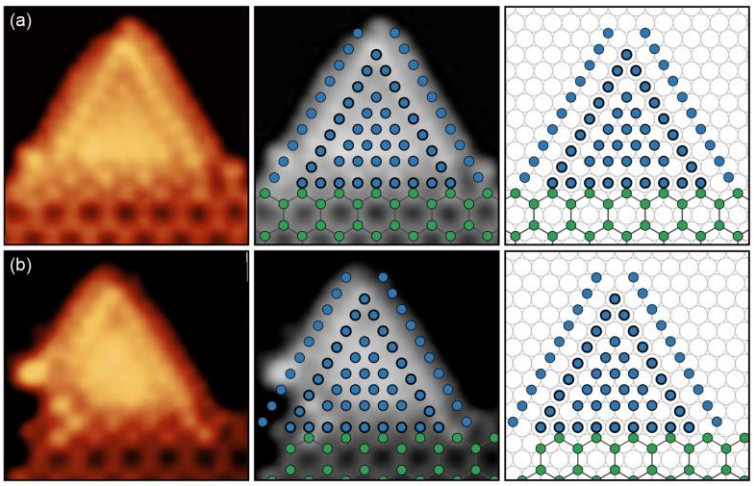

Figure 9-33 STM images of two types of Bay-T_9 with structural models. Image size: 3.8 nm × 3.7 nm. (a) V_s = 0.8 V, I_t = 0.4 nA; (b) V_s = 1.0 V, I_t = 0.6 nA.

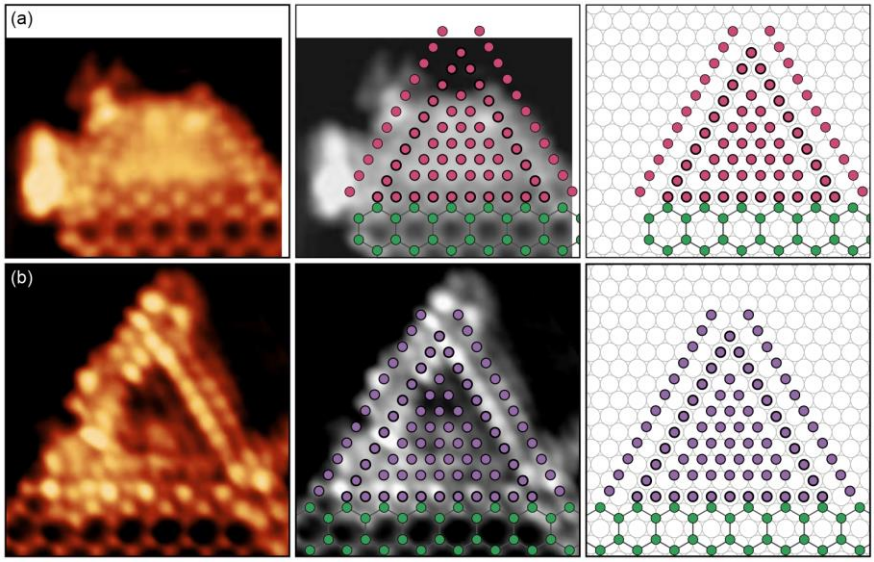

Figure 9-34 STM images with structural models of (a) Bay-T_{10} (frame size: 4.4 nm × 3.9 nm, V_s = 0.7 V, I_t = 0.6 nA); (b) Bay-T_{11} (4.4 nm × 4.5 nm, V_s = 0.5 V, I_t = 0.3 nA).

9.3.2 Inlaid-T

An Inlaid-T is usually formed at the HC edges with two sides of the outside triangle rim lost and two sides of the inside triangle rim integrated into the HC lattice. In contrast to the independently-standing triangles and Bay-Ts, Nb atoms from the inside triangle rim are located at hollow sites, while Nb atoms from the remaining side of the outside triangle rim and the core (n > 4) are at on-top sites. Figure 9-35(a) and Figure 9-38(c) are STM images of Inlaid-T_3 and Inlaid-T_6 taken at negative sample biases. It is not easy to obtain the filled-state STM images

which can atomically resolve the O atoms in the (2 × 2) Nb_2O_3 honeycomb structure. However, these two STM images do not help in elucidating the O atom configurations of the Inlaid-Ts. Electronic states of the Nb atoms might also affect the tunneling process, which hindered the observation of O atoms. Figure 9-36 – Figure 9-40 display Inlaid-Ts from T_4 to T_8, which is the largest inlaid triangular structure observed in the experiment.

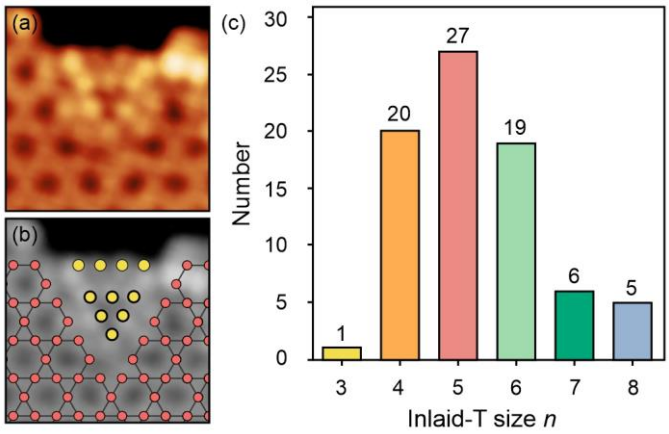

Figure 9-35 (a) Filled-state STM image of Inlaid-T_3 (2.3 nm × 2.2 nm, V_s = -0.8 V, I_t = 1.0 nA). (b) Lattice model superimposed on (a) in grayscale. Noting that all the schematics for Inlaid-T structures focus on the relative positions between the Inlaid triangle and the HC lattice, and do not bother with the slight position deviation of the boundary atoms or defective sites. Yellow: Nb; light red: O. (c) The occurrence of Nb oxide Inlaid-Ts according to the triangle size *n*.

The inlaid triangle's two sides interact with the HC lattice in the same way as the H-T boundary between the Bay-T and the Z-66 edge. Modest position deviation of the side Nb atoms can be observed from the STM images. But for simplicity, we still keep the ideal triangle shape with straight lines in the schematic models. Notably, atoms at the intersection of the triangle vertex and the HC, which is named the "wedge corner", have various configurations. In Figure 9-36(a), the atom in the black box can be regarded as a shared atom by the Inlaid-T_4 and the hexagon. The wedge corner in frame (b) possesses a great signal intensity, which can be attributed to two Nb atoms that are too close to be resolved independently. By contrast, we can identify the two Nb atoms in frame (c), one of which was embedded in the hexagon hollow center. Figure 9-37 shows three different wedge corners of the Inlaid-T_5, which are referred to as types A, B, and

C. These three types have been frequently observed in other Inlaid-Ts as well as Confined-Ts (e.g., Figure 9-41).

Apart from the wedge corner, the contrast difference at the parallel sides on the top of Inlaid-Ts should be noted. The upper side is from the outside triangle rim where Nb atoms are supposed to be located at the on-top sites. The lower side belongs to the inside triangle rim, and the Nb atoms occupy the hollow sites. There is a discrepancy between the topographical model and experimental observation. If only considering the topographical difference, atoms at on-top sites should be brighter than those at the hollow sites in the STM images. However, in the Inlaid-Ts, atoms from the lower side are much brighter than that from the upper side. This indicates that the Nb-O bonding conditions or the electronic structure of the cations could be varied at the two sides. The proposed models that only consider the topographical features fail to explain the fine details.

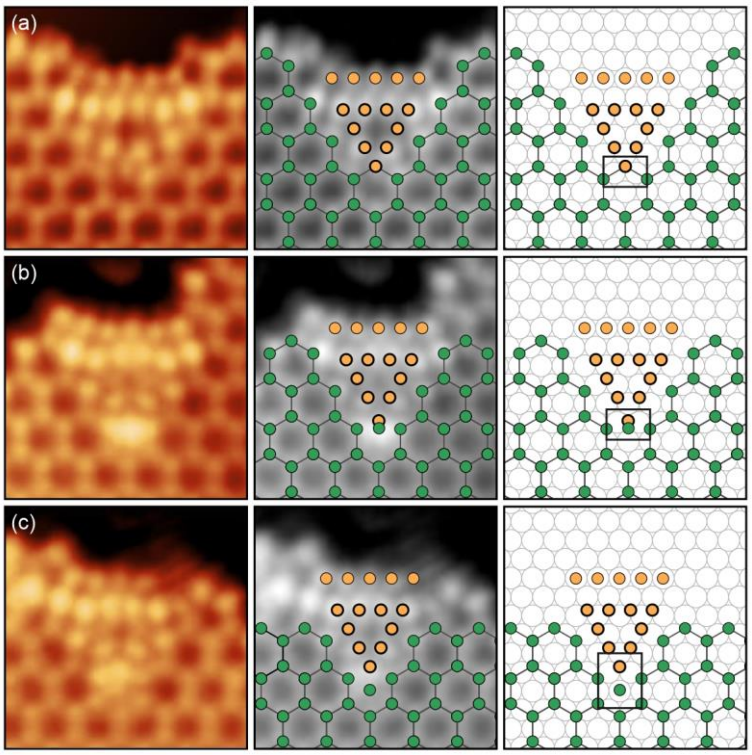

Figure 9-36 STM images of Inlaid-T_4 with different wedge corners. Image size: 3.2 nm × 3.2 nm. (a) V_s = 1.2 V, I_t = 0.75 nA; (b) V_s = 1.0 V, I_t = 0.3 nA; (c) V_s = 1.0 V, I_t = 0.3 nA.

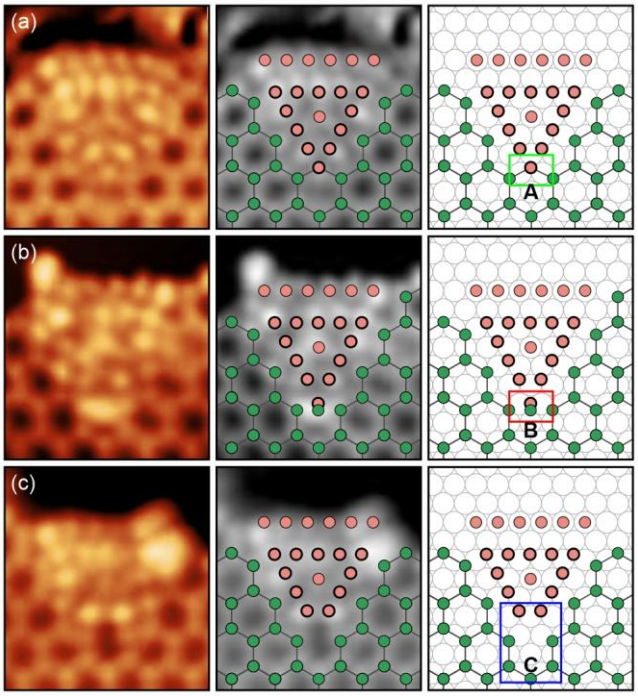

Figure 9-37 STM images of Inlaid-T_5 with three different types of wedge corner, denoted as A, B, and C. Image size: 2.7 nm × 3.0 nm. (a) V_s = 0.7 V, I_t = 0. 5 nA; (b) V_s = 0.7 V, I_t = 0.6 nA; (c) V_s = 1.0 V, I_t = 0.3 nA.

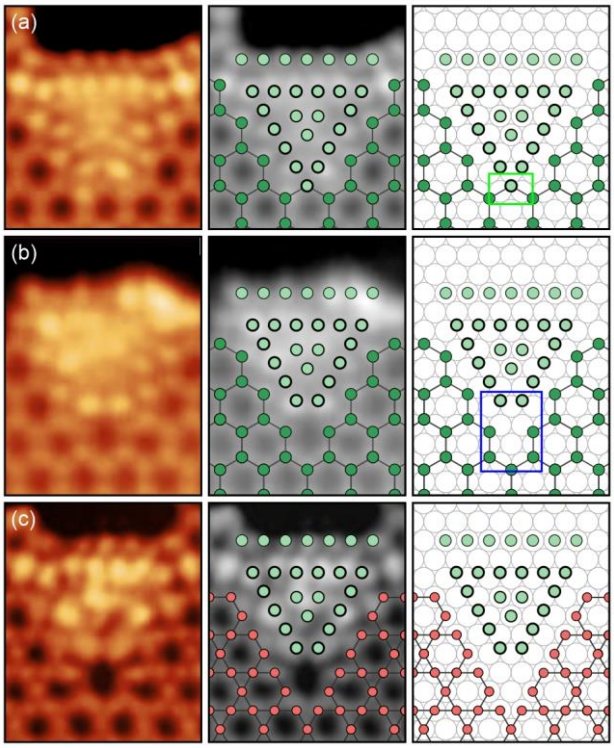

Figure 9-38 STM images of Inlaid-T_6 with wedge corner (a) type A (2.6 nm × 3.0 nm, V_s = 0.7 V, I_t = 0.5 nA); (b) type B (2.6 nm × 3.4 nm, V_s = 1.0 V, I_t = 0.3 nA). (c) Filled-state STM image of Inlaid-T_6 (2.6 nm × 3.2 nm, V_s = -1.5 V, I_t = 1.5 nA). Light green: Nb; light red: O.

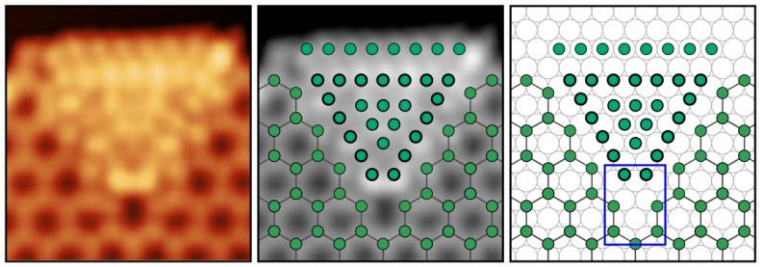

Figure 9-39 STM images of Inlaid-T_7 with wedge corner type C (3.2 nm × 3.4 nm, V_s = 0.7 V, I_t = 0.5 nA).

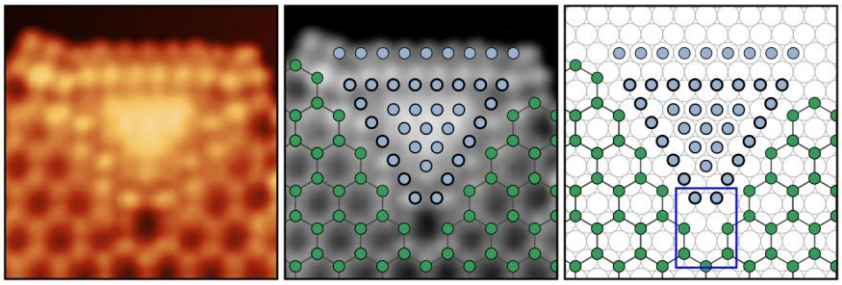

Figure 9-40 STM images of Inlaid-T_8 with wedge corner type C (3.6 nm × 3.6 nm, V_s = 0.7 V, I_t = 0.6 nA).

9.3.3 Confined-T

A Confined-T is entirely enclosed by the HC lattice and only the inside triangle sides remain. Technically, the side atoms of the triangle were shifted from the original sites. As demonstrated in Figure 9-41(a), (b), and (d), the atoms at the dent sites (e.g., atoms marked by "2" in orange) approached the HC lattice, while the atoms above the terminal atoms of the Z-66 were pushed away towards the core (e.g., atoms marked by "3"). Similar to the wedge corner of an Inlaid-T, atoms at the three vertices (e.g., the site labelled by "1") have three common configurations, namely type A, B, and C [Figure 9-41(f)]. Figure 9-41 displays a set of STM images showing Confined-T_5 with various corner combinations. Figure 9-41(l) is a STM image at a negative bias, but O atoms were still unable to be resolved, as was the case in Figure 9-35(a) (Inlaid-T_3), Figure 9-38(c) (Inlaid-T_6), and Figure 9-42(e) (Confined-T_7).

A remarkable characteristic of Confined-Ts compared with other triangle structures is that only the sizes with odd *n* were observed in the experiment, and no even number was found. Figure

9-41 – Figure 9-44 display STM images of Confined-T_5, T_7, T_9, and T_{11} (assuming an intact structure for T_{11}).

Moreover, Inlaid-T and Confined-T play important roles in the domain boundaries of the Nb_2O_3 honeycomb monolayers. We have shown that the Inlaid-T can be a termination of a domain boundary with random Nb atom arrangement (Figure 8-31). The Confined-T is able to act as a junction of two of three domain boundaries with an intersection (Figure 8-33). Compared with the (2 × 2) honeycomb lattice, the triangle structures can accommodate more cations in the same area, and the Nb atoms do not need to keep a strict (2 × 2) epitaxial registry with respect to the Au(111) surface.

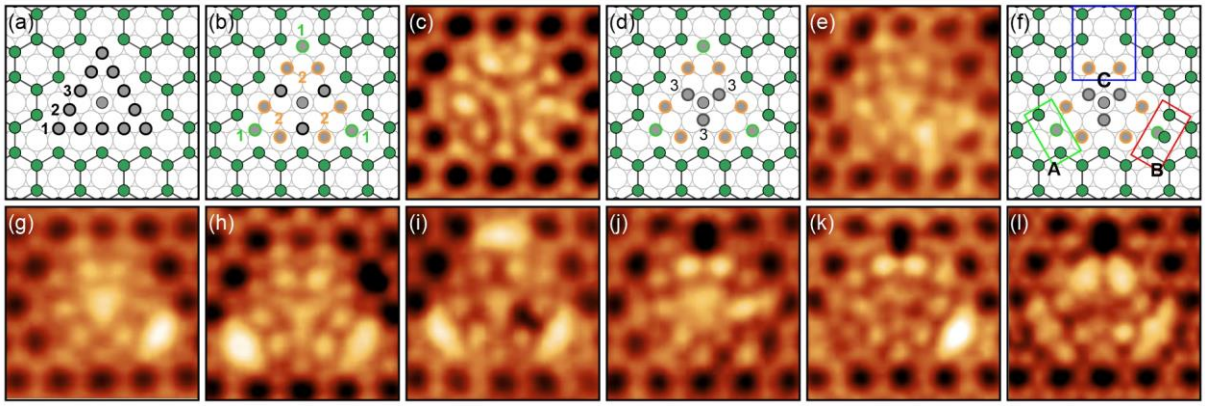

Figure 9-41 Schematics of (a) an ideal T_5 confined in the HC; (b) side atoms of the T_5 deviated from the original sites. Atoms labelled by "1" are pushed towards the HC; atoms marked by "2" in orange at the dent sites approaching the HC. (c) STM image of a Confined-T_5, a good example corresponding to structural model in (b) where the atoms at position 3 were not yet deviated (V_s = 0.7 V, I_t = 0.5 nA). (d) Schematic showing the atoms marked by "3" moved towards the triangle core. (e) STM image of a Confined-T_5 with atoms at position 3 accumulated at the core. Atoms at the core are so close to each other that they cannot be independently resolved in the STM images (V_s = 0.7 V, I_t = 0.6 nA). (f) Schematic of a Confined-T_5 with three different vertices which are denoted as A, B, C and in consistent with the wedge corner of Inlaid-Ts. (g) – (k) are STM images showing Confined-T_5 with different vertex combinations (description follows bottom left, bottom right, middle). (g) ABA (V_s = 1.0 V, I_t = 0.68 nA). (h) BBA (V_s = 0.8 V, I_t = 0.4 nA). (i) BBB (V_s = 0.7 V, I_t = 0.6 nA). (j) AAC (V_s = 0.8 V, I_t = 0.5 nA). (k) ABC (V_s = 0.7 V, I_t = 0.5 nA). (l) Filled-state STM image of Confined-T_5 (V_s = -1.5 V, I_t = 1.5 nA). Frame/image size: 2.6 nm × 2.6 nm.

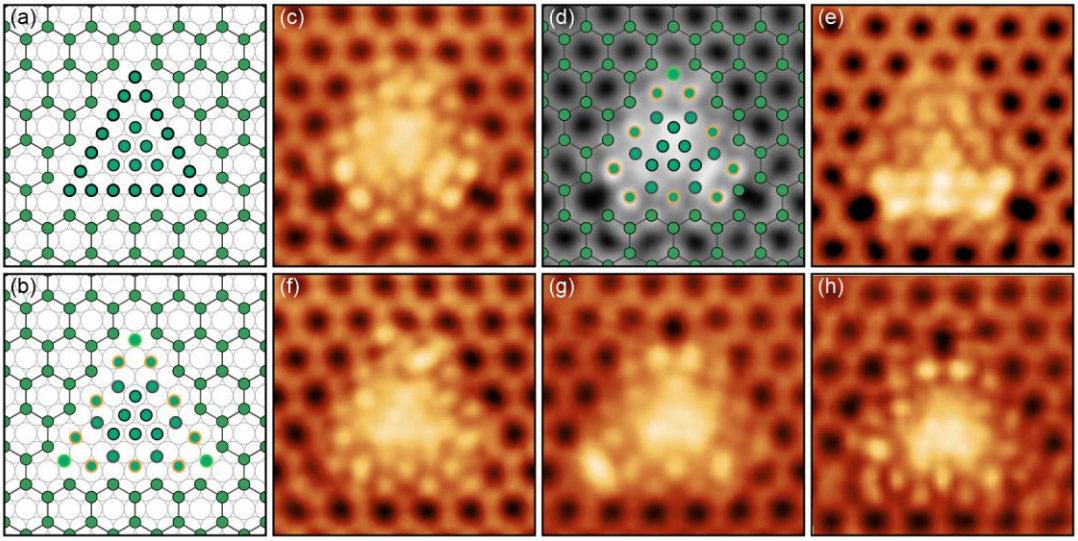

Figure 9-42 Schematics of (a) an ideal T_7 confined in the HC; (b) side atoms deviated from the original sites. (c) STM image of a Confined-T_7 with CAC vertices (V_s = 0.7 V, I_t = 0.5 nA). (d) Structural model superimposed on (c) in grayscale. (e) Filled-state STM image of the Confined-T_7 (V_s = -0.8 V, I_t = 1.0 nA). (f) – (h) STM images of Confined-T_7 with different vertex combinations: (f) AAA (V_s = 0.7 V, I_t = 0.5 nA). (g) BAC (V_s = 1.0 V, I_t = 0.2 nA). (h) AAC (V_s = 1.0 V, I_t = 0.2 nA). Frame/image size: 3.5 nm × 3.5 nm.

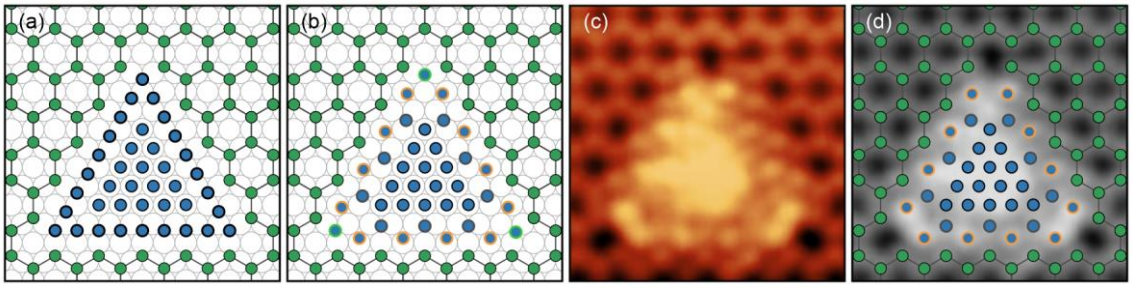

Figure 9-43 Schematics of (a) an ideal T_9 confined in the HC; (b) side atoms deviated from the original sites. (c) STM image of a Confined-T_9 with CCC vertices (V_s = 1.0 V, I_t = 0.2 nA). (d) Structural model superimposed on (c) in grayscale. Frame/image size: 3.6 nm × 3.6 nm.

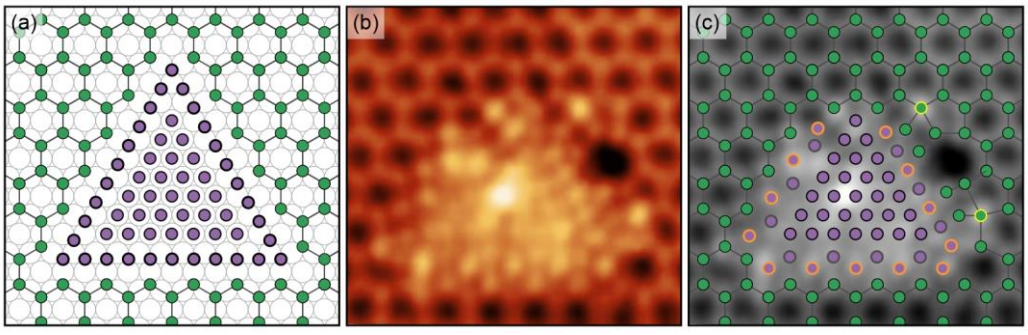

Figure 9-44 (a) Schematics of a T_{11} confined in the HC. (b) STM image of a Confined-T_{11} assuming an intact structure without defects (V_s = 0.75 V, I_t = 0.5 nA). (c) Structural model superimposed on (b) in grayscale. Frame/image size: 4.2 nm × 4.2 nm.

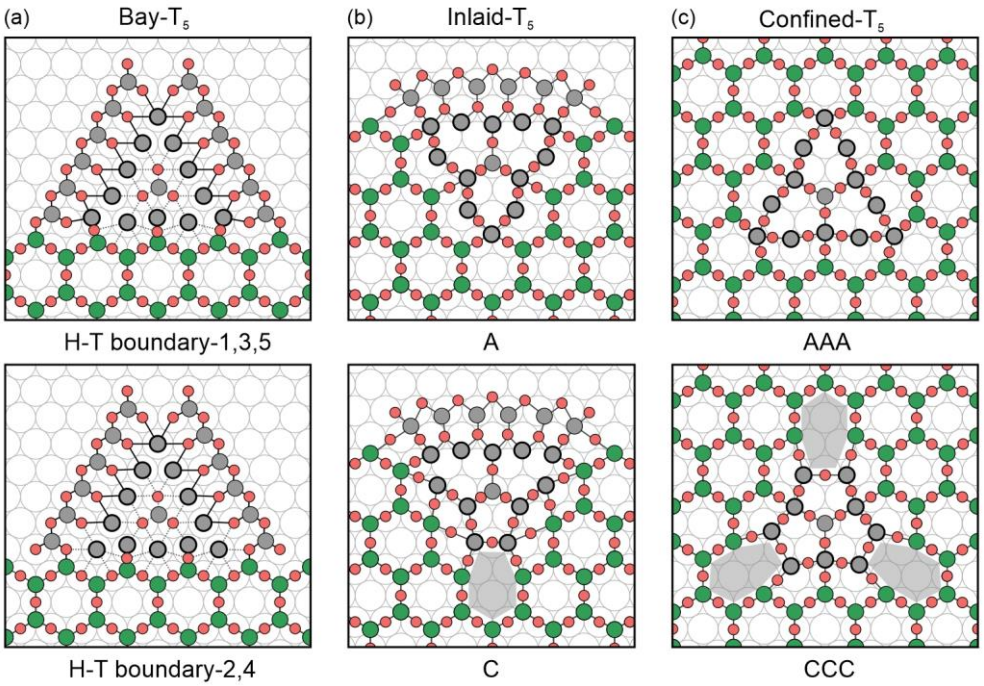

Figure 9-45 Schematics of atom configurations of (a) Bay-T_5 with two types of H-T boundary. (b) Inlaid-T_5 with two types of wedge corners: A, C. (c) Confined-T_5 with two types of vertex combinations: AAA, CCC. The grey and green circles represent Nb atoms in the triangle and the honeycomb, respectively; the light red circles represent O atoms. Solid lines connect the Nb with O atoms but do not represent the actual Nb-O bonding. Dash lines in column (a) are speculated connections with less confidence.

Although the filled-state STM images failed to reveal the O atoms arrangement, we took T_5 as an example and proposed several models for the HC-connected triangles with both Nb and O atoms in Figure 9-45. We speculated that there were three O atoms in the triangle core, which is consistent with the proposed configuration in Figure 9-7(a).

However, we found that the proposed atom configurations for Bay-T_5 in Figure 9-45(a) were unconscionable when we were trying to connect Nb with surrounding O atoms. The solid lines could be acceptable, but problems occurred at the triangle core and H-T boundaries, as depicted by dash lines. In the two schematics in column (a), the triangle's side Nb atoms at the dent sites is fivefold or even sixfold coordinated with O atoms. This is not reasonable given that a Nb atom possesses five valence electrons. The Nb atoms in the oxide nanostructures supported on the Au(111) substrate generally have electrons transferred to the Au substrate, so the actual oxidation state is higher than the coordination number. Meanwhile, the terminal Nb atoms of

Z-66 still bond to three oxygen in the two schematics, which contradicts the explanation for its higher brightness due to the higher oxidation state. Proposed models for Inlaid-T_5 and Confined-T_5 in Figure 9-45(b) and (c) are more sensible. In particular, the Nb atoms that bonds with four O atoms in the schematics correspond to the protrusions with higher brightness in the experimental STM images. But many fine features in the STM images cannot be explained by these simplified models. The actual atom arrangements, Nb-O bonding, and film-substrate should be far more complicated and cannot be revealed by these 2D schematic drawings.

Overall, it is unfortunate that the study in this work is not able to elucidate the complete structure of Nb oxide triangles, especially at the H-T boundaries. Further experiments and theoretical calculations are required to work out the exact atom configurations.

9.4 Ti oxide triangle and pinwheel structures

Ti oxide triangles and pinwheel structures can be obtained by post-oxidation in 1×10^{-7} Pa O_2 at 500 ℃ for 15 ~ 30 mins, using a lower oxygen pressure and shorter annealing time than the preparation for the (2 × 2) Ti_2O_3 honeycomb monolayers. The triangles were formed prior to the pinwheel network with a small amount of metal deposition. Depending on the preparation routes, both triangles and the pinwheel network could be grown into free or embedded monolayers. Nb oxides also form the free-pinwheel and the emb-pinwheel, but we only observed free triangles and did not find any embedded triangles.

Figure 9-46(a) and (b) display a free Ti oxide triangle and an embedded triangle. The atom arrangement of free triangles/pinwheels is essentially the same as their embedded counterparts inside the monolayers, but the edges are usually incomplete or decorated by adatoms. Hence, we evaluate the free triangle size by the number of Ti atoms at a side of the second rim, using n or T_n to represent. For an embedded triangle, n is set to be the number of Ti atoms at a side

of the triangle against the dark background in the STM images. Therefore, triangles in Figure 9-46(a) and (b) can be denoted as free-T_5 and emb-T_4, respectively.

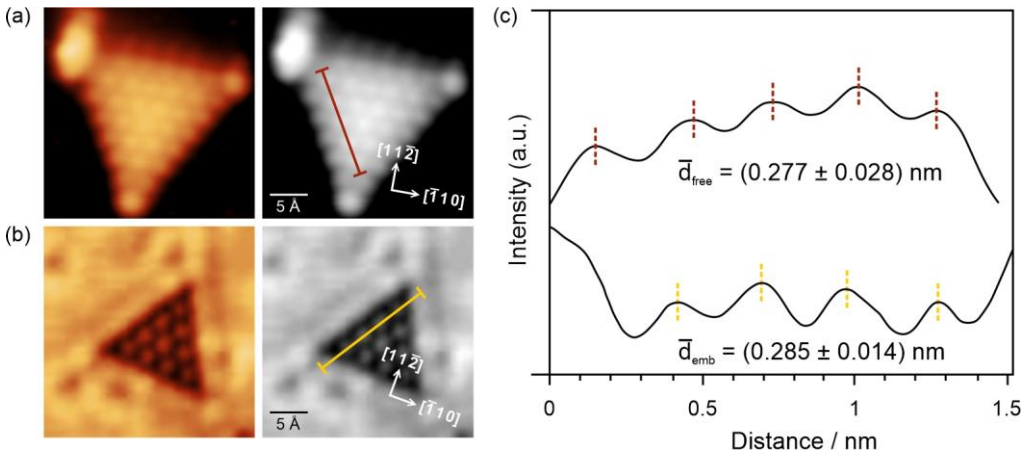

Figure 9-46 STM images of Ti oxide grown into (a) a free triangle (T_5) (2.8 nm × 2.8 nm, V_s = 0.8 V, I_t = 0.5 nA); (b) an embedded triangle (T_4) (2.8 nm × 2.8 nm, V_s = 0.6 V, I_t = 0.8 nA). (c) Profiles of the red and yellow lines in (a) and (b) showing the periodicity calculations.

Figure 9-46(c) shows the profiles of the red and yellow lines in frame (a) and (b). The calculated periodicities are quite close to the lattice constant of the Au(111) surface unit cell, indicating that Ti oxide triangles had a (1 × 1) epitaxial growth. The cation configuration in Ti oxide triangles is distinct from that in Nb oxide triangles. A Nb oxide triangle consists of an outside rim and an inside rim with Nb locations altered, whereas a Ti oxide triangle has a close-packed atom arrangement, so they are not visually double-rimmed.

We have demonstrated that the triangle building block model works well with our experimental observations from Nb oxides. The same idea can be applied to Ti oxide as well because we found that the Ti lattice in triangles or pinwheel monolayers has no rotation with respect to the Au(111) surface. This is not in agreement with previous reports from Wu [42] and Tumino [43]. They used the Moiré pattern model to interpret the Ti oxide pinwheel structures but reached different conclusions regarding the lattice mismatch, rotation angles, and thus the expressions for the superstructures. Compared with the Moiré pattern model, the triangle building model is more suitable for multiple triangles/pinwheel networks that are composed of triangle elements

with various sizes. However, both models can only interpret the image contrast from the topographical perspective, and the model constructions are limited by the lack of information on O atom configuration and Ti-O bonding.

9.4.1 Free and embedded triangles

Figure 9-47 shows the close-packed triangle models from T_1 to T_{10}, in which Ti atoms are supposed to occupy the hollow sites of Au(111). Figure 9-48 displays the STM images of T_2 – T_{12}, but the biggest Ti oxide triangle that can independently stand on Au(111) is T_{10}. Triangles with high indices (e.g., T_{11} and T_{12}) were found in pinwheel networks, so they are technically not single triangles. The STM images of embedded triangles (T_1 – T_7) are presented in Figure 9-49(a), (b). The embedded Ti oxide triangles in the "dark pits" were surrounded by three "ridges". Presumably, the ridges were due to surface Au atoms that were not atomically resolved. The bar chart in Figure 9-49(c) shows the occurrence of embedded triangles according to the size, which indicates that T_4 is the most common and stable embedded triangle.

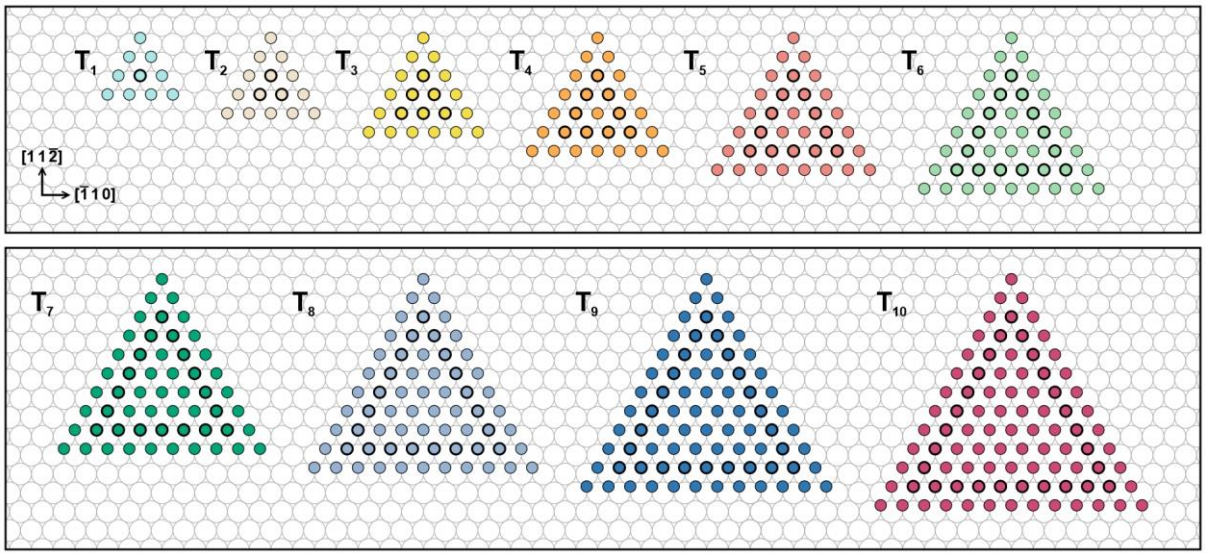

Figure 9-47 Schematics of Ti oxide single triangle models from T_1 to T_{10}. All Ti atoms are supposed to occupy the hollow sites with a close-packed arrangement. The size of the triangle is evaluated by the second rim triangle which is represented by circles with a bold perimeter.

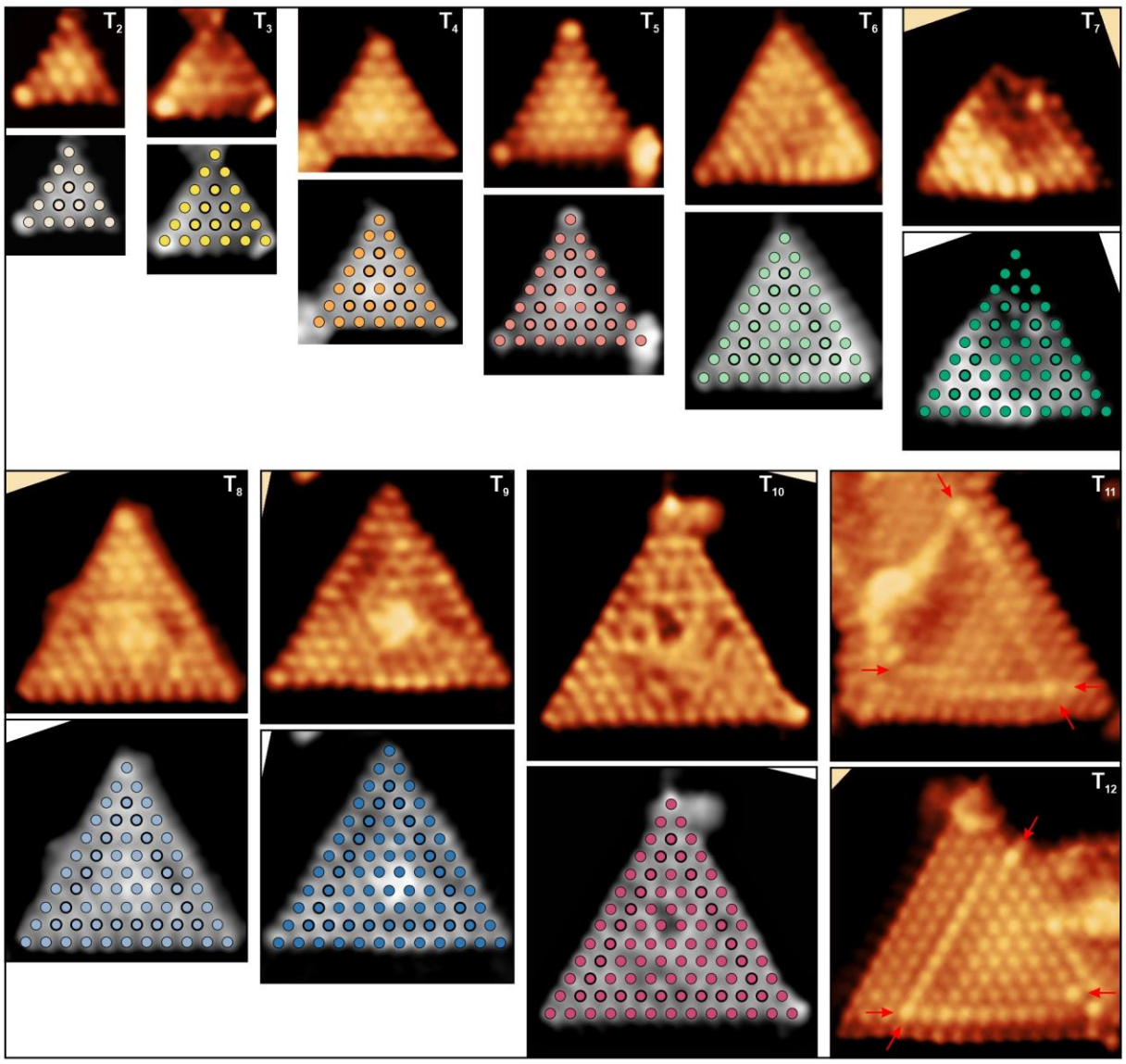

Figure 9-48 STM images of Ti oxide free triangles from T_2 to T_{12} with model masks superimposed on the images below. T_{11} and T_{12} cannot be seen as single triangles but a part of the pinwheel monolayers, so the schematics were not depicted. Red arrows indicate the double-row boundaries. Frame/image height and imaging conditions: T_2: 1.7 nm, V_s = 0.8 V, I_t = 0.5 nA; T_3: 1.9 nm, V_s = 0.8 V, I_t = 0.5 nA; T_4: 2.4 nm, V_s = 0.4 V, I_t = 0.7 nA; T_5: 2.6 nm, V_s = 0.8 V, I_t = 0.5 nA; T_6: 2.8 nm, V_s = 0.4 V, I_t = 0.9 nA; T_7: 3.1 nm, V_s = 0.7 V, I_t = 0.6 nA; T_8: 3.5 nm, V_s = 0.3 V, I_t = 1.2 nA; T_9: 3.6 nm, V_s = 0.5 V, I_t = 0.5 nA; T_{10}: 4.1 nm, V_s = 0.3 V, I_t = 1.0 nA; T_{11}: 4.1 nm, V_s = 1.0 V, I_t = 0.3 nA; T_{12}: 4.1 nm, V_s = 0.4 V, I_t = 1.0 nA.

An interesting tiny structure can be seen in the black box in Figure 9-49(a). If following the nomenclature for embedded triangles, it should be called T_0 as there is no protrusion confined in the dark pit. However, it is not a Ti oxide structure but generated by a Ti atom substituting an Au atom at the L_2 layer, while the surface Au atoms were not removed [Figure 9-49(f)]. The discussion of *M*-Au substitutions and *M*-induced triangular ring patterns (*M* = Nb, Ti, V, Mn)

has been demonstrated in Chapter 4. Figure 9-49(d) is the same structure as the one in the black box but with atomic resolution. Figure 9-49(e) is a DFT-simulated STM image which confirms that it is a Ti-Au substitution at the L_2 layer. In sharp contrast, the formation of embedded triangle structures results from removing surface Au atoms and oxidizing Ti atoms.

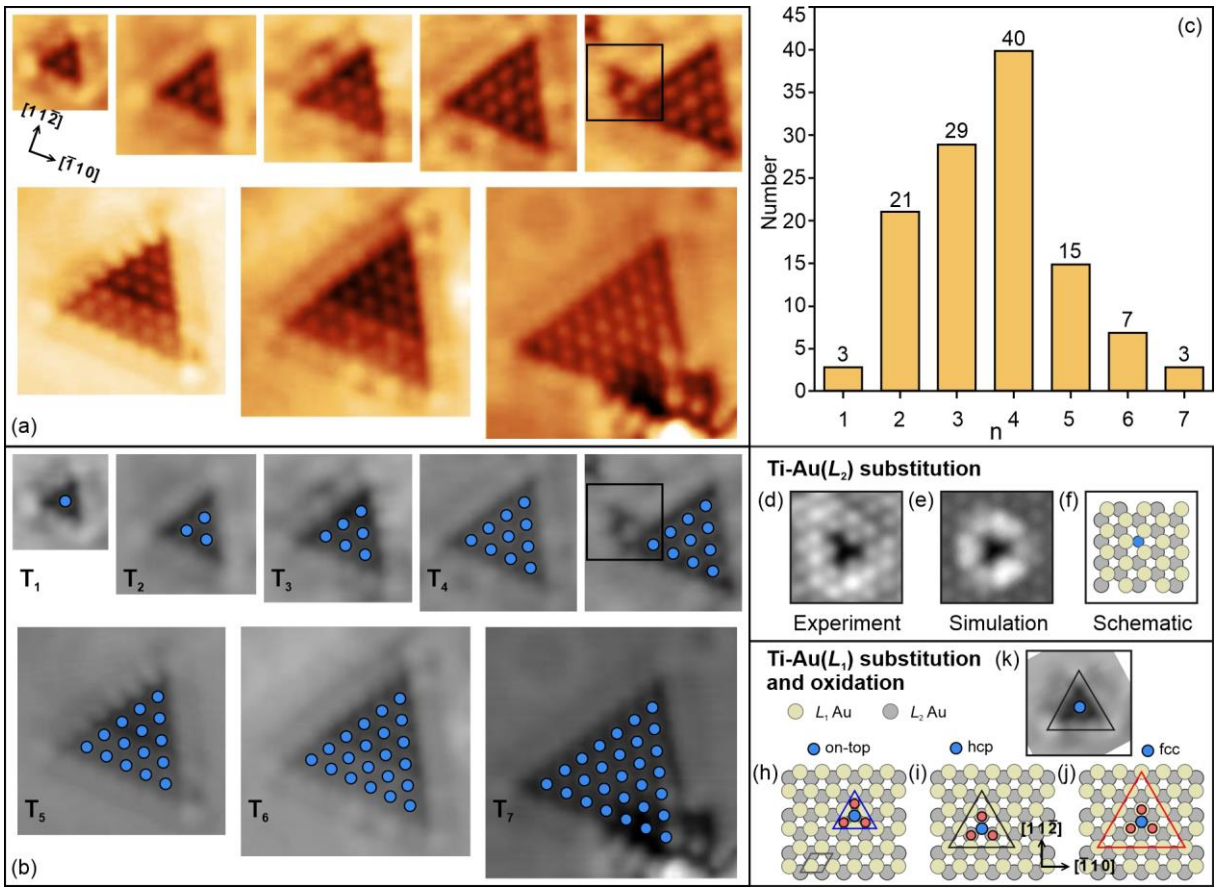

Figure 9-49 (a), (b) STM images of Ti oxide embedded triangles from T_1 to T_7. The triangle size n is determined by the number of side atoms in the "dark pits". Image sizes and imaging conditions: T_1: 1.3 nm × 1.3 nm, V_s = 0.8 V, I_t = 0.6 nA; T_2: 1.9 nm × 1.9 nm, V_s = 0.5 V, I_t = 0.9 nA; T_3: 2.0 nm × 2.0 nm, V_s = 0.8 V, I_t = 0.8 nA; T_4: 2.1 nm × 2.1 nm, V_s = 0.6 V, I_t = 0.8 nA; T_4 with Ti-Au (L_2) substitution: 2.1 nm × 2.1 nm, V_s = 0.5 V, I_t = 0.9 nA; T_5: 2.8 nm × 2.8 nm, V_s = 0.8 V, I_t = 0.8 nA; T_6: 3.0 nm × 3.0 nm, V_s = 0.8 V, I_t = 0.8 nA; T_7: 3.3 nm × 3.3 nm, V_s = 0.4 V, I_t = 0.8 nA; (c) The occurrence of Ti oxide embedded triangles according to the size n. (d) Atomically-resolved STM image of a Ti-induced ring patten due to Ti-Au substitution at the L_2 layer (1.5 nm × 1.5 nm, V_s = 0.4 V, I_t = 0.8 nA). (e) DFT simulated STM image of the Ti-Au (L_2) substitution (V_s = 0.5 V). (f) Schematic of the Ti-Au substitution at the L_2 layer. A blue circle (Ti) replaced a grey circle (L_2 Au), and the pale-yellow circles (L_1 Au) remained unchanged. (k) The same image as T_1 in (b). (h) – (j) Three possible atom configurations: (h) the Ti atom is at the on-top site of the L_2 layer, no Au atom from the L_1 layer is removed; (i) the Ti atom substitutes a L_1 Au atom, occupying the hcp site of the L_2 layer; (j) More L_1 Au atoms are removed, the Ti atom occupies the fcc site of the L_2 layer. Blue circles: Ti atoms; light red: O atoms; pale-yellow: L_1 Au atoms; light grey: L_2 Au atoms.

The schematics in Figure 9-49(h), (i), (j) show three possible atom configurations, taking the simplest embedded triangle T_1 as an example. The Ti atom is assumed to be bonded with three O atoms. Based on the theoretical calculations for the (2 × 2) Ti_2O_3 honeycomb structure on Au(111), Ti cations in the triangle/pinwheel structures may also have electrons transferred to the Au substrate, making them approach the surface while O atoms are extending outward. For simplicity, we only show the 2D schematic drawings in this chapter.

Prior to analyzing any embedded structures, the relative positions of Au(111) layers should be clarified at the beginning. We take the L_2 layer as the reference and let the Au atoms from the surface layer (L_1) occupy the hcp sites. The parallelogram at the bottom of Figure 9-49(h) indicates the unit cell of the Au(111) L_2 layer. In frame (h), the Ti atom was put at the on-top site of the L_2 layer, which is also the fcc hollow site of the L_1 layer. As a result, no L_1 Au atom had to be removed. In frame (i), the Ti atom replaced a surface Au atom, occupying the hcp site. In frame (j), the Ti atom is set to occupy the fcc site, causing more surface Au atoms to detach. We outlined the footprints (the triangles drawn in blue, black, and red solid lines) and compared them with the experimental STM images. It can be seen that the model in frame (i) would be the best to reproduce the structural features of the embedded triangle. In short, the protrusions in the "dark pits" are attributed to Ti atoms that replaced the surface Au atoms.

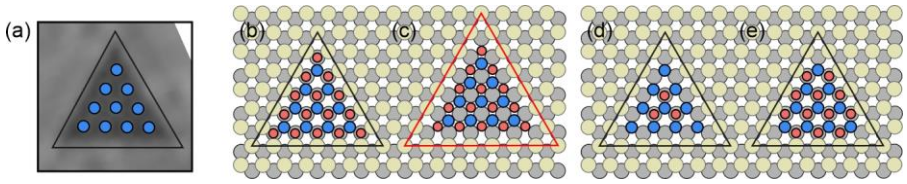

Figure 9-50 (a) STM image of a Ti oxide embedded triangle T_4, the same image as the T_4 shown in Figure 9-49(b). (b) – (e) possible atom configurations: (b) Ti atoms replace the L_1 Au atoms sitting at the hcp sites of the L_2 layer. Ti and O atoms are arranged alternatively with a stoichiometry of $T_{10}O_{15}$. The three edges of the triangle are O-terminated. (c) The same atom configuration as (b), but Ti atoms are put on the fcc sites so more L_1 Au atoms are removed. (d) The same Ti atom configuration as (b) but with fewer O atoms leading to an unreasonable stoichiometry of $T_{10}O_3$. The three edges of the triangle are Ti-terminated. (d) The same Ti atom configuration as (b), but the O lattice is truncated with three atoms at the vertices removed. The stoichiometry is $Nb_{10}O_{12}$. The sides are O-terminated while the corners are Ti-terminated.

Figure 9-50 takes emb-T_4 as an example for further analysis of the structure. Frame (b) is a reasonable structural model (black outline) where Ti atoms replace the surface Au atoms and occupy the hcp hollow sites. The schematic of the same atom configuration but with Ti shifted to the fcc sites results in a larger footprint (red outline) in frame (c), so it seems inappropriate. It is worth noting that the O atom configuration in (b) or (c) adopts a (1 × 1) periodicity, which is similar to the structural models of triangular FeO nanostructures [138] but distinct from the Nb oxide triangle models (Figure 9-6, Figure 9-7) due to their double triangle rims. The stoichiometry of emb-T_4 based on the structural model in frame (b) is $Ti_{10}O_{15}$. If the edge of an embedded triangle is completely Ti-terminated, like the structural model in frame (d), the stoichiometry is $Ti_{10}O_3$, which should not be practical. In frame (e), the O atoms at three vertices have been reduced, giving rise to a stoichiometry of $Ti_{10}O_{12}$. This atom configuration with a truncated shape could be possible as the oxidation state of the corner cations may be varied from the side Ti atoms due to complex interactions with Au or adatoms.

Ti oxide embedded triangles can form multiple triangle nanostructures, similar to Double-T, Triple-T, and triangle continuous films of Nb oxides. Figure 9-51(a) and (b) show double embedded triangles which can be denoted as T_1-T_1 and T_4-T_4 according to the sizes of the triangle elements. As mentioned above, we speculated that the "ridges" surrounding the "dark pits" were L_1 Au atoms rather than Ti atoms, so they are marked by grey circles. The boundaries between triangle elements are highlighted by the white circles and exhibit distinct features from Nb oxides. There are two types of boundaries: one is called single-row boundary indicated by the white arrows; the other is called double-row boundary indicated by the red arrows in Figure 9-48 (T_{11}, T_{12}) and Figure 9-51(e).

The signal intensity of protrusions along a single-row boundary is nearly identical. However, it is common to find a brightness gradient at the double-row boundaries, which is unfavorable for identifying the triangle elements. For instance, in Figure 9-53(a), we can roughly judge the

locations of the double-row boundaries, as marked by the red rectangles on the free-pinwheel pattern. However, it is very challenging to determine the arrangement of triangle elements and their sizes as the selection could be ambiguous. In contrast, for the pinwheel pattern only with single-row boundaries like the example in Figure 9-53(c), the protrusions at the boundaries exhibit approximate brightness, which can well segregate the adjacent triangle elements. Therefore, it is straightforward to interpret the structure using the triangle building block model.

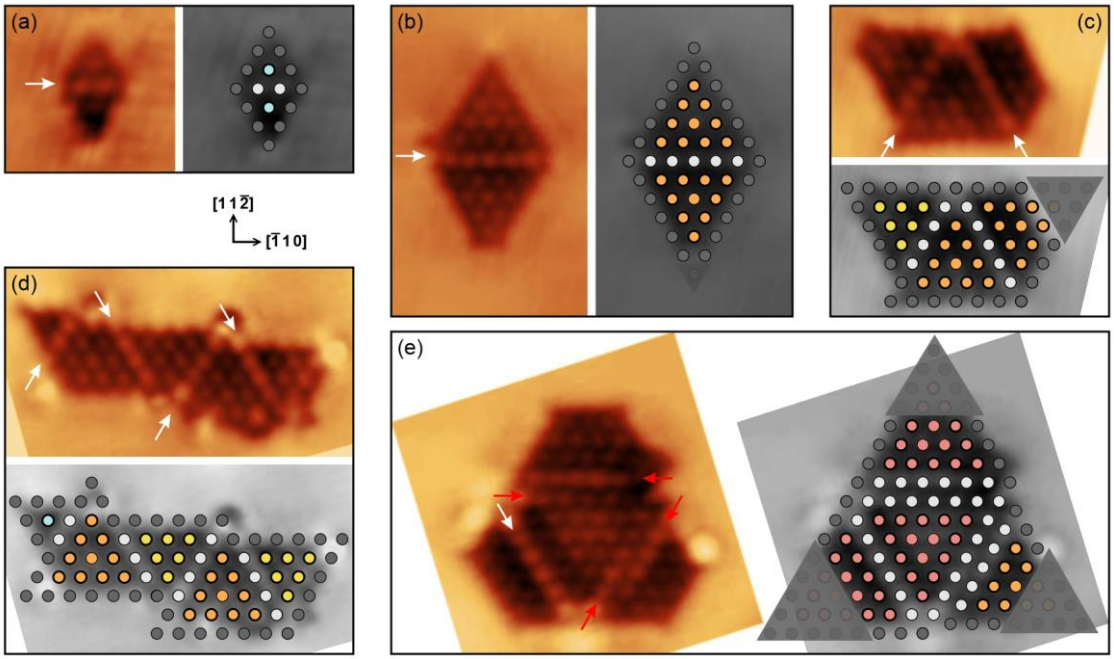

Figure 9-51 STM images of Ti oxide multiple triangle nanostructures. The triangle building block model can be applied to the structural analysis. The grey circles represent L_1 Au atoms surrounding the "dark pits". The white circles represent Ti atoms at the boundaries. The half-transparent triangles in dark grey are used to cover the incomplete sites of the triangles. The white arrows indicate single-row boundaries; the red arrows indicate the double-row boundaries with a brightness gradient. (a) T_1-T_1 (2.3 nm × 2.2 nm, V_s = 0.4 V, I_t = 1.0 nA). (b) T_4-T_4 (2.6 nm × 4.1 nm, V_s = 0.4 V, I_t = 0.7 nA). (c) T_3-T_4-T_4 (incomplete) (3.7 nm × 2.0 nm, V_s = 0.4 V, I_t = 1.2 nA). (d) T_1-T_4-T_3-T_4-T_3 (4.6 nm × 2.5 nm, V_s = 0.5 V, I_t = 0.8 nA). (e) An embedded multiple triangle nanostructure with a truncated shape (V_s = 1.1 V, I_t = 0.2 nA).

9.4.2 Ti oxide pinwheel structure

Ti oxide can form free-pinwheel monolayers as well as emb-pinwheel monolayers depending on the preparation route, as shown in Figure 9-52 (a) – (d). The embedded structure has never been presented in the previous reports on Ti oxide pinwheel structure on various

substrates [33,39,42,43,131–135]. The profiles in Figure 9-52(e) confirm that the Ti oxide pinwheel monolayers can epitaxially grow on Au(111) with a (1 × 1) periodicity, which means the triangle building block model should be workable. A free-pinwheel example and an emb-pinwheel example are selected and displayed with triangle building blocks in different colors in Figure 9-53. We did not mark the double-row boundaries with white circles but used red triangles to outline the triangle elements in frame (b). The offsets between triangle elements and the central "hub" can be better visualized by using these red lines. We can see from these two examples that the Ti oxide pinwheel network is composed of triangles with different sizes, similar to the Nb oxide pinwheel network. The triangle building block model has an advantage in interpreting such pinwheel structures, but the prerequisite is that the cation lattice has an epitaxial registry with no rotation angle against the substrate surface.

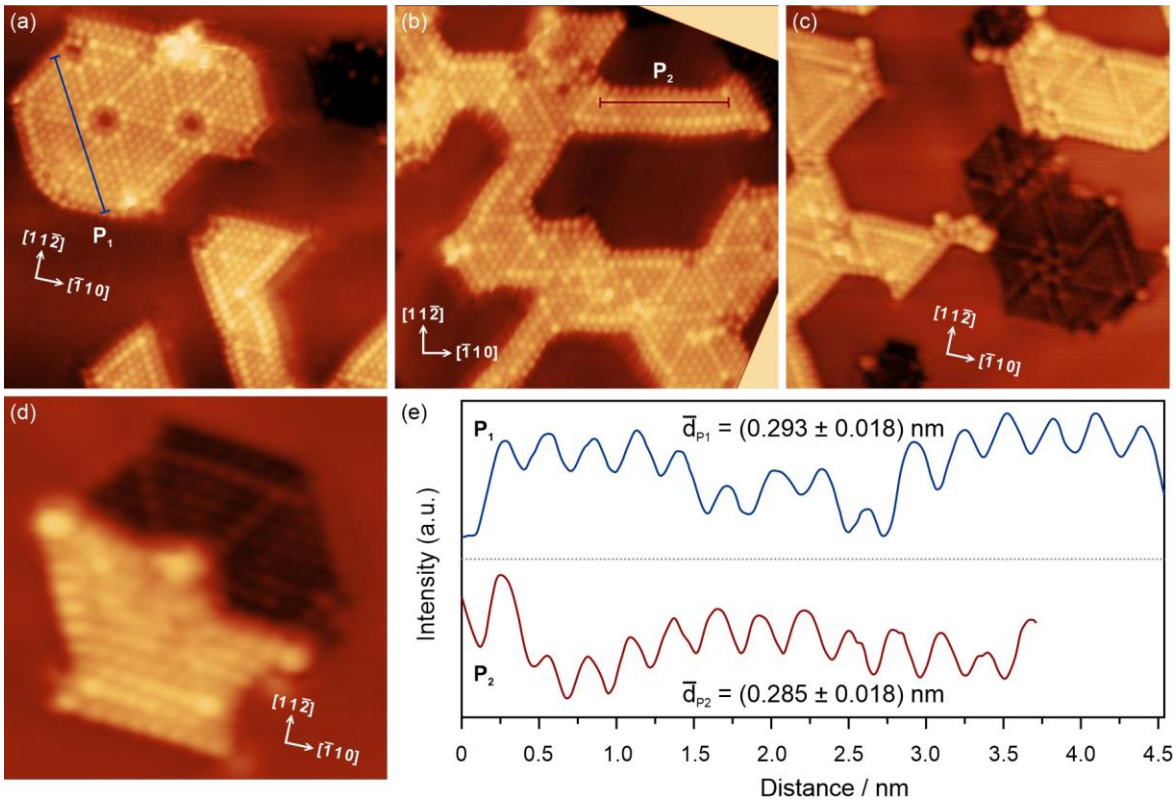

Figure 9-52 STM images of (a), (b) Ti oxide free-pinwheel monolayers (a: 11.3 nm × 11.3 nm, V_s = 0.5 V, I_t = 0.6 nA; b: 12.5 nm × 12.5 nm, V_s = 0.6 V, I_t = 0.5 nA). (c), (d) Coexistence of the free-pinwheel and the emb-pinwheel (c: 15.9 nm × 15.9 nm, V_s = 0.5 V, I_t = 0.9 nA; d: 5.5 nm × 5.5 nm, V_s = 0.8 V, I_t = 0.8 nA). (e) Profiles of the lines P_1 and P_2 in (a) and (b). The periodicity is around 0.29 nm, indicating a (1 × 1) epitaxial growth on Au(111).

Wu [42] and Tumino [43] used the Moiré pattern models to elucidate the Ti oxide pinwheel structure on Au(111) and reported different values of the periodicity and the tilting angle. However, in this work, the measured periodicity in Figure 9-52(e) is not identical to either of them, and we applied the triangle building block model based on the assumption that there is no tilting angle. All three structural analyses are likely to be appropriate if the Ti oxides have irregular pinwheel structures or suffer from lattice strain. External factors including the substrate temperature, annealing time, oxygen gas pressure, and impurities may affect the growth of the pinwheel monolayers, which give rise to varied periodicities and tilting angles.

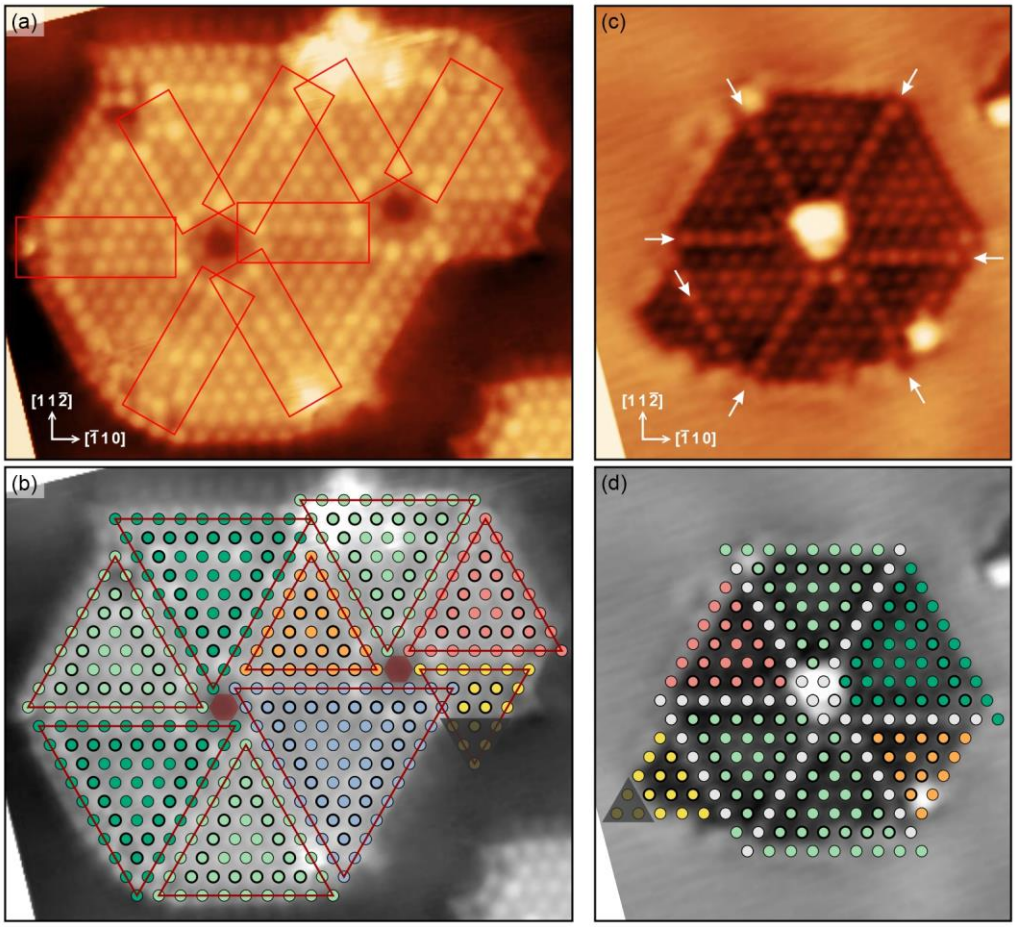

Figure 9-53 (a) STM image of a Ti oxide free-pinwheel island (7.5 nm × 6.0 nm, V_s = 0.5 V, I_t = 0.6 nA). The red rectangles mark the double-row boundaries. Triangle building blocks are superimposed on (b) and are outlined in red lines. The sites of parallel lines correspond to the double-row boundaries. (c) STM image of a Ti oxide emb-pinwheel island (5.5 nm × 6.0 nm, V_s = 0.4 V, I_t = 1.3 nA). It only contains the single-row boundaries, indicated by the white arrows. Triangle building blocks are superimposed on (d) using the white circles to denote atoms at the single-row boundaries. The high contrast at the central “hub” is probably due to some adatoms, which cannot be interpreted by the model mask.

9.4.3 Ti oxide honeycomb-pinwheel (H-P) boundary

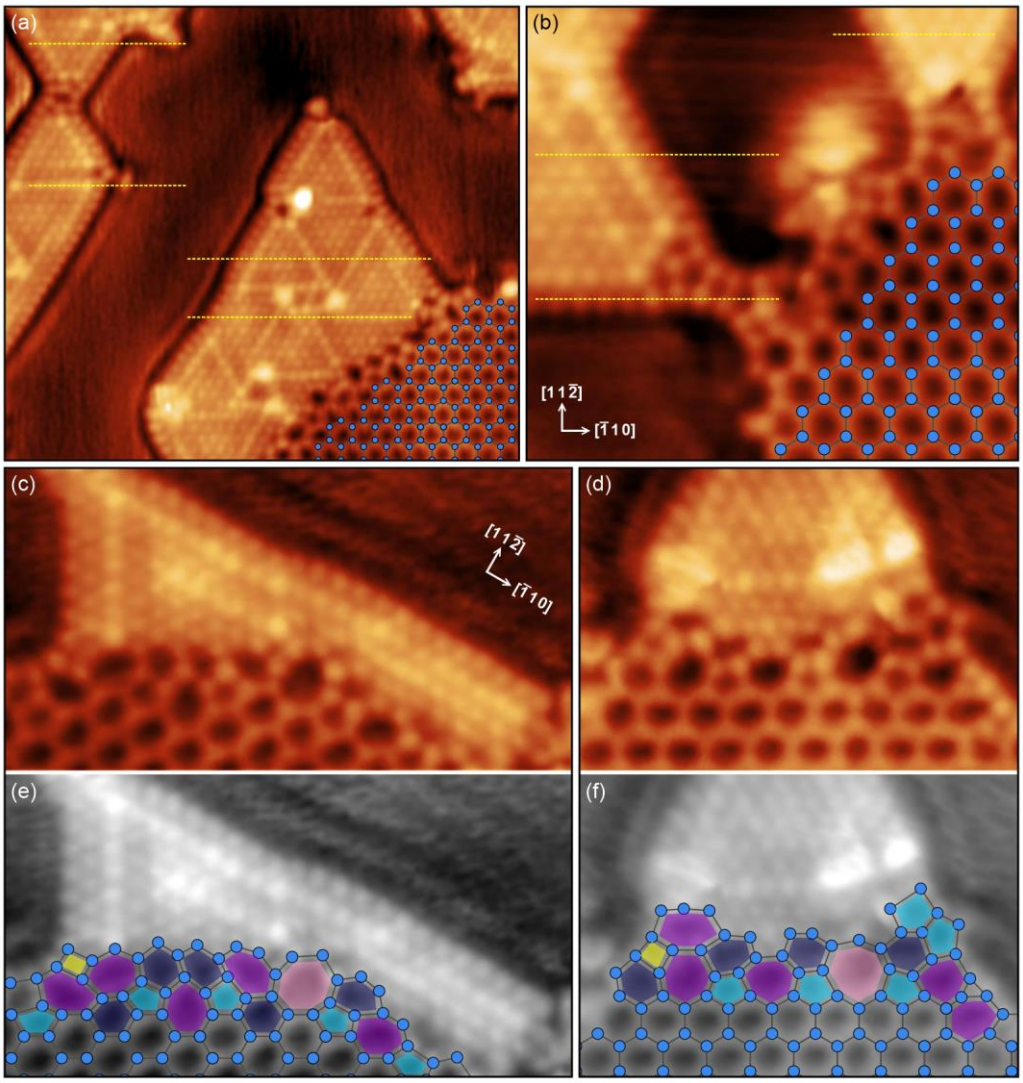

Figure 9-54 STM images of the Ti oxide pinwheel structure coexisting with the (2 × 2) Nb_2O_3 honeycomb structure. The yellow dashed lines mark the horizontal atom arrangement in the pinwheel monolayers. (a) 13.0 nm × 11.5 nm, V_s = 0.5 V, I_t = 0.9 nA; (b) 6.5 nm × 6.0 nm, V_s = 1.0 V, I_t = 0.6 nA; (c) 7.5 nm × 4.0 nm, V_s = 0.5 V, I_t = 0.8 nA; (d) 5.8 nm × 4.0 nm, V_s = 0.5 V, I_t = 0.8 nA. (e), (f) Lattice masks are superimposed on the STM images in (c) and (d) in grayscale. Blue circles: Ti atoms; yellow: four-membered ring; cyan: pentagon; navy: distorted hexagon; purple: heptagon; pink: octagon.

Ti oxide pinwheel structure can integrate into the (2 × 2) Ti_2O_3 honeycomb structure with distinctive atom configurations at the boundary (referred to as the H-P boundary). Figure 9-54(a) – (d) show four regions where the pinwheel and the honeycomb coexisted on the Au(111) substrates. The (2 × 2) honeycomb lattice can act as an excellent crystallographic marker for image calibration. The horizontal yellow dash lines in frame (a) and (b) are aligned with the

[$\bar{1}10$] direction, indicating that the Ti lattice in the pinwheel monolayer has no rotation with respect to Au(111). However, as these pinwheel/triangle regions were integrated into the honeycomb monolayers, the local structures could be affected by the honeycomb and thus have an epitaxial growth without a titling angle against the substrate. If the pinwheel monolayers were independently grown on the substrate with higher coverage, the Ti lattice might rotate slightly with respect to Au(111) in order to minimize the film strain. This may explain why Wu and Tumino observed a small tilting angle of around 2°.

Figure 9-54 (e) and (f) are close-ups of the Ti oxide H-P boundaries. In Section 9.3.1 we have demonstrated the H-T boundaries between the (2 × 2) Nb_2O_3 honeycomb structure and the Nb oxide Bay-Ts. They exhibit regular atom arrangements according to the parity of the triangle size *n*. Nb atoms of the Bay-T at the H-T boundary are either above the terminal atoms or at the dent sites of the HC Z-66 edge. In contrast, the H-P boundaries of Ti oxide monolayers comprise multiple rings, mainly including the pentagons, heptagons, and distorted hexagons. Such atom configurations are consistent with Ti_2O_3 honeycomb defect domains and domain boundaries where the pentagon-heptagon rings (5-7 rings) are usually found (Figure 8-38, Figure 8-41). Four-membered rings and octagons were also observed but with a fewer number than 5-7 rings.

In conclusion, the formation of multiple rings and the flexible combination should be an effective way for Ti oxide monolayers to release the film strain at defective sites or transition regions including (i) the domain boundary formed by two HC sublattices with a translation offset; (ii) the H-P boundary between the HC structure and the pinwheel structure; (iii) the HC edges where the oxide monolayers terminate.

9.5 V oxide pinwheel structure

We also studied the V oxide monolayers on the Au(111) substrates in this work. It has been reported that V oxide thin films can form hexagonal lattices [48] or stripe patterns [50,51] on Au substrates, but the pinwheel structure on Au(111) has not yet been reported. Surnev [58] and Schoiswohl [70] studied the V oxide pinwheel monolayers on Pd(111) and Rh(111) and used the Moiré pattern model to elucidate the structures.

V oxide pinwheel monolayers on Au(111) were obtained by annealing V in 3×10^{-7} Pa oxygen at 700 ℃ after e-beam metal deposition for 30 mins. A surface with high coverage of the V oxide pinwheel network can be seen in Figure 9-55(a). A hexagonal commensurate superstructure with six triangle elements and a central hub is marked on the image. Similar to Nb/Ti oxide, V oxide can also form free-pinwheel and emb-pinwheel monolayers by altering the preparation routes, as shown in Figure 9-55(b) – (f). Due to the substrate effect, V oxide pinwheel islands were usually grown in a hexagonal or truncated triangle shape at low coverage. A periodicity of ~ 0.287 nm can be calculated from the profiles in Figure 9-55(h), suggesting that the V oxide pinwheel may have a (1 × 1) epitaxial growth on the Au(111) substrates.

We have demonstrated that the triangle building block model can be successfully applied to Nb and Ti oxide pinwheel networks. However, the model is not workable for the V oxide pinwheel. There are two prerequisites when applying the triangle building block model: (i) the oxide can form independently-standing triangle nanostructures such as Nb oxide single triangles and Ti oxide embedded triangles. But we found that instead of intact triangles, V oxide could only form truncated triangles on Au(111) like the one at the bottom right in Figure 9-55(d). (ii) The triangle/pinwheel structure should have a (1 × 1) periodicity with no rotation against the Au(111) surface. Otherwise, the Moiré fringes may cause a contrast variation, thus affecting the identification of triangle elements. Although the measured periodicity is quite close to the lattice

constant of the Au(111) surface, we cannot confirm that the V oxide pinwheel has no rotation with respect to the substrate. It is challenging to achieve a precise crystallographic calibration without any other determined structures for reference (e.g., Nb_2O_3/Ti_2O_3 HC lattice).

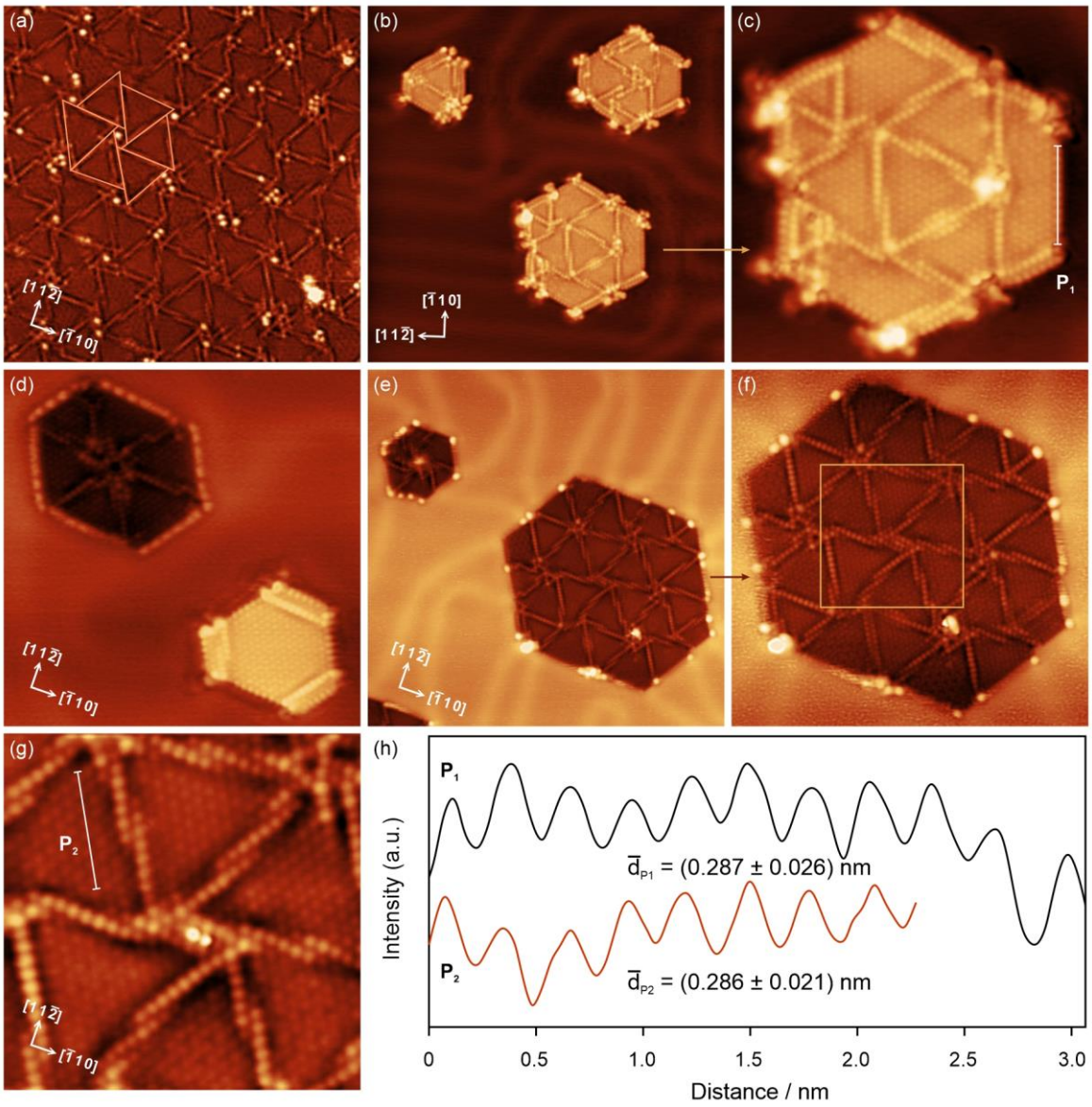

Figure 9-55 STM images of (a) V oxide pinwheel network on Au(111) with a high coverage. A hexagonal commensurate superstructure is marked on the image (24.5 nm × 24.5 nm, V_s = 2.0 V, I_t = 0.16 nA). (b) V oxide free-pinwheel islands (27 nm × 27 nm, V_s = 0.65 V, I_t = 0.33 nA). (c) A close-up of the free-pinwheel island indicated by the arrow in (b) (12.5 nm × 12.5 nm, V_s = 0.4 V, I_t = 0.4 nA). (d) Coexistence of a free-pinwheel island and an emb-pinwheel island (14.5 nm × 14.5 nm, V_s = 0.45 V, I_t = 0.8 nA). (e) V oxide emb-pinwheel islands (27 nm × 27 nm, V_s = 0.8 V, I_t = 0.5 nA). (f) A close-up of the emb-pinwheel island indicated by the arrow in (e) (17 nm × 17 nm, V_s = 0.8 V, I_t = 0.5 nA). (g) A close-up of the atom arrangement in the yellow box in (d) (7 nm × 7 nm, V_s = 0.8 V, I_t = 0.5 nA). (h) Profiles of the lines P_1 and P_2 in (c) and (g). The periodicity of the V oxide pinwheel structure is about 0.287 nm, quite close to Au-Au distance (0.289 nm) of the (111) plane.

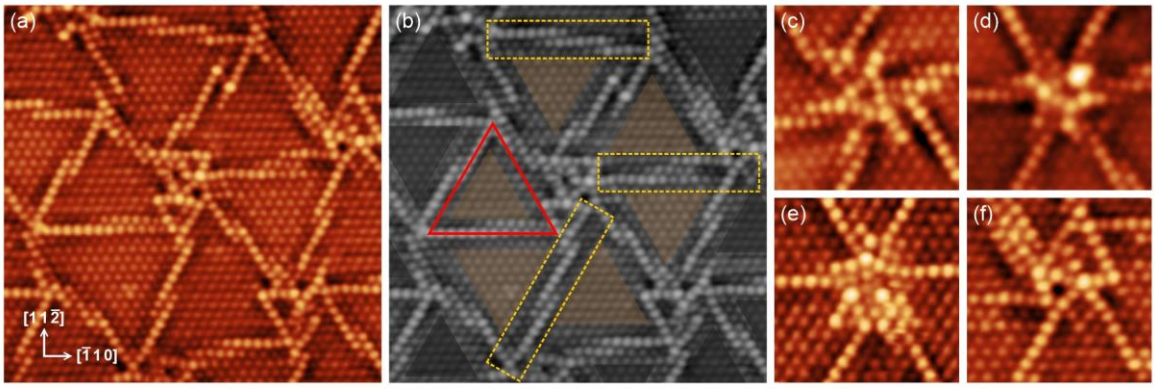

Figure 9-56 (a) STM image of the inner structure of a pinwheel monolayer (10 nm × 10 nm, V_s = 0.8 V, I_t = 0.8 nA). (b) The same image as (a) in grayscale, the half-transparent triangles in brown mark the six triangle elements of a hexagonal-like pinwheel superstructure. The red triangle indicates the size of a triangle element: 13 atoms at the side. (c) – (f) Four examples of pinwheel "hubs" with complex atom arrangements. Image size: 3.5 nm × 3.5 nm, c: V_s = 0.8 V, I_t = 0.5 nA; d: V_s = 0.8 V, I_t = 0.5 nA; e: V_s = 0.8 V, I_t = 0.8 nA; f: V_s = 0.8 V, I_t = 0.8 nA.

The hexagonal commensurate superstructure superimposed on Figure 9-55(a) is a rough schematic that cannot reflect the atom arrangement and contrast variation in detail. A close-up of the pinwheel network is shown in Figure 9-56. The brown triangles in frame (b) indicate six triangle elements arranged along a "hub" of a hexagonal-like pinwheel pattern. The "spokes", which are highlighted in the yellow dashed rectangles, are not single lines but comprise double rows or even triple rows with a brightness gradient. This feature is similar to, but more complex than, the double-row boundaries of the Ti oxide pinwheel structure [Figure 9-51(e), Figure 9-53(a)]. Generally, these double-row or triple-row boundaries are strong indicators of the Moiré patterns. The V atoms at the boundaries are located either at on-top sites or bridge sites, so their physical positions are higher than the V atoms sitting at hollow sites in the triangle elements. A typical schematic of the Moiré pattern with this feature can be seen in Figure 2-34(c), which is used for explaining the V oxide pinwheel structure on Rh(111). However, the "spokes" or the boundaries were still treated as a single array of V atoms rather than two rows.

In this work, we did not propose a Moiré pattern model to elucidate the V oxide pinwheel on Au(111) because of the random occurrence of the double-row or triple-row boundaries and the dynamic changes of the Au substrate below (discussed later in Figure 9-57). Although it is

difficult to determine the size of the triangle elements due to the ambiguity of the boundary, we drew a red triangle in Figure 9-56(b) for reference. The number of V atoms at the side is 13, which is much larger than any common triangle building block in Nb/Ti pinwheel networks. In addition, Figure 9-56(c) – (f) give four examples of the pinwheel "hub" structures. The atom arrangement is too sophisticated to be described or modeled. Neither the triangle building block model nor the Moiré pattern model is able to explain the formation independently. This is another reason why we have not yet been able to propose a Moiré pattern model.

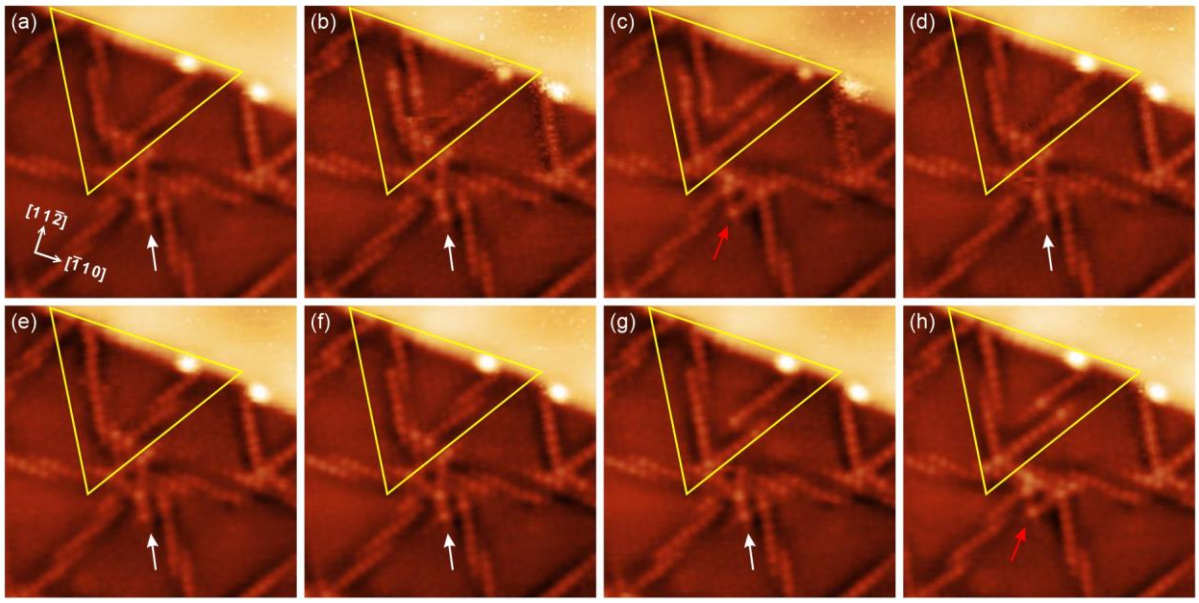

Figure 9-57 Series-scanned STM images showing the dynamic changes of the "spokes" (marked by the yellow triangles) and the "hub" (white and red arrows) of a V oxide pinwheel network (7 nm × 7 nm, V_s = 0.8 V, I_t = 0.5 nA).

We also observed an interesting but intractable phenomenon at the "spokes" of the V oxide pinwheel network. In the image series in Figure 9-57, the brightness of the protrusions that form the "spokes" (marked by yellow lines) could be altered with the tip scanning the surface. Visually, the movement of the protrusions causes the row to split or merge, but the atoms still maintain their sites in the lattice without any position shift. This phenomenon implies dynamic changes of Au atoms from the L_2 layer (this pinwheel monolayer adopted the embedded growth mode). It is common to see the movement of Au substrate edges during STM scanning at room

temperature, which indicates the topmost Au atoms can deviate from the original hollow sites. In Figure 9-57, the positions of V cations remained unchanged, but the locations of the "spokes" can be affected by the movement of Au atoms below. Unlike the Au atoms from a free edge, the L_2 Au atoms cannot deviate too much from their original sites due to the close-packed structure. That is why the visual change of the spoke location is no more than one atom row. The Moiré pattern model rarely considers the dynamic changes of the lattice, so it is challenging to apply a static model to elucidate the V oxide pinwheel structure on Au(111). In addition, both the triangle building block model and the Moiré pattern model are tentative models that reveal the topographical features and exclude the electronic effects. Presumably, the unique electronic properties of V oxide and the interaction with the Au(111) substrate may contribute to the phenomenon as well.

9.6 Conclusion

In this chapter, we analyzed the triangle and pinwheel structures of Nb, Ti, and V oxides on the Au(111) substrates. The two structures have been observed and modeled in a few 2D materials, but there are not many reports on these three oxides on Au(111). The present study may open new avenues in understanding the structural properties of the three oxide materials. The findings can be summarized as follows:

(1) Nb oxide can form triangle nanostructures on the Au surface, but no embedded triangle was observed. Ti oxide can form both free-triangles and emb-triangles on Au(111). We did not find any intact triangle nanostructure of V oxide.

(2) We obtained free-pinwheel and emb-pinwheel monolayers of Nb/Ti/V oxides using different preparation routes. A large number of *M*-Au substitutions (*M* = Nb, Ti, V) can act as a precursor structure for generating any embedded monolayer.

(3) The triangle/pinwheel structures of the three oxides are epitaxially grown on Au(111). With the help of Nb_2O_3/Ti_2O_3 HC references, we can confirm that the cation lattice of Nb/Ti oxide triangles/pinwheels has a (1 × 1) periodicity without rotation against the surface. But we cannot determine whether there is a minimal tilting angle between the V oxide pinwheel and Au(111).

(4) We proposed the triangle building block model to elucidate the pinwheel structure. This model has the advantage of interpreting a network that comprises triangle elements with various sizes. The "spokes" of the pinwheel network can be attributed to the boundaries between triangle elements. The model works well for Nb and Ti oxides but is impractical for V oxide.

(5) The triangle/pinwheel structures can coexist with the honeycomb structures of Nb and Ti oxides. In Nb oxide, atoms at the H-T boundary are arranged in a constant pattern determined by the parity of the triangle size. While in Ti oxide, the H-P boundary is composed of multiple rings such as 5-7 rings and distorted hexagons.

(6) The study is limited by the lack of information on the O atom configurations and electronic properties of the three oxide materials. Many fine details in the STM images cannot be well explained as we attributed the contrast difference to the height difference of atom positions on Au(111) using tentative models. Further experimental investigation and theoretical calculations are required to address the issues of how to incorporate O atoms in the films and compare the electronic structures of the three oxides.

Chapter 10 Conclusions

10.1 Overview

This project focuses on the structural characterization of epitaxial oxide thin films, including Nb, Ti, and V oxides, on the Au(111) substrates using scanning tunneling microscopy. The three oxide nanostructures behave differently on the same substrate and exhibit distinctive properties compared with their bulk counterparts. Prior to studying oxide materials, we report the ring patterns created by *M*-Au substitutions (*M* = Nb, Ti, V, Mn) in Chapter 4. The triangular rings usually show three bright rounded corners in the STM images due to the curvature anisotropy of the Au isoenergy surface in ***k***-space. The ring's radius and center depend on the substitutional site, which enables the 3D mapping of the impurity distribution below the Au(111) surface. Moreover, we found that a large number of Nb/Ti/V-induced rings can act as a precursor structure for forming any embedded oxide monolayers.

The metallic Nb/Ti/V can be oxidized, forming oxide monolayers with diverse structures on Au(111) by altering the annealing temperature and oxygen pressure. Nb oxides have been studied intensively in this project. A general description of Nb oxides on Au(111) and a central emphasis on the fourfold coordinated Nb are presented in Chapter 5 and Chapter 6. Several unique structural properties are discussed separately and compared with Ti/V oxides. In Chapter 7 and Chapter 8, we discuss the edges, defects, and domain boundaries in the (2 × 2) Nb_2O_3 and Ti_2O_3 honeycomb monolayers. Chapter 9 compares the Nb/Ti oxide triangles and Nb/Ti/V oxide pinwheel structures. Tentative models have been proposed to interpret the cation arrangements but cannot satisfactorily explain many details revealed from the STM images. Further experimental work and theoretical simulations are required to elucidate the structures of these oxide thin films.

10.2 Nb oxides on Au(111)

Nb oxides can form a variety of nanostructures on Au(111) under the conditions that $p(O_2)$ < 10^{-4} Pa, T < 900 ℃. It has been shown that the (2 × 2) Nb_2O_3 honeycomb structure is most thermodynamically stable within the range. A minimal amount of metal deposition at a low oxygen chemical potential (e.g., $p(O_2)$ ~ 10^{-7} Pa, T ~ 400℃) gives rise to Nb oxide clusters with various shapes such as rectangles, rings, ring-ring bipods, ring-rectangle bipods, and tripods. Nb oxide triangles and triangle continuous films can be generated by further improving the annealing temperature (T = 700℃). The Nb pinwheel structure is essentially the same as the triangle but with higher coverage. All the clusters, triangles, and pinwheel structures can be converted to the (2 × 2) Nb_2O_3 honeycomb structure by prolonged annealing in oxygen. The Nb_2O_3 honeycomb can also be obtained at one time in 10^{-6} Pa O_2. Annealing temperature affects the honeycomb edge reconstruction. We successfully prepared Nb oxide embedded pinwheel and honeycomb monolayers grown on the second Au(111) layer. There is no discrepancy between the free and embedded monolayers regarding the inner structures, but the edges of embedded monolayers are influenced by the confinement of the Au surface.

A Nb atom has five valence electrons, so it is capable of oxidation states up to +5. DFT calculations have shown that the oxidation state of a Nb cation in the Au-supported Nb_2O_3 honeycomb monolayers is higher than +3 due to the electron transfer to the Au substrate. We observed protrusions with elevated brightness and fourfold coordination, and attributed them to Nb cations with a higher oxidation state. Given the electron transfer, the actual oxidation state of the fourfold coordinated Nb should be higher than +4. In other words, based on the contrast difference and the coordination number in the STM images, we are able to clarify the oxidation states of Nb cations at atomic resolution. The fourfold coordinated Nb cations are crucial to the honeycomb monolayers as they are usually involved in defects and domain boundaries.

10.3 Comparison between Nb, Ti, and V oxides on Au(111)

10.3.1 Nb_2O_3 and Ti_2O_3 honeycomb monolayers

Both Nb and Ti oxides can form (2 × 2) honeycomb monolayers on Au(111), but they behave differently in terms of edge reconstructions, defects, and domain boundaries. We have identified seven common edge structures in Nb_2O_3 honeycomb monolayers: A-66, A-56, Z-66, Z-46, Z-646, Z-K, and Z-rK. Nb_2O_3 free-HC possesses all the reconstruction types, but we only observed Z-66 and Z-K edges in the emb-HC which are governed by the stacking sequence of Au(111) layers. In contrast, edge reconstruction in the Ti_2O_3 honeycomb is achieved by a random arrangement of polygons such as triangle-heptagon (3-7) pairs. We defined the density of edge atoms and calculated the density difference in order to clarify the degree of edge reconstruction. For an arbitrary honeycomb edge, Ti_2O_3 usually has a higher density difference, which means it is subjected to a stronger edge reconstruction than Nb_2O_3.

It is common to find point defects and line defects (domain boundaries) in Nb_2O_3/Ti_2O_3 honeycomb monolayers. Simple vacancy sites, the SW defect, and divacancies have been characterized in both oxides. We reported our new findings of tetravacancies in the Nb_2O_3 HC. Regarding the domain boundaries, Nb_2O_3 and Ti_2O_3 have the same solutions to Z1, Z2, and A1 boundaries, which are Z1-5775, Z2-558, and A1-48. DFT calculations have confirmed that DB formation for an A2 boundary requires much higher energy than the other three types, which explains why we did not observe a periodic DB solution to A2 along the armchair extension direction in Nb_2O_3 or Ti_2O_3. Instead, we found that Nb can construct intermediate boundaries with tilting angles, while Ti forms multiple rings with a random arrangement to fill the A2 boundary gap. In addition, triple junctions created by three DBs have been discovered in Nb_2O_3, they are rarely seen in 2D thin films. The fourfold coordinated Nb atoms provide alternative ways for defect reconstruction and domain boundary formation.

10.3.2 Nb/Ti/V oxides triangle and pinwheel structures

Nb and Ti oxides can form independently standing triangles on Au(111) but the cations are arranged differently. Ti cations follow a strict epitaxial registry with the (1 × 1) periodicity, whereas Nb oxide triangles are double- rimmed with Nb cations either sitting at hollow sites (outside rim) or on-top sites (inside rim). Apart from free triangles grown on the surface layer, Ti oxide can also form embedded triangles. Single Nb/Ti oxide triangles can be integrated into multiple triangles with identifiable boundaries. In contrast, we did not observe any intact V oxide triangles other than some nanostructures with a truncated shape.

Nb/Ti/V oxides form free and embedded pinwheel monolayers on Au(111) depending on the preparation routes. Similarly, a large number of *M*-Au substitutions (*M* = Nb, Ti, V) would be a precursor structure for the emb-pinwheel. We proposed a triangle building block model to elucidate the pinwheel structures. It has the advantage of interpreting a network composed of triangle elements with various sizes. The model works well for Nb and Ti oxide pinwheel structures but fails to explain V oxide pinwheel networks which comprise double-row or triple-row “spokes” and “hubs” with complex atom arrangements.

Nb and Ti oxide pinwheel monolayers can be incorporated into the Nb_2O_3/Ti_2O_3 honeycomb monolayers by forming boundaries. The H-T boundaries in Nb have regular atom arrangements and only vary with the parity of the triangle size. In contrast, Ti forms multiple rings at the transition region between the honeycomb and the pinwheel, in which the 5-7 rings and distorted hexagons are commonly seen. Such characteristics are consistent with the other transition regions in Ti_2O_3 honeycomb monolayers such as the domain boundaries and the island edges. We did not obtain V oxide honeycomb monolayers on Au(111) under the normal conditions we used for preparing oxide monolayers in this work.

10.4 Future work

10.4.1 Coherent scattering in Chapter 4

Chapter 4 with Appendix II has been integrated into a research paper and is currently in correction. At the very beginning, we excluded Friedel oscillations as the origin of the scattering ring patterns because the STM imaging was carried out at room temperature rather than in a cryogenic environment where most Friedel oscillations were found. However, the coherent scattering can occur at elevated temperatures with a length scale longer than several lattice constants. We used "directional density of states" to explain the three bright corners and did not consider any changes in the pattern due to constructive or destructive interference. We recently obtained two STM images showing the same region at different sample biases (0.6 V, 2.0 V). At the low bias, the ring patterns in this region are consistent with what we have presented in Chapter 4 and the DFT-simulated STM images. Whereas the contrast of the ring patterns is completely converted at the high bias. In other words, the three bright corners become dark while the depressed center becomes a protrusion. This is a strong indicator of coherent interference considering the distance between the tip and the sample was changed when using different biases in a constant current mode. Therefore, we should modify our theoretical analysis, combining the coherent scattering with the DDOS. This issue will be sorted out soon.

10.4.2 Mixed oxide assumption based on the fourfold coordinated Nb

Chapter 5 discusses the fourfold coordinated Nb atoms in point defects and domain boundaries. We can utilize the contrast difference and coordination number to map the oxidation state of Nb cations at the atomic level. Besides, the fourfold coordinated Nb is of great potential in the studies of mixed oxides. We have tried preparing Nb-Ti-O mixed oxide monolayers on Au(111) as both Nb_2O_3 and Ti_2O_3 can form the (2 × 2) honeycomb lattice. We cannot discriminate Nb

and Ti cations in the STM images, and did not find any discrepancy in the oxide behaviors between the mixed oxide and the binary oxides.

In contrast, there is no evidence showing that metal elements from the Group III can form honeycomb monolayers on noble metal substrates. Cations in an Au-supported honeycomb monolayer with a M_2O_3 stoichiometry have an oxidation state higher than +3 due to the charge transfer to the substrate. In other words, the metal atom should possess at least four valence electrons in order to form a (2× 2) honeycomb lattice on Au substrates. The Group III elements, for example, Sc, cannot independently form Sc_2O_3 honeycomb on Au(111). But things may change if it is mixed with Nb, forming Sc-Nb-O mixed oxide monolayers.

We have shown that Nb cations have additional electrons to bond with the fourth O atoms becoming the fourfold coordinated Nb. If these extra electrons could be transferred to Sc cations in a mixed oxide monolayer, Sc would be capable of bonding with three O atoms and having electrons transferred to the Au substrate at the same time. We have analyzed the feasibility of the Group III element-Nb mixed oxide from the perspective of the charge transfer, but we have not done a comprehensive literature review or any primary experimental exploration so far. We believe it is an exciting topic and look forward to examining our assumptions in the near future.

10.4.3 O configurations in the HC edges, defects, and domain boundaries

The most obvious limitation in this project is the unknown O atom configurations. We proposed a variety of structural models for honeycomb edges, defects, and domain boundaries based on the empty-state STM images. O atoms were inserted into these tentative models, giving rise to various stoichiometries. DFT calculations can help to clarify which atom configurations are more stable according to the formation energy. Our collaborators, Jacek Goniakowski and Claudine Noguera, are currently conducting the theoretical work. The preliminary results are very promising and instructive for the structural analysis.

The oxidation and reduction processes were realized by O_2 and UHV annealing in this work. I did not try other methods, for example, H_2 reduction. The DFT calculations have shown that the edge reconstruction can be varied by changing the oxygen chemical potential. Therefore, we can design a cycling test using O_2 and H_2 to oxidize and reduce the Nb_2O_3 HC samples, and observe the changes in the edge structure. The difficulty will be the island coalescence during repeated annealing, which may also affect the edge reconstruction.

Besides, I did not investigate the effect of water absorption on defective sites including edges and domain boundaries. Previous reports on graphene have shown that the adatoms can influence the edge reconstruction and DB formation, as discussed in Section 2.2. Therefore, it is worth exploring the interactions between H_2O molecules and the HC edges and DBs. Presumably, new edge structures and boundary solutions can be created due to the H_2O effect.

10.4.4 V oxides and Mn oxides

This thesis mainly discusses Nb/Ti oxides on Au(111) with a small amount of work concerning V/Mn-induced ring patterns and the V oxide pinwheel structure in Chapter 4 and Chapter 9. In fact, I have obtained some preliminary results on V oxides and Mn oxides on Au(111) with very good quality (see Appendix III). A few new structures have been identified, including V oxide porous network, V oxide square lattice grown on top of the pinwheel structure, Mn oxide "fish-bone" structure, and Mn oxide rectangle structure with a complex unit cell. The structural models for the newly-identified oxide monolayers have not yet been constructed. These studies are not as systematic as the studies of Nb/Ti oxides on Au(111) due to the time limitation. In the future, apart from altering parameters of oxygen pressure and annealing temperature to see if new structures can be created, other characterization methods including LEED, AES, and STS, can be exploited to investigate the crystallographic orientation, oxidation state, and the electronic structures of these oxide thin films.

Appendix I SNR and measurement number n

The relation between the signal-to-noise ratio (SNR) and the number of measurements (n) is proved as follows.

Shot noise and Poisson distribution of the quantum particles

As the image records the data in 2D pixels, it is necessary to define the SNR of a STM image before discussing how to improve the value. In many imaging systems, it is common to treat the "signal" strength as the mean pixel value, so the "noise" can be calculated by the standard deviation from the neighboring pixels around the target pixel [261]. However, this method does not consider why there is a deviation and where the deviation comes from. For an electronic system with quantum particles, the electron-electron interaction is a major source of the shot noise [262–264]. An event that involves the electrons can be modeled by a Poisson process, which comprises electrons with integer numbers. The noise is so-called the Poisson noise [265,266]. The Poisson probability distribution *P* over a time interval can be expressed as:

$$P(\mathrm{X}=\mathrm{k})=\frac{\mathrm{e}^{-\lambda}\,\lambda^{\mathrm{k}}}{\mathrm{k}!}\ \ (\mathrm{k}\geq 0,\mathrm{integer}). \tag{A1}$$

where λ is the expected value of the number in the event X. Many physical phenomena can be modeled by the Poisson processes such as the emission of electrons from a cathode, the generation of electron/hole pairs in a photodiode, and the quantum tunneling between two electrodes [266]. It is worth noting that a Poisson process can be approximated to a normal distribution when λ is sufficiently large. In a Poisson process containing a large number of quantum particles, the individual behavior of a particle is no longer concerned.

Improving the SNR by image averaging

Assuming the imaging system is linear and space invariant, each pixel in an image can be treated independently. A pixel can be seen as a source that can emit particles as well as a detector that can receive particles. The pixel value is determined by the net number of particles over a time interval. The brightness of a pixel can then be defined as the number of particles incident on the detector over the time interval. The numbers of the particles recorded in a pixel are always integers and follow a Poisson distribution. For an empty-state STM image, the brightness of a pixel can be attributed to a tunneling electron ensemble that travels from the tip to the sample surface. The number of the tunneling electrons recorded in a pixel in one event (image capture) is sufficiently large that the distribution of the number can be approximated to a normal distribution. Therefore, we can denote the signal (X) of a pixel as:

$$X \sim N(\mu, \sigma^2). \tag{A2}$$

μ is the expected value of the signal, namely the brightness of a pixel in an image; σ^2 is the variance, which is treated as the noise. If we carry on a serial scanning on the same area with the same imaging condition for *n* times, the signal of a specific pixel in image *i* is an independent random variable that can be denoted as:

$$X_i \sim N(\mu_i, \sigma_i^2). \tag{A3}$$

$$\mu_i \equiv \mu, \qquad \sigma_i^2 \equiv \sigma^2. \tag{A4}$$

According to the probability theory, the sum of random variables with the same normal distribution also follows a normal distribution. The sum (Z) of the brightness of the specific pixel X_i from n images is:

$$Z = \sum_{i=1}^{n} X_i\,, \tag{A5}$$

and follow the normal distribution as:

$$Z \sim N(n\mu, n\sigma^2)$$

The SNR is defined as the average signal over the root mean square of the noise. Hence the SNR of a specific pixel calculated from *n* images (SNR_{sum}) is:

$$SNR_{sum} = \frac{n\mu}{\sqrt{n\sigma^2}} = \sqrt{n} \cdot SNR_{one}, \tag{A6}$$

in which the signal-to-noise ratio in one measurement for the specific pixel is $SNR_{one} = \mu/\sigma$. It is noteworthy that we modeled the process by normal distribution twice. Firstly, we approximate the Poisson process of the particle interaction (tunneling electrons recorded in a pixel) to a normal distribution assuming the number of the involved particles is sufficiently large. Secondly, we used the probability theory to show that the sum of the variables with the same normal distribution also follows a normal distribution. By calculating the average, we reproduce the mean value but with an improvement of the SNR by $\sqrt{n}$.

Appendix II Theoretical support for Chapter 4

Here we present the calculation methods used in Chapter 4, and the theoretical analysis for the triangular ring patterns with three bright corners.

Calculation methods

Theoretical calculations were performed within the Perdew–Burke–Ernzerhof (PBE) generalized gradient approximation (GGA) [267] using the projector-augmented wave (PAW) formalism [268], as implemented in the GPAW code [269–271]. The calculations used standard PAW datasets, periodic boundary conditions and a plane-wave basis (400 eV cutoff energy) to describe the wavefunctions. The Au(111) substrate was modelled as a 6 × 6 slab with 6 atomic layers, with a vacuum region of 10 Å separating periodic replicas and a 4 × 4 × 1 sampling of reciprocal space. Geometry optimizations were carried out with all atoms and in-plane lattice vectors allowed to relax, until forces and pressures were below 0.025 eV/Å and 0.1 GPa, respectively. Single impurity atoms were placed in the 2nd, 3rd, 4th, and 5th layers (labelled as L2, L3, L4, and L5) below the surface (the surface layer is labelled as L1). STM images were simulated in constant height mode within the Tersoff-Hamann approach [153,272], integrating the local density-of-states from the Fermi energy ϵ_F to $\epsilon_F + eV_s$.

Theoretical analysis

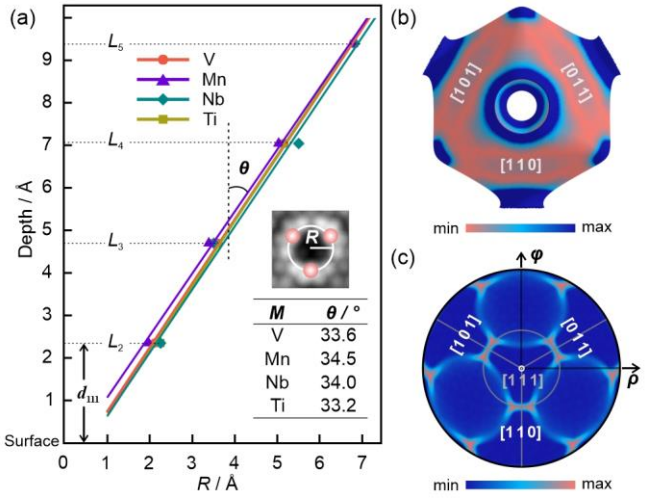

Figure S1 (a) Plot of ring radius from simulated STM images. Inset: an example simulated ring shows the radius and a summary of the maximum intensity scattering angle. (b) Isoenergy surface of Au fcc structure at Vs = 0.5 V. The smooth surface is obtained by diagonalizing Hamiltonian in fine k grid using Wannier90 [273,274]. (c) Map projection of DDOS in a polar coordinate. $\varphi \in [0,2\pi], \rho \in [0,\pi/2]$.

We now turn to the question of why the scattering cone is most intense along the <110> directions. Weismann et al. [189] showed similar ring patterns created by buried Co impurities in a Cu(111) substrate, and explained their observations through a stationary phase approximation to correlate the change of local density of states (ΔLDOS) to the Gaussian curvature K of the isoenergy surface ($\Delta LDOS \propto \frac{1}{|K|d^2}$, d is the distance between the impurity and the detection point). Here we analyse the effect in terms of the group velocity of the Bloch wavefunction, making similar arguments to Sharvin and Fisher [275].

The perturbation of the impurity potential (V_{im}) results in the transition of the electrons from an initial Bloch state with quantum number $\boldsymbol{k_i}$ to a final state with quantum number $\boldsymbol{k_f}$ and amplitude $\langle \boldsymbol{k_i}|V_{im}|\boldsymbol{k_f}\rangle$. Although k-space itself is homogeneous, the distribution of the group velocity (defined as $\boldsymbol{v_G} = \nabla_{\boldsymbol{k}}\epsilon(\boldsymbol{k})/\hbar$, where $\epsilon(\boldsymbol{k})$is the energy spectrum of the solid) is not necessarily uniform. As such, at a given energy the density of electron states varies with propagation direction. It is convenient to introduce a "directional density-of-states" (DDOS) which counts the number of states at a given energy with group velocities pointing along a particular direction $\hat{\boldsymbol{n}}$. Formally, this is achieved through the Gauss map N: $S \rightarrow S^2$ [276] which maps a curved surface S to the normal vector in a unit sphere S^2. Then, the DDOS $g(\epsilon, \hat{\boldsymbol{n}})$ can be written as:

$$g(\epsilon, \hat{\boldsymbol{n}}) = \lim_{\delta A \to 0} \frac{1}{4\pi^3} \sum_{P_m \in \boldsymbol{N^{-1}}(\hat{\boldsymbol{n}})} \frac{1}{|\boldsymbol{\nabla}\epsilon(P_m)|} \frac{\delta A_m}{\delta A}, \tag{B1}$$

where $\frac{1}{4\pi^3}\frac{1}{|\boldsymbol{\nabla}\epsilon(P_m)|}$ is the normalization factor by which the solid angle integration of the DDOS gives us the density of states as usual. Pm (m = 1, 2, 3 …) are points contained in $\boldsymbol{N^{-1}}(\hat{\boldsymbol{n}})$ on S_ϵ and δA_m are infinitesimal areas around each Pm. Furthermore, it can be shown that:

$$g(\epsilon, \hat{\boldsymbol{n}}) \propto \sum_{P \in \boldsymbol{N^{-1}}(\hat{\boldsymbol{n}})} \frac{1}{|\boldsymbol{\nabla}\epsilon(P)|} \frac{1}{|K_P|}, \tag{B2}$$

where K_P is the Gaussian curvature of the isoenergy surface at point P. The mathematical derivation of Formula (B2) can be seen in the following section. Formula (B2) shows that the DDOS has the same inverse relation to the Gaussian curvature as was found for the LDOS in [189]. Accordingly, we expect any singularities or anomalies in the DDOS to also appear in the STM images.

Figure S1(b) shows the isoenergy surface of the Au fcc structure colored according to the Gaussian curvature K at Vs = 0.5 V. The variance of K leads to an inhomogeneous distribution of the DDOS on the isoenergy surface. Regions around the <110> directions are very flat, so the Gaussian curvatures are small and the DDOSs are relatively large. We plot the integration of DDOS from 0 to V_s in polar coordinates [Figure S1(c)]. The angle between the maximum

DDOS directions and the [111] direction is 34.4°, which demonstrates good agreement between the experimental results [Figure S1(b)] and the simulation [Figure S1(a)]. It is worth noting that this angle is a little smaller than the exact angle between [110] and [111] (35.3°). This is because normal vectors at points with zero curvature are close but not exactly along the <110> directions. In addition, Bragg scattering forces the isoenergy surface to be normal to the Brillouin zone near the boundary of the 1st Brillouin zone, and that is why we see holes along <111> directions in Figure S1(b). Regions around <111> directions are substantially curved, so the DDOS in the [111] direction is very low, resulting in much lower intensity or even depression of the ring patterns in STM images.

Mathematical derivation of Formula (B2)

Here we present details of the mathematical derivation of Formula (B2). We will show how to obtain

$$\lim_{\delta \to 0} \frac{\delta A_p}{\delta A} = \frac{1}{|K_P|}, \tag{B3}$$

where A_p is an infinitesimal area around point P; K_p is the Gaussian curvature at point P and $K_p \neq 0$.

Let S_ϵ be a local parametric isoenergy surface around point P:

$$\boldsymbol{k}: (u, v) \to S_\epsilon. \tag{B4}$$

The partial derivatives of $\boldsymbol{k}$ with respect to u and v are the tangent vectors and will be denoted as $\boldsymbol{k}_u$ and $\boldsymbol{k}_v$. The Gauss Map N of S_ϵ gives rise to a unit normal vector $\hat{\boldsymbol{n}}$ to each point of S_ϵ. The normal vector $\hat{\boldsymbol{n}}$ is perpendicular to the tangent vectors $\boldsymbol{k}_u$ and $\boldsymbol{k}_v$, so it is given by:

$$\hat{\boldsymbol{n}} = \boldsymbol{N}(u, v) = \frac{\boldsymbol{k}_u \times \boldsymbol{k}_v}{|\boldsymbol{k}_u \times \boldsymbol{k}_v|}. \tag{B5}$$

The partial derivatives of N with respect to u and v are the tangent vectors on a unit spherical surface and will be denoted as $\boldsymbol{N}_u$ and $\boldsymbol{N}_v$.

An infinitesimal small change of local parameters gives rises to an infinitesimal parallelogram with a vertex at $\boldsymbol{k}(u, v)$ and is spanned by two tangent vectors $\boldsymbol{k_u}$ and $\boldsymbol{k}_v$. The area δA_p of this infinitesimal parallelogram can be expressed by:

$$\delta A_P = |\boldsymbol{k_u} \times \boldsymbol{k_v}| du dv. \tag{B6}$$

The infinitesimal small change of local parameters on S_ϵ results in δA_p. Correspondingly, the area changes on the S^2 can be calculated by:

$$\delta A = |\boldsymbol{N_u} \times \boldsymbol{N_v}| dudv. \tag{B7}$$

The Gaussian curvature for a parametric surface is defined through the first and second fundamental forms of the surface which are usually given by matrices. Here, for simplicity, we just show the results which have been proved by R. Goldman [277]. The Gaussian curvature K can be expressed by:

$$K = \frac{(\boldsymbol{k}_u \times \boldsymbol{k}_v) \cdot (\boldsymbol{N}_u \times \boldsymbol{N}_v)}{|\boldsymbol{k}_u \times \boldsymbol{k}_v|^2}. \tag{B8}$$

Therefore, around the point P ($P \in S_\epsilon$), the Gaussian curvature K_P satisfies:

$$\lim_{\delta \to 0} \frac{\delta A_P}{\delta A} = \frac{|\boldsymbol{k}_u \times \boldsymbol{k}_v| dudv}{|\boldsymbol{N}_u \times \boldsymbol{N}_v| dudv} = \frac{|\boldsymbol{k}_u \times \boldsymbol{k}_v|^2}{|(\boldsymbol{k}_u \times \boldsymbol{k}_v) \cdot (\boldsymbol{N}_u \times \boldsymbol{N}_v)|} = \frac{1}{|K_P|}, \tag{B9}$$

where $K_P \neq 0$. We yield this result based on $(\boldsymbol{k}_u \times \boldsymbol{k}_v) \parallel (\boldsymbol{N}_u \times \boldsymbol{N}_v)$. The absolute value is considered due to the physical meaning of an area.

Appendix III V oxides and Mn oxides on Au(111)

A few good results of V oxides and Mn oxides have been obtained but are not presented in the preceding chapters. Figure S2 displays some STM images of V oxides on Au(111). Apart from the pinwheel structure, we observed another two structures which are temporarily named the porous structure and the square lattice according to their morphologies. The porous structure was obtained by oxidizing a small quantity of V in 10^{-6} Pa O_2 at 600 ℃. The square lattice was formed by annealing the as-prepared pinwheel structure in 10^{-6} Pa O_2.

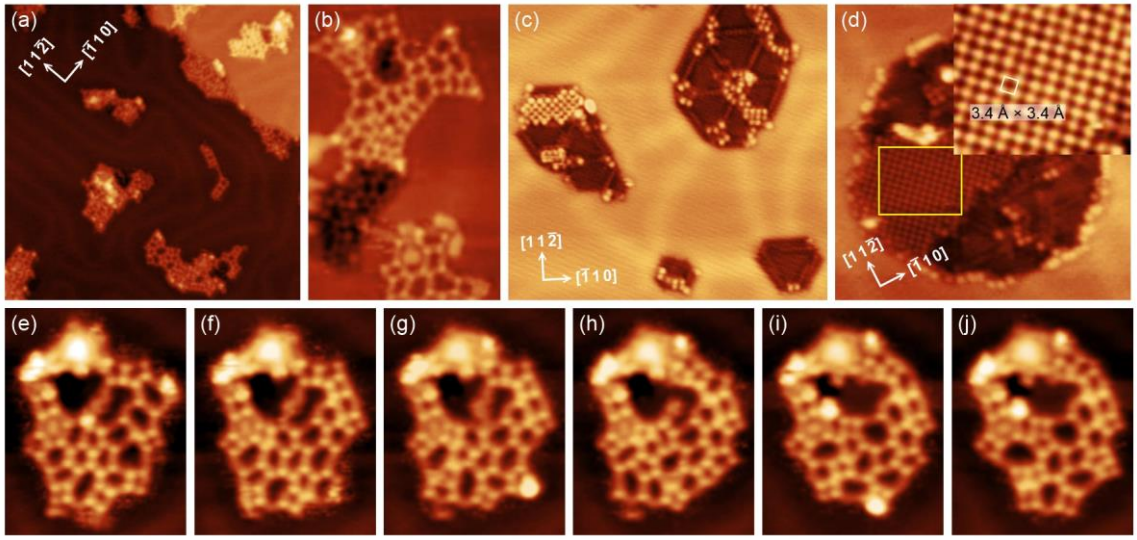

Figure S2 STM images of (a) V oxide porous nanostructures on Au(111) (37.8 nm × 37.8 nm, V_s = 2.0 V, I_t = 0.08 nA). (b) Free and embedded porous monolayers (8.2 nm × 12.6 nm, V_s = 2.0 V, I_t = 0.16 nA). (c) Square lattice started to grow on V oxide emb-pinwheel monolayers (19.4 nm × 18 nm, V_s = 0.5 V, I_t = 0.15 nA). Some sporadic protrusions are distributed along the edges of the embedded islands and the pinwheel's "hub". (d) An extensive square lattice on a large emb-pinwheel island (14.5 nm × 14.5 nm, V_s = 2.6 V, I_t = 0.35 nA). The inset (4.0 nm × 3.4 nm) is a close-up of the region in the yellow box. The white square marks the lattice unit cell with a size of 3.4 Å × 3.4 Å. (e) – (j) Image series showing the change in the porous structure during tip scanning (8 nm × 10 nm, V_s = 2.0 V, I_t = 0.16 nA).

Figure S2(a) shows some small porous islands which resemble the porous network on Pd(111) [Figure 2-8(a)] [61]. We can see the free porous monolayer as well as the embedded porous monolayer in Figure S2(b). The porous monolayer has a very loose structure that can be easily changed by tip scanning, as displayed in the image series in Figure S2(e) – (j). The average length between two protrusions is about 0.6 nm, and the longest distance can be up to 1 nm. This is impractical for a general bonding length if assuming a V-O-V configuration, and we have not yet developed any reasonable structural models. Figure S2(c) and (d) show the square lattices with a unit cell of 3.4 Å × 3.4 Å grown on top of the pinwheel structure. Surnev et al. reported a rectangular lattice (VO_2-rect) with a unit cell of 3.0 Å × 3.8 Å on Pd(111) [Figure 2-11(a)] [56]. Presumably, the V oxide square lattice on Au(111) has a stoichiometry of VO_2.

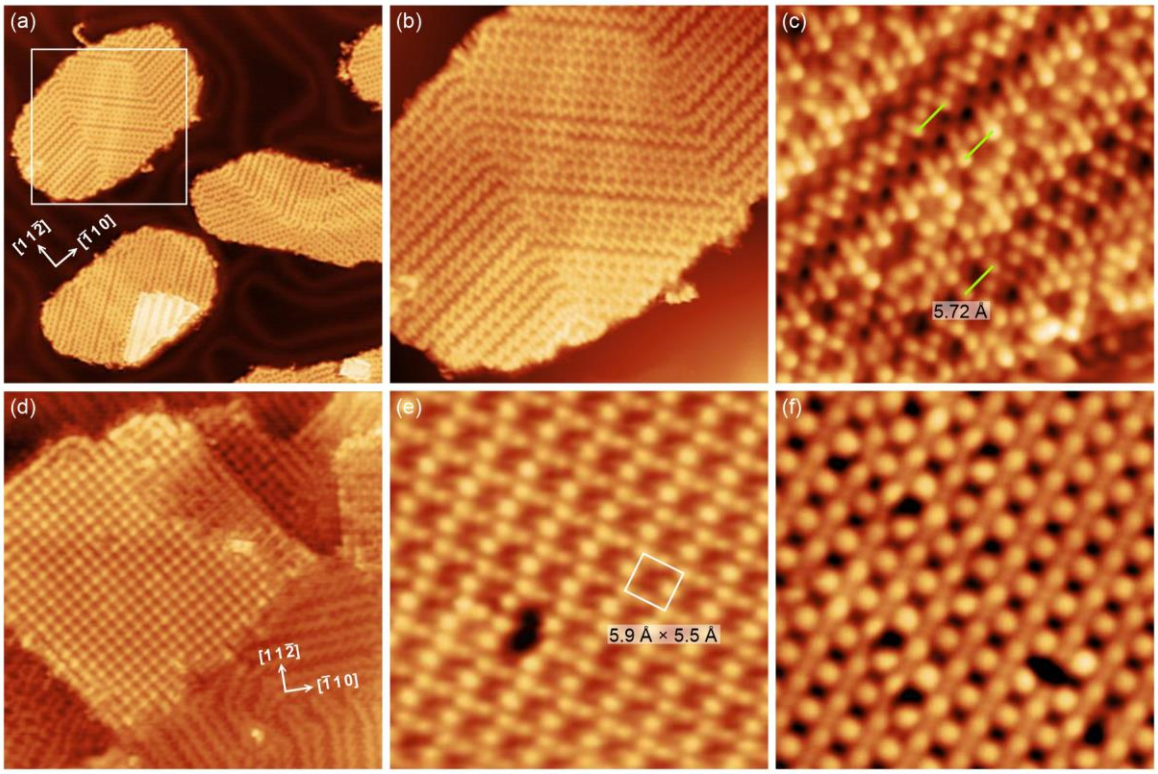

Figure S3 STM images of (a) Mn oxide "fish-bone" monolayers on Au(111) (40 nm × 40 nm, V_s = 0.4 V, I_t = 0.8 nA). (b) A close-up of the region in the white box in (a) (16 nm × 16 nm, V_s = 0.4 V, I_t = 0.8 nA). (c) "Fish-bone" structure at atomic resolution (5.5 nm × 5.5 nm, V_s = 0.5 V, I_t = 0.7 nA). The green lines indicate a periodicity of 5.72 Å along a row, approximate to twice the lattice constant of the Au(111) plane (5.76 Å). (d) Mn oxide rectangle lattice coexisted with the "fish-bone" structure (18 nm × 18 nm, V_s = 1.0 V, I_t = 0.2 nA). (e) Atomically-resolved empty-state STM image of the rectangle lattice (5 nm × 5 nm, V_s = 1.0 V, I_t = 1.0 nA). The unit cell is marked by a white box with a size of 5.9 Å × 5.5 Å. (f) Atomically-resolved filled-state STM image of the rectangle lattice (5 nm × 5 nm, V_s = -2.0 V, I_t = 0.5 nA).

Compared with Nb, Ti, or V, Mn behaves distinctively on Au(111) under the same oxidizing condition (1 × 10^{-6} Pa O_2, 500 ℃ for 0.5 ~1 h) as no ring network (honeycomb or porous) was found. Instead, Mn oxide forms monolayers with stripe structures that look like "fish-bone", as shown in Figure S3(a), (b). A close-up of the "fish-bone" structure in Figure S3(c) reveals that the periodicity along a row (5.72 Å) is close to twice the lattice constant of Au(111) unit cell (5.76 Å). Visually, the protrusions along different rows exhibit a height variation. Besides, unlike the V oxide square lattice that can be grown on the emb-pinwheel with a tiny amount, the Mn oxide rectangular phase can only be obtained with a large deposition amount (> 1 ML) after the "fish-bone" covering the whole surface [Figure S3(d)]. Notably, the rectangular phase has a complex unit cell (5.9 Å × 5.5 Å), in which totally three protrusions can be seen from either the empty-state or filled-state STM image [Figure S3(e), (f)]. The "fish-bone" structure has been reported by Liu *et al.* [278], whereas the structural models they proposed are probably incorrect due to the insufficient resolution of the STM images. They also discovered a rectangular phase, for the same reason, they only identified a simple rectangular unit cell but failed to resolve the protrusions at the bridge sites.

Reference

[1] X. Yu, T. J. Marks, and A. Facchetti, *Metal oxides for optoelectronic applications*, Nat. Mater. **15**, 383 (2016).

[2] Z. Z. Bandic and R. H. Victora, *Advances in magnetic data storage technologies*, Proc. IEEE **96**, 1749 (2008).

[3] M. B. Gawande, R. K. Pandey, and R. V. Jayaram, *Role of mixed metal oxides in catalysis science - Versatile applications in organic synthesis*, Catal. Sci. Technol. **2**, 1113 (2012).

[4] J. Zhu, H. Li, L. Zhong, P. Xiao, X. Xu, X. Yang, Z. Zhao, and J. Li, *Perovskite oxides: Preparation, characterizations, and applications in heterogeneous catalysis*, ACS Catal. **4**, 2917 (2014).

[5] C. Wang, L. Yin, L. Zhang, D. Xiang, and R. Gao, *Metal oxide gas sensors: Sensitivity and influencing factors*, Sensors **10**, 2088 (2010).

[6] P. Kumbhakar, C. Chowde Gowda, P. L. Mahapatra, M. Mukherjee, K. D. Malviya, M. Chaker, A. Chandra, B. Lahiri, P. M. Ajayan, D. Jariwala, et al., *Emerging 2D metal oxides and their applications*, Mater. Today **45**, 142 (2021).

[7] S. Gangopadhyay, D. D. Frolov, A. E. Masunov, and S. Seal, *Structure and properties of cerium oxides in bulk and nanoparticulate forms*, J. Alloys Compd. **584**, 199 (2014).

[8] K. Hoang and M. D. Johannes, *Defect chemistry in layered transition-metal oxides from screened hybrid density functional calculations*, J. Mater. Chem. A **2**, 5224 (2014).

[9] N. A. Richter, S. Sicolo, S. V. Levchenko, J. Sauer, and M. Scheffler, *Concentration of vacancies at metal-oxide surfaces: Case study of MgO(100)*, Phys. Rev. Lett. **111**, 045502 (2013).

[10] N. Baguer, V. Georgieva, L. Calderin, I. T. Todorov, S. Van Gils, and A. Bogaerts, *Study of the nucleation and growth of TiO2 and ZnO thin films by means of molecular dynamics simulations*, J. Cryst. Growth **311**, 4034 (2009).

[11] M. E. Garcia, E. W. Ill, S. H. Garofalini, E. Webb, and S. H. Garofalini, *Molecular Dynamics Simulation of V2O5/Li2SiO3 Interface*, J. Electrochem. Soc. **145**, 2155 (1998).

[12] K. Tanabe, *Application of niobium oxides as catalysts*, Catal. Today **8**, 1 (1990).

[13] O. Carp, C. L. Huisman, and A. Reller, *Photoinduced reactivity of titanium dioxide*, Prog. Solid State Chem. **32**, 33 (2004).

[14] H. Miyazaki, T. Matsuura, and T. Ota, *Vanadium oxide-based photochromic composite film*, RSC Adv. **7**, 2388 (2017).

[15] S. Jose, D. Joshy, S. B. Narendranath, and P. Periyat, *Recent advances in infrared reflective inorganic pigments*, Sol. Energy Mater. Sol. Cells **194**, 7 (2019).

[16] X. Xia, Y. Zhang, D. Chao, C. Guan, Y. Zhang, L. Li, X. Ge, I. M. Bacho, J. Tu, and H. J. Fan, *Solution synthesis of metal oxides for electrochemical energy storage applications*, Nanoscale **6**, 5008 (2014).

[17] F. P. Netzer and A. Fortunelli, *Oxide materials at the two-dimensional limit*, (Springer, 2016).

[18] L. Ter Minassian-Saraga, *Thin films including layers: terminology in relation to their preparation and characterization*, Pure Appl. Chem. **66**, 1667 (1994).

[19] J. Venables, *Introduction to surface and thin film processes*, (Cambridge University Press, 2000).

[20] J. Zhou, L. Zhu, L. Sun, B. Wang, and P. Xiao, *Influence of nb on the structure and high temperature performance of billet for high-rise structural steel*, Metals (Basel). **11**, 1721 (2021).

[21] X. Ye, B. Yang, Y. Nie, S. Yu, and Y. Li, *Influence of Nb addition on the oxidation behavior of novel Ni-base superalloy*, Corros. Sci. **185**, 109436 (2021).

[22] Y. Lvovsky, E. W. Stautner, and T. Zhang, *Novel technologies and configurations of superconducting magnets for MRI*, Supercond. Sci. Technol. **26**, 093001 (2013).

[23] K. Tanabe, *Catalytic application of niobium compounds*, Catal. Today **78**, 65 (2003).

[24] M. Nakayama, M. Xue, W. An, P. Liu, and M. G. White, *Influence of Cluster-Support Interactions on Reactivity of Size-Selected NbxOy Clusters*, J. Phys. Chem. C **119**, 14756 (2015).

[25] J. M. Jehng and I. E. Wachs, *The molecular structures and reactivity of supported niobium oxide catalysts*, Catal. Today **8**, 37 (1990).

[26] L. Xie, D. Wang, C. Zhong, X. Guo, T. Ushikubo, and K. Wada, *The preparation of and water adsorption on thin films of niobium oxide on Pt(111)*, Surf. Sci. **320**, 62 (1994).

[27] S. Wang, J. Goniakowski, C. Noguera, and M. R. Castell, *Atomic and electronic structure of an epitaxial Nb2O3 honeycomb monolayer on Au(111)*, Phys. Rev. B **100**, 125408 (2019).

[28] D. E. Starr, F. M. T. Mendes, J. Middeke, R. P. Blum, H. Niehus, D. Lahav, S. Guimond, A. Uhl, T. Kluener, M. Schmal, et al., *Preparation and characterization of well-ordered, thin niobia films on a metal substrate*, Surf. Sci. **599**, 14 (2005).

[29] U. Bach, D. Lupo, P. Comte, J.-E. Moser, F. Weissörtel, J. Salbeck, H. Spreitzer, and M. Grätzel, *Solid-state dye-sensitized mesoporous TiO2 solar cells with high photon-to-electron conversion efficiencies*, Nature **395**, 583 (1998).

[30] G. K. Mor, M. A. Carvalho, O. K. Varghese, M. V Pishko, and C. A. Grimes, *A room-temperature TiO2-nanotube hydrogen sensor able to self-clean photoactively from environmental contamination*, J. Mater. Res. **19**, 628 (2004).

[31] S. J. Tauster, S. C. Fung, and R. L. Garten, *Strong metal-support interactions. Group 8 noble metals supported on titanium dioxide*, J. Am. Chem. Soc. **100**, 170 (1978).

[32] S. Surnev, M. Sock, G. Kresse, J. N. Andersen, M. G. Ramsey, and F. P. Netzer, *Unusual CO adsorption sites on vanadium oxide-Pd(111) "Inverse Model Catalyst" surfaces*, J. Phys. Chem. B **107**, 4777 (2003).

[33] F. Sedona, G. A. Rizzi, S. Agnoli, F. X. Llabrés i Xamena, A. Papageorgiou, D. Ostermann, M. Sambi, P. Finetti, K. Schierbaum, and G. Granozzi, *Ultrathin TiOx films on Pt(111): A LEED, XPS, and STM investigation*, J. Phys. Chem. B **109**, 24411 (2005).

[34] T. Orzali, M. Casarin, G. Granozzi, M. Sambi, and A. Vittadini, *Bottom-up assembly of single-domain titania nanosheets on (1 × 2)-Pt(110)*, Phys. Rev. Lett. **97**, 156101 (2006).

[35] T. Matsumoto, M. Batzill, S. Hsieh, and B. E. Koel, *Fundamental studies of titanium oxide-Pt(100) interfaces I. Stable high temperature structures formed by annealing TiOx films on Pt(100)*, Surf. Sci. **572**, 127 (2004).

[36] Y. Zhang, L. Giordano, G. Pacchioni, A. Vittadini, F. Sedona, P. Finetti, and G. Granozzi, *The structure of a stoichiometric TiO2 nanophase on Pt(111)*, Surf. Sci. **601**, 3488 (2007).

[37] S. Hsieh, D. Beck, T. Matsumoto, and B. E. Koel, *Thermal stability of ultrathin titanium films on a Pt(111) substrate*, Thin Solid Films **466**, 123 (2004).

[38] S. Agnoli, T. Orzali, M. Sambi, A. Vittadini, M. Casarin, and G. Granozzi, *Ultrathin TiO2 films on (1 × 2)-Pt(110): A LEED, photoemission, STM, and theoretical investigation*, J. Phys. Chem. C **112**, 20038 (2008).

[39] F. Sedona, S. Agnoli, and G. Granozzi, *Ultrathin wagon-wheel-like TiOx phases on Pt(111): A combined low-energy electron diffraction and scanning tunneling microscopy investigation*, J. Phys. Chem. B **110**, 15359 (2006).

[40] M. H. Farstad, D. Ragazzon, H. Grönbeck, M. D. Strømsheim, C. Stavrakas, J. Gustafson, A. Sandell, and A. Borg, *TiOx thin films grown on Pd(100) and Pd(111) by chemical vapor deposition*, Surf. Sci. **649**, 80 (2016).

[41] A. Atrei, A. M. Ferrari, D. Szieberth, B. Cortigiani, and G. Rovida, *Lepidocrocite-like structure of the TiO2 monolayer grown on Ag(100)*, Phys. Chem. Chem. Phys. **12**, 11587 (2010).

[42] C. Wu, M. S. J. Marshall, and M. R. Castell, *Surface structures of ultrathin TiOx films on Au(111)*, J. Phys. Chem. C **115**, 8643 (2011).

[43] F. Tumino, P. Carrozzo, L. Mascaretti, C. S. Casari, M. Passoni, S. Tosoni, C. E. Bottani, and A. L. Bassi, *Two-dimensional TiOx nanostructures on Au(111): A scanning tunneling microscopy and spectroscopy investigation*, 2D Mater. **2**, 45011 (2015).

[44] T. K. Mukherjee, S. P. Chakraborty, A. C. Bidaye, and C. K. Gupta, *Recovery of pure vanadium oxide from bayer sludge*, Miner. Eng. **3**, 345 (1990).

[45] S. Nishio and M. Kakihana, *Evidence for visible light photochromism of V2O5*, Chem. Mater. **14**, 3730 (2002).

[46] N. Bahlawane and D. Lenoble, *Vanadium oxide compounds: structure, properties, and growth from the gas phase*, Chem. Vap. Depos. **20**, 299 (2014).

[47] I. E. Wachs and B. M. Weckhuysen, *Structure and reactivity of surface vanadium oxide species on oxide supports*, Appl. Catal. A Gen. **157**, 67 (1997).

[48] K. B. Lewis, S. T. Oyama, and G. A. Somorjai, *The preparation and reactivity of thin, ordered films of vanadium oxide on Au(111)*, Surf. Sci. **233**, 75 (1990).

[49] Y. Romanyshyn, S. Guimond, D. Göbke, J. M. Sturm, H. Kuhlenbeck, J. Döbler, M. V. Ganduglia-Pirovano, J. Sauer, and H. J. Freund, *Methanol adsorption on V2O3(0001)*, Top. Catal. **54**, 669 (2011).

[50] S. Guimond, J. M. Sturm, D. Göbke, Y. Romanyshyn, M. Naschitzki, H. Kuhlenbeck, and H. J. Freund, *Well-ordered V2O5(001) thin films on Au(111): Growth and thermal stability*, J. Phys. Chem. C **112**, 11835 (2008).

[51] S. Guimond, D. Göbke, Y. Romanyshyn, J. M. Sturm, M. Naschitzki, H. Kuhlenbeck, and H. J. Freund, *Growth and characterization of ultrathin V2Oy (y ≈ 5) Films on Au(111)*, J. Phys. Chem. C **112**, 12363 (2008).

[52] J. Seifert, E. Meyer, H. Winter, and H. Kuhlenbeck, *Surface termination of an ultrathin V2O3 film on Au(111) studied via ion beam triangulation*, Surf. Sci. **606**, L41 (2012).

[53] A.-C. Dupuis, M. Abu Haija, B. Richter, H. Kuhlenbeck, and H.-J. Freund, *V2O3 (0001) on Au(111) and W(110): growth, termination and electronic structure*, Surf. Sci. **539**, 99 (2003).

[54] H. Niehus, R.-P. Blum, and D. Ahlbehrendt, *Structure of Vanadium Oxide (V2O3) Grown on Cu3Au(100)*, Surf. Rev. Lett. **10**, 353 (2003).

[55] S. Surnev, G. Kresse, M. Sock, M. G. Ramsey, and F. P. Netzer, *Surface structures of ultrathin vanadium oxide films on Pd(111)*, Surf. Sci. **495**, 91 (2001).

[56] S. Surnev, G. Kresse, M. G. Ramsey, and F. P. Netzer, *Novel interface-mediated metastable oxide phases: Vanadium oxides on Pd(111)*, Phys. Rev. Lett. **87**, 861021

(2001).

[57] M. Kratzer, S. Surnev, F. P. Netzer, and A. Winkler, *Model reaction studies on vanadium oxide nanostructures on Pd(111)*, J. Chem. Phys. **125**, 074703 (2006).

[58] S. Surnev, L. Vitali, M. Ramsey, F. Netzer, G. Kresse, and J. Hafner, *Growth and structure of ultrathin vanadium oxide layers on Pd(111)*, Phys. Rev. B - Condens. Matter Mater. Phys. **61**, 13945 (2000).

[59] F. P. Leisenberger, S. Surnev, L. Vitali, M. G. Ramsey, and F. P. Netzer, *Nature, growth, and stability of vanadium oxides on Pd(111)*, J. Vac. Sci. Technol. A Vacuum, Surfaces, Film. **17**, 1743 (1999).

[60] J. Schoiswohl, M. Sock, Q. Chen, G. Thornton, G. Kresse, M. G. Ramsey, S. Surnev, and F. P. Netzer, *Metal supported oxide nanostructures: Model systems for advanced catalysis*, Top. Catal. **46**, 137 (2007).

[61] C. Klein, G. Kresse, S. Surnev, F. P. Netzer, M. Schmid, and P. Varga, *Vanadium surface oxides on Pd(111): A structural analysis*, Phys. Rev. B - Condens. Matter Mater. Phys. **68**, 235416 (2003).

[62] J. Schoiswohl, S. Surnev, and F. P. Netzer, *Reactions on inverse model catalyst surfaces: atomic views by STM*, Top. Catal. **36**, 91 (2005).

[63] G. Kresse, S. Surnev, M. G. Ramsey, and F. P. Netzer, *First-principles calculations for VxOy grown on Pd(111)*, Surf. Sci. **492**, 329 (2001).

[64] F. P. Leisenberger, S. Surnev, G. Koller, M. G. Ramsey, and F. P. Netzer, *Probing the metal sites of a vanadium oxide-Pd(111) "inverse catalyst": Adsorption of CO*, Surf. Sci. **444**, 211 (2000).

[65] J. Schoiswohl, S. Surnev, and F. P. Netzer, *Vanadium oxide overlayers on vicinal Rh(15 15 13): The influence of surface steps*, J. Phys. Chem. C **111**, 10503 (2007).

[66] F. P. Netzer, F. Allegretti, and S. Surnev, *Low-dimensional oxide nanostructures on metals: Hybrid systems with novel properties*, J. Vac. Sci. Technol. B Microelectron. Nanom. Struct. **28**, 1 (2010).

[67] J. Schoiswohl, S. Eck, M. G. Ramsey, J. N. Andersen, S. Surnev, and F. P. Netzer, *Vanadium oxide nanostructures on Rh(111): Promotion effect of CO adsorption and oxidation*, Surf. Sci. **580**, 122 (2005).

[68] G. Krenn, J. Schoiswohl, S. Surnev, F. P. Netzer, and R. Schennach, *Metal-oxide boundary effects in vanadium oxide – Rh(111) inverse model catalysts: a RAIRS, STM and TPD study*, Top. Catal. **46**, 231 (2007).

[69] J. Schoiswohl, S. Surnev, M. Sock, S. Eck, M. G. Ramsey, F. P. Netzer, and G. Kresse, *Reduction of vanadium-oxide monolayer structures*, Phys. Rev. B - Condens. Matter Mater. Phys. **71**, 165437 (2005).

[70] J. Schoiswohl, M. Sock, S. Eck, S. Surnev, M. G. Ramsey, F. P. Netzer, and G. Kresse, *Atomic-level growth study of vanadium oxide nanostructures on Rh(111)*, Phys. Rev. B - Condens. Matter Mater. Phys. **69**, 155403 (2004).

[71] J. Schoiswohl, G. Kresse, S. Surnev, M. Sock, M. G. Ramsey, and F. P. Netzer, *Planar vanadium oxide clusters: Two-dimensional evaporation and diffusion on Rh(111)*, Phys. Rev. Lett. **92**, 206103 (2004).

[72] A. J. Mannix, B. Kiraly, M. C. Hersam, and N. P. Guisinger, *Synthesis and chemistry of elemental 2D materials*, Nat. Rev. Chem. **1**, 0014 (2017).

[73] A. K. Geim and K. S. Novoselov, *The rise of graphene*, Nat. Mater. **6**, 183 (2007).

[74] C. Tan, X. Cao, X. J. Wu, Q. He, J. Yang, X. Zhang, J. Chen, W. Zhao, S. Han, G. H. Nam, et al., *Recent Advances in Ultrathin Two-Dimensional Nanomaterials*, Chem. Rev. **117**, 6225 (2017).

[75] R. Mas-Ballesté, C. Gómez-Navarro, J. Gómez-Herrero, and F. Zamora, *2D materials: To graphene and beyond*, Nanoscale **3**, 20 (2011).

[76] H. Liu, W. Lei, Z. Tong, X. Li, Z. Wu, Q. Jia, S. Zhang, and H. Zhang, *Defect Engineering of 2D Materials for Electrochemical Energy Storage*, Adv. Mater. Interfaces **7**, 2000494 (2020).

[77] J. Jiang, T. Xu, J. Lu, L. Sun, and Z. Ni, *Defect Engineering in 2D Materials: Precise Manipulation and Improved Functionalities*, Research **2019**, 4641739 (2019).

[78] R. Dettori, E. Cadelano, and L. Colombo, *Elastic fields and moduli in defected graphene*, J. Phys. Condens. Matter **24**, 104020 (2012).

[79] A. Hashimoto, K. Suenaga, A. Gloter, K. Urita, and S. Iijima, *Direct evidence for atomic defects in graphene layers*, Nature **430**, 870 (2004).

[80] A. J. Stone and D. J. Wales, *Theoretical studies of icosahedral C60 and some related species*, Chem. Phys. Lett. **128**, 501 (1986).

[81] M. Batzill, *The surface science of graphene: Metal interfaces, CVD synthesis, nanoribbons, chemical modifications, and defects*, Surf. Sci. Rep. **67**, 83 (2012).

[82] B. Yang, J. A. Boscoboinik, X. Yu, S. Shaikhutdinov, and H. J. Freund, *Patterned defect structures predicted for graphene are observed on single-layer silica films*, Nano Lett. **13**, 4422 (2013).

[83] M. T. Lusk and L. D. Carr, *Nanoengineering defect structures on graphene*, Phys. Rev. Lett. **100**, 175503 (2008).

[84] H. Terrones, M. Terrones, E. Hernández, N. Grobert, J. C. Charlier, and P. M. Ajayan, *New metallic allotropes of planar and tubular carbon*, Phys. Rev. Lett. **84**, 1716 (2000).

[85] O. V Yazyev and S. G. Louie, *Topological defects in graphene: dislocations and grain boundaries*, Phys. Rev. B - Condens. Matter Mater. Phys. **81**, 195420 (2010).

[86] J. C. Meyer, C. Kisielowski, R. Erni, M. D. Rossell, M. F. Crommie, and A. Zettl, *Direct imaging of lattice atoms and topological defects in graphene membranes*, Nano Lett. **8**, 3582 (2008).

[87] F. Banhart, J. Kotakoski, and A. V. Krasheninnikov, *Structural defects in graphene*, ACS Nano **5**, 26 (2011).

[88] S. Wang, X. Hu, J. Goniakowski, C. Noguera, and M. R. Castell, *Influence of the support on stabilizing local defects in strained monolayer oxide films*, Nanoscale **11**, 2412 (2019).

[89] J. Zhang, R. Sun, D. Ruan, M. Zhang, Y. Li, K. Zhang, F. Cheng, Z. Wang, and Z. M. Wang, *Point defects in two-dimensional hexagonal boron nitride: A perspective*, J. Appl. Phys. **128**, 100902 (2020).

[90] A. R. Botello-Méndez, X. Declerck, M. Terrones, H. Terrones, and J. C. Charlier, *One-dimensional extended lines of divacancy defects in graphene*, Nanoscale **3**, 2868 (2011).

[91] X. Lu, Z. Chen, and P. V. R. Schleyer, *Are stone-wales defect sites always more reactive than perfect sites in the sidewalls of single-wall carbon nanotubes?*, J. Am. Chem. Soc. **127**, 20 (2005).

[92] O. V. Yazyev, *Polycrystalline graphene: Atomic structure, energetics and transport properties*, Solid State Commun. **152**, 1431 (2012).

[93] P. Y. Huang, C. S. Ruiz-Vargas, A. M. Van Der Zande, W. S. Whitney, M. P. Levendorf, J. W. Kevek, S. Garg, J. S. Alden, C. J. Hustedt, Y. Zhu, et al., *Grains and grain boundaries in single-layer graphene atomic patchwork quilts*, Nature **469**, 389 (2011).

[94] Q. Li, X. Zou, M. Liu, J. Sun, Y. Gao, Y. Qi, X. Zhou, B. I. Yakobson, Y. Zhang, and Z. Liu, *Grain Boundary Structures and Electronic Properties of Hexagonal Boron Nitride on Cu(111)*, Nano Lett. **15**, 5804 (2015).

[95] T. H. Liu, C. W. Pao, and C. C. Chang, *Effects of dislocation densities and distributions on graphene grain boundary failure strengths from atomistic simulations*, Carbon N. Y. **50**, 3465 (2012).

[96] K. Kim, Z. Lee, W. Regan, C. Kisielowski, M. F. Crommie, and A. Zettl, *Grain boundary mapping in polycrystalline graphene*, ACS Nano **5**, 2142 (2011).

[97] J. Lahiri, Y. Lin, P. Bozkurt, I. I. Oleynik, and M. Batzill, *An extended defect in graphene as a metallic wire*, Nat. Nanotechnol. **5**, 326 (2010).

[98] K. S. Kim, Y. Zhao, H. Jang, S. Y. Lee, J. M. Kim, K. S. Kim, J. H. Ahn, P. Kim, J. Y. Choi, and B. H. Hong, *Large-scale pattern growth of graphene films for stretchable*

transparent electrodes, Nature **457**, 706 (2009).

[99] C. Ma, H. Sun, Y. Zhao, B. Li, Q. Li, A. Zhao, X. Wang, Y. Luo, J. Yang, B. Wang, et al., *Evidence of van Hove singularities in ordered grain boundaries of graphene*, Phys. Rev. Lett. **112**, 226802 (2014).

[100] Y. Tison, J. Lagoute, V. Repain, C. Chacon, Y. Girard, F. Joucken, R. Sporken, F. Gargiulo, O. V Yazyev, and S. Rousset, *Grain boundaries in graphene on SiC(0001¯) substrate*, Nano Lett. **14**, 6382 (2014).

[101] J. Zhang, J. Zhao, and J. Lu, *Intrinsic strength and failure behaviors of graphene grain boundaries*, ACS Nano **6**, 2704 (2012).

[102] A. L. Gibb, N. Alem, J. H. Chen, K. J. Erickson, J. Ciston, A. Gautam, M. Linck, and A. Zettl, *Atomic resolution imaging of grain boundary defects in monolayer chemical vapor deposition-grown hexagonal boron nitride*, J. Am. Chem. Soc. **135**, 6758 (2013).

[103] Y. Liu, X. Zou, and B. I. Yakobson, *Dislocations and grain boundaries in two-dimensional boron nitride*, ACS Nano **6**, 7053 (2012).

[104] T. K. Todorova, M. Sierka, J. Sauer, S. Kaya, J. Weissenrieder, J. L. Lu, H. J. Gao, S. Shaikhutdinov, and H. J. Freund, *Atomic structure of a thin silica film on a Mo(112) substrate: A combined experimental and theoretical study*, Phys. Rev. B - Condens. Matter Mater. Phys. **73**, 165414 (2006).

[105] J. Weissenrieder, S. Kaya, J. L. Lu, H. J. Gao, S. Shaikhutdinov, H. J. Freund, M. Sierka, T. K. Todorova, and J. Sauer, *Atomic structure of a thin silica film on a Mo(112) substrate: A two-dimensional network of SiO4 tetrahedra*, Phys. Rev. Lett. **95**, 076103 (2005).

[106] S. Shaikhutdinov and H. J. Freund, *Ultrathin silica films on metals: The long and winding road to understanding the atomic structure*, Adv. Mater. **25**, 49 (2013).

[107] Y. Oh, Y. Cho, H. Kwon, J. Lee, I. Jeon, W. Ko, H. W. Kim, J. Ku, G. Kim, H. Suh, et al., *Electronic structure and switching behavior of the metastable silicene domain boundary*, Appl. Phys. Lett. **110**, 263112 (2017).

[108] X. Zou, Y. Liu, and B. I. Yakobson, *Predicting dislocations and grain boundaries in two-dimensional metal-disulfides from the first principles*, Nano Lett. **13**, 253 (2013).

[109] D. J. Klein, *Graphitic polymer strips with edge states*, Chem. Phys. Lett. **217**, 261 (1994).

[110] K. He, A. W. Robertson, S. Lee, E. Yoon, G. Do Lee, and J. H. Warner, *Extended klein edges in graphene*, ACS Nano **8**, 12272 (2014).

[111] S. M. Aghaei, M. M. Monshi, I. Torres, and I. Calizo, *Edge functionalization and doping effects on the stability, electronic and magnetic properties of silicene nanoribbons*, RSC Adv. **6**, 17046 (2016).

[112] A. Gupta, T. Sakthivel, and S. Seal, *Recent development in 2D materials beyond graphene*, Prog. Mater. Sci. **73**, 44 (2015).

[113] M. Acik and Y. J. Chabal, *Nature of graphene edges: A review*, Jpn. J. Appl. Phys. **50**, 070101 (2011).

[114] P. Koskinen, S. Malola, and H. Häkkinen, *Self-passivating edge reconstructions of graphene*, Phys. Rev. Lett. **101**, 115502 (2008).

[115] B. Huang, H. Lee, B. L. Gu, F. Liu, and W. Duan, *Edge stability of boron nitride nanoribbons and its application in designing hybrid BNC structures*, Nano Res. **5**, 62 (2012).

[116] P. Koskinen, S. Malola, and H. Häkkinen, *Evidence for graphene edges beyond zigzag and armchair*, Phys. Rev. B - Condens. Matter Mater. Phys. **80**, 073401 (2009).

[117] Ç. Ö. Girit, J. C. Meyer, R. Erni, M. D. Rossell, C. Kisielowski, L. Yang, C. H. Park, M. F. Crommie, M. L. Cohen, S. G. Louie, et al., *Graphene at the edge: Stability and dynamics*, Science **323**, 1705 (2009).

[118] J. Gao, J. Zhao, and F. Ding, *Transition metal surface passivation induced graphene edge reconstruction*, J. Am. Chem. Soc. **134**, 6204 (2012).

[119] Y. Gao, D. Xu, T. Cui, and D. Li, *Stability of hydrogen-terminated graphene edges*, Phys. Chem. Chem. Phys. **23**, 13261 (2021).

[120] Y. Ding and Y. Wang, *Electronic structures of reconstructed zigzag silicene nanoribbons*, Appl. Phys. Lett. **104**, 083111 (2014).

[121] T. Hu, Y. Han, and J. Dong, *Edge reconstructions of hexagonal boron nitride nanoribbons: A first-principles study*, Phys. E Low-Dimensional Syst. Nanostructures **54**, 191 (2013).

[122] Q. Pang, Y. Zhang, J. M. Zhang, V. Ji, and K. W. Xu, *Electronic and magnetic properties of pristine and chemically functionalized germanene nanoribbons*, Nanoscale **3**, 4330 (2011).

[123] W. Hu, L. Lin, and C. Yang, *Edge reconstruction in armchair phosphorene nanoribbons revealed by discontinuous Galerkin density functional theory*, Phys. Chem. Chem. Phys. **17**, 31397 (2015).

[124] L. P. Hansen, Q. M. Ramasse, C. Kisielowski, M. Brorson, E. Johnson, H. Topsøe, and S. Helveg, *Atomic-scale edge structures on industrial-style MoS2 nanocatalysts*, Angew. Chemie - Int. Ed. **50**, 10153 (2011).

[125] Y. Sayed-Ahmad-Baraza and C. P. Ewels, *Stability, Structure and Reconstruction of 1H-Edges in MoS2*, Chem. - A Eur. J. **26**, 6686 (2020).

[126] M. Topsakal, S. Cahangirov, E. Bekaroglu, and S. Ciraci, *First-principles study of zinc oxide honeycomb structures*, Phys. Rev. B - Condens. Matter Mater. Phys. **80**, 235119

(2009).

[127] C. Möller, H. Fedderwitz, C. Noguera, J. Goniakowski, and N. Nilius, *Temperature-dependent phase evolution of copper-oxide thin-films on Au(111)*, Phys. Chem. Chem. Phys. **20**, 5636 (2018).

[128] L. Zhang, J. van Ek, and U. Diebold, *Highly ordered nanoscale surface alloy formed through Cr-induced Pt(111) reconstruction*, Phys. Rev. B - Condens. Matter Mater. Phys. **57**, R4285 (1998).

[129] L. P. Zhang, J. van Ek, and U. Diebold, *Spatial self-organization of a nanoscale structure on the Pt(111) surface*, Phys. Rev. B - Condens. Matter Mater. Phys. **59**, 5837 (1999).

[130] H. C. Diaz, Y. Ma, R. Chaghi, and M. Batzill, *High density of (pseudo) periodic twin-grain boundaries in molecular beam epitaxy-grown van der Waals heterostructure: MoTe2/MoS2*, Appl. Phys. Lett. **108**, 191606 (2016).

[131] R. Gubó, C. M. Yim, M. Allan, C. L. Pang, A. Berkó, and G. Thornton, *Variation of SMSI with the Au:Pd Ratio of Bimetallic Nanoparticles on TiO2(110)*, Top. Catal. **61**, 308 (2018).

[132] F. Silly and M. R. Castell, *Encapsulated Pd nanocrystals supported by Nanoline-Structured SrTiO3(001)*, J. Phys. Chem. B **109**, 12316 (2005).

[133] Y. Gao, P. Chen, and M. R. Castell, *Encapsulated Pd crystals on anatase supports: High precision determination of the titanate overlayer moiré structure*, Surf. Sci. **715**, 121941 (2022).

[134] P. Mutombo, R. Gubó, and A. Berkó, *Interaction of Gold with a Pinwheel TiO∼1.2 Film Formed on Rh(111) Facet: STM and DFT Studies*, J. Phys. Chem. C **120**, 12917 (2016).

[135] A. Berkó, R. Gubó, L. Óvári, L. Bugyi, I. Szenti, and Z. Kónya, *Interaction of Rh with Rh nanoparticles encapsulated by ordered ultrathin TiO1+x film on TiO2(110) surface*, Langmuir **29**, 15868 (2013).

[136] M. Ritter, W. Ranke, and W. Weiss, *Growth and structure of ultrathin FeO films on Pt(111) studied by STM and LEED*, Phys. Rev. B - Condens. Matter Mater. Phys. **57**, 7240 (1998).

[137] L. R. Merte, J. Knudsen, L. C. Grabow, R. T. Vang, E. Lægsgaard, M. Mavrikakis, and F. Besenbacher, *Correlating STM contrast and atomic-scale structure by chemical modification: Vacancy dislocation loops on FeO/Pt(111)*, Surf. Sci. **603**, L15 (2009).

[138] Y. Liu, Y. Ning, L. Yu, Z. Zhou, Q. Liu, Y. Zhang, H. Chen, J. Xiao, P. Liu, F. Yang, et al., *Structure and Electronic Properties of Interface-Confined Oxide Nanostructures*, ACS Nano **11**, 11449 (2017).

[139] H. F. Liu, S. L. Wong, and D. Z. Chi, *CVD Growth of MoS2-based Two-dimensional*

Materials, Chem. Vap. Depos. **21**, 241 (2015).

[140] J. Sun, X. Li, W. Guo, M. Zhao, X. Fan, Y. Dong, C. Xu, J. Deng, and Y. Fu, *Synthesis methods of two-dimensional MoS2: A brief review*, Crystals **7**, 198 (2017).

[141] P. Chen, W. Xu, Y. Gao, P. Holdway, J. H. Warner, and M. R. Castell, *Thermal Degradation of Monolayer MoS2 on SrTiO3 Supports*, J. Phys. Chem. C **123**, 3876 (2019).

[142] A. S. Walton, J. V. Lauritsen, H. Topsøe, and F. Besenbacher, *MoS2 nanoparticle morphologies in hydrodesulfurization catalysis studied by scanning tunneling microscopy*, J. Catal. **308**, 306 (2013).

[143] S. Wang, C. Han, L. Ye, G. Zhang, Y. Hu, W. Li, and Y. Jiang, *Electronic properties of triangle molybdenum disulfide (Mos2) clusters with different sizes and edges*, Molecules **26**, 1157 (2021).

[144] D. C. Grinter, S. D. Senanayake, and J. I. Flege, *In situ growth, structure, and real-time chemical reactivity of well-defined CeOx-Ru(0001) model surfaces*, Appl. Catal. B Environ. **197**, 286 (2016).

[145] *JEOL JSTM4500XT Manual 2.0*, (1984).

[146] C. Julian Chen, *Introduction to scanning tunneling microscopy*, (Oxford University Press, 2021).

[147] A. I. Kirkland and S. J. Haigh, *Nanocharacterisation*, (Royal Society of Chemistry, Cambridge, 2015).

[148] B. Voigtländer, *Scanning probe microscopy: Atomic force microscopy and scanning tunneling microscopy*, (Springer, 2015).

[149] H. Neddermeyer, *Scanning Tunneling Microscopy*, (Springer Netherlands, 2012).

[150] C. Bai, *Scanning Tunneling Microscopy and Its Application*, (Springer Science & Business Media, 2000).

[151] M. Bowker and P. R. Davies, *Scanning Tunneling Microscopy in Surface Science, Nanoscience and Catalysis*, (Wiley-VCH, 2009).

[152] D. C. Mattis and J. Bardeen, *Theory of the anomalous skin effect in normal and superconducting metals*, Phys. Rev. **111**, 412 (1958).

[153] J. Tersoff and D. R. Hamann, *Theory and application for the scanning tunneling microscope*, Phys. Rev. Lett. **50**, 1998 (1983).

[154] J. Tersoff and D. R. Hamann, *Theory of the scanning tunneling microscope*, Phys. Rev. B **31**, 805 (1985).

[155] J. P. Song, N. H. Pryds, K. Glejbøl, K. A. Mørch, A. R. Thölén, and L. N. Christensen, *A development in the preparation of sharp scanning tunneling microscopy tips*, Rev. Sci. Instrum. **64**, 900 (1993).

[156] G. A. Fried, X. D. Wang, and K. W. Hipps, *Gold-coated tungsten tips for scanning tunneling microscopy*, Rev. Sci. Instrum. **64**, 1495 (1993).

[157] J. P. Ibe, P. P. Bey, S. L. Brandow, R. A. Brizzolara, N. A. Burnham, D. P. DiLella, K. P. Lee, C. R. K. Marrian, and R. J. Colton, *On the electrochemical etching of tips for scanning tunneling microscopy*, J. Vac. Sci. Technol. A Vacuum, Surfaces, Film. **8**, 3570 (1990).

[158] I. Ekvall, E. Wahlström, D. Claesson, H. Olin, and E. Olsson, *Preparation and characterization of electrochemically etched W tips for STM*, Meas. Sci. Technol. **10**, 11 (1999).

[159] L. A. Nagahara, T. Thundat, and S. M. Lindsay, *Preparation and characterization of STM tips for electrochemical studies*, Rev. Sci. Instrum. **60**, 3128 (1989).

[160] A. J. Melmed, *The art and science and other aspects of making sharp tips*, J. Vac. Sci. Technol. B Microelectron. Nanom. Struct. **9**, 601 (1991).

[161] S. Kerfriden, A. H. Nahlé, S. A. Campbell, F. C. Walsh, and J. R. Smith, *The electrochemical etching of tungsten STM tips*, Electrochim. Acta **43**, 1939 (1998).

[162] PSP Vacuum Technology, *Instruction Manual for PSP Vacuum Technology Ion Source ISIS3000*, (n.d.).

[163] R. Behrisch and K. Wittmaack, *Sputtering by particle bombardment*, (Springer-Verlag Berlin, 1981).

[164] K. Wasa, M. Kitabatake, and H. Adachi, *Thin film materials technology: sputtering of control compound materials*, (Springer Science & Business Media, 2004).

[165] Oxford Applied Research, *Operating and Service Manual for Mini E-beam Evaporator Model EGN4*, (1997).

[166] S. Miyazaki, H. Nishimura, M. Fukuda, L. Ley, and J. Ristein, *Structure and electronic states of ultrathin SiO 2 thermally grown on Si(100) and Si(111) surfaces*, Appl. Surf. Sci. **113**, 585 (1997).

[167] M. Bäumer, D. Cappus, H. Kuhlenbeck, H. J. Freund, G. Wilhelmi, A. Brodde, and H. Neddermeye, *The structure of thin NiO(100) films grown on Ni(100) as determined by low-energy-electron diffraction and scanning tunneling microscopy*, Surf. Sci. **253**, 116 (1991).

[168] C. Wöll, S. Chiang, R. J. Wilson, and P. H. Lippel, *Determination of atom positions at stacking-fault dislocations on Au(111) by scanning tunneling microscopy*, Phys. Rev. B **39**, 7988 (1989).

[169] J. Perdereau, J. P. Biberian, and G. E. Rhead, *Adsorption and surface alloying of lead monolayers on (111) and (110) faces of gold*, J. Phys. F Met. Phys. **4**, 798 (1974).

[170] H. Melle and E. Menzel, *Superstructures on Spherical Gold Crystals*, Zeitschrift Fur Naturforsch. - Sect. A J. Phys. Sci. **33**, 282 (1978).

[171] N. Takeuchi, C. T. Chan, and K. M. Ho, *Au(111): A theoretical study of the surface reconstruction and the surface electronic structure*, Phys. Rev. B **43**, 13899 (1991).

[172] S. Surnev, M. G. Ramsey, and F. P. Netzer, *Vanadium oxide surface studies*, Prog. Surf. Sci. **73**, 117 (2003).

[173] L. Jones, H. Yang, T. J. Pennycook, M. S. J. Marshall, S. Van Aert, N. D. Browning, M. R. Castell, and P. D. Nellist, *Smart Align—a new tool for robust non-rigid registration of scanning microscope data*, Adv. Struct. Chem. Imaging **1**, 8 (2015).

[174] L. Jones, S. Wang, X. Hu, S. ur Rahman, and M. R. Castell, *Maximising the resolving power of the scanning tunneling microscope*, Adv. Struct. Chem. Imaging **4**, 7 (2018).

[175] J. Sun, M. Passacantando, M. Palummo, M. Nardone, K. Kaasbjerg, A. Grillo, A. Di Bartolomeo, J. M. Caridad, and L. Camilli, *Impact of Impurities on the Electrical Conduction of Anisotropic Two-Dimensional Materials*, Phys. Rev. Appl. **13**, 044063 (2020).

[176] S. M. Tan and M. Pumera, *Two-Dimensional Materials on the Rocks: Positive and Negative Role of Dopants and Impurities in Electrochemistry*, ACS Nano **13**, 2681 (2019).

[177] P. K. Chow, R. B. Jacobs-Gedrim, J. Gao, T. M. Lu, B. Yu, H. Terrones, and N. Koratkar, *Defect-induced photoluminescence in monolayer semiconducting transition metal dichalcogenides*, ACS Nano **9**, 1520 (2015).

[178] M. F. Crommie, C. P. Lutz, and D. M. Eigler, *Confinement of electrons to quantum corrals on a metal surface*, Science **262**, 218 (1993).

[179] M. F. Crommie, C. P. Lutz, and D. M. Eigler, *Imaging standing waves in a two-dimensional electron gas*, Nature **363**, 524 (1993).

[180] E. J. Heller, M. F. Crommie, C. P. Lutz, and D. M. Eigler, *Scattering and absorption of surface electron waves in quantum corrals*, Nature **369**, 464 (1994).

[181] N. Knorr, H. Brune, M. Epple, A. Hirstein, M. A. Schneider, and K. Kern, *Long-range adsorbate interactions mediated by a two-dimensional electron gas*, Phys. Rev. B - Condens. Matter Mater. Phys. **65**, 115420 (2002).

[182] P. Avouris, *Real space imaging of electron scattering phenomena at metal surfaces*, J. Vac. Sci. Technol. B Microelectron. Nanom. Struct. **12**, 1447 (1994).

[183] W. Lefebvre, F. F. F. Vurpillot, X. Sauvage, W. Lefebvre, F. F. F. Vurpillot, and X. Sauvage, *Atom probe tomography: put theory into practice*, (Academic Press, 2016).

[184] A. Devaraj, R. Colby, F. Vurpillot, and S. Thevuthasan, *Understanding atom probe tomography of oxide-supported metal nanoparticles by correlation with atomic-resolution electron microscopy and field evaporation simulation*, J. Phys. Chem. Lett. **5**, 1361 (2014).

[185] P. M. Voyles, D. A. Muller, J. L. Grazul, P. H. Citrin, and H. J. L. Gossmann, *Atomic-scale imaging of individual dopant atoms and clusters in highly n-type bulk Si*, Nature **416**, 826 (2002).

[186] K. Van Benthem, A. R. Lupini, M. Kim, H. S. Baik, S. Doh, J. H. Lee, M. P. Oxley, S. D. Findlay, L. J. Allen, J. T. Luck, et al., *Three-dimensional imaging of individual hafnium atoms inside a semiconductor device*, Appl. Phys. Lett. **87**, 034104 (2005).

[187] A. Y. Borisevich, A. R. Lupini, and S. J. Pennycook, *Depth sectioning with the aberration-corrected scanning transmission electron microscope*, Proc. Natl. Acad. Sci. U. S. A. **103**, 3044 (2006).

[188] N. Shibata, S. D. Findlay, S. Azuma, T. Mizoguchi, T. Yamamoto, and Y. Ikuhara, *Atomic-scale imaging of individual dopant atoms in a buried interface*, Nat. Mater. **8**, 654 (2009).

[189] A. Weismann, M. Wenderoth, S. Lounis, P. Zahn, N. Quaas, R. G. Ulbrich, P. H. Dederichs, and S. Blügel, *Seeing the fermi surface in real space by nanoscale electron focusing*, Science **323**, 1190 (2009).

[190] T. Siahaan, O. Kurnosikov, H. J. M. Swagten, B. Koopmans, S. V. Kolesnikov, A. M. Saletsky, and A. L. Klavsyuk, *Co diffusion in the near-surface region of Cu*, Phys. Rev. B **94**, 195435 (2016).

[191] M. B. Johnson, O. Albrektsen, R. M. Feenstra, and H. W. M. Salemink, *Direct imaging of dopants in GaAs with cross-sectional scanning tunneling microscopy*, Appl. Phys. Lett. **63**, 2923 (1993).

[192] J. F. Zheng, X. Liu, N. Newman, E. R. Weber, D. F. Ogletree, and M. Salmeron, *Scanning tunneling microscopy studies of Si donors (SiGa) in GaAs*, Phys. Rev. Lett. **72**, 1490 (1994).

[193] M. C. M. M. van der Wielen, A. J. A. van Roij, and H. van Kempen, *Direct observation of friedel oscillations around incorporated SiGa dopants in GaAs by low-temperature scanning tunneling microscopy*, Phys. Rev. Lett. **76**, 1075 (1996).

[194] C. Domke, M. Heinrich, P. Ebert, and K. Urban, *Oscillating contrast in room-temperature scanning tunneling microscope images of localized charges in III–V semiconductor cleavage surfaces*, J. Vac. Sci. Technol. B **16**, 2825 (1998).

[195] C. Wittneven, R. Dombrowski, M. Morgenstern, and R. Wiesendanger, *Scattering states of ionized dopants probed by low temperature scanning tunneling spectroscopy*, Phys. Rev. Lett. **81**, 5616 (1998).

[196] M. R. Castell, D. A. Muller, and P. M. Voyles, *Dopant mapping for the*

nanotechnology age, Nat. Mater. **2**, 129 (2003).

[197] Y. S. Avotina, Y. A. Kolesnichenko, A. N. Omelyanchouk, A. F. Otte, and J. M. Van Ruitenbeek, *Method to determine defect positions below a metal surface by STM*, Phys. Rev. B - Condens. Matter Mater. Phys. **71**, 115430 (2005).

[198] Y. S. Avotina, Y. A. Kolesnichenko, S. B. Roobol, and J. M. Van Ruitenbeek, *Conductance of a tunnel point contact of noble metals in the presence of a single defect*, Low Temp. Phys. **34**, 207 (2008).

[199] Y. S. Avotina, Y. A. Kolesnichenko, and J. M. Van Ruitenbeek, *The signature of subsurface Kondo impurities in the local tunnel current*, J. Phys. Condens. Matter **20**, 115208 (2008).

[200] Y. S. Avotina, Y. A. Kolesnichenko, and J. M. van Ruitenbeek, *Theory of oscillations in STM conductance caused by subsurface defects*, Low Temp. Phys. **36**, 849 (2010).

[201] A. K. Schmid, J. C. Hamilton, N. C. Bartelt, and R. Q. Hwang, *Surface alloy formation by interdiffusion across a linear interface*, Phys. Rev. Lett. **77**, 2977 (1996).

[202] T. Flores, S. Junghans, and M. Wuttig, *Atomic mechanisms for the diffusion of Mn atoms incorporated in the Cu(100) surface: An STM study*, Surf. Sci. **371**, 1 (1997).

[203] M. L. Grant, B. S. Swartzentruber, N. C. Bartelt, and J. B. Hannon, *Diffusion kinetics in the Pd/Cu(001) surface alloy*, Phys. Rev. Lett. **86**, 4588 (2001).

[204] R. Van Gastel, E. Somfai, S. B. Van Albada, W. Van Saarloos, and J. W. M. Frenken, *Nothing moves a surface: Vacancy mediated surface diffusion*, Phys. Rev. Lett. **86**, 1562 (2001).

[205] R. Van Gastel, E. Somfai, W. Van Saarloos, and J. W. M. Frenken, *A giant atomic slide-puzzle*, Nature **408**, 665 (2000).

[206] R. Van Gastel, R. Van Moere, H. J. W. Zandvliet, and B. Poelsema, *Vacancy-mediated diffusion of Co atoms embedded in Cu(001)*, Surf. Sci. **605**, 1956 (2011).

[207] O. A. O. Adam, O. Kurnosikov, J. T. Kohlhepp, H. J. M. Swagten, W. J. M. De Jonge, and B. Koopmans, *Single-atom manipulation of Co embedded in Cu(001) surfaces*, Japanese J. Appl. Physics, Part 1 Regul. Pap. Short Notes Rev. Pap. **45**, 2014 (2006).

[208] O. Kurnosikov, J. T. Kohlhepp, and W. J. M. De Jonge, *Can surface embedded atoms be moved with an STM tip?*, Europhys. Lett. **64**, 77 (2003).

[209] M. L. Anderson, M. J. D'Amato, P. J. Feibelman, and B. S. Swartzentruber, *Vacancy-mediated and exchange diffusion in a Pb/Cu(111) surface alloy: Concurrent diffusion on two length scales*, Phys. Rev. Lett. **90**, 126102 (2003).

[210] A. S. Prostnev and B. R. Shub, *Diffusion of atoms incorporated in the surface layer of the fcc(111) face*, Russ. J. Phys. Chem. B **8**, 420 (2014).

[211] S. V. Kolesnikov, A. L. Klavsyuk, and A. M. Saletsky, *The role of the diffusion of dimers in the formation of Co nanostructures embedded into Cu(100) surface*, Eur. Phys. J. B **86**, 399 (2013).

[212] O. Bénichou and G. Oshanin, *Atomic slide puzzle: Self-diffusion of an impure atom*, Phys. Rev. E - Stat. Physics, Plasmas, Fluids, Relat. Interdiscip. Top. **64**, 4 (2001).

[213] S. V. Kolesnikov, A. L. Klavsyuk, and A. M. Saletsky, *Vacancy formation on stepped Cu(100) accelerated with STM: Molecular dynamics and kinetic Monte Carlo simulations*, Phys. Rev. B - Condens. Matter Mater. Phys. **80**, 245412 (2009).

[214] A. S. Prostnev and B. R. Shub, *Features of Diffusion of Lead Atoms Embedded into a Defective Cu(111) Surface*, Russ. J. Phys. Chem. B **13**, 543 (2019).

[215] L. Jones, S. Q. Wang, X. Hu, S. U. Rahman, and M. R. Castell, *Maximising the resolving power of the scanning tunneling microscope*, Adv. Struct. Chem. Imaging **4**, 7 (2018).

[216] J. Welker, A. J. Weymouth, and F. J. Giessibl, *The influence of chemical bonding configuration on atomic identification by force spectroscopy*, ACS Nano **7**, 7377 (2013).

[217] T. Hofmann, F. Pielmeier, and F. J. Giessibl, *Chemical and crystallographic characterization of the tip apex in scanning probe microscopy*, Phys. Rev. Lett. **112**, 066101 (2014).

[218] S. P. Jarvis, *Resolving intra- and inter-molecular structure with non-contact atomic force microscopy*, Int. J. Mol. Sci. **16**, 19936 (2015).

[219] M. Wagner, M. Setvín, M. Schmid, and U. Diebold, *Sexiphenyl on Cu(100): nc-AFM tip functionalization and identification*, Surf. Sci. **678**, 124 (2018).

[220] N. Knorr, M. A. Schneider, L. Diekhöner, P. Wahl, and K. Kern, *Kondo Effect of Single Co Adatoms on Cu Surfaces*, Phys. Rev. Lett. **88**, 4 (2002).

[221] V. S. Stepanyuk, A. N. Baranov, D. V. Tsivlin, W. Hergert, P. Bruno, N. Knorr, M. A. Schneider, and K. Kern, *Quantum interference and long-range adsorbate-adsorbate interactions*, Phys. Rev. B - Condens. Matter Mater. Phys. **68**, 205410 (2003).

[222] H. Prüser, M. Wenderoth, A. Weismann, and R. G. Ulbrich, *Mapping itinerant electrons around Kondo impurities*, Phys. Rev. Lett. **108**, 166604 (2012).

[223] K. A. Vikulov, A. Andreini, E. K. Poels, and A. Bliek, *Selective catalytic reduction of NO with NH3 over Nb2O5-promoted V2O5/TiO2 catalysts*, Catal. Letters **25**, 49 (1994).

[224] M. Xue, M. Nakayama, P. Liu, and M. G. White, *Electronic Interactions of Size-Selected Oxide Clusters on Metallic and Thin Film Oxide Supports*, J. Phys. Chem. C **121**, 22234 (2017).

[225] K. Suenaga and M. Koshino, *Atom-by-atom spectroscopy at graphene edge*, Nature **468**, 1088 (2010).

[226] E. Okunishi, H. Sawada, Y. Kondo, and M. Kersker, *Atomic resolution elemental map of EELS with a Cs corrected STEM*, Microsc. Microanal. **12**, 1150 (2006).

[227] H. Tan, S. Turner, E. Yücelen, J. Verbeeck, and G. Van Tendeloo, *2D atomic mapping of oxidation states in transition metal oxides by scanning transmission electron microscopy and electron energy-loss spectroscopy*, Phys. Rev. Lett. **107**, 107602 (2011).

[228] N. D. Browning, M. F. Chisholm, and S. J. Pennycook, *Atomic-resolution chemical analysis using a scanning transmission electron microscope*, Nature **366**, 143 (1993).

[229] K. Suenaga, Y. Sato, Z. Liu, H. Kataura, T. Okazaki, K. Kimoto, H. Sawada, T. Sasaki, K. Omoto, T. Tomita, et al., *Visualizing and identifying single atoms using electron energy-loss spectroscopy with low accelerating voltage*, Nat. Chem. **1**, 415 (2009).

[230] J. C. Meyer, S. Kurasch, H. J. Park, V. Skakalova, D. Künzel, A. Großß, A. Chuvilin, G. Algara-Siller, S. Roth, T. Iwasaki, et al., *Experimental analysis of charge redistribution due to chemical bonding by high-resolution transmission electron microscopy*, Nat. Mater. **10**, 209 (2011).

[231] W. Zhou, M. D. Kapetanakis, M. P. Prange, S. T. Pantelides, S. J. Pennycook, and J. C. Idrobo, *Direct determination of the chemical bonding of individual impurities in graphene*, Phys. Rev. Lett. **109**, 206803 (2012).

[232] M. Varela, M. P. Oxley, W. Luo, J. Tao, M. Watanabe, A. R. Lupini, S. T. Pantelides, and S. J. Pennycook, *Atomic-resolution imaging of oxidation states in manganites*, Phys. Rev. B - Condens. Matter Mater. Phys. **79**, 085117 (2009).

[233] H. Tian, J. Verbeeck, S. Brück, M. Paul, D. Kufer, M. Sing, R. Claessen, and G. Van Tendeloo, *Interface-induced modulation of charge and polarization in thin film Fe3O4*, Adv. Mater. **26**, 461 (2014).

[234] I. W. Lyo, P. Avouris, B. Schubert, and R. Hoffmann, *Elucidation of the initial stages of the oxidation of Si(111) using scanning tunneling microscopy and spectroscopy*, J. Phys. Chem. **94**, 4400 (1990).

[235] J. P. Pelz, *Successive oxidation stages and annealing behavior of the Si(111) 7×7 surface observed with scanning tunneling microscopy and scanning tunneling spectroscopy*, J. Vac. Sci. Technol. B Microelectron. Nanom. Struct. **9**, 775 (1991).

[236] D. Kaya, R. J. Cobley, and R. E. Palmer, *Combining scanning tunneling microscope (STM) imaging and local manipulation to probe the high dose oxidation structure of the Si(111)-7×7 surface*, Nano Res. **13**, 145 (2020).

[237] C. M. Yim, M. B. Watkins, M. J. Wolf, C. L. Pang, K. Hermansson, and G. Thornton, *Engineering Polarons at a Metal Oxide Surface*, Phys. Rev. Lett. **117**, 116402 (2016).

[238] J. K. Hulm, C. K. Jones, R. A. Hein, and J. W. Gibson, *Superconductivity in the TiO and NbO systems*, J. Low Temp. Phys. **7**, 291 (1972).

[239] K. Kunimori, Z. Hu, T. Uchijima, K. Asakura, Y. Iwasawa, and M. Soma, *Rhodium-niobia interaction in niobia-promoted Rh/SiO2 catalysts: formation of RhNbO4 on SiO2*, Catal. Today **8**, 85 (1990).

[240] S.-I. Ito, T. Fujimori, K. Nagashima, K. Yuzaki, and K. Kunimori, *Strong rhodium–niobia interaction in Rh/Nb2O5, Nb2O5–Rh/SiO2 and RhNbO4/SiO2 catalysts*, Catal. Today **57**, 247 (2002).

[241] J. Gao, J. Zhang, H. Liu, Q. Zhang, and J. Zhao, *Structures, mobilities, electronic and magnetic properties of point defects in silicene*, Nanoscale **5**, 9785 (2013).

[242] G. J. Slotman and A. Fasolino, *Structure, stability and defects of single layer hexagonal BN in comparison to graphene*, J. Phys. Condens. Matter **25**, 045009 (2013).

[243] T. Björkman, S. Kurasch, O. Lehtinen, J. Kotakoski, O. V. Yazyev, A. Srivastava, V. Skakalova, J. H. Smet, U. Kaiser, and A. V. Krasheninnikov, *Defects in bilayer silica and graphene: Common trends in diverse hexagonal two-dimensional systems*, Sci. Rep. **3**, 3482 (2013).

[244] J. Goniakowski and C. Noguera, *Properties of M2O3/Au(111) Honeycomb Monolayers (M = Sc, Ti, V, Cr, Mn, Fe, Co, Ni)*, J. Phys. Chem. C **123**, 9272 (2019).

[245] J. Goniakowski and C. Noguera, *Intrinsic Properties of Pure and Mixed Monolayer Oxides in the Honeycomb Structure: M2O3 and MM'O3 (M, M' = Ti, V, Cr, Fe)*, J. Phys. Chem. C **123**, 7898 (2019).

[246] B. S. Murty, M. K. Datta, and S. K. Pabi, *Structure and thermal stability of nanocrystalline materials*, Sadhana - Acad. Proc. Eng. Sci. **28**, 23 (2003).

[247] G. R. Harp, D. K. Saldin, and B. P. Tonner, *Finite-size effects and short-range crystalline order in Si and SiO 2 studied by X-ray absorption fine structure spectroscopy*, J. Phys. Condens. Matter **5**, 5377 (1993).

[248] J. Holovský and C. Ballif, *Thin-film limit formalism applied to surface defect absorption*, Opt. Express **22**, 31466 (2014).

[249] M. Ziolek, P. Decyk, I. Sobczak, M. Trejda, J. Florek, H. G. W. Klimas, and A. Wojtaszek, *Catalytic performance of niobium species in crystalline and amorphous solids - Gas and liquid phase oxidation*, Appl. Catal. A Gen. **391**, 194 (2011).

[250] Y. Xin, N. Zhang, Q. Li, Z. Zhang, X. Cao, L. Zheng, Y. Zeng, and J. A. Anderson, *Selective catalytic reduction of NOx with NH3 over short-range ordered W–O–Fe structures with high thermal stability*, Appl. Catal. B Environ. **229**, 81 (2018).

[251] L. Lichtenstein, M. Heyde, and H. J. Freund, *Crystalline-vitreous interface in two dimensional silica*, Phys. Rev. Lett. **109**, 106101 (2012).

[252] Y. Wei, J. Wu, H. Yin, X. Shi, R. Yang, and M. Dresselhaus, *The nature of strength enhancement and weakening by pentagon-heptagon defects in graphene*, Nat. Mater. **11**, 759 (2012).

[253] L. Gao, J. R. Guest, and N. P. Guisinger, *Epitaxial graphene on Cu(111)*, Nano Lett. **10**, 3512 (2010).

[254] S. Wang, X. Hu, J. Goniakowski, C. Noguera, and M. R. Castell, *Epitaxially Constrained Grain Boundary Structures in an Oxide Honeycomb Monolayer*, Adv. Mater. Interfaces **2102213**, (2022).

[255] A. W. Robertson, G. Do Lee, K. He, E. Yoon, A. I. Kirkland, and J. H. Warner, *Stability and dynamics of the tetravacancy in graphene*, Nano Lett. **14**, 1634 (2014).

[256] A. W. Robertson, G. Do Lee, K. He, E. Yoon, A. I. Kirkland, and J. H. Warner, *The role of the bridging atom in stabilizing odd numbered graphene vacancies*, Nano Lett. **14**, 3972 (2014).

[257] P. Hirvonen, Z. Fan, M. M. Ervasti, A. Harju, K. R. Elder, and T. Ala-Nissila, *Energetics and structure of grain boundary triple junctions in graphene*, Sci. Rep. **7**, 4754 (2017).

[258] S. Costantini, P. Alippi, L. Colombo, and F. Cleri, *Triple junctions and elastic stability of polycrystalline silicon*, Phys. Rev. B - Condens. Matter Mater. Phys. **63**, 453021 (2001).

[259] S. G. Srinivasan, J. W. Cahn, H. Jónsson, and G. Kalonji, *Excess energy of grain-boundary trijunctions: an atomistic simulation study*, Acta Mater. **47**, 2821 (1999).

[260] J. Engbæk, J. Schiøtz, B. Dahl-Madsen, and S. Horch, *Atomic structure of screw dislocations intersecting the Au(111) surface: A combined scanning tunneling microscopy and molecular dynamics study*, Phys. Rev. B - Condens. Matter Mater. Phys. **74**, 195434 (2006).

[261] R. C. Gonzalez, *Digital image processing, 3rd Edition*, (Pearson Education International, 1992).

[262] L. S. Levitov and G. B. Lesovik, *Charge distribution in quantum shot noise*, JETP Lett. C/C PIS'MA V ZHURNAL Eksp. Teor. Fiz. **58**, 230 (1993).

[263] B. Picinbono, C. Bendjaballah, and J. Pouget, *Photoelectron shot noise*, J. Math. Phys. **11**, 2166 (1970).

[264] H. Löwe and A. Van Herwijnen, *A Poisson shot noise model for micro-penetration of snow*, Cold Reg. Sci. Technol. **70**, 62 (2012).

[265] Y. M. Blanter and M. Büttiker, *Shot noise in mesoscopic conductors*, Phys. Rep. **336**, 1 (2000).

[266] W. C. van Etten, *Introduction to Random Signals and Noise*, (John Wiley & Sons, Ltd,

Chichester, UK, 2005).

[267] J. P. Perdew, K. Burke, and M. Ernzerhof, *Generalized gradient approximation made simple*, Phys. Rev. Lett. **77**, 3865 (1996).

[268] P. E. Blöchl, *Projector augmented-wave method*, Phys. Rev. B **50**, 17953 (1994).

[269] A. H. Larsen, J. J. Mortensen, J. Blomqvist, I. E. Castelli, R. Christensen, M. Dułak, J. Friis, M. N. Groves, B. Hammer, C. Hargus, et al., *The atomic simulation environment - A Python library for working with atoms*, J. Phys. Condens. Matter **29**, 273002 (2017).

[270] J. J. Mortensen, L. B. Hansen, and K. W. Jacobsen, *Real-space grid implementation of the projector augmented wave method*, Phys. Rev. B - Condens. Matter Mater. Phys. **71**, 035109 (2005).

[271] J. Enkovaara, C. Rostgaard, J. J. Mortensen, J. Chen, M. Dułak, L. Ferrighi, J. Gavnholt, C. Glinsvad, V. Haikola, H. A. Hansen, et al., *Electronic structure calculations with GPAW: A real-space implementation of the projector augmented-wave method*, J. Phys. Condens. Matter **22**, 253202 (2010).

[272] J. Tersoff and D. R. Hamann, *Theory of the scanning tunneling microscope*, Phys. Rev. B **31**, 805 (1985).

[273] A. A. Mostofi, J. R. Yates, G. Pizzi, Y.-S. Lee, I. Souza, D. Vanderbilt, and N. Marzari, *An updated version of wannier90: A tool for obtaining maximally-localised Wannier functions*, Comput. Phys. Commun. **185**, 2309 (2014).

[274] G. Pizzi, V. Vitale, R. Arita, S. Blügel, F. Freimuth, G. Géranton, M. Gibertini, D. Gresch, C. Johnson, and T. Koretsune, *Wannier90 as a community code: new features and applications*, J. Phys. Condens. Matter **32**, 165902 (2020).

[275] V. Y. Sharvin and M. L. Fisher., *Observation of focused electron beams in a metal*, ZhETF Pisma Redaktsiiu **1**, 152 (1965).

[276] T. F. Banchoff and S. T. Lovett, *Differential geometry of curves and surfaces*, (AK Peters/CRC Press, 2010).

[277] R. Goldman, *Curvature formulas for implicit curves and surfaces*, Comput. Aided Geom. Des. **22**, 632 (2005).

[278] Y. Liu, R. Zhang, Y. Ling, L. Lin, R. Mu, and Q. Fu, *Dynamic Structural Evolution of Mn-Au Alloy and MnOxNanostructures on Au(111) under Different Atmospheres*, J. Phys. Chem. C **125**, 15335 (2021).